Forschungszentrum Karlsruhe
Technik und Umwelt

Wissenschaftliche Berichte
FZKA 6198

Hot Plasma Target Interaction and Quantification of Erosion of the ITER Slot Divertor during Disruptions and ELMs

H. Würz, S. Pestchanyi, I. Landman, V. Safronov, F. Kappler, B. Bazylev, V. Tolkach, A. Burdakov, V. Koidan, D. Solyakov, V. Tereshin

Institut für Neutronenphysik und Reaktortechnik
Projekt Kernfusion

März 1999

Forschungszentrum Karlsruhe

Technik und Umwelt

Wissenschaftliche Berichte

FZKA 6198

Hot plasma target interaction and quantification of erosion of the ITER slot divertor during disruptions and ELMs

compiled by H. Würz

with contributions from

S. Pestchanyi[1], I. Landman[1], V. Safronov[1], F. Kappler,
B. Bazylev[2], V. Tolkach[2], A. Burdakov[3], V. Koidan[3], D. Solyakov[4],
V. Tereshin[4]

Institut für Neutronenphysik und Reaktortechnik

Projekt Kernfusion

[1] Troitsk Institute for Innovation and Fusion Research, 142092 Troitsk, Russia
[2] Luikov Institute of Heat and Mass Transfer, 220072 Minsk, Belarus
[3] Budker Institute of Nuclear Physics, 630090 Novosibirsk, Russia
[4] National Science Center Kharkov Institute of Plasma Physics, 310108 Kharkov, Ukrain

Forschungszentrum Karlsruhe GmbH, Karlsruhe
1999

The authors would like to dedicate this comprehensive report to Prof. Günther Keßler on occasion of his 65th anniversary. Without his continuous support and his encouragement as concerns cooperation with Russian Institutes this work couldn't have been completed.

Als Manuskript gedruckt

Forschungszentrum Karlsruhe GmbH
Postfach 3640, 76021 Karlsruhe

Mitglied der Hermann von Helmholtz-Gemeinschaft
Deutscher Forschungszentren (HGF)

ISSN 0947-8620

Abstract

For modelling of plasma shield efficiency and erosion by vaporization of the ITER slot divertor the 1 dim radiation-magnetohydrodynamics (R-MHD) code FOREV-1 and very recently the 2 dim R-MHD code FOREV-2 were developed. FOREV-2 uses a fully consistent 2 dim modelling based on a 2½ dim MHD model and a 2 dim radiation transport. This report discusses details of FOREV-2 and its validation against analytical and experimental results from disruption simulation experiments. The 2 dim analysis of the simulation experiments reveals that close to the target the MHD motion of the plasma shield becomes quite complex. Important are the boundary conditions for the magnetic field lines at the bulk target. Quite different plasma shield motion for carbon and quartz thus can be understood.

In the simulation experiments electron heat conduction is the dominating target heat flux. Radiation and energy deposition by the impacting hot plasma play only a minor role. In the tokamak case with hot plasma impact energy of 10 keV direct energy deposition by the hot SOL plasma and if peak power densities along the separatrix are above 50 MW/cm^2 radiation are the dominating target heat fluxes. At impact energies of the hot SOL plasma of 1 keV direct energy deposition becomes unimportant. Then the dominating target heat load sources are electron heat conduction and radiation rather similar to the situation at the simulation experiments. The good agreement of calculated and measured erosion for graphite and quartz targets despite their different magnetic properties and the different MHD behaviour of the plasma shields demonstrate that the numerical models used in FOREV-2 are adequate.

Results of a 2 dim analysis of the MHD motion of plasma shields for typical ITER tokamak not normal operating conditions are presented for horizontal (target perpendicular to the poloidal magnetic field) and vertical (target inclined to it) graphite targets. The influence of the MHD motion on target erosion is demonstrated and the nature of the MHD flow across the guiding magnetic field lines is clarified. The results demonstrate quite clearly that a 2 dim R-MHD modelling of the hot plasma wall interaction is of key importance for a quantification of erosion of the ITER slot divertor at not normal operating conditions.

Concerning melt splashing the analysis performed has demonstrated that up to now no adequate validation of models is available. The experiments performed up to now at the plasma gun facilities VIKA, PLADIS and QSPA are not at all tokamak typical and because of power densities above 2 MW/cm^2 mainly resulted in volumetric boiling but not in triggering of fluiddynamic instabilities. Therefore models claimed to exist for describing those instabilities can't be verified and conclusions for the tokamak situation can't be drawn up to now. Enhanced erosion as observed in e-beam experiments with several 10 keV electron energies at the facilities GOL-3 and JUDITH is confirmed by numerical results based on volumetric heating and phase transition inside the material using empirical values for the destruction threshold which for graphite is 10 kJ/g.

Zusammenfassung

Plasma Target Wechselwirkung und Erosion im ITER Schlitz Divertor während Plasmaabbrüchen und ELMs

Zur Berechnung der Abschirmwirkung eines Plasmaschildes und der Erosion durch Verdampfen wurde das 1 dim Strahlungs-Magnetohydrodynamik (S-MHD) Programm FOREV-1 und wird das 2 dim S-MHD-Programm FOREV-2 entwickelt. FOREV-2 basiert auf einer konsistenten 2 dim Modellierung mit einem 2½ dim MHD Modell und einem 2 dim Strahlungstransport. Dieser Bericht beschreibt FOREV-2 und seine Validierung an Hand von analytischen und experimentellen Resultaten aus Simulationsexperimenten. Die 2 dim Analyse der Simulationsexperimente zeigt eine komplexe MHD Bewegung des Plasmaschildes nahe am Target. Wichtig werden Randbedingungen für das Magnetfeld am Target. Damit können recht unterschiedliche Bewegungen des Plasmaschildes bei Graphit und Quarz Target interpretiert werden.

In den Simulationsexperimenten sind Elektronenwärmeleitung und Strahlung die dominierenden Wärmeflüsse am Target. Energiedeposition durch das auftreffende heiße Plasma spielt eine untergeordnete Rolle. Im Tokamakfall bei Impaktenergie des heißen Plasmas von 10 keV sind direkte Energiedeposition durch das heiße SOL Plasma und wenn Spitzenleistungsdichten größer 50 MW/cm^2 (entlang der Magnetfeldlinien) vorliegen auch Strahlung die dominierenden Wärmeflüsse. Bei Impaktenergien des heißen SOL Plasmas von 1 keV spielt die direkte Energiedeposition keine Rolle. Die dominierenden Targetwärmeflüsse sind dann Elektronenwärmeleitung und Strahlung. Diese Situation ist der in den Simulationsexperimenten sehr ähnlich.

Resultate einer 2 dim Analyse der MHD Bewegung von Plasmaschilden für ITER typische Plasmaabbrüche werden für horizontale (Target senkrecht zum poloidalen Magnetfeld) und vertikale (Target geneigt) Graphit Targets präsentiert. Der Einfluß der MHD Bewegung auf die Targeterosion wird demonstriert und die Ursache des Plasmaflusses quer zu den Vakuummagnetfeldlinien wird diskutiert. Die Resultate zeigen, daß eine 2 dim S-MHD Modellierung der heißen Plasma Wand Wechselwirkung von entscheidender Bedeutung ist für die Größe der Erosion im ITER Schlitz Divertor.

Was die Erosion aufgeschmolzener Schichten betrifft hat die durchgeführte Analyse gezeigt, daß bis jetzt keine realistische Modellvalidierung erfolgt ist. Die bisher durchgeführten Experimente an den Plasmagunanlagen VIKA, PLADIS und QSPA sind allesamt nicht Tokamak typisch und wegen der verwendeten Leistungsdichten größer 2 MW/cm^2 waren überwiegend volumetrisches Sieden und nicht fluiddynamische Instabilitäten für die Erosion der Schmelzschicht verantwortlich. Eventuell existierende Modelle zur Beschreibung fluiddynamischer Instabilitäten können somit nicht verifiziert werden. Damit können auch keine Folgerungen für die Tokamak Situation gezogen werden. Die verstärkte Erosion wie sie in Experimenten mit Elektronenstrahlen und mehreren 10 keV Elektronenenergien an den Anlagen GOL-3 und JUDITH beobachtet werden, wird durch numerische Ergebnisse basierend auf volumetrischer Heizung und Plasmaumwandlung im Innern des Materials ausreichend gut bestätigt, wenn empirische Werte für die Zerstörungsenergie (für Graphit 10 kJ/g) verwendet werden.

CONTENT

1. Introduction

During the thermal quench phase of a tokamak plasma disruption and during edge-localized models (ELMs), the divertor plates are hit by an intense flow of hot plasma. In the International Thermonuclear Experimental Reactor (ITER) this flow is estimated to have the following upper limit values: particle energy around 10 keV, pulse duration > 100 μs, and energy density up to 150 MJ/m^2 for disruptions and up to 10 MJ/m^2 for ELMs [1]. This high divertor heat load causes sudden evaporation of a thin layer of divertor plate material, which acts as a plasma shield and protects the divertor from further excessive evaporation [2]. After formation of the plasma shield the energy finally arriving at the target surface is by direct heating by the hot particles not stopped in the plasma shield, by radiation, and by electron heat conduction. A description of all these processes requires calculation of energy deposition into plasma shield and target, calculation of heat conduction inside the bulk target, including melt and vaporization front propagation, requires calculation of energy transport in the plasma shield, calculation of lateral radiative energy losses from the radiating plasma shield, calculation of momentum transfer from the hot plasma to the plasma shield, calculation of evolution of magnetic field inside the plasma shield and the target and calculation of the MHD movement of the plasma shield in the external magnetic field. A rather general discussion of the plasma shield effect is given in [3]. Theoretical tools for 1 dim numerical modelling of hot plasma wall interaction and for prediction of ITER divertor plate erosion by vaporization have been developed at several laboratories [4 - 6]. Recently the physical properties of essentially one-dimensional non-LTE carbon plasma shields formed in disruption simulation experiments were studied experimentally and theoretically [7]. The calculated plasma shield parameters such as time dependent plasma temperature and electron density distributions, conversion efficiency of deposited energy into radiation in the plasma shield, total and soft x-ray (SXR) radiation leakage fluxes from and energy balance in the plasma shield were in quite good agreement with the experimental values [8] thus demonstrating that the physical models used for a description of the hot plasma wall interaction at target heat load levels of MW/cm^2 are adequate.

The validated models then were used in detailed one-dimensional radiation-magnetohydrodynamics (R-MHD) calculations for ITER hard disruptions [9, 10]. Lat-

eral losses of plasma mass by across magnetic field motion and radiation from the plasma shield due to the finite width of the incoming hot plasma were taken into account in these 1 dim calculations by using simplified models [11]. Despite the fact that the inclined magnetic field decreases the expansion of the plasma shield perpendicular to the target, its shielding efficiency increased only slightly in comparison with zero magnetic field [12]. The plasma shields formed in powerful tokamak hot plasma wall interactions are two temperature plasmas with a rather cold, dense plasma close to the wall (atom densities up to 10^{19} cm^{-3}) and a low dense plasma corona (atom densities typically around 10^{15} cm^{-3}) with temperatures up to a few hundred eV [10].

Typical results on 1 dim calculated disruptive erosion are listed in Table 1 for graphite and beryllium. It was assumed that the impact energy of the hot plasma is 10 keV and that ions and Maxwellian distributed electrons contribute equally to the deposited energy. The erosion with plasma shield is reduced at least by a factor of 40 in comparison with the case without plasma shield. The thickness of the melt layer remains comparable for both cases. For metallic targets melt layer stability becomes quite important. A detailed analysis of melt layer erosion triggered by fluid dynamic instabilities and magnetic forces still needs to be done for ITER conditions. However because of rather large damages, if melt layer splashing can't be excluded, the use of beryllium as material for the slot divertor side walls must be excluded.

Going down in the heat load below 0.1 MW/cm^2 erosion by vaporization despite rather small erosion rates at surface temperatures slightly below boiling temperature becomes rather large in case without plasma shield. A first calculation of hot plasma target interaction for this case reveals that an effective plasma shield which could shield and absorb the hot plasma electrons is not existing as long as the temperature of the Maxwellian electrons is 10 keV and a sheath potential is not formed. The hot plasma ions always are fully stopped in the vapor above the target. The vapor density always remains below 10^{17} cm^{-3}. Therefore under the conditions hitherto assumed hot plasma streams of low power density could cause rather large erosion.

However before drawing final conclusions the following has to be checked: 1) what is the influence of the electron impact energy?, 2) what is the influence of the sheath potential which effectively decelerates electrons? and 3) what are the consequences

of a possible ExB drift of the impacting hot SOL plasma [13]? All these effects could result in an improved shielding of the plasma/vapor shield and thus could again decrease the quite large erosion values indicated in Table 1 for heat loads of the hot SOL plasma below 0.1 MW/cm^2.

For ITER a 2 dim modelling of hot plasma target interaction is required because of the tilting of the target in the poloidal plane and the subsequent complicated MHD behaviour of the plasma shield [14] and because of quantification of possible damages of the divertor wings by radiation emitted from the intensely radiating plasma shield in front of the in- and outboard targets [15].

The 2 dim radiation magnetohydrodynamics (R-MHD) code FOREV-2 is described and its validation against analytical solutions, against results from the 1 dim R-MHD code FOREV-1 and against results from disruption simulation experiments is discussed. Finally results of a 2 dim analysis of the MHD motion of plasma shields and of erosion by vaporization of the ITER slot divertor made from graphite and tungsten for power densities of the impacting hot plasma along the separatrix in the range of 3 to 100 MW/cm^2 are presented.

Hot plasma electrons and run away electrons are responsible for enhanced erosion. This type of erosion is based on volumetric heating and on phase transitions inside of the bulk target. Plasma shield effects here are unimportant. Phase transitions solid to melt may occur for volumetric target heating by electrons of several tens of keV. Experimental evidence was demonstrated in experiments at the facilities GOL-3 [16] and JUDITH [17]. In case of surface energy deposition (plasma streams and hot SOL plasma ions) overheating may occur. For this the target heat load must be above 2 MW/cm^2. In this case the temperature inside the melt layer may increase above boiling temperature. Explosive like boiling and volumetric bubble formation then may result in melt layer splashing. Experimental evidence is seen from experiments performed at the plasma gun facilities VIKA [18] and QSPA [19]. However the geometry was not at all ITER typical, the power density of the rather cold plasma stream was rather high and the time duration of the pulsed heat load was rather short. At power densities below 1 MW/cm^2 enhanced erosion is not occurring. Nevertheless melt layer erosion could occur initiated by fluiddynamic instabilities such a

Kelvin Helmholtz (tangential forces) and Rayleigh Taylor instabilities (forces perpendicular to the surface).

However an analysis of the consequences of such instabilities still is lacking for typical tokamak disruption conditions. Moreover lacking are experimental results based on experiments with plasma streams. For performance power densities below 1 MW/cm^2 should be used. The time duration of the pulse should be several hundreds of microseconds. Only results from those experiments could be used for testing of numerical models on melt layer erosion.

2. The simplified ITER slot divertor

The outboard wing of the slot divertor is shown schematically in Fig. 1a in the poloidal plane. The distance from the x point to the dump plate is about 2.0 m. The side wall distance is about 60 cm. The upper part of the side walls, the dump plate and most part of the dome are inclined (vertical target) with respect to the separatrix with downstream separatrix strike point (SSP). The coordinate system used in the 2 dim plasma target calculations is also indicated. The x coordinate is parallel to the separatrix, the y coordinate is across the SOL and the z coordinate is the toroidal direction. During disruptions and ELMs a shift of the separatrix can't be excluded [20]. Therefore the smaller dump plate and the tungsten dome could be hit during such an event too. In this case the following two different situations might arise: horizontal target and vertical target with separatrix upstream. This case is shown in Fig. 1b indicating the geometry as used in the 2 dim calculations with FOREV-2 and the asymmetrical (realistic) power density profile of the impacting hot plasma across the scrape off layer (SOL). In the case of separatrix downstream the power density profile is inverted as shown for the horizontal target. For the vertical target the target inclination angle is assumed to be 20°. In x direction the computational region extended up to 2.5 m. The unperturbed magnetic field lines $\vec{B}_0$ are assumed to have components in x- and z-direction according to $\vec{B}_0 = (B_x, B_y, B_z) = (0.5\ T, 0, 5\ T)$. Thus the impact angle of the hot SOL plasma in toroidal direction is 5°. The disruptive hot SOL plasma is assumed to consist from 10 keV plasma ions and 10 keV Maxwellian plasma electrons with equal energy carried by ions and electrons. FOREV-2 calcula-

tions were performed for Gaußian and for realistic power density profiles across the SOL. In the case of separatrix downstream the power density profile is inverted as shown for the horizontal target. The half width for the Gaußian profile was 5 cm, for the realistic profile was 4 cm. Peak power densities along the magnetic field lines ranging from 3 MW/cm^2 up to 100 MW/cm^2 were used up to now. (All power density values given are along the field lines.) In this 2 dim analysis of the ITER slot divertor only graphite targets (horizontal and vertical) were considered. For vertical targets the cases separatrix up- and downstream (this always is with reference to the x-point) were modelled.

Fig. 1c shows a horizontal target together with the evolving plasma shield, the inclined guiding magnetic field lines and because of the limited width D_{SOL} of the impacting plasma lateral radiation fluxes which hit the side walls and may cause damage there. Moreover MHD motion of cold target plasma across magnetic field lines may result in plasma mass losses (indicated as m_y in Fig. 1c) which could decrease the shielding efficiency of the plasma shield at the SSP.

The principle of hot SOL plasma target interaction schematically is shown in Fig. 1d.α denotes the inclination angle in z direction. At the beginning of this process the hot SOL plasma heats up the target, melting and vaporization occurs. The vaporized material starting with sound velocity perpendicular to the surface is further heated up by the hot plasma is ionized and expands along and across the external magnetic field lines. The energy after formation of the plasma shield finally arriving at the target surface at $x=x_o$ is by radiation S_r (x_o, y), by electron heat conduction S_c (x_o,y,α) and by direct heating by the hot plasma particles not stopped in the plasma shield (S_e (x_o, y, α) and S_i (x_o, y, α_o)).

A description of all these processes thus requires calculation of heat conduction inside the bulk target,including melt and vaporization front propagation, requires calculation of energy transport in the plasma shield, calculation of lateral radiative energy losses from the radiating plasma shield, calculation of energy deposition into shield and target, of momentum transfer from the hot plasma to the plasma shield, calculation of evolution of magnetic field inside the plasma shield and calculation of the MHD movement of the plasma shield in the external magnetic field.

3. The 2 dim radiation magnetohydrodynamics (R-MHD) code FOREV-2

3.1 The equations for plasma shield formation and time evolution

FOREV-2 is developed for a 2 dim modelling of the hot plasma target interaction in the ITER slot divertor in presence of an external magnetic field. FOREV-2 uses a 2½ dim MHD model which takes into account all 3 components of $\vec{B} = (B_x, B_y, B_z)$ but uses the fact that the main component B_z is constant along z (toroidal direction). 2½ dim means that all vector variables such as magnetic field, inductance and plasma velocity have three components, but in planar geometry variables depend only from the two coordinates x and y. The system of equations describing the 2½ dim MH model consists of the five conservation equations for the mass, for the three components of momentum and for the total energy of plasma and magnetic field, of the 4 Maxwell equations for the magnetic and electric field in the plasma and of Ohm's law.

$$\frac{\partial \rho}{\partial t} + \vec{\nabla}\rho\vec{u} = 0$$

$$\frac{\partial \rho u_x}{\partial t} + \vec{\nabla}\rho u_x\vec{u} + \frac{\partial}{\partial x}\left\{P + \frac{B^2}{2\mu_0}\right\} - \frac{1}{\mu_0}\left(\vec{B}\vec{\nabla}\right)B_x = F_x$$

$$\frac{\partial \rho u_y}{\partial t} + \vec{\nabla}\rho u_y\vec{u} + \frac{\partial}{\partial y}\left\{P + \frac{B^2}{2\mu_0}\right\} - \frac{1}{\mu_0}\left(\vec{B}\vec{\nabla}\right)B_y = 0 \qquad (1)$$

$$\frac{\partial \rho u_z}{\partial t} + \vec{\nabla}\rho u_z\vec{u} - \frac{1}{\mu_0}\left(\vec{B}\vec{\nabla}\right)B_z = 0$$

$$\frac{\partial}{\partial t}\left\{\rho e_i + \frac{\rho u^2}{2} + \frac{B^2}{2\mu_0}\right\} + \vec{\nabla}\left\{\vec{u}\left(\rho e_i + \frac{\rho u^2}{2}\right) + \hat{P}\cdot\vec{u} - \kappa\vec{\nabla}T_e + \vec{S}_{rad} + \frac{\vec{E}\times\vec{B}}{\mu_0}\right\} = Q$$

$$\frac{\partial \vec{B}}{\partial t} = -\vec{\nabla}\times\vec{E}$$

$$\frac{1}{\mu_0}\vec{\nabla}\mathrm{x}\vec{B} = \vec{j}$$

$$\vec{\nabla}\cdot\vec{B} = 0$$

$$\vec{\nabla} \cdot \vec{E} = \rho_e$$

$$\vec{E} + \vec{u} \times \vec{B} = \frac{1}{\sigma} \vec{j}$$

with ρ, $\vec{u}$, e_i, P the target plasma density, the velocity, the thermal energy and the pressure,

T_e the target plasma electron temperature,

$\vec{B}$ the magnetic field inductance,

$\vec{E}$ the electric field,

$\hat{P}$ the total pressure tensor of plasma and magnetic field,

σ the plasma conductivity,

$\hat{\kappa}$ the tensor of electron heat conductivity,

$\vec{j}$ the electric current density,

ρ_e the electric charge density,

F_x the volumetric force due to momentum transfer from the incoming hot SOL plasma,

Q power density deposited to the target plasma and the target by the incoming hot SOL plasma by collisional stopping,

$\vec{S}_{rad}$ the radiation heat flux,

$\vec{\nabla} \equiv \vec{i} \frac{\partial}{\partial x} + \vec{j} \frac{\partial}{\partial y}$ the gradient operator in 2 dim space of the model,

$\vec{i}$ and $\vec{j}$ are unit vectors in the x and the y direction correspondingly.

Viscosity terms in the momentum equation are neglected because of strong external heating by the impacting hot plasma. The external heating keeps energy transformation from directed motion into thermal energy negligible. For the calculation of the energy deposition Q into the plasma shield up to now only collisional stopping is modelled. Electric stopping of the hot plasma by electric fields was analysed [13], but up to now it is not implemented into the energy deposition model used in FOREV-2.

Boundary conditions for this system are provided by the treatment of the heat transport inside of the solid target and the vaporization of target material. The target heat load is given by the heat flux from the impacting hot SOL plasma, by electron heat conduction and by radiation from the target plasma. It is assumed that the target consists from bulk material. A reflective boundary condition is used at the target surface for the target plasma with an additional source of target substance due to vaporization. Boundary conditions for the side walls can be chosen as reflective, transparent or semitransparent for the target plasma and the magnetic field, with or with-

out vaporization of the side walls. Semitransparent boundary conditions with different degree of transparency simulate the side walls constructed from rods with different spaces in between.

Of concern are the boundary conditions for the magnetic field components B_x and B_z in the bulk target. B_z the toroidal magnetic field is parallel to the target heat surface and thus B_z moves freely at the target. The boundary condition for B_x at the target surface depends on the electric conductivity σ of the target material. For high σ B_x remains frozen in in the target despite a possible pushing out of B_x (diamagnetic effect) in the plasma shield. In this case a y component of magnetic field arises. The extension of the behaviour of the magnetic field into the bulk target allows a consistent description of the diamagnetic effect and its influence on the MHD behaviour of the plasma shield (see chapter 8.1). For medium conductivity σ (as for graphite) the magnetic field diffusion inside the bulk target has to be taken into account. The characteristic time τ for this diffusion is estimated to be

$$\tau = \frac{L^2}{v_m} \tag{2}$$

with L the target thickness and $v_m = c^2/4\pi\sigma$ the magnetic field diffusion coefficient with c the velocity of light.

B_x at the target surface (B_{BC}) is given according to

$$B_{BC}(t) = B_x(t) + \frac{t}{t+\tau}\Delta B_x(t) \tag{3}$$

with $\Delta B_x = B'_x - B_x$ and B'_x the magnetic field in the plasma shield and B_x the magnetic field in the target.

The system of equations is transformed into the identical form:

$$\frac{\partial \rho}{\partial t} = -\vec{\nabla}\rho\vec{u}$$

$$\frac{\partial \rho u_x}{\partial t} = -\vec{\nabla}\rho u_x\vec{u} - \frac{\partial}{\partial x}\left\{P + \frac{B^2}{2\mu_0}\right\} + \frac{1}{\mu_0}\left(\vec{B}\vec{\nabla}\right)B_x + F_x$$

$$\frac{\partial \rho u_y}{\partial t} = -\vec{\nabla}\rho u_y \vec{u} - \frac{\partial}{\partial y}\left\{P + \frac{B^2}{2\mu_0}\right\} + \frac{1}{\mu_0}\left(\vec{B}\vec{\nabla}\right)B_y$$

$$\frac{\partial \rho u_z}{\partial t} = -\vec{\nabla}\rho u_z \vec{u} + \frac{1}{\mu_0}\left(\vec{B}\vec{\nabla}\right)B_z \qquad (4)$$

$$\frac{\partial}{\partial t}\left\{\rho e_i + \frac{\rho u^2}{2} + \frac{B^2}{2\mu_0}\right\} + \vec{\nabla}\left\{\vec{u}\left(\rho e_i + \frac{\rho u^2}{2} + \frac{B^2}{2\mu_0}\right) + \left(\hat{P} + \frac{B^2}{2\mu_0}\right)\cdot\vec{u} - \frac{1}{\mu_0}\vec{B}\left(\vec{u}\vec{B}\right)\right\} +$$

$$\vec{B}\vec{\nabla}\times\left(\frac{1}{\sigma\mu_0^2}\vec{\nabla}\times\vec{B}\right) + \frac{1}{\sigma\mu_0^2}\left(\vec{\nabla}\times\vec{B}\right)^2 - \vec{\nabla}\left(\hat{\kappa}\vec{\nabla}T_e\right) + \vec{\nabla}\vec{S}_{rad} = Q$$

$$\frac{\partial \vec{B}}{\partial t} = \vec{\nabla}\left(\frac{1}{\sigma\mu_0}\vec{\nabla}\vec{B}\right) + \left(\vec{B}\vec{\nabla}\right)\vec{u} - \vec{B}\left(\vec{\nabla}\vec{u}\right) - \left(\vec{u}\vec{\nabla}\right)\vec{B}$$

where the Poynting vector term $\vec{\nabla}\frac{\vec{E}x\vec{B}}{\mu_o}$ and the equation for the magnetic field (see appendix A1) were rewritten by use of Ohm's law and Maxwell's equation. In the last equation of system (4) (the equation for the magnetic field) the first term on the right side describes the diffusion, the second term the convection of the magnetic field. The magnetic field equations for B_x, B_y, B_z write as follows:

$$\frac{\partial B_x}{\partial t} = \frac{\partial}{\partial x}\left(\frac{1}{\sigma\mu_0}\frac{\partial B_x}{\partial x}\right) + \frac{\partial}{\partial y}\left(\frac{1}{\sigma\mu_0}\frac{\partial B_x}{\partial y}\right) + \frac{\partial}{\partial y}\left(B_y u_x - B_x u_y\right)$$

$$\frac{\partial B_y}{\partial t} = \frac{\partial}{\partial x}\left(\frac{1}{\sigma\mu_0}\frac{\partial B_y}{\partial x}\right) + \frac{\partial}{\partial y}\left(\frac{1}{\sigma\mu_0}\frac{\partial B_y}{\partial y}\right) + \frac{\partial}{\partial x}\left(B_x u_y - B_y u_x\right) \qquad (5)$$

$$\frac{\partial B_z}{\partial t} = \frac{\partial}{\partial x}\left(\frac{1}{\sigma\mu_0}\frac{\partial B_z}{\partial x}\right) + \left(\frac{1}{\sigma\mu_0}\frac{\partial B_y}{\partial x}\right) + \frac{\partial}{\partial x}\left(B_x u_z - B_z u_x\right) + \frac{\partial}{\partial y}\left(B_y u_z - B_z u_y\right)$$

3.2 The splitting procedure

To solve the system of equations (4) the 'Large Particles' method [21] is used. In this method full time step calculation is splitted into several substeps following each other and taking into account different physical processes described by the system of equations (4). These processes are

1. MHD movement of the plasma shield,
2. magnetic field diffusion
3. heating and momentum transfer to the target plasma by incoming hot plasma,
4. radiation transport,
5. energy redistribution between ions, electrons and internal excitations of ions,
6. electron heat conduction,
7. solid target heating by incoming hot SOL plasma, by radiation and by electron heat conduction to the target,
8. heat conduction inside the solid target,
9. target melting
10. target vaporization

According to the Large Particle method the MHD movement of the target plasma is split into two substeps a Lagrangian and an Eulerian one, with the Lagrangian step as first substep. It is followed by the Eulerian substep. In the Lagrangian substep of the splitting method mesh boundary velocities are calculated using the terms of the system of equations (4) which contain force terms only.

$$\frac{\partial \rho}{\partial t} = 0$$

$$\frac{\partial \rho u_x}{\partial t} + \frac{\partial}{\partial x}\left\{P + \frac{B^2}{2\mu_0}\right\} - \frac{1}{\mu_0}\left(\vec{B}\vec{\nabla}\right)B_x = 0$$

$$\frac{\partial \rho u_y}{\partial t} + \frac{\partial}{\partial y}\left\{P + \frac{B^2}{2\mu_0}\right\} - \frac{1}{\mu_0}\left(\vec{B}\vec{\nabla}\right)B_y = 0 \qquad (6)$$

$$\frac{\partial \rho u_z}{\partial t} - \frac{1}{\mu_0}\left(\vec{B}\vec{\nabla}\right)B_z = 0$$

$$\frac{\partial}{\partial t}\left\{\rho e_i + \frac{\rho u^2}{2} + \frac{B^2}{2\mu_0}\right\} + \vec{\nabla}\left\{\left(\hat{P} + \frac{B^2}{2\mu_0}\right)\cdot\vec{u}\right\} - \frac{1}{\mu_0}\left(\vec{B}\vec{\nabla}\right)\left(\vec{u}\vec{B}\right) = 0$$

$$\frac{\partial B_x}{\partial t} = 0$$

$$\frac{\partial B_y}{\partial t} = 0$$

$$\frac{\partial B_z}{\partial t} = \left(\vec{B}\vec{\nabla}\right)u_z$$

The term $(\vec{B}\vec{\nabla})(\vec{u}\vec{B})$ in the energy balance equation was obtained from $\vec{\nabla}(\vec{B}(\vec{u}\vec{B}))$ according to:

$$\vec{\nabla}(\vec{B}(\vec{u}\vec{B})) = (\vec{u}\vec{B})(\vec{\nabla}\vec{B}) + (\vec{B}\vec{\nabla})(\vec{u}\vec{B}) = (\vec{B}\vec{\nabla})\ (\vec{u}\vec{B})$$

As a result of the Lagrangian substep the mesh is shifted and stretched by the velocity field calculated in this substep (expanded mesh). Fig. 2 schematically indicates this situation and shows the Eulerian mesh and the new positions of the expanded mesh. The shifting of the meshes is enlarged for better unstanding.

The remaining system of equations still to be solved is given as:

$$\begin{aligned}
&\frac{\partial \rho}{\partial t} + \vec{\nabla}\rho\vec{u} = 0 \\
&\frac{\partial \rho u_x}{\partial t} + \vec{\nabla}\rho u_x\vec{u} = 0 \\
&\frac{\partial \rho u_y}{\partial t} + \vec{\nabla}\rho u_y\vec{u} = 0 \\
&\frac{\partial \rho u_z}{\partial t} + \vec{\nabla}\rho u_z\vec{u} = 0 \\
&\frac{\partial}{\partial t}\left\{\rho e_i + \frac{\rho u^2}{2} + \frac{B^2}{2\mu_0}\right\} + \vec{\nabla}\left\{\vec{u}\left(\rho e_i + \frac{\rho u^2}{2} + \frac{B^2}{2\mu_0}\right)\right\} = 0 \\
&\frac{\partial \rho A_z}{\partial t} + \vec{\nabla}\left(\rho A_z\vec{u}\right) = 0 \\
&\frac{\partial B_z}{\partial t} + \vec{\nabla}\left(B_z\vec{u}\right) = 0
\end{aligned} \tag{7}$$

where the z-component of the vector-potential A_z is used instead of 2 components of the magnetic field B_x and B_y:

$$B_x = \frac{\partial A_z}{\partial y} \quad B_y = \frac{\partial A_z}{\partial x} \tag{8}$$

The magnetic field equation with the vector potential A_z describes the convective terms in the expressions of the magnetic field components B_x and B_y (see Appendix A.2).

For the z component of the convective term in the equation of the magnetic field the following expression was used (see Appendix A.1)

$$\frac{\partial B_z}{\partial t}\left(\vec{B}\vec{\nabla}\right)u_z - \vec{\nabla}\left(B_z\vec{u}\right) \tag{9}$$

The first term of the right hand side (RHS) is used in the Lagrangian substep, the second term in the Eulerian substep of the MHD splitting step.

The system of equations (5) contains convective terms. According to [21] it is solved automatically by redistributing of all physical quantities from the expanded mesh back to the Eulerian mesh. For this redistribution it is assumed that all quantities are uniformly distributed in the meshes. New values for the Eulerian meshes are obtained by summing up and averaging the values from all expanded meshes which are covered by the Eulerian mesh. For example the new mass M_n of an Eulerian mesh is obtained from the expression

$$M_n = (1/S)\,\Sigma M_i DS_i \tag{10}$$

with S the area of the Eulerian mesh, M_i the masses of the evolved expanded meshes and DS_i their contribution to the Eulerian mesh.

In the heating substep heating and momentum transfer from the incoming hot SOL plasma is taken into account by solving the equations.

$$\frac{\partial \rho u_x}{\partial t} = F_x \tag{11}$$
$$\frac{\partial}{\partial t}\left\{\rho e_i + \frac{\rho u^2}{2}\right\} = Q$$

Q the power density deposited by the incoming hot plasma into the solid target and the target plasma is calculated for collisional stopping of hot plasma ions and electrons. The plasma ions are assumed to be monoenergetic. The plasma electrons are Maxwellian distributed.

Q is given according to

$$Q = Q_{hi} + Q_{he\|} = N_{ion} v_{ion} \frac{dE_{ion}}{dx} + \sum_l N_l v_l \frac{dE_l}{dx} \qquad (12)$$

with $v_l = \int_{\Delta v_l} v f_M(v) dv$ and $f_M(v)$ the Maxwellian distribution function of the plasma electrons. For the calculation of the energy deposition dE/dx and the energy groups Δv_l see chapter 6.

The densities N_{ion} and $N = \Sigma N_l$ are obtained from the requirement that ions and electrons each are carrying 50 % of the energy of the hot plasma.

The momentum transfer F_x of the hot ions to the target plasma is given according to

$$F_x = N v_{ion} \frac{dp_{ion}}{dx} = N v_{ion} \sqrt{\frac{M}{2E_{ion}}} \frac{dE_{ion}}{dx} \qquad (13)$$

with E_{ion} the energy of the hot ions

and M the ion mass.

In the magnetic field diffusion substep the following terms in the system of equations (4) are taken into account.

$$\frac{\partial \vec{B}}{\partial t} = \vec{\nabla}\left(\frac{1}{\sigma\mu_0}\vec{\nabla}\vec{B}\right)$$

$$\frac{\partial \vec{u}}{\partial t} = 0 \qquad (14)$$

$$\frac{\partial}{\partial t}\left\{\rho e_i + \frac{\rho u^2}{2} + \frac{B^2}{2\mu_0}\right\} + \vec{B}\vec{\nabla}\times\left(\frac{1}{\sigma\mu_0^2}\vec{\nabla}\times\vec{B}\right) - \frac{1}{\sigma\mu_0^2}\left(\vec{\nabla}\times\vec{B}\right)^2 = 0$$

The last equation of this system is transformed using the first and the second one into the following equation

$$\frac{\partial}{\partial t}\{\rho e_i\} + \frac{1}{\sigma\mu_0^2}\left(\vec{\nabla}\times\vec{B}\right)^2 = 0, \qquad (15)$$

Eq. (15) describes Ohmic heating during diffusion.

The first equation of system (14) is the magnetic field diffusion equation with the diffusion coefficient $D = 1/\sigma\mu_0$. In classical magnetic field diffusion the Spitzer expression for the conductivity σ [47] is used according to

$$\sigma_{\parallel} = 2.0\sigma_{\perp} = 2.0\frac{Ne^2\tau_e}{m_e} \tag{16}$$

With N the electron density, e the electron charge, me the electron mass and τe the electron collisional time, given as

$$\tau_e = \frac{\sqrt[3]{m_e}(kT_e)^{3/2}}{\sqrt[4]{2\pi}n\lambda e^4} \tag{17}$$

with k the Boltzmann constant, T_e the electron temperature and λ the Coulomb logarithm. The real diffusion coefficient in the plasma shield is unknown and could be determined by plasma turbulence. To estimate the influence of turbulence on the MHD behaviour of the plasma shield Bohm diffusion coefficient D_{Bohm} could be used as an upper limit. D_{Bohm} is given as

$$D_{Bohm} = \frac{D_{cl}}{16}\cdot(1+\omega_{ce}\tau_e) \tag{18}$$

With D_{cl} the classical diffusion coefficient with Spitzer conductivity and $\omega_{ce} = \frac{eB}{m_e c}$ the electron cyclotron frequency with Be the magnetic field and c the velocity of light.

In the electron heat conduction substep the following equation has to be solved

$$\frac{\partial}{\partial t}\{\rho e_i\} - \vec{\nabla}\left(\hat{\kappa}\vec{\nabla}T_e\right) = 0 \tag{19}$$

where the electron heat conductivity coefficient $\hat{k}_e$ has two different eigenvalues: parallel and perpendicular to the direction of the magnetic field lines.

The two eigenvalues $\kappa_{\parallel}$ and $\kappa_{\perp}$ according to [22] are given as

$$\kappa_{\perp} = W_{\perp} \frac{N_e T_e \tau_e}{m_e}$$
$$\kappa_{\parallel} = W_{\parallel} \frac{N_e T_e}{m_e \omega_{ce}^2 \tau_e} \qquad (20)$$

The calculation of electron heat conduction fluxes in the plasma shield is straight forward. The calculation of these fluxes to the target is rather delicate. For a detailed discussion see chapter 8.1.

The dimenless factors $W_{\parallel}$ and $W_{\perp}$ depend on the effective charge and the plasma frequency ω_{ce} via the parameter $X_e = \omega_{ce}\tau_e$ as

$$W_{\parallel} = 12.5 - \frac{9.34}{1+0.223(Z-)} \quad W_{\perp} \frac{g_0 + g_1 x_e^2}{d_0 + d_1 x_e^2 + x_e^4} \qquad (21)$$

With the additional coefficients g_0, g_1, d_0 and d_1 given as

$$g_0 = 1.2 + \frac{10.72}{1+1.805(Z-1)}, \qquad g_1 = 3.25 + \frac{1.414}{Z}$$
$$d_0 = 0.096 + \frac{3.674}{1+3.285(Z-1)}, \qquad d_1 = 7.482 + \frac{7.308}{1+1.211(Z-1)} \qquad (22)$$

The given approximations for the factors $W_{\parallel}$ and $W_{\perp}$ agree with the corresponding tables of ref. [22] within 10 %.

In the substep dealing with radiation transport a newly developed 2 dim angular dependent radiation transport scheme based on the forward-reverse method with multigroup opacities as described in chapter 4 is used.

3.3 Physical processes inside the target

The treatment of the physical processes inside the target is a matter of two substeps. The first one is the calculation of the heat conduction in the solid and the liquid target using the heat fluxes from the plasma region. This substep has to be performed after calculation of all fluxes during substeps dealing with the plasma shield. For the solution of the 2 dim heat conduction equation for the target with volumetric and surface sources of heating and with phase transition between solid and liquid a local one-

dimensional technique is used. It is assumed that the incoming heat fluxes from hot SOL plasma ions q_{hi}, from radiation q_{rad} and from electron heat conduction q_{el} are deposited at the target surface. The Maxwellian plasma electrons from the incoming hot SOL plasma are volumetrically heating the bulk of the target.

The 2 dim heat conduction equation is given as

$$\rho c \frac{\partial T}{\partial t} + \vec{\nabla}\left(\kappa \vec{\nabla} T\right) = Q_{he} \tag{23}$$

The heat capacity c(T) is given as

$$c(T) = \begin{cases} c_s, if\ T < T_m - \dfrac{\Delta T}{2} \\ \dfrac{1}{2}(c_s + c_l) + \dfrac{Q_m}{\Delta T}, if\ T_m - \dfrac{\Delta T}{2} < T < T + \dfrac{\Delta T}{2} \\ c_l, if\ T_m + \dfrac{\Delta T}{2} < T < T_v \end{cases} \tag{24}$$

With c_s the heat capacity of the solid target

c_l the heat capacity of the liquid

Q_m the heat of melting

$\Delta T \ll T_m$ small temperature intervall (usually ΔT = 0.01 T_m) used for numerical simulation of the phase transition between the solid and the liquid phase

$$\kappa(T) = \begin{cases} \kappa_s, T < T_m \\ \kappa_l, T > T_m \end{cases} \tag{25}$$

Q_{he} the volumetric heating by hot plasma electrons

The boundary between the solid and liquid phase inside the target is defined by the condition $T(x,y) = T_m + \Delta T$. The heat conduction equation is solved in 3 substeps by using a one dimensional technique in x and y direction, according to

$$\begin{aligned} \rho c \frac{\partial T}{\partial x} &= \frac{\partial}{\partial x}\left(\kappa \frac{\partial T}{\partial x}\right) \\ \rho c \frac{\partial T}{\partial t} &= \frac{\partial}{\partial y}\left(\kappa \frac{\partial T}{\partial y}\right) \end{aligned} \tag{26}$$

The volumetric heating by the hot plasma is taken into account according to

$$\rho c \frac{\partial T}{\partial t} = Q_{he} = \sum_l N_l v_l \frac{dE_l}{dx} \tag{27}$$

For calculation of $\frac{dE_l}{dx}$ of see chapter 6.2.

The boundary conditions for eq.(23) are

$T_{x\to\infty} \to T_{room}$ and at the evaporating surface

$$\begin{aligned} -\kappa \frac{\partial T}{\partial t}\Big|_{x=0} &= q_{el} + q_{hi} + q_{rad} = q_\Sigma \; if \; T(x=0) < T_{boil} \\ and \; T &= T_{boil} \; if \; T = T_{boil} \; and \; q_\Sigma > -\kappa \frac{\partial T}{\partial x}\Big|_{x=0} \end{aligned} \tag{28}$$

If at some time moment q_Σ becames smaller than the heat flux into the wall then the boundary condition is switched to the first one:

$$-\kappa \frac{\partial T}{\partial x}\Big|_{x=0} = q_\Sigma$$

Although principally the 2 dim heat conduction equation is used in FOREV-2 its solution in x-direction only is sufficient because the characteristic length of the temperature distribution in y-direction (along the target) is about 4 orders of magnitude larger than in x-direction.

The substep dealing with solid wall vaporization follows the substep of heat conduction into the target. The heat flux into the target $\left(-\kappa \frac{\partial T}{\partial x}\Big|_{x=0}\right)$ is compared with the total heat flux q_Σ from the plasma region onto the target. If the last one is greater than the first one then the difference between these two fluxes is spent for vaporization $q_{vap} = q_\Sigma + \kappa \frac{\partial T}{\partial x}\Big|_{x=0}$. The evaporated material is deposited to the plasma shield adjacent to the mesh where vaporization occurred.

3.4 Boundary conditions

FOREV-2 allows to calculate for horizontal and vertical targets as is schematically shown in Fig. 3 a and b. Horizontal and vertical is with reference to the poloidal plane (x,y). In toroidal direction (z) the inclination angle of the hot plasma always is given by $\vec{B} = (B_x, B_y, B_z) = (0.5\ T, 0, 5\ T)$. Available are transparent and reflecting (non-transparent) boundary conditions. Transparent means the plasma expands freely into vacuum or into a low dense background gas, nontransparent means the plasma expansion is stopped at rigid walls. For dealing with boundary conditions artificial meshes are created as is shown in Fig. 3. The boundary conditions then are imposed as physical values on these artificial meshes. In case of the horizontal target the artificial meshes just are an additional layer of Eulerian meshes. In case of the vertical target the artificial meshes are chosen as meshes adjacent to the meshes crossed by the target (see Fig. 3 b).

In case of horizontal target and transparent walls the momentum vector in the artificial meshes is identical to that of the neighbouring meshes. In case of nontransparency the perpendicular momentum has negative sign in comparison with the neighbouring meshes. In case of vertical target the artificial meshes are reflected at the target plane to obtain the image meshes. Now in case of transparency the momentum vector of the artificial mesh is identical to that of the image mesh what means $\partial u_\perp/\partial n = 0$. In case of nontransparency the perpendicular momentum in the artificial mesh has opposite sign to that of the image mesh what means $u_\perp = 0$ at the boundary. All other physical parameters such as temperature and density are identical to the neighbouring respective the image meshes.

Intermediate conditions between transparency and non transparency are also possible. The two parameters α and β are used according to

$$\alpha \frac{du_\perp}{dx} + \beta u_\perp = 0 \tag{29}$$

For the momentum ρu^a in the artificial mesh it is obtained from eq. (29):

$$u^a = \frac{2\alpha - \beta\Delta x}{2\alpha + \beta\Delta x} u^b \tag{30}$$

with ρu^b the momentum in the boundary mesh and Δx the width of the mesh.

3.5 Features of the code

FOREV-2 uses the physical models developed for the 1 dim Lagrangian code FOREV-1 and validated against experimental results from simulation experiments [8]. The features implemented in FOREV-2 are listed in Table 2. Two separate grids are used for solid and vapor, the meshes are non-uniform in x-direction and up to date optical data are used in tabulated form for the 2 dim radiation transport (see chapter 5).

For numerical solution of the system of equations (4) all equations are integrated over the rectangular mesh. For example for the equation of the x component of the momentum ρu_x (second equation of the system) it is obtained

$$\iint_{\text{cell area}} \left(\frac{\partial \rho u_x}{\partial t} + \frac{\partial}{\partial x}\left\{ P + \frac{B^2}{2\mu_0} \right\} - \frac{1}{\mu_0}(\vec{B}\vec{\nabla})B_x \right) dxdy = 0. \tag{31}$$

This equation describes the x component of the total plasma momentum inside the mesh $P_x = \iint_{\text{mesh}} \rho u_x dxdy$.

After integration it is obtained

$$\frac{\partial P_x}{\partial t} + \int_{\substack{\text{left cell} \\ \text{boundary}}} \left\{ P - \frac{B^2}{2\mu_0} \right\} dv - \int_{\substack{\text{right cell} \\ \text{boundary}}} \left\{ P - \frac{B^2}{2\mu_0} \right\} dy - \iint_{\text{cell area}} \left(\frac{1}{\mu_0}(\vec{B}\vec{\nabla})B_x \right) dxdy = 0. \tag{32}$$

The last term of this equation and the similar terms in the third, forth, fifth and eighth equation of system (4) can be written as

$$(\vec{B}\vec{\nabla})f = \left(B_x \frac{df}{dx} + B_y \frac{df}{dy} \right) = \left[\vec{\nabla} f \times \vec{\nabla} A_z \right]_z \tag{33}$$

with A_z the component of the vector potential and f = B_y, B_x, B_z, $(\vec{u}\vec{B})$ and/or u_z. Integration of eq. (21) over the mesh results in

$$\iint_{\text{cell area}} \left[\vec{\nabla} f \times \vec{\nabla} A_z\right] dxdy = \oint_{\text{cell boundary}} f\, dA_z \tag{34}$$

For a rectangular mesh the RHS integral yields

$$\oint_{\text{cell boundary}} f\, dA_z = f_1\left(A_z^{12} - A_z^{14}\right) + f_2\left(A_z^{23} - A_z^{12}\right) + f_3\left(A_z^{34} - A_z^{23}\right) + f_4\left(A_z^{14} - A_z^{34}\right) \tag{35}$$

where the indices 1 – 4 designate the mesh boundaries and the pairs 12, 23, 34, 14 the corners between corresponding boundaries. Finally eq. (31) is written as

$$\begin{aligned} P_{x,i,j}^{n+1} = P_{x,i,j}^{n} + dt * \Bigg(& \left\{ P_{i-1/2,j}^{n} + \frac{B_{i-1/2j}^{n\ 2}}{2\mu_0} \right\} L_y - \left\{ P_{i+1/2,j}^{n} + \frac{B_{i+1/2j}^{n\ 2}}{2\mu_0} \right\} L_y + \\ & B_{x,i-1/2j}^{n}\left(A_{z,i-1/2,j-1/2}^{n} - A_{z,i-1/2,j+1/2}^{n}\right) + B_{x,i,j-1/2}^{n}\left(A_{z,i+1/2,j-1/2}^{n} - A_{z,i-1/2,j-1/2}^{n}\right) + \\ & B_{x,i+1/2,j}^{n}\left(A_{z,i+1/2,j+1/2}^{n} - A_{z,i+1/2,j-1/2}^{n}\right) + B_{x,i,j-1/2}^{n}\left(A_{z,i-1/2,j+1/2}^{n} - A_{z,i+1/2,j+1/2}^{n}\right) \Bigg) \end{aligned} \tag{36}$$

with (i,j) the mesh center and i the time step. In the Eulerian substep the system of eqs. (7) is solved.

All these equations have the same form:

$$\frac{\partial g}{\partial t} + \vec{\nabla} g\vec{u} = 0 \tag{37}$$

With $g = \rho, \rho u_x, \rho u_y, \rho u_z, \left\{ \rho e_i + \frac{\rho u^2}{2} + \frac{B^2}{2\mu_0} \right\}, \rho A_z, B_z$ correspondingly. After performance of the same integration over a mesh as in the Lagrange substep the following expression is obtained

$$\frac{\partial G}{\partial t} + \oint_{\text{cell boundary}} d\vec{S} \cdot g\vec{u} = 0 \tag{38}$$

where $G = \iint_{\text{cell area}} g dxdy$ is total quantity of physical value g inside the cell and the second term of the equation represents the algebraic sum of the fluxes $\vec{F} = g\vec{u}$ through

the cell boundaries and is treated according to the Belocerkovsky technique using Lagrangian and Eulerian meshes [21].

4. Improvement of the code FOREV-2

Code improvement concentrated on the following activities: 1) investigation and removal of various instabilities resulting in sudden changes of plasma temperature and in sharp drops of time step sizes, 2) taking into account the full magnetic field equations for all three magnetic field components B_x, B_y and B_z, 3) handling of different opacities for emission and absorption (use of non-LTE optical data), 4) first activities to ensure that ions deposit their energy permanently into several meshes, 5) use of nonhomogeneous meshes in x direction, 6) drastic increase of time step size 7) improvement of numerical scheme for 2 dim calculation of anisotropic radiation transport and 8) magnetic field behaviour in the bulk target to arrive at a consistent treatment of possible diamagnetic effects of the plasma shield.

4.1 Instabilities

For MHD calculations of low β plasma $\left(\beta = \frac{8\pi P}{B^2} << 1\right)$ the Courant criterion is not sufficient for calculational stability. The plasma thermal energy is calculated as difference between the total energy and the magnetic field energy. In the background plasma region with $\beta << 1$ the magnetic field energy can be several orders of magnitude larger than the plasma thermal energy. The thermal energy thus is calculated as difference of two very large and almost equal numbers. Consequently, errors in the calculated values of the total and the magnetic field energy being small relatively to the value itself can be rather large in comparison with the plasma thermal energy. This can result either in artificial overheating or overcooling of the background plasma, or in a drastic (several orders of magnitude) decrease of the time step size. To overcome this difficulty second order terms for the time step are introduced into the total energy calculation. The expressions for the second order terms were de-

rived from the evolution of the x, y and z components of the plasma momentum, from the changes of the magnetic field and from the corresponding term in the equation of the total energy E. Taking into account only the terms with magnetic field it is obtained:

$$\frac{\partial B_i}{\partial t} = \left(\vec{B}\vec{\nabla}\right)u_i, \qquad i = (x, y, z),$$

$$\frac{\partial \rho u_i}{\partial t} = \frac{1}{\mu_0}\left(\vec{B}\vec{\nabla}\right)B_i, \tag{39}$$

$$\frac{\partial E}{\partial t} = \frac{1}{\mu_0}\left(\vec{B}\vec{\nabla}\right)u_i B_i,$$

with E the total energy defined according to

$$E = \frac{B^2}{2\mu_0} + \frac{\rho u^2}{2}.$$

To solve this system of partial differential equations it is approximated by finite differences. Thus the time evolution is given as

$$B_i^{n+1} = B_i^n + \left(\vec{B}^n\vec{\nabla}\right)u_i^n \Delta t$$

$$\mathrm{u}_\mathrm{i}^{\mathrm{n+1}} = \mathrm{u}_\mathrm{i}^{\mathrm{n}} + \frac{1}{\rho\mu_0}\left(\vec{\mathrm{B}}^{\mathrm{n}}\vec{\nabla}\right)\vec{\mathrm{B}}_\mathrm{i}^{\mathrm{n}}\Delta\mathrm{t} \tag{40}$$

$$E^{n+1} = E^n + \frac{1}{\mu_0}\left(\vec{B}^n\vec{\nabla}\right)u_i^n B_i^n \Delta t$$

The symbol $\left(\vec{B}^n\vec{\nabla}\right)F_i^n$ designates the finite difference operator which approximates the corresponding differential one. Instead of the last equation for E^{n+1} it is used in FOREV-2:

$$E^{n+1} = \frac{\left(B^{n+1}\right)^2}{\mu_0} + \rho\frac{\left(u^{n+1}\right)^2}{2} = \frac{\left(B_i^n + \left(\vec{B}^n\vec{\nabla}\right)u_i^n\Delta t\right)^2}{2\mu_0} + \rho\frac{\left(u_i^n + \frac{1}{\rho\mu_0}\left(\vec{B}^n\vec{\nabla}\right)B_i^n\Delta t\right)^2}{2} \tag{41}$$

By substituting the values of B^{n+1} and u^{n+1} from the first two equations of system (40) into the last equation of system (40) it is obtained:

$$E^{n+1} = \frac{\left(B^{n+1}\right)^2}{\mu_0} + \rho\frac{\left(u^{n+1}\right)^2}{2} = \frac{\left(B_i^n + \left(\vec{B}^n\vec{\nabla}\right)u_i^n\Delta t\right)^2}{2\mu_0} + \rho\frac{\left(u_i^n + \frac{1}{\rho\mu_0}\left(\vec{B}^n\vec{\nabla}\right)B_i^n\Delta t\right)^2}{2} = \tag{42}$$

$$E^n + \frac{1}{\mu_0}\left(\vec{B}^n\vec{\nabla}\right)u_i^n B_i^n\Delta t + \left\{\frac{\left[\left(\vec{B}^n\vec{\nabla}\right)u_i^n\right]^2}{2\mu_0} + \frac{\left[\left(\vec{B}^n\vec{\nabla}\right)B_i^n\right]^2}{2\rho\mu_0}\right\}(\Delta t)^2$$

This approximation has the same first order term in Δt as eq. (40) and differs only by terms of the order of $(\Delta t)^2$. These second order terms don't violate the first order approximation scheme, but allow an accurate calculation of the plasma thermal energy and a calculation according to the Courant criterion.

Test calculations, using the expression from eq. (42) for the total energy, have shown good stability and unphysical overheating and overcooling of plasma vanished. The time steps are of size Δt below 10^{-10} s.

In a next step diffusion of the magnetic field components B_x and B_y was taken into account. The diffusion of the transverse components of the magnetic field occurs at another substep of the splitting method. The diffusion equation for the vector potential A_z according to

$$\frac{dA_z}{dt} = \frac{1}{\mu_o\sigma}\Delta A_z \tag{43}$$

is solved by means of the transversal longitudinal chase method. By taking into account the diffusion of the transversal components of the magnetic field three times larger time steps could be used.

To guarantee that ions deposit their energy permanently into several meshes the mesh size was fitted to the energy deposition profile into the plasma shield. By this simple measure explosive like expansion of single cells fully heated by the incoming ions and subsequent backward motion of plasma beyond the heated cell was prevented. Due to this simple measure an uniformly directed expansion of the total plasma shield became possible.

4.2 Increase of time step size

For the ITER slot divertor typically 3000 meshes non-uniformly distributed in x direction and uniform grid in y direction are needed for the MHD part and minimum 24 frequency group Rosseland opacities for the radiation transport part were used. The background plasma density should be of the order 10^{13} - 10^{14} cm^{-3}. With typical time step sizes of the order of (3 - 5) 10^{-11} s those 2 dim calculations require extensive CPU times at workstations. For routine 2 dim calculations thus a drastic increase of the time step without increase of the density of the background plasma is required. The time step in FOREV-2 is determined by the Courant criterium with the Alfven velocity as characteristic velocity. The Alfven velocity $v_A = B/\sqrt{4\pi\rho}$ is inversely proportional to the square root of the plasma density. Therefore the usual way to reduce this velocity (and consequently to increase the time step) by increasing the minimum value of the background plasma density can't be used here. To overcome this problem the calculational region was divided into 2 subregions: the target plasma region (TPR) and the background plasma region (BGR). The plasma of the TPR region has densities larger than typically 10^{14} cm^{-3} and the plasma in the BGR region has lower densities. Initially all meshes belong to the BGR. When the plasma density in a mesh reaches the threshold value and if this all is touching the TPR region or the evaporating target surface then it is added to the TPR. Despite this division all calculations are performed by FOREV-2 on the full calculational region independent on whether the mesh belongs to the TPR or BGR. In the Lagrangian time step it is assumed that the background plasma particles have larger mass than the target plasma particles. This measure effectively reduces the maximum value of the Alfven velocity in the BGR region and thus results in an increase of the time step size.

The main physical process in the BGR is magnetic field pressure and background plasma pressure equilibration by means of ion sound propagation (magnetic field pressure several orders of magnitude larger than background plasma pressure). In reality this process is much faster in comparison with processes in TPR and it remains much faster too in the improved version of FOREV-2 even taking into account artificial reduction of Alfven velocity. For background plasma it is assumed that the particles mass increases with logarithmic dependence from density. The mass of the background particles increased in such a way that the overall mass of the substance in the background cell corresponds to some artificial density. The dependence of the

artificial background plasma density from the plasma density is shown in Fig. 4. The broken line shows the real density of the background plasma.

Numerical details and what is typically achieved in FOREV-2 is listed in Table 3. The time step size is typically 10^{-9} s. Therefore for a physical time of 100 μs several 10^5 time steps are necessary. The overall CPU time on a RISC 6000 Model 519 Workstation with 100 MFLOPS amounts up to 25 hours using 24 frequency groups and a computational region of 200 x 30 cm^2 with up to 100 meshes in x- and 30 meshes in y-direction.

Test calculations of target plasma expansion were performed with and without this new TS size criterion. A comparison of results is given in Fig. 5. From this Figure it is seen that the results are very similar even after 200 μs when the leading edge of the expanding target plasma reaches the end of the calculational region. The code version with increased time steps calculates a factor of 10 - 30 times faster and the calculations were performed with a background plasma density of 1.5 x 10^{12} cm^{-3}. Thus the target plasma expansion can be calculated for densities down to 10^{13} cm^{-3}.

4.3 Improvement of the 2 dim radiation transport scheme

Originally in FOREV-2 a 2 dim forward reverse method (MFR) based on the assumption of isotropy of the radiation flux inside the meshes and at the mesh boundaries was used for calculation of the 2 dim radiation fluxes [10].

Isotropy of radiation fluxes is only valid for optically thick plasma. The plasma shield is optically thick only for line radiation but optically thin for continuum radiation. To account for such a situation and for calculation of angular dependent leakage radiation fluxes the 2 dim S_N method would be most suited. However this method is rather time consuming and additionally has the disadvantage that the calculation of the divergence of the radiation flux in the mesh center is inaccurate. In the plasma shield zones of rather different plasma densities are existing. An inaccuracy in the calculated divergence can result in overheating of low dense plasma regions and this in turn will reduce drastically the size of the time steps of the MHD calculations.

To circumvent these problems and to account for the anisotropy of the radiation flux an improved forward reverse method (IFRM) was developed, adopting and generalizing a method developed for 1 dim radiation transport [23]. IFRM uses averaged cosines and sines of the radiation flux at the mesh boundaries as obtained from 2 dim SN calculations [24] and a normalization of the radiation flux outgoing from the mesh.

4.3.1 The 2 dim MFR method

The 2 dim radiation transport equation is given according to:

$$\mu\frac{\partial I_\omega}{\partial x}+\nu\frac{\partial I_\omega}{\partial y}=\eta_\omega-\kappa_\omega I_\omega \tag{44}$$

with ω the frequency, I_ω the spectral radiation flux, μ = cosφ, $\nu=\sqrt{1-\mu^2}$, η_ω the plasma emissivity with $\eta_\omega=\beta_\omega I_\omega^P$ and κ_ω the absorption coefficient, β_ω the emission coefficient and I_ω^P the Planckian spectral radiation flux. For calculation of β_ω and κ_ω see chapter 5.

Using angular integrated quantities, assuming weakly anisotropic radiation fluxes and omitting the frequency eq. (44) is reduced to the following system of 1 dim like forward reverse equations

$$\begin{aligned}
&\frac{\partial}{\partial x}\left(\mu_x^+F_x^+\right)=\eta-\kappa F_x^+\\
&\frac{\partial}{\partial x}\left(\mu_x^-F_x^-\right)=\eta-\kappa F_x^-\\
&\frac{\partial}{\partial y}\left(\nu_y^+F_y^+\right)=\eta-\kappa F_y^+\\
&\frac{\partial}{\partial y}\left(\nu_y^-F_y^-\right)=\eta-\kappa F_y^-
\end{aligned} \tag{45}$$

$$\begin{aligned}
\textit{with}\quad F_n&=\int_{\varphi_n} I(\varphi)d\varphi\\
\mu_n&=\int_{\varphi_n} \cos\varphi I(\varphi)d\varphi / F_n\\
\nu_n&=\int_{\varphi_n} \sin\varphi I(\varphi)d\varphi / F_n
\end{aligned}$$

n the quadrant number

$$F_x^+ = F_1 + F_4, F_x^- = F_2 + F_3, \mu_x^+ = \frac{\mu_1 + \mu_4}{F_x^+}; \mu_x^- = \frac{\mu_2 + \mu_3}{F_x^-}$$

and

$$F_y^+ = F_1 + F_2, F_y^- = F_3 + F_4; \nu_y^+ = \frac{\nu_1 + \nu_2}{F_y^+}; \nu_y^- = \frac{\nu_3 + \nu_4}{F_y^-}$$

The x and y components of the radiative flux are given according to

$$S_x^+ = \mu_x^+ F_x^+; \; S_x^- = \mu_x^- F_x^-; \; S_y^+ = \nu_y^+ F_y^+; \; S_y^- = \nu_y^- F_y^-$$

$$S_x = \mu_x^+ F_x^+ + \mu_x^- F_x^- \text{ and } S_y = \nu_y^+ F_y^+ + \nu_y^- F_y^- \qquad (46)$$

In eq. (45) the averaged quantities μ_n, ν_n, F_n are introduced under the derivatives. These functionals can be taken as constant during several hundred time steps. For their recalculation the exact S_N method is used.

The system of eqs. (45) has the formal solution for the fluxes F_x^+, F_y^+ outgoing from the mesh:

$$F_x^+ = \frac{F_x^{out} + \eta L_x}{1 + \kappa L_x}$$

$$F_y^+ = \frac{F_y^{out} + \eta L_y}{1 + \kappa L_y} \qquad (47)$$

with L_x and L_y the effective length of the photon trajectory in the mesh and F_x^{out} and F_y^{out} the outgoing fluxes for an empty mesh produced by the incoming fluxes F_{x0} and F_{y0} (see Fig. 6).

The outgoing radiation fluxes F_x^+, F_y^+ are calculated under the assumptions that the radiation flux is isotropic and that the radiation intensity along each mesh boundary is constant. Knowing the incoming intensities the outgoing fluxes are calculated as integral over all angles and all trajectories of the incoming intensities.

The outgoing fluxes F^{out} are connected with the incoming fluxes according to

$$F_x^{out} = A_{xx}F_{xo} + A_{xy}F_{yo}$$

$$F_y^{out} = A_{yx}F_{xo} + A_{yy}F_{yo} \tag{48}$$

with the matrix elements of A given as

$$A_{xx} = \sqrt{1+\frac{a^2}{b^2}} - \frac{a}{b};\ A_{xy} = \frac{a}{b}(1-A_{yy})$$

$$A_{yx} = \frac{b}{a}(1-A_{xx});\ A_{yy} = \sqrt{1+\frac{b^2}{a^2}} - \frac{b}{a} \tag{49}$$

where x = a and y = b are the mesh boundaries.

4.3.2 Improved Forward Reverse Method (IFRM)

In case of isotropy of radiation fluxes the average inclination angle in each quadrant is $\pi/4$. For anisotropic fluxes the inclination angle may differ from $\pi/4$. This can be taken into account by an angular transformation in the matrix elements in the following way: instead of the tangens of the mesh diagonal a/b a corrected tangens a/b $\sqrt{1-\mu^2}/\mu$ is used for the matrix element A_{xx} and the corrected tangens a/b $\sqrt{1-\nu^2}/\nu$ A_{yy} with μ the average cosine calculated along the x-direction and ν the average sine along the y-direction. The quantities A_{xy} and A_{yx} are obtained from the conservation of the total radiation flux passing through the mesh. Thus the matrix elements are given according to

$$\tilde{a} = a\sqrt{1-\mu^2};\ \tilde{b} = b\mu;\hat{a} = a\sqrt{1-\nu^2};\hat{b} = b\nu$$

$$A_{xx} = \sqrt{1+\frac{\tilde{a}^2}{\tilde{b}^2}} - \frac{\tilde{a}}{\tilde{b}} \qquad A_{xy} = \frac{\hat{a}}{\hat{b}}(1-A_{yy}) \tag{50}$$

$$A_{yx} = \frac{\hat{b}}{\hat{a}}(1-A_{xx}) \qquad A_{yy} = \sqrt{1+\frac{\hat{b}^2}{\hat{a}^2}} - \frac{\hat{b}}{\hat{a}}$$

The averaged cosines and sines of the radiation flux at the mesh boundaries needed for the IFRM method are obtained from 2 dim S_N calculations. As the 2 dim S_N method is about a factor of 20 more time consuming than the MFR method the following compromise was adopted: once per 500 time steps mean cosines are calculated with 2 dim S_N, new IFRM radiation fluxes are calculated once per 20 time steps.

Test calculations performed after this step on several fixed temperature and density profiles showed that the vector field of the radiation fluxes is in good agreement with the radiative field obtained from the 2 dim S_N calculations. But the magnitudes of the radiative fluxes differed from the S_N results by up to a factor of 3. This is because the absorption of the incoming fluxes inside the mesh is not taken into account correctly for non-isotropic fluxes (the quantities L_x, L_y of eq. (47) are valid only for isotropic fluxes). The characteristic lengths of absorption L_x and L_y should be modified too. However a sequential approach for taking into account absorption results in introduction of additional effective lengths and very complicate expressions for their calculation which exclude calculation in advance and therefore are rather time consuming.

Therefore another way was used to solve this problem. A renormalization factor was introduced. For each mesh boundary the ratio of the radiation fluxes obtained from the 2 dim S_N method and from the IFRM method is determined. A mean factor $\overline{\eta} = F_{out}(S_N) / F_{out}(IFRM)$ averaged over all η values of the meshes is calculated and applied for correction of the IFRM fluxes.

4.4 Comparison of results from MFR and IFRM

2 dim radiation fluxes were calculated by the 2 dim S_N, by the IFRM and the MFR method. For the comparisons the following two cases were used. Case 1: given temperature and density profiles as obtained from a 2 dim R-MHD calculation with MFR method of radiation transport were used. The temperature and density profiles belong to the time moment 36 μs without side wall erosion. Case 2 uses a fully consistent 2 dim R-MHD calculation with 2 dim MFR and IFRM radiation transport again for a perpendicular target, side wall distance 20 cm and hot plasma with peak power density of 100 MW/cm^2 Gaußian distributed with half width of 5 cm.

Results of the comparison of the x component of the radiation fluxes and of the lateral radiation flux are shown in Figs. 7a and b. According to these Figs. the differences between the S_N fluxes and the IFRM fluxes remain below 30 %, but the MFR results differ rather strongly from the other values. This is not only valid for the x component of the radiation flux at the middle section of the calculational region but also for the y component (lateral radiation flux).

A comparison of results from fully consistent 2 dim R-MHD calculations using MFR and IFRM is shown in Figs. 8a and b for a horizontal graphite target and a hot magnetized plasma of 100 MW/cm^2 with Gaußian profile of half width of 5 cm along B with (B_x, B_y, B_z) = (0.5 T, 0, 5 T) at 100 μs. The computational region of 300 x 20 cm^2 was covered by 60 nonhomogeneous meshes in x-direction and 20 homogeneous meshes in y-direction. Rosseland opacities with optimized 24 frequency groups were used (see chapter 5). With MFR radiation fluxes generally are overestimated resulting in larger target and side wall erosion and in broadening of the erosion profile at the target (see Fig. 8b). In total the eroded mass is a factor of 2 less for the 2 dim-IFRM radiation transport.

Fully consistent 2 dim R-MHD calculations based on the 2 dim IFRM method for radiation transport were performed to study the influence of the number of frequency groups and of Planck and Rosseland opacities on target erosion, on angular distribution of lateral leakage radiation fluxes and on side wall evaporation. One such example is shown in Fig. 9, where radiation fluxes for a carbon plasma calculated with 24 Rosseland and 69 Planck group opacities are compared. Shown are radiation fluxes to the side wall (lateral radiation fluxes) and to the target for a realistic ITER situation with inclined target and asymmetrical power density profile (see Figs 1a and b). The peak power density along the separatrix is 100 MW/cm^2. From the good agreement it is concluded that line radiation (mainly from He like ions) is contributing only weakly to the heat loads at the target and the side walls.

5. Optical properties of plasmas

The optical properties of a plasma are described by the frequency, temperature and density dependent absorption and emission coefficients $\kappa=\kappa(\omega,T,N)$ and $\beta=\beta$

(ω,T,N). κ and β describe the probability of a photon of frequency ω passing 1 cm to be absorbed or emitted in a plasma of temperature T and density N. In the absorption process the photon energy $\hbar\omega$ is transferred to the interaction partner either a bound or a free electron. For the calculation of κ and β the electron population of levels for multicharged plasma ions has to be known. In the CRE model collisional and radiative processes are taken into account. In a collisional process free electrons transfer energy to bound electrons (collisional excitation and ionization). In a radiative process photons transfer their energy to an electron (inverse bremsstrahlung, photoexcitation and photoionization). The inverse processes are collisional deexcitation and recombination, radiative deexcitation, spontaneous and induced emission, bremsstrahlung and dielectronic recombination [25, 26].

From the level populations the absorption and emission coefficients are determined by calculating the transition probabilities between the various population states. Transitions between free-free, bound-free and bound-bound states are taken into account. Bound-bound transitions result in emission and absorption of line radiation. Bound-free transitions are due to transitions of electrons between the bound and the free state and result in continuum recombination radiation. The radiation due to this process shows the typical edges at frequencies corresponding to the ionization energies of the bound states. The free-free transitions are due to collisional processes between free electrons and ions. These transitions produce the continous bremsstrahlung.

For plasma densities above 10^{18} cm^{-3} and temperatures below 10 eV a plasma is in local thermodynamic equilibrium (LTE). In a LTE plasma deexcitation and recombination processes are collisionally dominated. The SAHA equations [27] are used for calculation of the ion concentrations. The level populations are calculated by Boltzmann, the spectral radiation flux is Planckian and the emission coefficient β_ω is identical to the absorption coefficient κ_ω (Kirchhoff law). At plasma densities below 10^{17} cm^{-3} and temperatures above 10 eV the LTE condition no longer is valid. Radiative deexcitation and recombination and dielectronic recombination are becoming important. In comparison with a LTE plasma the non-LTE plasma shows a population of excited levels and has a lower ionization degree. As a consequence the emission coefficient of a non-LTE plasma is smaller. For optically thin plasma ($\kappa L \ll 1$) the

transition frequencies v of all collisional and radiative processes are only dependent on plasma temperature and density. Radiative excitation and ionization processes are not taken into account. A carbon plasma with densities below 10^{17} cm^{-3} and temperatures above 2.5 eV is optically thin for most part of the continuum radiation except for recombination radiation from the transitions of H to He like ions but is optically thick for lines from K shell emission of He like ions.

In optically not thin plasma reabsorption of radiation is occurring. Radiative excitation (re) and ionization(ri) has to be taken into account. The transition probabilities for these two processes are given according to [25]

$$v_{zk}^{ri} = \int_{Izk/\hbar}^{\infty} d\omega \int d\Omega \frac{I_\omega}{\hbar\omega} \sigma_{zk}^{ph}$$
$$v_{zkk'}^{re} = \frac{2\pi^2 n^2}{m_e c} f_{zkk'} \int_{-\infty}^{+\infty} d\omega L(\omega)_{zkk'} \int \frac{I_\omega d\Omega}{\hbar\omega} \qquad (51)$$

Both quantities are dependent on the local radiation flux Iω, which is obtained from radiation transport calculations for homogeneous plasma layers with constant temperature and density.

Reabsorption of radiation decreases the spontaneous decay rate and thus results in higher population of excited levels and in larger ionization. The effective spontaneous decay $\overline{A}_{zk'k}$ is given as

$$\overline{A}_{zk'k} = A_{zk'k}\, \Theta_{zk'k} \qquad (52)$$

with $\Theta_{zk'k}$ the escaping factor

In the Biberman Holstein approximation the escaping factor Θ for homogeneous plasma with constant temperature and density is given for plane geometry according to [25]

$$\Theta = 2\tau \int dr\, L_\omega^2 E_1(\tau L_\omega) + 2 \int d\omega L_\omega \exp[-\tau L_\omega] \qquad (53)$$

with L_ω line shape

$\tau = \kappa_0 d$ the optical width

d thickness of layer and

κ_0 the absorption coefficient in the line center

For $\tau \gg 1$ it is obtained for the escaping factor Θ

$$\Theta = \frac{0.67}{\sqrt{\pi\tau}} \quad \text{for a Lorentz line shape}$$

$$\Theta = \frac{0.5}{\sqrt{\pi \ln \tau}} \quad \text{for a Doppler line shape} \qquad (54)$$

$$\Theta = \frac{0.22}{\tau^{3/5}} \quad \text{for a Holtzmark line shape}$$

For $\tau \sim 1$ and more complicated line shapes (for example Voigt profile) it is not possible to derive a simple analytical expression for the escaping factor. In TOPATOM tables of escaping factors in a wide range of τ ($0.001 < \tau < 100$) are used for mixed shapes such as Lorentz-Doppler (Voigt), Lorentz-Holtzmark [28] and Doppler-Holtzmark.

Emission coefficients are calculated with the code TOPATOM [29]. For optically thin plasma the CRE model is used. Reabsorption of radiation in optically not thin plasma is taken into account by the escaping factor Θ (see eq. (53)).

5.1 Carbon plasma

Carbon ion concentrations are shown in Fig. 10 for a 1 cm layer of a carbon plasma of density of 10^{17} cm^{-3}. There are existing wide temperature areas in which Li-He and H-like ions are only possible. The optical properties of these ions are well known and thus the optical coefficients can be calculated on a straight forward manner. For this the code TOPATOM (thermodynamic and optical properties of atoms and ions) [29] was used.

Fig. 11 shows absorption coefficients for carbon for a plasma density of 10^{17} cm^{-3} for the plasma temperatures 2.0 eV and 25 eV. 5000 frequency groups were used. For 2.0 eV the lines are from CII, CIII and CIV ions. Most lines and a part of the continuum recombination radiation is optically thick for plasma densities above 10^{17} cm^{-3}.

For plasma temperatures above 10 eV the plasma of density of 10^{17} cm^{-3} is optically thick only for a few lines close to the H like ionization edge. Most radiation is emitted as SXR radiation in the photon energy region from 308 eV up to 400 eV. A comparison of LTE and non-LTE emission coefficients is given in Fig. 12. The LTE conditions overestimates considerably the emission coefficient β_ω for continuum radiation because collisional ionization is not balanced by radiative recombination. Comparing the results from the CRE model the β_ω obtained with escaping factor correction are larger. Due to radiative ionzation in non-LTE plasma reabsorption results in changes of the ion population. In the example shown in Fig. 12 H like ions are produced by reabsorption resulting in increased emissivities for H to He like ion recombination radiation (edge at $\hbar\omega$ = 394 eV). Fig. 13 shows lines from the K shell of carbon CV ions in more detail for the three cases. Again the higher amplitudes of the lines for the CRE model with escaping factor are due to the increase of population of excited levels. Interesting is that for LTE-β_ω there appears an intense line from CVI ions due to the overestimation of higher ionization states in the LTE model.

Using LTE emission coefficients for non-LTE plasma results in overestimation of radiation and thus yields a too low plasma temperature in the interaction region of the external beam with the target plasma. In this region the plasma temperature is determined by the balance between heating due to energy deposition by the external beam and radiation. If LTE-β_ω are used the temperature in the plasma corona remains rather low.

5.2 Quartz plasma

The term quartz is used, the plasma actually consist of silizium and oxygen ions. The thermodynamic and optical properties of the quartz plasma were calculated in the frame of the CRE model using TOPATOM in a manner rather similar to the calculations for graphite. However quartz has a number of features which considerably complicate the calculation. The optical properties of neutral atoms can strongly differ from those of ions having the same number of electrons. Experimental data on energy levels and oszillator strengths which are used in TOPATOM are available for neutral atoms and low charged ions. However with increasing charge the number of

energy levels listed in the tables decreases and data on oscillator strengths are becoming scarse.

Fig. 14 shows concentrations of silizium and oxygen ions as function of plasma temperature for a quartz plasma of density of 10^{17} cm^{-3}. At temperatures of a few eV silizium is present as Na- und Ne-like ions and oxygen as Be-like ions. Only in this case the spectral shape of the coefficients is simple. Increasing the temperature the optical properties are determined by Li- and He-like ions of oxygen and O-. Ni- and C-like ions of silizium what results in a rather complex spectral shape of the absorption and emission coefficients. At temperatures of a few hundred eV oxygen will be completely ionized, silizium at such temperatures is present as Li- and He like ions. Only on this case the optical properties are simple. Figs. 15a and b show absorption and emission coefficients for quartz plasma of density of 10^{16} cm^{-3} and for the temperatures 1 eV and 10 eV.

For these calculations 1000 frequency groups were used. At temperatures below 1 eV molecules are existing in the plasma. Their influence on the optical properties is not taken into account. If taken into account the coefficients would increase at photon energies below 5 eV.

5.3 Tungsten plasma

Usually for high Z materials the assumption is made that the plasma is in local thermodynamic equilibrium (LTE). Then the concentrations of ion species are calculated using the Saha equations. Emission and absorption coefficients are identical (Kirchhoff law). For calculations of $\kappa\omega$ it is assumed that for S and P electrons level splitting is small and thus negligible for low Z materials. But for high Z materials for the P and for vacant D shells and especially if this shell is an inner one this conditions is not fulfilled. For tungsten and for the configuration $3d^4\ 6s^2$ the electrostatic and spin-orbital splitting is rather large [30]. Transitions like $5d^4\ 6s^2$ - $5d^3\ 6s^2\ 6p$ can split up into 10^3 lines. As a result numerous lines with strong intersecting profiles are obtained instead of one line. Thus a quasicontinuum is established with a complicate frequency dependence of the absorption coefficient. To use LTE conditions for the calculation of the optical properties thus is not adequate. Therefore for tungsten a

CRE model was used and electrostatic and spin-orbital splitting was taken into account for vacant p, d and f shells. Fig. 16 shows concentrations of tungsten ions as function of plasma temperature for a tungsten plasma of density of 10^{18} cm^{-3}. At each temperature the plasma consists of several tungsten ions. As a consequence the spectral shape of the coefficients will become rather complicate. Non-LTE absorption- and emission coefficients were calculated [31] in the density and temperature range from 10^{15} to 10^{20} cm^{-3} and from 0.5 to 500 eV. For the frequency interval from 0.05 eV to 500 eV 5000 and 25000 frequency groups with a logarithmically uniform mesh were used. Figs. 17a and b show the absorption and emission coefficients for a tungsten plasma of temperatures of 1 eV and 10 eV and density 10^{17} c m^{-3}.

5.4 Multigroup opacities

For the solution of the radiation transfer equation the absorption and emission coefficients have to be used (see for example eq.(44)). These contain lines. To resolve a line in detail needs several frequency intervals. Thus the total number of frequency groups to be used in the transfer equations can easily sum up to a few thousands. This together with a 2 dim R-MHD calculation would need extremely excessive computational time and memory. Therefore it is necessary to perform a frequency averaging of the optical coefficients. This usually is done by Rosseland and Planck averaging of β_ω and κ_ω. Planck averaging is done according to

$$\kappa_k^P = \int_{\omega_k}^{\omega_k+\Delta\omega_k} \kappa(\omega) I^P(\omega) d\omega \Big/ \int_{\omega_k}^{\omega_k+\Delta\omega} I^P(\omega) d\omega \qquad (55)$$

with $I^P(\omega)=\frac{\omega^3 \exp(-\hbar\omega/T)}{1-\exp(-\hbar\omega/T)}$ the Planck spectrum, ω_k the left boundary of the frequency group k and $\Delta\omega_k$ the group width.

Rosseland averaging of β and κ is done according to

$$I_k^{Ros} = \int_{\omega_k}^{\omega_k+\Delta\omega_k} \frac{1}{\kappa(\omega)} \frac{\partial}{\partial T} I^P(\omega) d\omega \Big/ \int_{\omega_k}^{\omega_k+\Delta\omega_k} \frac{\partial}{\partial T} I^P(\omega) d\omega \qquad (56)$$

with l_k^{Ros} the Rosseland mean free path. The Rosseland group opacities κ_k^{Ros} are obtained from the Rosseland mean free path according to

$$\kappa_k^{Ros} = 1/l_k^{Ros} \qquad (57)$$

For carbon with its rather weakly changing spectral shape of the coefficients with plasma temperature a not equidistant frequency group structure optimized with respect to the absorption edges was used for the averaging procedure. In total 24 frequency groups were used for the Rosseland opacities. For Planck opacities the most prominent lines for Li-, He- and H-like ions were added. The group width in these lines was chosen in such a way as to resolve the line shape of these most important lines. Two sets of Planck group opacities were generated with 69 and 512 frequency groups. A comparison of the 24 group Rosseland and 69 group Planck opacities for absorption and emission is shown for carbon in Figs. 18a and b.

Formally the same group structure for the averaging procedure as for carbon could be applied for quartz. However the spectral shape of the coefficients is rather complex and at different plasma temperatures different species of Si and O-ions will be present what results in changing of absorption edges and lines. Therefore a frequency group optimized structure for few group opacities was not tried. Instead of that a simple 40 group structure with logarithmically non-uniform mesh was used for the averaging. 40 group Rosseland opacities for absorption and emission are shown in Fig. 19a for a plasma temperature of 10 eV and a density of 10^{17} cm^{-3}. These opacities should be adequate for R-MHD survey calculations as long as the radiative energy flux to the target is not larger than the target heat fluxes due to direct energy deposition of the impacting beam and due to electron heat conducting. Fig. 19b shows a comparison of Rosseland opacities for absorption for different temperatures and a plasma density of 10^{17} cm^{-3}. Comparing quartz- and carbon Rosseland opacities (Figs. 18 and 19) it is seen that carbon plasma has a larger transparency than quartz plasma in the frequency range from 100 to 400 eV. Below 60 eV the opacities are rather comparable.

The difficulties with averaging as described for quartz are still increasing for tungsten. For performance of overview calculations with tungsten targets it was decided to use few group Planck and Rosseland opacities based on a simple logarithmically non-

uniform group structure with 45 frequency groups. Fig. 20 shows Rosseland opacities for absorption and emission for the two plasma temperatures 1 eV and 10 eV. Fig. 21 shows a comparison of 45 group Rosseland and Planck opacities for a tungsten plasma of temperature 10 eV. The rather large differences between Planck and Rosseland opacities are to be expected because of drastic overestimation of lines by Planck averaging using such a rough frequency mesh. A comparison of opacities for absorption and absorption coefficients for tungsten is shown in Figs. 17a and b. Because of the large number of lines in the optical spectra of tungsten Rosseland averaging which levels out lines results in an underestimation of the radiation properties of tungsten. Spectral calculations with a very large number of frequency groups are too time consuming. Therefore for tungsten an averaging approach was used which accounts for the real weight of the lines and which preserves the weight fraction of frequency integrated optically thick and optically thin plasma properties. In this Lebesgue averaging procedure the frequency range is divided into frequency groups of such width $\Delta\omega_i$ that the Planck function (the averaging function see eqs. (55) and (56)) can be assumed to be constant in each group. Then the equivalent spectrum within the group i is approximated by a histogram using equidistant subintervals $\Delta\kappa_j$ and $\Delta\beta_j$ to which are belonging frequency subgroups of varying width ω_{ij}. The weight of the subgroup j of frequency group i is given as $\Delta\omega_{ij}/\Delta\omega_i$. Fig. 22 shows a comparison of Lebesgues, Planck and Rosseland opacities. For the Lebesgues opacities 21 frequency groups with 6 equidistant subintervals in κ and β per decade were used. For the Rosseland opacities 45 frequency groups were used. The line structure of the spectral coefficient is reasonably reproduced with the 21 Lebesques groups and thus this averaging in comparison with Planck and Rosseland averaging results in an improved description of the optical properties of tungsten.

The Lebesgues averaging procedure requires a modified scheme for calculation of radiative transfer. Within a spatial mesh (mesh size Δx in 1 dim calculations), with constant plasma temperature and density, the spectral flux for group i (group width $\Delta\omega_i$) outgoing from the mesh for Rosseland and Planck opacities is calculated according to

$$I_{out}(i)=I_{in}(i)e^{-\kappa_i\Delta x}+\frac{\beta_i}{\kappa_i}\int_{\Delta\omega_i} I_i^P(1-e^{-\kappa_i\Delta x})\,d\omega \qquad (58)$$

with $I_{in}(i)$ the incoming spectral flux, κ_i and β_i the Rosseland or Planck opacities for absorption and emission and I_i^P the Planckian function.

Applying the Lebesgues averaging the spectral flux for group i ($\omega_i + \Delta\omega_i$) outgoing from a mesh is calculated according to

$$I_{out}(i)=I_{in}(i)\sum_j \frac{\Delta\omega_{ij}}{\Delta\omega_i}e^{-\kappa_j\Delta x}+\sum_j \frac{\Delta\omega_{ij}}{\Delta\omega_i}\frac{\beta_i}{\kappa_i}\int_{\Delta\omega_i} I_i^P(1-e^{-\kappa_j\Delta x})d\omega \qquad (59)$$

with β_j and κ_j the equivalent Lebesgues opacity values of the subgroup j of width $\Delta\omega_{ij}$.

From mesh to mesh radiation is transferred within frequency groups, but inside the mesh radiation is transferred within subgroups. For a given frequency groups in the structure of the subgroups can be different in different spatial meshes.

5.5 Optical properties of molecules

The optical properties of a plasma at temperatures below 1 eV are determined to a large extent by molecular absorption. For carbon and carbon-hydrogen plasma the moleculres H_2, CH, C_2 and C_3 contribute to the optical properties. The molecular spectra differ strongly from atom/ion spectra. Electronic, vibrational and ratational transitions in the visible, nearest infrared and ultraviolett frequency range are important. In the plasma flow target interaction the plasma density near the target exceeds values of 5 x 10^{18} cm^{-3} at temperatures below 3 eV. Thus the plasma is in LTE and molecules have to be taken into account. The concentrations of the molecular species was calculated using the law of mass action according to [32]

$$\frac{p_A^X p_B^Y p_C^Z}{p_M}=\kappa_p(T) \qquad (60)$$

with M molecule i nthe form of $A_XB_YC_Z$ consisting of atoms A, B, C, with X, Y, Z atom numbers. p_A, p_B, p_C partical pressure of the atoms A, B, C, $\kappa_p(T)$ the equilibrium constant.

In a similar manner the following expression is used for charged particles

$$\frac{p_A p_B}{p_{AB} + p_e} = \kappa(T) \tag{61}$$

The total system of the equations consists of the equations (29) for all moleculres, of the Saha equations for all atoms and ions as well as the balance equations for each sort of atoms and of the electrons. The problem is reduced to the solution of a system of nonlinear algebraic equations.

The first step is to find an approximate solution of the system of equations.

For each element (for example A) of a mixture the most probable molecule is determined. As usual this molecule is A_2 or A_3 of A_n. The ratios between concentrations of atoms (A) and molecules (A_n) are obtained from the eq. (60). A similar procedure is performed for the other elements of the mixture. This procedure permetis to estimate the concentrations of the main elements with an accuracy of factor 2. In a second step the other molecules are taken into account. Their contribution can be estimated by using the perturbation method. In this case is rewritting in the following form:

$$\frac{\left(p_A^0 + dp_A\right)^X \left(p_B^0 + dp_B\right)^Y \left(p_C^0 + dp_C\right)^Z}{p_M^0 + dp_M} = \kappa_p(T) \tag{62}$$

Here p_A^0, p_B^0, p_C^0 are the partial pressure of the atoms obtained at the first step. Subtracting the eq. (60) from eq. (62) a linearized system is obtained. An iterative method is used to obtain theexact solution of the eq. (60).

For carbon plasma such molecules as C, C_2, C_3, C^-_2, C^- are taken into account as well as all ions Cn+t. For the carbon-hydrogen plasma such moleculres and atoms as H, C, H_2, C_2, CH, CH^+, H^+_2, C^-_2, CH^-, C_3, C_2H, CH_3, C_2H_2, H^-, C^-, H^+ are taken into account. For calculation of the molecular optical properties electron – vibrational rotational transitions as well as photo dissociation and photo ionization of the two atomic molecules are taken into accout. Strengths of electron transitions are taken from experimental data and vibrational transition probabilities (Frank-Condon factors) are obtained by solving the Schrödinger equation using the Morse potential U_m.

$$U_m(R - R_0) = D_e\,(1 - \exp\,(-\,\beta\,(R - R_0))^2 \tag{63}$$

With D_e the energy of dissociation, R_0 the equilibrium distance between atoms. The parameter β is taken from experimental data [33].

Rotational transition probabilities are calculated uisng the non rigid rotator assumption. The molecule C_2 plays the main role in the values of the absorption coefficient in the photon energy region between 0.4 and 7 eV. There are 6 strong bands from ground and first excited states. Vibrational – rotational transitions of three and more atom molecules are not taken into account because their bands extend into the far infrared region.

Temperature dependent concentrations of molecules and atoms are shown in Fig. 23a for a carbon plasma of density of 10^{18} cm^{-3}. At low temperatures (around 0.5 eV) neutral carbon is the main component in a carbon plasma. The concentration of the C_2 molecules is about 15 %. Only at low temperatures (below 0.5 eV) and at high densities (~ 10^{19} cm^{-3}) C_4 and C_5 molecules are occurring. These molecules are not taken into account because reliable data are not available. With increasing temperature the molecules dissociate and thier contribution to the absorption coefficient decreases. For temperatures above 1.2 eV C^+ ions are dominating. The concentration of ions CII, CIII etc. increases with increasing plasma temperatures (see Fig. 10). The concentrations of the C_2 and C_3 molecules decrease sharply with increasing plasma temperature and are becoming negligible for temperatures above 0.5 eV.

Photoabsorption from ground state and from inner shells essentially starts at photon energies above 10 eV. Below 10 eV the absorption is determined by photo processes from excited levels and by bremsstrahlung. At plasma temperatures below 1 eV the population of excited levels is small and bremsstrahlung is negligible because of small concentration of free electrons. Therefore the absorption coefficient for photon energies below 10 eV is rather small (see Fig. 23b). The presence of molecules with concentrations in the range of 1 – 10 % leads to a significant increase of the absorption coefficient (as is seen from Fig. 23b). With increasing plasma temperature the contribution of the photoabsorption from excited states increses simultaneously with a decrease of the number of molecules. Thus at temperatures above 1 eV the contribution of molecules to the absorption coefficient becomes negligible.

6. Collisional stopping of hot plasma

For calculation of the collisional stopping of the hot plasma and thus for calculation of the energy deposition of the hot plasma into the bulk target and into the plasma shield it is assumed that the ions are monoenergetic whereas the electrons have a Maxwellian energy distribution.

6.1 Energy deposition of ions

For ions because of their small penetration depths in solids [34] it is sufficient to consider only their slowing down in vapor. In solids the mean range of ions R_s is small in comparison with the heat penetration length L_h. For example the penetration depth of 200 keV protons in solid carbon is R_s = 0.3 mg/cm^2. The target heat load duration is surely larger than to = 1 µs. Therefore the minimum heat penetration depth is

$$L_h(\min)=\sqrt{At_o}=5\mu m \text{ with } A=\frac{\kappa}{\rho c_p}=0.3\frac{cm^2}{s}$$

Therefore the ion beam energy deposition in solids can be treated as a surface heat source.

Ions and electrons are slowed down by target ions of mean charge $\bar{Z}$, by bound electrons and by the free electrons of the quasineutral plasma.

6.1.1 Energy deposition due to bound particles

The energy deposition of ions $(dE/dx)_i$ is written as

$$\left(\frac{dE}{dx}\right)_{ib}=\left(\frac{dE}{dx}\right)_{in}+\left(\frac{dE}{dx}\right)_{ibe}$$
$$\left(\frac{dE}{dx}\right)_{if}=\left(\frac{dE}{dx}\right)_{ii}+\left(\frac{dE}{dx}\right)_{ife} \qquad (64)$$

with i ion; be bound electron, fe free electron, n nucleus.

The principle ions have charge Z_1 and mass A_1, the target ions have charge Z_2 and mass A_2.

Typical target plasmas in the plasma disruption cases (see Fig. 5) have densities in the range $10^{14} - 10^{19}$ cm^{-3}. Near the target surface the plasma temperature can be as low as 0.5 eV, thus the degree of ionization is rather small and stopping by bound particles becomes important. In all cases the contribution of target ions to dE/dx is small and thus the formulas are not given here, but their contribution was taken into account $(dE/dx)_{ibe}$ is calculated according to [35 – 37] as $(dE/dx)_{Bethe}$ or $(dE/dx)_{LSS}$.

$$with \left(\frac{dE}{dx}\right)_{Bethe} = 23.9 Z_{1eff}^2 \left(Z_2 - \overline{Z}\right)\frac{N}{E}\ln\left(\frac{1.6 E_s \left(Z_2 - \overline{Z}\right)}{A_1 Z_2^2}\right) \tag{65}$$

$$and \left(\frac{dE}{dx}\right)_{LSS} = 12.1 Z_1^{1.16} \frac{Z_2 - \overline{Z}}{Z_q \sqrt{A_1}} N_s \sqrt{E_s} \tag{66}$$

$$with\ Z_q = \left(Z_1^{0.66} + \left(Z_2 - \overline{Z}\right)^{0.66}\right)^{0.66};\ E_s = E/E_0, T_s = T/T_0$$

$N_s = N/N_0$ and $\overline{Z}$ the mean charge with $N_0 = 10^{18}$ cm^{-3}, $T_0 = 1$ eV, $E_0 = 10$ keV.

How to choose between the LSS- or the Bethe formula is discussed below.

According to [34] Z_{1eff} is calculated for a cold plasma as

$$Z_{1eff} = 1 - \exp(-0.632\sqrt{E_s}) - 0.012 E_s - 1.4\ 10^{-3} E_s^2$$

For low ion beam energies the Bethe formula is not valid, and the LSS formula (eq. (66)) has to be used, up to the maximum energy E_{max} given as

$$E_{max} = 17\, A1 \frac{Z_2^2}{Z_2 - \overline{Z}} (keV)$$

For collisional stopping of protons in carbon E_{max} is given as $E_{max} \approx 100$ keV. Therefore for beam energies up to 10 keV the LSS formula has to be used.

6.1.2 Ion energie deposition due to free particles

Again the contribution of target ions is omitted here. According to [35] $(dE/dx)_{ife}$ is calculated as

$$\left(\frac{dE}{dx}\right)_{ife} = 23.9\bar{Z}\,Z_{1eff}^2\,A_1\,\frac{N_s}{E_s}G(Y)\ln(L) \tag{67}$$

with

$$\begin{aligned} G(Y) &= erf\sqrt{Y} - 2\sqrt{\frac{Y}{\pi}}\exp(-Y) \\ Y &= 5.45\,\frac{E_s}{A_1 T_s} \\ L &= 142\sqrt{\frac{E_s}{N_s Z A_1}}R\frac{1}{Z_{1eff}\max(1.03\sqrt{R}/Z_{1eff}} \\ R &= \frac{E_s}{A_1} + 0.184T_s \end{aligned} \tag{68}$$

Figs. 24a and 24b show results of calculated energy deposition for protons in carbon. Fig. 24a shows the dE/dx as function of the proton energy for different temperatures of the carbon plasma for a plasma density of 10^{18} cm^{-3}. dE/dx depends strongly on the plasma temperature of 3 eV. For proton energies of 10 keV the increase of dE/dx with increasing plasma temperature is less and continuously so in this case range shortening occurs. Fig. 24b shows the stopping power of 10 keV protons in a carbon plasma as a function of the plasma temperature.

6.2 Energy deposition of electrons

6.2.1 Monoenergetic electrons

With analytical formulas the range R of the electrons is calculated for perpendicular impact. The formulas used for calculation of the energy loss are [36]

$$(dE/dx)_{be} = 1.3x10^{-2}\,(Z-\bar{Z})\frac{N_s}{E_s}\ln\left(1830\,\frac{E_s}{Z}\right)$$
$$(dE/dx)_{fe} = 1.3x10^{-2}\,\bar{Z}\frac{N_s}{E_s}\left(3810\sqrt{\frac{E_s T_s}{N_s \bar{Z}}}\right) \qquad (69)$$

With x the coordinate into the target, E(x) the man energy of the electron beam having the initial energy E_0 at x = 0, (be) bound electrons and (fe) free electrons of the substance to be penetrated with the dimensionless values N_s = N/N', E_s = E/E', T_s = T/T', with $\bar{Z}$ the mean charge of the plasma ions, and with Z the nuclear charge. The units are N' = 10^{18} cm^{-3}, E' = 10 keV, T' = 1 eV.

The solution of the differential equation

$$\frac{dE}{dx} = \left(\frac{dE}{dx}\right)_{fe} + \left(\frac{dE}{dx}\right)_{be}, E(0) = E_0 \qquad (70)$$

till E = 0 results in the range R corresponding to the initial value of the energy E_0.

The curves dE/dx obtained from eq. (70) show rather pronounced Bragg peaks at the end of the penetration range. The used formulas describe the range R of the electrons but are not able to describe the distribution of the deposited energy because theydon't take into account scattering events (diffusion processes) which result in a smearing out of the Bragg peak. To take this into account an approximation formula is used for describing the distribution of the energy deposition in th depth of the target [35].

The formula was derived from results of calculations with the Monte Carlo Code EMSH [39]. Introducing the dimensionless quantity u = x/R the approximation formula is given as

$$K(u,E) = \frac{1}{E}\frac{dE}{du} = 2.25(0.4+u)\exp(-6u^{4.5}) \quad with \int_0^1 K(u)\,du = 1 \qquad (71)$$

The energy deposition dE/dx is obtained from K(u,E) according to

$$\frac{dE}{dx} = \frac{E}{R}K(u,E) \qquad (72)$$

Range R(α) and deposited energy dE(α,x)/dx of magnetized electrons for impact angles α<90° are obtained from the values for α = 90° by applying a sinαcorrection according to

$$R(\alpha) = R\sin\alpha$$
$$dE(\alpha)/dx = \frac{E}{R(\alpha)} K\left(\frac{x}{R(\alpha)}\right) \tag{73}$$

Results of calculations of deposited energy applying the formulas (71) – (73) are shown in Fig. 25 for an impact angle of 5° for a carbon plasma of density 1018 cm-3 and temperature 5 eV. Fig. 26 shows results for solid carbon for perpendicular impact. For quantification of the quality of the simple energy deposition models used the energy deposition was calculated by the Monte Carlo method [40]. In these calculations the collision probability of the impacting electrons with the bound and free electrons and with the nuclei of the target plasma and the energy loss by collisions with bound and free electrons are calculated. A static magnetic field was taken into account. After a collision the Larmor radius of the electron may change according to the collisional energy loss but the direction of the movement along the magnetic field lines remains unaffected. A comparison of the results from Onte Carlo calculations and from the simple formuals (see Figs. 25, 26) shows that the simple formuals underestimate the energy deposition for the plasma and thus predict a too high range of the electron beam in the target plasma. For solid carbon of perpendicular impact the agreement is rather good.

6.2.2 Maxwellian distributed electrons

The Maxwellian distribution function is described by a set of energy groups with mean energies E_l and power densities Q_l (l = 1, ..., L). The Q_l are given according to

$$Q_l = N_l \int_{v_{l-1}}^{v_l} \frac{1}{2} m_e v^3 f_M(v) dv = N_l v_l E_l \tag{74}$$

Fig. 27 shows the normalized beam power density distribution for Maxwellian distributed electrons of temperature of 10 keV for 32 and 256 discrete beam energy groups

g. In case of 32 energy groups the last group with a mean energy of 66 keV contributes with about 2.5 % to the total power density. In case of 256 energy groups two additional energy groups with mean energies of 82 and 96 keV are appearing but the contribution of the 3 last energy groups to the total power density is only 2 %.

Using the equations (10) – (14) the energy deposition ΣdEl/dx was calculated for Maxwellian distributed electrons of temperature 10 keV in a carbon plasma of density 10^{18} cm^{-3} and temperature 10 eV. 32 and 256 energy groups were used. The results are shown in Fig. 28 for $\alpha = 90°$. In case of 256 energy groups the maximum range is larger caused by the contribution of the high energetic tails. Differences in the energy deposition between 32 and 256 energy groups are becoming apparent for rather low energy deposition values below 0.2 % of the initial value. In Fig. 28 are also indicated results of Monte Carlo calculations [40]. Similar to the case with monoenergetic electrons the energy deposition calculated by Monte Carlo is larger and the range is smaller.

Fig. 29 shows the volumetric energy deposition of Maxwellian electrons of temperature of 10 keV into solid graphite for the two impact angles 90° and 5° calculated with the Monte Carlo programm EMSH. The power density of the hot electrons is 10 MW/cm^2. For $\alpha = 5°$ the energy deposition close to the target surface is higher. Changing the incidence angle from 90° to 5° reduces the depth for which the same energy deposition is achieved by about a factor of 3.

For a plasma the results on energy deposition obtained from the models used in FOREV-2 are conservative because of an overestimation of the range. This results in an overestimation of the direct heat load at the target by the external beam. The deposited energy shows a rather weak dependence on the plasma temperature. A variation of the plasma temperature from 0.5 up to 10 eV changes the stopping power by a factor of 3. The maximum value is achieved at T = 5 eV.

6.3 Power deposition into the plasma and target

The energy deposition decreases with increasing impact energy. Therefore it is of importance to check whether the high energetic tail of the Maxwellian distributed

electrons is able to deposit its energy of part of it directly into the target resulting in a decrease of the shielding efficiency of the plasma shield and in an increase of erosion.

The power $\Delta Q_l(x_i)$ deposited by the energy group l of the electron beam with Maxwellian distribution into a target plasma of thickness Δx_l is obtained from eq. (13) as $\Delta Q_l = Q_l K(u_i)\,\Delta u_i$ with $Q_l = n_l v_l E_l$ the initial value for the group l. The power density deposited into the solid target is given as:

$$Q_{target} = Q_0 - \sum_l \Delta Q_l = \sum_l Q_l \left[1 - \int_0^{D/R_l} K(u)du \right] \tag{75}$$

with D the total thickness of the target plasma layer.

The power deposited into a homogeneous carbon plasma of density of 5 x 10^{18} cm^{-3} and thickness of 40 cm is shown in Fig. 30. Monoenergetic electrons of power density of 10 MW/cm^2 under an impact angle of 90° were used. 100 keV electrons deposit only 25 % of their beam power into the plasma whereas for 50 keV electrons only 2 % of the beam power is ariving at the target. The deposited power was calculated additionally for the same homogeneous carbon plasma layer for Maxwellian electrons of temperature of 10 keV. For the Maxwellian distribution 32 energy groups were used. The results are shown in Fig. 34. The contribution of the tail becomes evident for power fractions below 0.5 % and amounts up to 0.01 MW/cm^2. It is evident that 32 beamlets are sufficient for an adequate description of the beam power deposition into the plasma and the solid target for Maxwellian electrons.

6.4 Effect of volumetric energy deposition

Hot plasma electrons as was demonstrated in Fig. 29 deposit energy volumetrically into the solid target. Its influence on the temperature profile inside the bulk materail was calculated for 10 keV Maxwellian electrons for a target heat load of 10 MW/cm^2. The results are shown in Fig. 32. Vaporization was not taken into account. Therefore the surface temperature exceeds vaporization temperature. According to Fig. 32 the

temperature profile inside the target at times larger than 10 μs deviates fro mthe behaviour typical for surface energy deposition. At 50 μs it shows a maximum inside of the target. From this it is concluded that the volumetric energy deposition of 10 keV Maxwellian distributed plasma electrons might change the characteristic temperature profile and thus could initate a new type of erosion (see chapter 14). However before drawing any conclusions on that more detailed FOREV-2 calculations have to be performed taking into account all the heat sources which deposit energy to the target surface. All the calculations for ITER conditions performed up to now and to be reported here (chapters 9 and 10) were obtained by assuming that the hot plasma electrons also deposit their energy into the target surface.

7. Testing of the code

FOREV-2 results were checked against analytical solutions, against results of the 1 dim R-MHD code FOREV-1 and also against experimental results from simulation experiments performed at the plasma gun facilities 2 MK-200 CUSP and MK-200 CUSP at TRINITI Troitsk [43 - 45] and performed at the QSPA facility at IPP Kharkov [46].

7.1 Check against analytical solutions

For very large explosions in gases the hydrodynamic equations given as

$$\frac{\partial N}{\partial t} + \vec{\nabla} N \vec{v} = 0$$

$$\frac{\partial N \vec{v}}{\partial t} + \vec{\nabla} N \vec{v} \bullet \vec{v} + \vec{\nabla} P = 0 \qquad (76)$$

$$\frac{\partial}{\partial t}\left(\frac{3}{2} NT + \frac{Nv^2}{2}\right) + \vec{\nabla}\left\{\vec{v}\left[\frac{3}{2} NT + \frac{Nv^2}{2}\right] + P\vec{v}\right\} = 0$$

have analytical solutions for one, two and three dimensions and for arbitrary exponents γ of the pressure dependent density (P/N^{γ} = const) [41]. The solutions are shock waves which expand with the velocity v_2 into an unperturbed region (the index 2 indicates values at the shock front. The unperturbed region outside of the shock wave ($r>r_2$ with r_2 the shockwave front) has uniform gas pressure P_1, temperature T_1, density N_1 and zero velocity v_1. The quantities N,P,T,v behind the shock front ($r<r_2$) (a circle of radius $r_2(t)$ for a 2 dim problem and a sphere of radius $r_2(t)$ for a 3 dim problem) are time and position dependent.

Analytical solutions for the parameters N,v,P normalized to the shock front values (i.e. N/N_2, P/P_2, v/v_2) describing the situation behind the shock front ($r<r_2$) are shown in Fig. 33. The dimensionless quantities are independent from time. In Fig. 33 the analytical solutions are plotted for two different values of γ (γ=5/3 and 2).

To compare analytical with numerical solutions the gasdynamic problem of eq. (76) was calculated with FOREV-2. The geometry used is shown in Fig. 34. The calculational region was 1×1 m, covered by 100×100 meshes. The gas density was 10^{17} cm^{-3} and the temperature was 10^{-4} eV everywhere except at the quadratic region with 2×2 meshes in the lower left corner of the grid where the temperature was assumed to be T=20 eV. Reflective boundary conditions were used. In Fig. 35 - 37 the calculated values of gas pressure, density and velocity are compared with the analytical values at four time moments. There is full agreement between numerical and analytical results. For a monoatomic gas with exponent γ=5/3 the maximum density at the shock wave is equal to $N_2 = 4\ N_1$.

For 1 and 2 dim problems an analytical solution can also be found for the simplified magneto hydrodynamic system of equations with frozen in magnetic field lines which moreover are perpendicular to the xy plane [42]. The system of equations with B = $(B_x, B_y, B_z) = (0,0,B_z)$ and with v_z=0 writes as

$$\frac{\partial N}{\partial t}+\vec{\nabla}N\vec{v}=0$$

$$\frac{\partial N\vec{v}}{\partial t}+\vec{\nabla}N\vec{v}\bullet\vec{v}+\vec{\nabla}\left[P+\frac{B_z^2}{2\mu_o}\right]=0$$

$$\frac{\partial}{\partial t}\left[\frac{3}{2}NT+\frac{Nv^2}{2}+\frac{B_z^2}{2\mu_o}\right]+\vec{\nabla}\left\{\vec{v}\left[\frac{3}{2}NT+\frac{N_v^2}{2}+\frac{B_z^2}{2\mu_o}\right]+\left(P+\frac{B_z^2}{2\mu_o}\right)\vec{v}\right\}=0 \qquad (77)$$

$$\frac{\partial B_z}{\partial t}=\vec{v}\times\left(\vec{v}\times\vec{B}\right)$$

In [30] it is shown that in case of frozen in magnetic field lines perpendicular to the plasma velocity and parallel to the discontinuity surface the Hugoniot adiabatic condition at the discontinuity surface is the same as for the hydrodynamic system of equations with corresponding change of effective pressure and energy of the gas. In this case as shown in [41] the magnetic field can be excluded from the magnetohydrodynamic system of equations by changing the energy e into

$$e=\frac{3}{2}NT+\frac{B_z^2}{2\mu_o} \text{ and the pressure P into}$$

$$P_{eff}=P+\frac{B_z^2}{8\pi}=\text{const } N^{\gamma_{eff}} \text{ with the exponent } \gamma_{eff} \text{ given as} \qquad (78)$$

$$\gamma_{eff}=\frac{\gamma\beta+2}{\beta+1}$$

$$\text{with } \beta=\frac{8\pi NT}{B_z^2}$$

For γ_{eff} it is valid $\gamma<\gamma_{eff}<2$

Despite the fact that the exponent γ_{eff} is not constant (it depends on density N) the same solution as for the system of equations (76) is still valid for this case.

A magnetohydrodynamic problem was calculated with FOREV-2. The geometry is shown in Fig. 38. In the computational region of 1× 1m covered by 150 × 150 meshes there was assumed a background plasma of temperature 20 eV and density 10^{15} cm^{-3} in the whole computational region and a background magnetic field $\vec{B}$ = (B_x, B_y, B_z) = (0, 0, 0,05 T). In the lower left corner of the calculational grid the magnetic field strength was assumed to be 5000 T in a region of 3×3 meshes. Reflective boundary conditions were used. In Figs. 39-41 the calculated values gas pressure,

density and velocity again are compared with the analytical solutions at 4 different times. Again there is rather good agreement. The numerical solution gives still more information. For instance Fig. 42a shows the time evolution of the magnetic field B_z and Fig. 42b the time evolution of the plasma temperature. The high initial magnetic pressure drives the plasma expansion. The magnetic field strength drops quickly and the magnetic energy is converted into heating of the plasma with a sudden temperature rise up to 10^8 eV within 0.5 ns. Compression of the background plasma results in formation of a shock wave. For a gas with exponent $5/3<\gamma_{eff}<2$ the maximum density of the compressed background plasma is in the range $3N_1<N_2<4N_1$ (see Fig. 39). The shock front is heated up to several 10^6 eV by the decaying magnetic field and by the work performed by the rather large pressure gradient (see Fig. 40). The degree of approximation of circular symmetry of the numerical calculation by using 150×150 meshes can be seen from Fig. 43 where plasma density contours are shown.

According to the analytical solution the shock wave radius depends on time according to

$$r_2=\left(\frac{E}{N_1}\right)^{1/3} t^{2/3} \text{ in one-dim case}$$
$$\text{and } r_2=\left(\frac{E}{N_1}\right)^{14} t^{1/2} \text{ in two-dim case} \qquad (79)$$

where the constant E depends on the total energy in the shock wave region with $r \leq r_2$. The dependence of the shock wave radius r_2 on time is shown in Fig. 44. The slope of the numerically calculated curve $d \ln r_2(t)/d\ln t = 0{,}5$ is in agreement with the analytical square root dependence.

7.2 Check against the 1 dim Lagrangian code FOREV-1

Results of FOREV-2 were compared with results from the 1dim Lagrangian code FOREV-1. FOREV-1 in turn was checked against disruption simulation experiments and it was shown that rather good agreement is achieved [8]. A horizontal target arrangement was used. The geometry is shown in Fig. 3a. The target is at x = 0 cm.

The magnetic field lines in toroidal direction are inclined. It was assumed B_x = 0.5 T and B_z = 5 T. The impact angle is 5°. The FOREV-2 calculations were performed with a spatial region of size of 300 x 40 cm^2 and 60 x 40 meshes being nonuniform in x direction with size increasing in geometric progression with $\Delta x_n = x_1 q^n$ with q = 1.075 with Δx_1 = 0.29 cm near the target and Δx_n = 21 cm at 3 m distance. The background plasma density in the FOREV-2 calculations was 1.5 x 10^{12} cm^{-3}. The optical properties of the carbon plasma were described by frequency group optimized 24 group Rosseland opacities. The power density of the incoming hot plasma with 10 keV ions and 10 keV Maxwellian distributed electrons was constant in time and in y direction (perpendicular to the velocity of the hot plasma). Calculations were performed for the two power densities 10 and 100 MW/cm^2. Heat conduction into the target and volumetric energy deposition by high energetic plasma electrons was calculated by using 12 meshes inside the target. FOREV-1 uses 64 Lagrangian meshes of nonuniform size. The mesh size in FOREV-1 is adjusted to resolve steep gradients of plasma density and temperature in the plasma shield. For the FOREV-1 calculation 512 group Planck opacities were used. The 24 group Rosseland and 512 group Planck opacities were condensed from the same data of optical coefficients. Moreover for both opacity sets frequency group optimized group structures were used.

The Figs. 45-48 show a comparison of the results for 10 MW/cm^2 and Figs. 49-51 for 100 MW/cm^2. Fig. 45 shows the movement of a plasma density wave (evolution of thickness of the plasma shield). After 50 μs it reaches a distance of 2 cm from the target, after 500 μs about 20 cm. Moreover the position of the leading edge is at 30 cm after 50 μs and at 2.5 m after 500 μs. There is good agreement in evolution of these two characteristic regions between FOREV-1 and FOREV-2. The existing differences in the region of the sharp density gradient are due to the finer mesh used in FOREV-1 and its continuous mesh adjustment. FOREV-2 is not using any mesh adjustment procedure. The increasing difference in the results of FOREV-1 and FOREV-2 after 500 μs is due to shifting of the density gradient to the region with coarse meshes and the position of the leading edge reaches the end of the calculational region of FOREV-2. Calculated profiles of plasma temperature are shown in Fig. 46. The three characteristic regions cold plasma near the target, corona region with high temperature and transition region with sharp temperature gradient are

clearly to be seen. In Fig. 47 erosion results are compared. Up to 1 ms erosion agrees within 30 %. Fig. 48 finally shows a comparison of target heat fluxes calculated with FOREV-1 and FOREV-2 for a horizontal graphite target and a constant power density of 10 MW/cm^2 in y direction with a width of 5 cm. Heat deposition by the impacting hot plasma dominates the target heat flux at all times. According to Fig. 48 there is agreement of results on evolution of heat deposition by the impacting hot plasma and by radiation from 1 dim calculations with FOREV-1 [8] and from 2 dim calculations with FOREV-2. Electron heat conduction only plays a role as target heat source at early times. At later times the plasma temperature profile in the plasma shield close to the target becomes constant in a layer of thickness of 0,4 mm, thus blocking the heat transfer by electron heat conduction.

From Fig. 48 it is clearly seen that the hot plasma ions immediately are stopped in the evolving plasma shield (sudden drop of target heating by a factor of 2 after evaporation has started at 4.5 μs). The domianting target heat load is direct heating by the impacting Maxwellian distributed hot plasma electrons. The radiative heat load to the target is negligible. Assuming a linear scaling of this heat load with the incoming power density and the heat load by direct impact independent from the power density it is concluded that below 50 MW/cm^2 target heating by the hot plasma electrons is the dominating target heat load.

The decrease of the radiative flux at times larger 100 μs is due to the expansion of the plasma shield. The radiation is coming from the transition region which moves away from the target. Thus with increasing distance of the radiating region from the target the radiative target heat load decreases. The total lateral radiation flux from the plasma shield of width 5 cm (curve 4 of Fig. 48) was calculated in FOREV-1 by taking into account a loss term which is consistently calculated together with the spectral radiation flux [7]. The energy laterally radiated away from the plasma shield after 1 ms amounts up to 85% of the input energy. Thus radiative energy deposition to side walls has to be studied carefully. Calculated plasma density and temperature profiles for a power density of 100 MW/cm^2 are shown in Figs. 49 and 50. The agreement of the results from FOREV-1 and FOREV-2 is even better than for the 10 MW/cm^2 case. A comparison of calculated erosion is shown in Fig. 51. Up to 500 μs the agreement again is within 30 %.

8. Validation of FOREV-2 using results from simulation experiments

Magnetized plasma stream target experiments were performed at the plasma gun facilities 2MK-200 CUSP [43], MK-200 CUSP [44] and MK-200 UG [45] at TRINITI Troitsk and at the QSPA facility at IPP Kharkov [46]. The facilities all have similar characteristics with respect to the hot plasma. The plasma β value is around 0.3. In the CUSP facilities the plasma ion temperature is around 500 eV. The Maxwellian distributed electrons have temperatures up to 300 eV. In the MK-200 UG facility the ion impact energy is about 1.5 keV, in the QSPA facility the about 250 eV, but the ion temperature is only around 20 eV. Experiments were performed with perpendicular and tilted graphite and quartz targets. For perpendicular targets the magnetic field lines are perpendicular to the target, thus simulating a horizontal target in the poloidal plane but neglecting the toroidal component of the magnetic field. In the calculations for the CUSP facilities the power density profile of the impacting magnetized plasma was assumed to be Gaußian with full width at half maximum (FWHW) of 0.8 cm. Its time evolution as shown in Fig. 52a has a half width of 10 µs. Peak power densities up to 42 MW/cm^2 are reached in the MK-200 CUSP facility after 3 µs. The power density remains constant for 5 µs and then decays exponentially. In the MK-200 CUSP facility the guiding magnetic field at the target position is 3.3 T. In the 2MK-200 CUSP facility with its larger trap the guiding magnetic field at the target position is 2 T. The peak power density achieved in this facility is 18 MW/cm^2. Its time evolution and the half width of the Gaußian power density profile are about the same as for the MK-200 CUSP facility (see Fig. 52a). In the MK-200 UG facility the Gaußian power density profile of the hot plasma has a full width at half maximum of 6.0 cm. The time evolution of the hot plasma as used in the calculations is shown in Fig. 52b. It has a full width at half maximum of around 25 µs. Peak power density is reached after about 10 µs, remains constant for 15 µs and then decays exponentially. The guiding magnetic field is 2 T at the target position. Peak power densities up to 35 MW/cm^2 are achieved. In the QSPA the Gaußian power density profile of the hot plasma has a full width at half maximum of 8 cm. The peak power density along the separatrix is 20 MW/cm^2. The time evolution of the hot plasma as used in the calculations is shown in Fig. 52c. It has a full width at half maximum of around 200 µs. Peak power density is reached after 100 µs, remains

constant for about 100 μs and decays again linearly. The guiding magnetic field at the target position is 0.55 T. The QSPA facility produces hot plasma streams of rather large duration thus target erosion should be reasonably large and what is still more important a comparison of measured and calculated electron densities in the plasma shield and of erosion should answer partly the question how the MHD movement of the plasma shield influences erosion and plasma shield efficiency. Moreover measurements by magnetic probes in the plasma shield could provide information on the behaviour of the guiding magnetic field and thus allow to check the adequacy of the boundary conditions used for B_x at the target and the time dependent re-diffusion of B_x back into the plasma shield.

From the simulation facilities experimental results are available for graphite and quartz targets. Quartz targets were used, because they allowed a measurement of erosion rates [8] and because of quite large erosion. The following boundary conditions (BC) for the magnetic field at the targets were used: for graphite frozen in and for quartz free movement. The frozen in situation is described either by $B_{BC}(t) = B_{ox}$ with B_{ox} the vacuum magnetic field or by use of eq. (3) with $\tau > 10$ μs. The boundary condition for free movement of B_x is either given by $B_{Bc}(t) = B'_x(t)$ with $B'_x(t)$ the magnetic field in the plasma shield or by use of eq. (3) with $\tau \leq 1$ μs. All these possibilities were used in the 2 dim calculations. For frozen in or $\tau > 10$ μs and for free or $\tau < 1$ μs the results were the same but the MHD behaviour drastically changes when going from frozen in to free.

A comparison of measured and calculated 2 dim lateral radiation fluxes from a carbon shield at the facility 2 MK-200 CUSP is discussed in [8]. It was shown that measured and calculated radiation fluxes agree within a factor of two. The code validation as discussed here concentrates on a comparison of measured and calculated profiles of electron density and plasma temperature in plasma shields and on a comparison of erosion.

8.1 Results from the 2 MK-200 CUSP facilities

Fig. 53 shows calculated target heat fluxes for a perpendicular graphite target at the 2 MK-200 CUSP facility. The peak power density is 18 MW/cm^2. According to Fig. 53

direct energy deposition is negligible. Electron heat conduction dominates the target heat flux. The radiation flux is around 0.1 MW/cm^2 and thus is a factor of 5 less than the electron heat conduction flux.

Calculated and measured electron temperature profiles in a carbon plasma shield in the 2 MK-200 CUSP along the separatrix (in x direction) at 10 μs are shown in Fig. 54. The energy density of the magnetized plasma was 200 J/cm^2. A horizontal target was used, the target size in y direction was 3 cm. The full width of the calculational region was 5 cm. Side walls were assumed to be fully transparent. At a distance of 1 cm from the target the temperature is up to 50 eV whereas in the tokamak plasma shield it is only 1 eV. Due to this steep temperature gradient close to the target electron heat conduction becomes the dominating target heat source in these simulation experiments. Direct energy deposition of the magnetized plasma to the target is negligible. Because of its low impact energy the magnetized hot plasma after 0.8 μs is fully stopped in the evolving plasma shield.

Calculated and measured electron density profiles in a carbon plasma shield at different distances from a graphite target and for different times are shown in Fig. 55 for the MK-200 CUSP facility for a peak power density of the magnetized plasma of 42 MW/cm^2 for a horizontal graphite target. The guiding magnetic field is 3.3 T. The calculated profiles and density values are in rather good agreement with the measured values. Simulation experiments performed at the QSPA facility [27] at IPP Kharkov yielded electron density values in carbon plasma shields of around $3 \cdot 10^{17}$ cm^{-3} at a distance of 0,5 cm from the target in very good agreement with the values shown in Fig. 55. For the 2 MK-200 CUSP facility calculated 2 dim plasma density contours and the plasma flow $\Gamma = nv$ (arrows)are shown in Fig. 56 in a carbon plasma shield at two different times for a peak power density of the magnetized plasma of 20 MW/cm^2. The guiding magnetic field is 2 T. The carbon density range for the contour plot is from 1.4×10^{16} up to 10^{17} cm^{-3}. The density decreases with increasing distance from the target. In the region closer to the target where the plasma flow is indicated the carbon density increases up to 5×10^{18} cm^{-3}. Up to 14 μs the plasma flows across the magnetic field lines to the separatrix (inward flow) and then along the separatrix upstream. The thickness of the layer in which this inward flow occurs is about 1.5 mm. The reason for the inward flow is pushing away

of the guiding magnetic field component B_x from the region of maximum power density (separatrix) to the sides resulting in depletion of B_x in the center as seen from Fig. 57a. Due to its high electric conductivity B_x is assumed to be frozen in at the graphite target. Thus the magnetic field lines are bent near the target and a y component of magnetic field (B_y) arises as shown in Fig. 57b for lateral (y direction) positions below the separatrix. Above the separatrix strike point (y > 2.5 cm) B_y changes its direction.

According to the y component of the motion equation (third equation of the system of eqs.(4)) which writes as

$$\frac{\partial \rho u_y}{\partial t} + \vec{\nabla} \rho u_y \vec{u} + \frac{\partial}{\partial y}\left(P + \frac{B^2}{2\mu_0} \right) = \frac{1}{\mu_0}\left(\vec{B}\vec{\nabla}\right) B_y \qquad (80)$$

the x and y dependence of B_y causes plasma movement to the separatrix according to

$$\frac{\partial \rho u_y}{\partial t} \approx \frac{1}{\mu_0}\left(\vec{B}\vec{\nabla}\right) B_y \qquad (81)$$

Later in time ($t \geq 20$ μs) B_x diffuses back into the cold dense part of the plasma shield and B_y disappears as is seen from Fig. 57b. Due to momentum transfer by the hot ions the plasma flow close to the target now changes its direction and flows outward as shown in Fig. 56 at t = 20 μs. Profiles of carbon density and plasma temperature along the separatrix are shown in Fig. 58 for the time moments 14 μs and 20 μs. At 14 μs the dense plasma extends over a layer of thickness of 7 mm, at 20 μs only over 1 mm. Due to the reduced plasma mass at 20 μs the plasma temperature in the first mesh adjacent to the target increases from 0.5 eV to 0.9 eV.

The electron heat conduction flux q_{el} along the magnetic field lines to the target is calculated according to

$$q_{el} = \alpha\, N_e\, \kappa_{\|}\, \Delta T/\Delta x \qquad (82)$$

with N_e the plasma electron density, $\kappa_{\|}$ the electron heat conductivity coefficient [47], α an accommodation coefficient and $\Delta T/\Delta x$ the temperature difference between the

target surface (at boiling temperature) and the plasma temperature in the first mesh. N_e is given as

$$N_e = Z_{eff}\, N_c \qquad (83)$$

with Z_{eff} the average charge and N_c the carbon density. At temperatures around 0.5 eV Z_{eff} is small and it changes within an energy interval of 0.1 eV by one order of magnitude. Despite of limited accuracy of q_{el} in these cases its influence on erosion is small because of a self regulating process which reduces q_{el} at larger erosion rates. This mechanism also is responsible for the negligible influence of the accommodation coefficient α on erosion.

The target heat flux by electron heat conduction is shown in Fig. 59 for graphite and quartz. During the period of plasma flow to the separatrix with high plasma density and low plasma temperature the target heat flux by electron heat conduction is small for graphite. After plasma flow reversal ($t > 20$ μs) the carbon plasma density close to the target decreases but the plasma temperature increases and thus the electron heat conduction flux to the graphite target increases again. The calculated erosion value for graphite is 0.25 μm. It is fully determined by electron heat conduction. The measured value is 0.2 μm.

Time dependent erosion rates during one single shot were measured for quartz under the same experimental conditions. Erosion values of 0.8 μm were obtained [8]. This experiment was also analysed with FOREV-2. Quartz has a smaller electric conductivity than graphite and therefore B_x is not frozen in at the target. Pushing out of B_x by the vaporized material now occurs also at the target. Consequently there is no magnetic field component B_y as seen from Fig. 57b and thus the plasma shield is experiencing no lateral magnetic force and momentum transfer from the hot plasma ions is dominating the movement. The plasma close to the target all the time flows along the target in outward direction away from the separatrix as shown in Fig. 60 for two different times. This outward flow just from the beginning reduces the plasma shield density at the center, and increases the plasma temperature in comparison with carbon and thus results for at least 10 μs in a higher electron heat conduction flux to the target in comparison with graphite as shown in Fig. 59. For quartz and for times larger than 10 μs, this target heat flux amounts up to 0.5 MW/cm^2. For both

target materials the radiative heat flux is around 0.02 MW/cm^2 and thus is negligible. Direct energy deposition of the magnetized hot plasma to the target is negligible too. Because of its low impact energy it is fully stopped after 0.8 μs in the evolving plasma shield. Fig. 61 shows a comparison of measured and calculated time dependencies of erosion of quartz at two different positions. The calculated erosion values are in good agreement with the measured ones. In the experiment the time dependent erosion left and right from the center differs because of the asymmetric power density profile of the magnetized plasma [8]. In the calculation a Gaußian profile was used. The target heat load and thus erosion in the CUSP experiments is fully determined by electron heat conduction.

The quite different MHD motion of carbon and quartz plasma shields can also be seen from a plasma mass balance as shown in Figs. 62 and 63. For carbon (Fig. 62) at times below 15 μs most plasma mass is accumulated in the center (at the position of the separatrix) indicating flow of plasma to the center. At later times the plasma mass in the center decreases because of plasma outflow from the center. For quartz the plasma mass in the center during all times remains rather small but due to permanent plasma outflow from the center the lateral width of the plasma shield increases (see Fig. 63). The total plasma mass in the center is larger for carbon than for quartz despite a factor of 3 larger erosion for quartz. At 25 μs and later the plasma flow in both cases is outward. The plasma mass at the separatrix and its distribution are comparable and thus also the electron heat conduction flux.

FOREV-2 also was used for a modelling of the MHD behaviour of the target plasma in case of a tilted graphite target (tilting angle 22°). Measurements were performed at the MK-200 CUSP with a magnetic field strength of 3,3 T at the target position [44]. In this case a rather drastic movement of target plasma along the target surface is observed in the experiments as is seen from Fig. 64a. The maximum electron density close to the target amounts up to $5 \cdot 10^{17}$ cm^{-3} and thus is comparable to the density for the horizontal target (see Fig. 54). 2 dim contour plots of electron density and the plasma flow at 10 μs calculated with FOREV-2 are shown in Fig. 64b. Pushing of the plasma shield along the target surface is clearly to be seen. Moreover the electron density values are in quite good agreement with the measured ones.

Thus the experimental results on the MHD behaviour of plasma shields at early times principally are confirmed.

8.2 Results from the MK-200 UG facility

In this facility measurements of erosion were performed for graphite and quartz targets tilted with respect to the guiding magnetic field with 2.0 T and for graphite oriented perpendicular. Moreover performed have been measurements of lateral leakage radiation fluxes from carbon and tungsten plasma shields. This latter is important for quantification of side wall damage by radiation. Calculated target heat fluxes for a tilted graphite target are shown in Fig. 65. The target heat loads from electron heat conduction and from radiation are comparable. Direct energy deposition continues up to 6 μs. Afterwards the hot plasma stream is fully stopped in the plasma shield. Its energy deposition to the target remains below 4.5 J/cm^2 and thus is rather small. The measured peak erosion for a tilted target is 0.22 μm. This value was determined as average value after 20 shots. The calculated value is 0.25 μm.

For the tilted quartz target the target heat loads are shown in Fig. 66. Radiation is dominating. Direct energy deposition by the impacting hot plasma drops to zero after 4 μs. Its overall contribution to the target heat load is quite small. To account for optical transparency of the quartz target it was assumed that 60 % of the radiative energy impinging onto the target is transmitted and only 40 % is absorbed. The absorption was assumed to occur at the target surface. For the tilted quartz target (inclination angle 20°) the measured peak erosion is 0.45 μm. Fig. 67a shows the measured erosion pattern which clearly demonstrates a modulation of the erosion. According to Fig. 67b the modulation wavelength is about 7 cm. Such an effect firstly was predicted theoretically [14] and then afterwards was confirmed experimentally [48, 49]. The calculated erosion value for a tilted quartz target is 0.7 μm and thus is a factor 1.5 larger. The calculated erosion profile is shown in Fig. 67c. Modulation of erosion of the tilted quartz target is occurring. The modulation length is about 5 cm. Fig. 68 shows the calculated erosion pattern for the tilted graphite target. Modulation

of erosion again is occurring. The modulation wavelength is about 7 cm. For a more detailed discussion on modulation of erosion see chapter 13 below.

8.3 Results from the QSPA facility

Measurements were performed for graphite and polished quartz targets oriented perpendicular and for quartz targets tilted with respect to the guiding magnetic field with 0.55 T. The quartz targets had a surface roughness below 1 μm. Originally they had been used as optical windows with full transparency for visible and UV radiation. In the calculations this was simulated by assuming that target heating by radiative energy can be neglected.

Measured erosion profiles for a perpendicular graphite and quartz target are shown in Figs. 69a and b and for a tilted quartz target in Fig. 69c. Maximum erosion for a perpendicular quartz target is 7 μm (Fig. 69a) and for a perpendicular graphite target is 2 μm (Fig. 69b). For the tilted target (inclination angle 20°) peak erosion was measured to be 7 μm and a quite clear modulation of erosion is to be seen (Fig. 69c).

Calculated target heat loads for the perpendicular targets are shown in Figs. 70a for quartz and in Fig. 70b for graphite. For the calculations the side wall distance was 40 cm, the target size was 10 cm and the separatrix position was in the center of the target. In both cases direct heating by the impacting hot plasma is negligible. The dominating heat flux is by electron heat conduction. This is rather similar to the results for quartz at the CUSP facility (see Fig. 59). However the time scale has expanded by one order of magnitude. For quartz typically heat fluxes from electron heat conduction now are 0.15 MW/cm^2 to be compared with 0.5 MW/cm^2 at the CUSP facility. The radiative target heat load is quite small. In the calculation of erosion this heat flux was neglected because of the assumption of full transparency of the polished target. Fig. 71 shows 2 dim plasma density contour lines (density range is from $7 \cdot 10^{18}$ to 10^{17} cm^{-3}) and the plasma flow pattern in a quartz plasma shield. The plasma flows outward, away from the separatrix, again similar to the situation at the CUSP facility. Fig. 72 shows the time dependent peak erosion. It

occurs at the position of the separatrix. A value of 6.5 μm is obtained. This has to be compared with the experimental value of 7 μm.

For a perpendicular graphite target averaged target heat fluxes from electron heat conduction are about 0.15 MW/cm^2 (see Fig. 70b) and thus are comparable to quartz. Also the radiative heat load with about 0.05 MW/cm^2 is comparable. Fig. 73 shows 2 dim plasma density contours and the flow pattern of the carbon plasma shield at 167 μs. The plasma flows to the separatrix Fig. 74 shows the time dependent peak erosion. A value of 1,5 μm is obtained. This has to be compared with the experimental value of 2.0 μm.

Fig. 75 shows the time dependent behaviour of B_x with B_{xo} = 0.55 T for the perpendicular graphite target. B_x after 40 μs is considerably pushed out from the plasma shield. After 300 μs B_x starts to diffuse back again into the plasma shield. Back diffusion is a quite slow process and it takes more than 100 μs til back diffusion is completed. This behaviour is independent from the distance to the target. Figs. 76a and b show time dependent electron and carbon densities in the plasma shield at the position of the peak power density and Fig. 77 shows the time dependence of the plasma temperature in the plasma shield. Calculated carbon density and temperature profiles (Fig. 776a and 77) are quite similar to those calculated for graphite for ITER conditions (see Figs. 45 and 46).

Table 4 gives a comparison of calculated and measured erosion values for the three different facilities and lists that source which dominates the target heat load. As is seen from Table 4 there is a rather large discrepancy in measured and calculated erosion for a tilted quartz target where the calculation yields a value being a factor of 10 lower than the measured one. The large reduction in comparison with the calculated value for a perpendicular target is caused by a decrease of the electron heat conduction flux (see chapter 12 for a more detailed discussion).

The rather large experimental value of erosion for the tilted target could be due to specific features of the QSPA facility. Indications for that are obtained from a comparison of the measured and calculated diamagnetic behavior of the carbon and quartz plasma shields. According to Fig. 75 the calculation predicts a pronounced diamagnetic effect. For carbon the guiding magnetic field at the position of the peak

power density is reduced by a factor of 3 and for quartz by a factor of 5. For quartz the effect is larger because of the free boundary condition at this target. First magnetic probe measurements show a less pronounced diamagnetic effect of the carbon plasma shield (magnetic field reduction factor is about 1.8) and a smaller diamagnetic effect for quartz. Smaller diamagnetic effects principally indicate lower temperatures in the plasma shield. An explanation for this could be impurities present in the free plasma stream. These impurities dissipate energy by radiation resulting in a cooling down of the plasma shield. However how this influences target heat loads still has to be analyzed in detail.

9. Energy balance for ITER targets and slot divertor side wall damage

The ITER conditions as described in chapter 2 were used. The unperturbed magnetic field lines $\vec{B}_0$ are assumed to have components in x and z directions with $\vec{B}_0$ = (0.5 T; 0; 5 T). The disruptive hot SOL plasma hits the target while flowing along the inclined magnetic field lines. It consists of 10 keV plasma ions and 10 keV Maxwellian plasma electrons with equal energy carried by ions and electrons. Results of 2 dim R-MHD calculations with FOREV-2 for hot SOL plasma target interactions at different peak power densities of the impacting hot plasma have been presented in [50, 51]. In all cases the classical diffusion coefficient was used in the magnetic field equations.

9.1 Horizontal graphite target

9.1.1 Gaußian power density profile

The time evolution of calculated target heat fluxes during a hot SOL plasma target interaction event is shown in Fig. 78 for a horizontal graphite target. The calculations were performed for Gaußian power density profiles with peak power densities of 3, 10 and 100 MW/cm^2 along the inclined magnetic field lines. The heat flux values are shown at the position of maximum erosion. As will be discussed below this position doesn't belong to the position of the separatrix strike point.

Shown in Fig. 78 are the heat flux into the bulk target, the target heating by the impacting hot SOL plasma and the heat fluxes deposited onto the target by radiative energy transfer from the plasma shield. The heat flux into the bulk target depends on the heat conduction coefficient κ and shows a $1/\sqrt{t}$ dependence on time. Constant target heating at early times means full deposition of beam power onto the target. At 3 MW/cm^2 vaporization starts after 25 μs, at 10 MW/cm^2 after 4.5 μs and at 100 MW/cm^2 after 0.1 μs. Immediately afterwards the hot plasma ions are stopped in the plasma shield, whereas the hot plasma electrons still deposit their energy into the target. For 3 and 10 MW/cm^2 the target heat load at all times up to the calculated latest time moment of 1 ms is fully determined by direct energy deposition of the hot plasma electrons. The contribution of radiation is negligible. For 10 MW/cm^2 the radiative target heat load becomes about 30 kW/cm^2. It remains constant up to 200 μs and then decreases. For 3 MW/cm^2 the radiative target heat load reaches about 3 kW/cm^2 in the time period 50 μs up to 200 μs and decreases afterwards. The rather sharp drop of the radiative target heat load in both cases is due to the expansion of the plasma shield. This results in an increasing distance of the radiative region from the target. For 100 MW/cm^2 the radiative target heat load becomes about 0.1 MW/cm^2 and remains essentially constant at least up to 1 ms. After 1 ms the direct target heating by the hot SOL plasma electrons drops to small values. After 600 μs the radiative target heat load becomes the dominating heat load.

Radiation fluxes to the side walls are shown in Fig. 79 for 10 MW/cm^2 and in Fig. 80 for 100 MW/cm^2. Maximum heat flux values to the side walls typically are 50 kW/cm^2 at early times and around 25 kW/cm^2 at later times for a slot width of 60 cm for 10 MW/cm^2. Up to 1 ms no evaporation occurs. For 100 MW/cm^2 maximum heat flux values at the side walls typically are 0.1 MW/cm^2. Evaporation of graphite side walls starts after 60 μs.

9.1.2 Realistic power density profile

The time evolution of calculated target heat fluxes is shown in Fig. 81 at the position of the separatrix strike point (SSP) which coincides in this case with the position of maximum erosion. Realistic power density profiles with peak power densities of 10

MW/cm^2 and 100 MW/cm^2 along the inclined magnetic field lines were used. The hot plasma ions after a few μs are fully stopped in the evolving plasma shield. For 10 MW/cm^2 heat deposition by the impacting hot plasma electrons dominates the target heat load at all times. The contribution of radiation to the target heat load is negligible everywhere. For 100 MW/cm^2 the radiative target heat load becomes about 0.2 MW/cm^2 and essentially remains constant up to 1 ms. After 600 μs the hot SOL plasma is fully stopped in the plasma shield and direct target heating by the SOL plasma stops. Then the radiative target heat load becomes the dominating heat load. Radiation fluxes to the side walls at different times are shown in Fig. 82 for 10 MW/cm^2 and in Fig. 83 for 100 MW/cm^2. The deposition width increases with time because of expansion of the plasma shield and reaches typically 1.5 m after 500 μs. Radiative heat flux values at the side walls typically are 50 kW/cm^2 at early times and around 25 kW/cm^2 at later times for a slot width of 60 cm for 10 MW/cm^2. For 100 MW/cm^2 maximum radiative heat flux values at the side walls are 150 kW/cm^2 at small distances from the target and typically around 100 kW/cm^2 at around 1 m distance from the target.

9.2 Vertical graphite target

For a vertical target with poloidal inclination angle of 20° the time evolution of calculated target heat fluxes is shown in Fig. 84a for the case separatrix down-stream at the SSP. Realistic power density profiles with peak power densities of 10 MW/cm^2 and 100 MW/cm^2 were used. For 10 MW/cm^2 the heat load by direct impact of hot plasma dominates up to 1 ms. The radiative target heat flux starts after 200 μs to contribute. It remains constant up to 1 ms and contributes about 30 % to the target heat load. For 100 MW/cm^2 the radiative target heat load dominates after 20 μs and the target heat load by direct impact of the hot SOL plasma becomes negligible after 100 μs. Fig. 84a reveals quite interesting features: for the 100 MW/cm^2 case the direct energy deposition at times larger than 10 μs is less than for the 10 MW/cm^2 case because of better shielding of the larger mass of the plasma shield for the 100 MW/cm^2 case and be . For the 10 MW/cm^2 case direct energy deposition dominates the target heat load. From this it is immediately evident that the impact energy of the plasma electrons has a quite large influence on the target damage as will be

discussed later in chapter 11. Comparing Figs. 81 and 84a it is seen that for the horizontal target the target heat load by direct enerrgy deposition of the hot plasma continues til later times. This is due to the different MHD behaviour of the plasma shield in both cases (see chapter 10).

Fig. 84b shows a comparison of the time evolution of the target heat loads for a vertical target with upstream and downstream separtrix strike point. The peak power density along the separatrix is 10 MW/cm^2. The heat fluxes are belonging to the position of maximum erosion. The radiative target heat load is the same for both cases, but the direct energy deposition by the hot plasma is less for the case with downstream separatrix. For the consequences on erosion see chapter 10.2.

For 100 MW/cm^2 the radiative target heat load achieves a value of around 0.1 MW/cm^2 and remains essentially constant up to 1 ms. The reason for the weak dependence of the radiative target heat load on time is that the highly radiating volume always remains rather close to the target as is seen from Fig. 85 which shows the 2 dim radiation field (arrows, change of size indicates the radiating region) and 2 dim plasma density profiles. Time dependent radiation fluxes to the upper side wall are shown in Fig. 86 for 10 MW/cm^2. Typical heat flux values are 15 kW/cm^2 and thus are a factor of 3 less than for a horizontal target with realistic power density profile. The deposition width typically is 1 m. Fig. 87 shows radiation fluxes to the upper side wall for a peak power density of 100 MW/cm^2 of the impacting hot SOL plasma. The peak radiative heat load is around 0.2 MW/cm^2. After around 0.1 ms the upper side wall starts to evaporate. Then because of the vapor shield effect the radiative heat load decreases further. After establishment of a vapor shield in front of the side wall made from vaporized material the radiative heat load drops down to 0.1 MW/cm^2 and remains constant for at least 0.6 ms. From Fig. 85 it is seen that the radiative flux is anisotropic with preferred direction to the upper side wall. From this follows that heating and start of vaporization will be different for both side walls. Evaporation of the lower side wall starts after 340 μs.

9.3 Side wall damage

FOREV-2 was used for estimation of side wall damage. For a peak power density of the impacting hot plasma of 10 MW/cm^2. Figs. 88 and 89 show profiles of surface temperatures of a graphite side wall at different times for a vertical and a horizontal graphite target. As the lateral radiative heat fluxes are larger for the horizontal target the surface temperature at the side wall is also larger for this case. After 1.0 ms it reaches 1800 °K for a vertical target and 2500 °K for a horizontal target. Vaporization starts after about 10 ms for graphite. For times up to 100 ms the surface temperature of tungsten side walls remains below 3000 °K. Below 10 MW/cm^2 melting of tungsten side walls does not occur within 1 sec. For a peak power density of 100 MW/cm^2 melting and evaporation of tungsten and graphite side walls occur. After 1 ms tungsten side walls start to melt over a length of about 1 m. Tungsten evaporation starts after about 5 ms. However the depth of erosion by vaporization remains rather small. It reaches only about 0.1 μm after 10 ms and thus remains negligible, whereas the melt layer thickness after 10 ms reaches 100 μm. With graphite as side wall material evaporation of the upper side wall will start after 0.10 ms as is seen from Fig. 90. After 1 ms peak erosion is 3 μm and the half width of the erosion profile is 1 m.

9.4 Extremely high power density of the impacting hot SOL plasma

To study the shielding efficiency of plasma shields against radiative energy there were performed two-dimensional calculations for a vertical target and separatrix upstream. A peak power density of 1000 MW/cm^2 along the inclined magnetic field lines was assumed. Fig. 91 shows the time evolution of the different target heat fluxes. Radiation dominates after 3 μs and direct target heating by the impacting hot plasma electrons becomes negligible at later times. Fig. 92 shows lateral radiation fluxes to the upper side wall at different times.

Evaporation of the upper graphite side wall starts after 2.5 μs. The evolving plasma shield in front of both side walls drastically reduces the radiative heat load to the wall. The radiative heat load finally achieves values of typically 0.1 MW/cm^2 over the full length of the slot divertor. The increase towards the upper end reflects the fact that

the impacting hot plasma with increasing time is stopped at increasing distances from the target by the plasma shield in front of the lower side wall which after 120 μs has moved beyond the separatrix which was assumed to be at a distance of 11 cm from the lower side wall. Fig. 93 shows radiation fluxes to the lower side wall at different times. Despite the fact that the separatrix is closer to the lower side wall, the radiative heat loads at later times are comparable to those at the upper side wall what again reflects the quite good shielding properties of a plasma shield against incoming radiation.

Figs. 94 shows y dependent profiles of the y component of the radiation flux (for definition of S_y see eq. (34)) at different times. Positive S_y values mean that the radiation flux is directed towards the upper side wall. The asymmetry of the curves is due to the asymmetrical power density profile of the impacting hot plasma with the separatrix position at y = 11 cm. The radiation flux at the wall decreases with time from 0.25 MW/cm^2 at 34 μs to 0.06 MW/cm^2 at 277 μs due to the increasing plasma mass in the plasma shield close to the side wall.

Inspection of the S_y curves (Fig. 94) shows that there is an enhancement of radiation inside of the plasma shield close to the wall. This enhancement arises because of the inadequate frequency group structure of the 24 frequency groups for plasma temperatures of around 1 eV. At such low temperatures a 24 group calculation results in an overestimation of the radiation flux in the photon energy region up to 10 eV as can be seen from Figs. 95a and b, showing spectral radiation fluxes calculated with 24 Rosseland and 568 Planck frequency groups (Fig. 95a) and showing the frequency integrated total radiation flux (Fig. 95b). For the results with 568 Planck frequency groups 2 dim plasma temperature and density profiles as calculated with FOREV-2 for the case with 24 frequency opacities were used. Fig. 96 shows radiative fluxes S_y at the same distance from the target (x position) as those of Fig. 94 but now calculated with 69 frequency group Planck opacities. The radiation fluxes to the wall are up to a factor of two larger than those calculated with the 24 frequency group Rosseland opacities.

However such a comparison only shows the situation at a fixed time moment. In a self consistent calculation despite changes in radiation fluxes up to a factor of two

when using 24 or 69 frequency groups the results in terms of erosion remain quite small because the evaporation is a selfregulating process.

10. MHD motion of plasma shields and target erosion for ITER conditions

10.1 Horizontal targets

10.1.1 Gaußian power density profile

Fig. 97 shows a contour plots of plasma density and plasma flow $\Gamma = nv$ (arrows) in the carbon plasma shield 400 μs after start of the target heating. The power density profile of the incoming hot plasma is Gaußian in y direction with a peak power density of 100 MW/cm^2 at the separatrix and a half width of 5 cm. A plasma flow to the separatrix (inward flow) is clearly to be seen. The reason for this flow regime is depletion of B_x and built up of a B_y component as shown in Figs. 98 and 99. The inward plasma flow along the target surface towards the center (position of the SSP) improves the shielding in this region and erosion at the SSP becomes less than at the wings of the power density profile as is seen from Fig. 100 showing a comparison of erosion profiles for different peak power densities at 1 ms. The increase in erosion width with increasing power density is due to erosion by radiative energy transfer from the plasma shield to the target. Fig. 101 shows the time dependent erosion at two different target positions, at maximum and at the position of the separatrix.

10.1.2 Realistic power density profile

The realistic power density profile across the SOL has a steep gradient at one side and shows a less pronounced decrease at the other side (see Fig. 1b). In this case the plasma all the time flows along the target to the side of the gradual decrease. From Fig. 102 it is seen that the shielding layer at the position of the peak power density continuously is depleted by this plasma flow. Figs. 103a and b show carbon plasma density and plasma temperature profiles in the plasma shield along theseaparatrix (in x-direction) with peak power density of te impacting hot plasma of 100 MW/cm^2. Figs. 104a and b show the same quantities but at a distance of 20 cm

from the separatrix. At this position the density is lessand the expansion velocity of the plasma shield in x-direction is larger. The profiles principally are similar to thos at the separatrix position. Quite high plasma temperatures are achieved despite he fact that the power density of the impacting hot plasma at this distance from the separatrix has dropped by one order of magnitude.

Figs. 105a and b show carbon plasma densisty and plasma temperature profiles along the separatrix for a peak power density of 10 MW/cm^2. Comparing Figs. 104a and b with Figs. 105a and b it is seen that they arerather similar including the expansion velocity in x direction, thus demonstrating the influence of the momentum transfer of hot ions into the plasma shield. Fig. 106 shows target erosion profiles at 0.5 ms for different peak power densities. The depletion of the plasma shield at the location of the peak power density (separatrix strike point) results in rather strong erosion. As long as the peak power density is above 10 MW/cm^2 erosion outside of this peak mainly is caused by radiation resulting in the rather broad erosion profile shown in Fig. 106. For peak power densities below 10 MW/cm^2 erosion during at least 0.5 ms is occurring practically only in the region of the separatrix strike point. Radiation is insufficient for broadening of the erosion profile. Fig. 107 shows the time dependence of the target erosion at the separatrix strike point (SSP) for the two peak power densities 10 and 100 MW/cm^2.

Figs. 108a – c finally show the time evolution of the three magnetic field components B_x, B_y and B_z with B_0 = (0.5 T, 0, 5 T) the initial unperturbed magnetic field for the case with 10 MW/cm^2 along the separatrix. The position of the separatrix (y = 22 cm) is clearly to be seen because of the largest diamagnetic effect in B_x and B_z at this position. Due to the rather small dilution of B_x only a small B_y component is occurring which can't stop the plasma flow away from the separatrix.

10.2 Vertical target

FOREV-2 calculations were performed for realistic power density profiles across the SOL with peak power densities of 3, 10 and 100 MW/cm^2 and with separatrix upstream and downstream (see Fig. 1b). 2 dim plasma density profiles and the plasma flow pattern (arrows) in the plasma shield are shown in Fig. 109 for

downstream separatrix strike point at 740 μs for a peak power density of 10 MW/cm^2 along the separatrix. The density lines correspond to densities in the range of 7 x 10^{15} to 10^{17} cm^{-3}. Close to the target the plasma is flowing along the tilted target downwards then changes its flow direction, forms a plasma bubble and moves outside of the hot plasma impact region towards the upper side wall and upwards (in x direction). The upward velocity typically is 10^5 cm/s. The plasma bubble with central plasma density of $3 \cdot 10^{17}$ cm^{-3} has plasma temperatures below 2 eV and is weakly heated by lateral radiation fluxes of up to 5 kW/cm^2 from the target plasma shield. In case of upstream separatrix strike point, the downward flow results in a depletion of shielding at the position of the strike point, whereas in case of downstream separatrix strike point the downward flow results in an improved shielding at the strike point position and thus in a reduction of the target heat load by the hot SOL plasma. From Fig. 110 it is seen that the erosion profiles are markedly different for both cases and for the downstream separatrix strike point peak erosion is about a factor of 10 less than for the case with upstream strike point.

Calculated erosion profiles and corresponding power density profiles again for the cases strike point up- and downstream are shown in Fig. 111 for a peak power density of 100 MW/cm^2. Despite of the tenfold increase of the peak power density the peak erosion for the upward strike point is about a factor of 3 smaller than for 10 MW/cm^2. In case of downstream separatrix erosion at 1 ms just reaches 1 μm and thus remains quite small.The increased width of the erosion profile upstream of the strike point where heating by the hot plasma is negligible indicates erosion by radiation. This can be seen from Fig. 85 where the arrows indicate angular dependent radiation fluxes hitting the target upstream of the strike point. The vaporized material predominantly flows downward along the target surface as is seen from Fig. 112 and thus increases shielding at the separatrix strike point. This causes a drastic decrease of peak erosion. Vaporization at both side walls clearly is to be seen from Fig. 112. At 800 μs the plasma from the lower side wall has approached the separatrix position.

2 dim plasma density profiles and the plasma flow pattern (arrows) in the plasma shield are shown in Fig. 113 for a vertical target, and downstream separatrix strike point for 100 MW/cm^2. The density lines correspond to carbon densities in the range

of 7 x 10^{16} to 10^{18} cm^{-3}. Plasma density and plasma flow pattern in the plasma shield are rather similar for the cases separatrix up- and downstream. In case of downstream separatrix the plasma bubble outside of the region of the incoming hot plasma is more clearly to be seen. In Fig. 114 calculated peak target erosion values are shown for the horizontal and the vertical graphite target with separatrix upstream for peak power densities of 10 MW/cm^2 and 100 MW/cm^2. Erosion of the horizontal and vertical target at 10 MW/cm^2 are comparable despite a factor of 3 lower heat load of the impacting hot plasma at the vertical target. Erosion of vertical targets and upstream separatrix is smaller at 100 MW/cm^2 than at 10 MW/cm^2. The reason is upstream target erosion by radiation in the 100 MW/cm^2 case and subsequent downward movement of the plasma shield providing increased shielding at the strike point of the separatrix. In the 10 MW/cm^2 case the plasma shield at the separatrix strike point permanently is depleted by downwards flow of the target plasma.

10.3 Vertical target and low peak power density

A first calculation was performed for a vertical target and separatrix upstream assuming a realistic power density profile with peak power density along the separatrix of 3 MW/cm^2 what means that the initial target heat load by the impacting hot plasma is 0.1 MW/cm^2. The energy of the hot plasma was assumed to be 10 keV, monoenergetic for the plasma ions and Maxwellian distributed for the plasma electrons. A target heat load of 0.1 MW/cm^2 is the lowest value to be handled presently by FOREV-2. For lower values code modifications have to be done and especially temperature dependent thermophysical data of the target materials have to be used.

Results for calculations are shown in Figs. 115 – 118. Target heat fluxes at the separatrix strike point (SSP) are shown in Fig. 115. For times up to 10 ms energy deposition by the impacting hot plasma is the dominating target heat load. The radiative target heat load remains an order of magnitude lower. Figs. 116a and b show profiles of calculated plasma temperatures and carbon densities in the plasma shield along the separatrix. According to Figs. 116a and b a plasmashield is formed. The temperature and density profiles are rather typical. The only difference to the

cases with higher power densities ofthe impacting hot plasma (see Figs. 103 – 105) is the lower carbon density and the drastically reduced expansion velocity of the plasma shield. Fig. 116c shows radiation fluxes to the upper side wall. The maximum radiative heat load at the wall is 5 kW/cm^2. Wall erosion by vaporization is not occurring. Fig. 117 shows the time dependent target erosion at the SSP. At 10 ms the erosion is 3 μm. Finally Fig. 118 shows the density distribution and the plasma flow pattern of the plasma shield at 4 ms. A plasma flow along the tilted target downwards is not observed. Outside of the separatrix the plasma is flowing upstream. The situation would change if the impact energy of the hot plasma would be smaller because of improved stopping its energy depositon into the target would stop at earlier times.

11. Parameters important for plasma shield behaviour and erosion

There are several parameters which influence the plasma shield behaviour. Easily accessible to numerical evaluation are such parameters as impact energy of the hot plasma ions and opacity type and number of frequency groups used in the 2 dim radiation transport calculations. Hardly to be estimated presently is whether classical diffusion is appropriate for describing the diffusive part of the external magnetic field in the plasma shield (see eq. (5) of chapter 3) or whether Bohm diffusion or even turbulent motion with rather fast re-diffusion of the magnetic field into the plasma shield has to be assumed. Concerning quantification of this last point only experiments could help to decide. Such experiments presently are underway.

A first calculation on formation and MHD behaviour of a carbon plasma shield assuming Bohm diffusion was performed. A horizontal graphite target and a Gaußian power density profile of the impacting hot plasma with a peak power density of 100 MW/cm^2 along the magnetic field lines was used. Fig. 119 shows a comparison of plasma density and plasma flow pattern of 40 μs for a carbon plasma shield with classical and Bohm diffusion. Despite the rather short time a drastic different MHD behaviour is to be seen for both diffusion coefficients. In case of Bohm diffusion the

stability of the plasma shield is reduced, lateral plasma jets are formed and the plasma mass at the separtrix position seems to be reduced too. A more detailed analysis still has to be performed.

Concerning the type of opacity (Rosseland or Planck) and number of frequency groups, typical results were discussed in chapter 4.4 and 5. All the results discussed in the previous chapters 9 and 10 were obtained for an impact energy of the hot plasma of 10 keV and with momentum transfer from the hot plasma ions to the plasma shield.

11.1 Impact energy of the hot SOL plasma

To study the influence of the impact energy of the hot plasma calculations were performed for an impact energy of 1 keV. A horizontal target and a realistic power density profile with peak power density along the separatrix of 100 MW/cm^2 were used. The reduced impact energy of the hot plasma results in a reduced range of the plasma species in the plasma shield. Therefore the contribution of the impacting hot plasma to the target heat load decreases as is seen from Fig. 120, showing the time evolution of calculated target heat fluxes. Direct energy deposition to the target ends at 1 μs whereas for 10 keV impact energy it continues up to 700 μs (see Fig. 89 for comparison). The radiative target heat load achieves about 0,1 MW/cm^2 and after 300 μs becomes the dominating heat load. Up to 100 μs electron heat conduction is the dominating heat load. The time dependent erosion is shown in Fig. 121. After about 300 μs the erosion rate becomes negligibly small. Thus erosion (typical value at 350 μs is 1.2 μm) remains rather small in comparison with the erosion value for hot plasma with impact energy of 10 keV. There the erosion value is 20 μm after 350 μs (see Fig. 107). The drastic decrease of the erosion rate at 350 μs is due to a pronounced decrease of the electron heat conduction flux to the target. This quantity is sensitively dependent on mesh sizes, on plasma temperature gradients close to the target surface and on diamagnetic effects in the plasma shield close to the target. All these three parameters are not so simply to be met in a 2 dim calculation. Therefore the results on target heat fluxes for times larger than 350 μs are preliminary. 2 dim contour plots of carbon density and plasma flow (arrows) in the

carbon plasma shield are shown in Figs. 122, 123and 124 at 3 different times. The plasma flows along the target away from the separatrix (Fig. 122). Outside of the separatrix it changes its flow direction (Fig. 123) and moves as plasma bubble upwards. Fig. 124 shows this plasma bubble (the density range is from $7 \cdot 10^{14}$ to 10^{16} cm^{-3}) at 353 µs. The temperature of this bubble is about 2 eV and its upward velocity is about 10^5 cm/s.

Fig. 125 shows carbon density profiles along the separatrix at the three different time moments 20, 91 and 353 µs. At all these times the hot plasma deposits its energy only into the plasma shield. To stop the impacting plasma carbon densities of typically $6 \cdot 10^{14}$ cm^{-3} are sufficient as is also seen from Fig. 125 where additionally to the carbon densities the incoming heat flux is shown. Fig. 126 finally shows the radiation flux to the "upper" side wall. Maximum radiative heat load here is around 60 kW/cm^2. Evaporation of side walls does not occur.

The results obtained for 1 keV impact energy are quite similar to the situation at the simulation facilities. Electron heat conduction and radiation are the dominating target heat loads. Radiation remains essentially uninfluenced by the MHD behaviour of the plasma shield as can be seen by comparing Figs. 78, 81 and 84a. The radiative target heat load for 100 MW/cm^2 remains in all three cases around 0.1 MW/cm2 and for 10 MW/cm^2 around 20 kW/cm^2 despite the quite different MHD behaviour and the quite different erosion at the SSP for the three cases.

11.2 Momentum transfer

The two cases horizontal target with Gaußian and realistic power density profile of the impacting hot plasma were considered. Calculations were performed for a peak power density of 100 MW/cm^2, with and without momentum transfer. All other parameters of the impacting hot plasma were identical for both cases. Fig. 127 and 128 shows 2 dim carbon density contours and the plasma flow pattern at the two different times 100 and 300 µs for a Gaußian power density profile. The density range is the same for all 4 plots. The plasma in both cases (with and without momentum transfer) flows towards the separatrix caused by pushing out of B_x and production of a B_y component of the magnetic field. With momentum transfer there

are evolving lateral plasma jets and the upstream expansion of the plasma along the separatrix is less pronounced. This is becoming evident more strongly at later times (see Fig. 128).

Fig. 129 shows the same for a realistic power density profile at 715 µs. In both cases the plasma is flowing away from the separatrix. With momentum transfer this flow is slightly enhanced as can be seen from the more established plasma bubble moving upstream between separatrix and upper side wall.

In concluding: the dominating influence on the MHD movement of the plasma shield is coming from the topology of the magnetic field.

12. Relevance of disruption simulation experiments

From Table 4 it is seen that there is quite good agreement between measured and calculated erosion for all except one case which still needs more detailed investigations. Because of low impact energies direct energy deposition is negligible as target heat load source in the simulation experiments. Dominating in all the experiments with perpendicular graphite and quartz targets and for tilted graphite is the electron heat conduction flux. For tilted quartz targets because of the boundary condition that the x component B_x of the unperturbed magnetic field at the target is free, target inclination results in a decrease of the electron heat conduction flux to the target and the radiative target heat load dominates. Because of this the transparency of polished quartz becomes important. In a first approximation it was assumed that quartz is transparent only for visible radiation taken roughly into account by the reduction of the radiative target heat load by a factor of 2.5. The radiative target heat load practically is independent from the MHD behaviour of the plasma shield, whereas electron heat conduction sensitively depends on the diamagnetic effect of the plasma shield and direct energy deposition to the target sensitively depends on the MHD behaviour of the plasma shield. Concerning electron heat conduction this is verified by the difference of erosion for a perpendicular graphite and quartz target, as observed and verified at the CUSP

facility. Concerning direct energy deposition of hot electrons, this is evident from the formulas on energy deposition and their dependence on plasma mass.

The good agreement of calculated and measured erosion for graphite and quartz despite their different magnetic properties and the consequently different MHD behaviour of the plasma shields allow to conclude that the physical models and their numerical treatment related with radiation transport, magnetic field evolution, diamagnetic effect and MHD of plasma shields are adequate. Validation of FOREV-2 against simulation experiments allows to conclude that FOREV-2 correctly describes the initial phase of the hot plasma target interaction, the early MHD behaviour of the plasma shield and the radiative energy transport. The long term behaviour of plasma shields can't be validated in the simulation experiments at Troitsk but could be checked at the QSPA facility at Kharkov because of considerably longer duration of the pulsed hot plasma.

For ITER the time intervall of the pulsed heat load is up to one order of magnitude larger than at the QSPA facility. This not only poses hard requirements onto the hydrodynamic calculational scheme but additionally increass the importance of the long term MHD behaviour of the plasma shield and its influence on erosion. Table 5 summarizes what can be learned from simulation experiments and what are the differences between these experiments and the tokamak reality. The energy transfer from the hot plasma to the target in the simulation experiments is by electron heat conduction and radiation. The same is valid for ITER in case of impact energies of the hot plasma of 1 keV. For ITER and hot plasma electrons of 10 keV impact energy the dominating target heat load is direct energy deposition. The erosion in this case is larger by one order of magnitude. Electron heat conduction is negligible and radiation contributes only if the peak power density of the hot plasma is above 50 MW/cm^2. The MHD behaviour of the plasma shield is influenced by the diamagnetic effect which in turn is determined by the magnetic field behaviour in the plasma shield, by the boundary condition for the magnetic field at the bulk target and by the plasma temperature and density (pressur balance between magnetic field pressure and plasma pressure) in the plasma shield. The numerical studies were performed assuming classical diffusion. The influence of other diffusive regimes (Bohm diffusion) on the MHD behaviour still needs to be demonstrated.

What type of diffusion actually is dominating the MHD behaviour of the plasma shield in ITER presently is unknown. The diamagnetic effect of the plasma shield is also unknown for the simulation experiments. However it could be determined from magnetic probe measurements in plasma shields. A pure hot plasma has to be available for these experiments. Impurities in the hot plasma dissipate energy of the plasma shield by radiation and thus are influencing the plasma temperature distribution in the plasma shield, its diamagnetism and the electron heat conduction flux to the target.

13. Impurity transport in the slot divertor

The plasma shield ions are moving upward in the ITER slot divertor towards the x-point. The MHD motion of these impurities was studied with FOREV-2 for a horizontal graphite target. For the incoming hot plasma a Gaussian distributed power density profile with peak power density of 10 MW/cm^2 and a half width of 5 cm was assumed. The time duration of the heat load was 40 μs. These conditions simulate a powerful ELM. Interactions of the impurity ions with the neutrals from the gaseous divertor and with the stationary SOL plasma were not taken into account in these first calculations.

The movement of the plasma shield in the (x,y) plane along and across the magnetic field lines with B_x = 0.5 T and B_z = 5 T is shown in Fig. 130 for a perpendicular target at x = 0. Early in time there is an effective MHD motion of cold plasma close to the target across B_z which stops the impurity expansion. After about 400 μs formation of an impurity plasma bubble of temperature below 1 eV is completed. This bubble driven by pressure gradients moves upward in the slot at velocities of about 5 x 10^5 cm/s as is seen from Fig. 131. About 1.1 ms after switching off heating the density of the mainly singly ionized impurities reaches a value of 4 x 10^{15} cm^{-3} at a distance of 2 m from the target. During a time period of 0.5 ms the impurity flux at the x point remains at a level of 2 x 10^{21} ions/cm^{2}s. Such a high impurity flux could trigger a radiative collapse which ultimately could run into a current quench disruption.

14. Modulation of erosion at inclined targets

FOREV-2 was used to analyse the situation with vertical targets tilted by 20° in the poloidal plane. Calculated density and velocity evolutions in a carbon plasma shield are shown in Fig. 132 for a constant power density of the hot plasma of 5 MW/cm^2 impacting along B_x = 0.5 T, B_z = 5 T. Clearly to be seen is an evolving modulation of the plasma density in the shield which is triggered by an incidental density fluctuation and which shows a periodic structure along the target [14]. The periodicity is to be seen from the erosion profiles shown in Fig. 133. The erosion ratio maximum to minimum is linearly growing with time and after 25 μs reaches a value of 3.7. This instability and consequently modulation of erosion along the target surface also is occurring in the toroidal direction of tokamaks because of hot plasma impact along inclined magnetic field lines.

14.1 Analytical model of modulation of erosion

Target erosion at early times mainly is caused by direct energy deposition of the hot plasma onto the target. At a later stage after plasma shield formation and collisional and electric stopping of the hot plasma in this shield, erosion is determined by radiative energy transfer to the target.

To confirm the numerical results on modulation of erosion two simple analytical models were developed describing the two stages heating by direct plasma impact and heating by radiative energy transfer.

14.1.1 Erosion stage dominated by direct heating

It is assumed that a plasma shield with layer thickness H is existing. The plasma shield has constant density ρ and temperature T. The energy deposition rate (depletion rate) of the incoming hot plasma is assumed to be constant. The situation schematically is shown in Fig. 134. The heat flux S to the target by direct heating from the impacting hot plasma is given as

$$S = S_o\left(1-\frac{kH}{\sin\alpha}\right)\sin\alpha = S_o(\sin\alpha - kH) \tag{84}$$

with S_o the power density of the hot plasma along the field lines in vacuum and k the power density depletion in the plasma shield. The heat flux S causes target heating, melting and evaporation. Evaporation of wall material increases the thickness of the plasma shield according to

$$\dot{H} = \frac{S_o}{H_{vap}\rho}(\sin\alpha - kH) \tag{85}$$

with H_{vap} the specific heat of evaporation. Assuming that the thickness of the shielding layer depends only on time and not on the x coordinate the following solution of eq. (85) is obtained:

$$H_o = \frac{\sin\alpha}{k}\left(1-\exp\left[-\frac{S_o k\sin\alpha}{H_{vap}\rho}t\right]\right) \tag{86}$$

For a stability analysis of this solution it is used

$$H(x,t) = H_o(t) + h(t)\sin\left(\frac{2\pi x}{\lambda}\right) \tag{87}$$

with arbitrary λ. Substituting this expression into eq. (85) it is obtained

$$\dot{H}_o + \dot{h}\sin\left(\frac{2\pi x}{\lambda}\right) = \frac{S_o}{H_{vap}\rho}\left\{\sin\alpha - k\left[H_o + h\sin\frac{2\pi(x+H_o ctg\alpha)}{\lambda}\right]\right\} \tag{88}$$

and finally

$$\dot{h}\sin\frac{2\pi x}{\lambda} = -\frac{S_o}{H_{vap}\rho}\,kh\sin\frac{2\pi(x+H_o ctg\alpha)}{\lambda} \tag{89}$$

Analysis of this solution is rather complicated. But assuming that the growth rate of h is much faster than the characteristic growth rate $\frac{S_o\kappa\sin\alpha}{H_{vap}\rho}$ of h_o (see eq. (86)) and therefore H_o = const in eq.(89) then the analysis becomes linear. In this case the

most unstable mode should have the wavelength $\lambda = 2\ H_o\ ctg\alpha$ and from eq. (89) it is obtained for h

$$h = h_o \exp\left(-\frac{S_o k}{H_{vap}\rho}t\right) \tag{90}$$

with h_o = const. From this solution it is seen that the growth rate H_o/h is equal to $\sin\alpha$ « 1 for the assumed conditions.

The evolution of the thickness of the shield at nonlinear stages is more complicated. At different time moments modes with different wavelengths should be most unstable and the real modulation is not sinusoidal as it can be seen from Figs. 135a and b showing erosion modulation as obtained from numerical calculations at 1 μs and 100 μs with constant power density of 5 MW/cm^2.

14.1.2 Erosion stage dominated by radiation

To obtain the equation describing the evolution of the modulation of the shielding layer at the radiation dominated stage the same assumptions as for the first stage, that is constant plasma density and temperature in the plasma shield are used. Additionally constant opacity κ is used. The radiative flux of frequency ω coming to the target under the angle δ is given according to

$$I_\omega(v) = I_{\omega P}\int_0^H \exp\left(\frac{\kappa x}{\cos\delta}\right)\frac{\kappa dx}{\cos\delta} = I_{\omega P}\left[1-\exp\left(-\frac{\kappa H}{\cos\delta}\right)\right] \tag{91}$$

with $I_{\omega P}$ the Planck function. The radiative heat flux to the target S_ω is obtained according to

$$S_\omega = 2\pi I_{\omega P}\int_0^{\pi/2} \cos\delta\sin\delta d\delta\left[1-ex\left(\frac{\kappa H}{\cos\delta}\right)\right] = 2\pi I_{\omega P}\left[\frac{1}{2}-E_3(\kappa H)\right] \tag{92}$$

with $E_n(z) = \int_1^\infty \exp(-zw)\frac{d\omega}{\omega^n}$ the exponential integral.

Using eq. (92) the evolution of the thickness of the shielding layer is given as

$$\dot{H} = \frac{\pi I_{\omega P}}{H_{vap}\rho}\left[1 - 2E_3(\kappa H)\right] \tag{93}$$

As in the case of direct heating the uniform solution $H = H_o(t)$ is to be obtained. Assuming now optically thin shielding layers and using the expansion

$$E_3(z)_{z\Rightarrow 0} = E_3(0) + zE_3'(0) = \frac{1}{2} - z$$

it is obtained from eq. (93)

$$\dot{H}_0 = \frac{\pi I_{\omega P}\kappa}{H_{vap}\rho} H_0 \tag{94}$$

with the solution

$$H_0 = A \exp \frac{\pi I_{\omega P}\kappa}{H_{vap}\rho} t \tag{95}$$

Assuming now the same nonuniformity of the layer thickness (see eq. (87)) the radiation heat flux at the target position x_o can be expressed in the following form

$$S_\omega(x_o) = 2\pi I_{\omega P} \int_o^{\pi/2} \cos\delta \sin\delta d\delta \left[1 - \exp\left(-\frac{\kappa H(x')}{\cos\delta}\right)\right] \tag{96}$$

The shield thickness H has to be taken at the point $x' = x_o + H_o ctg\alpha$, where the radiation inclined at angle δ starts thus

$$H(x') = H_o + h \sin \frac{2\pi(x_o + H_o ctg\alpha)}{\lambda} \tag{97}$$

Substituting eq. (97) into eq. (96) and making the usual substitution of the integration variables the radiation flux can be expressed in the following form

$$S_\omega(x_o) = 2\pi I_{\omega P}\left[\frac{1}{2} - E(\kappa H_o, \kappa h)\right] = 2\pi I_{\omega P}\left\{\frac{1}{2} - E(\kappa H_o, 0 + \kappa h\, E^+(\kappa H_o, 0)\right\} \tag{98}$$

with the function $E(t,\varepsilon)$ given according to

$$E(t,\varepsilon) = \int \frac{dz}{z^3} \exp\left\{ -tz - \varepsilon z \sin \frac{2\pi(H_o / \sqrt{z^2 - 1} + x_o}{\lambda} \right\} \tag{99}$$

and using a Taylor series expansion with respect to the second argument. For obtaining the equation for the evolution of h the newly introduced function E(t,ε) has to be analysed. First of all it is evident that E(x,o) = E_3(x). E'(t,o) is given as

$$E'(t,o) \frac{dE(t,\varepsilon)}{d\varepsilon}\bigg|_{\varepsilon=0} = \int \frac{dz}{z^3} z \sin \frac{2\pi(H_o / \sqrt{z^2 - 1} + x_o}{\lambda} \exp(-tz) \tag{100}$$

With the substitution $1/(z^2-1)=y^2$ eq. (100) can be transformed into

$$E(t,o) = \int_0^\infty \frac{dy}{(y^2+1)^{3/2}} \exp(-t \frac{\sqrt{y^2+1}}{y}) \sin \frac{2\pi H_o y + x_o}{\lambda} \tag{101}$$

or

$$E'(t,o) = A \cos\left(\frac{2\pi x_o}{\lambda}\right) + B \sin\left(\frac{2\pi x_o}{\lambda}\right) \tag{102}$$

with

$$A = \int_0^\infty \frac{dy}{(y^2+1)^{3/2}} \exp\left(-t \frac{\sqrt{y^2+1}}{y}\right) \sin\left(\frac{2\pi H_o y}{\lambda}\right) \tag{103}$$

and

$$B = \int_0^\infty \frac{dy}{(y^2+1)^{3/2}} \exp\left(-t \frac{\sqrt{y^2+1}}{y}\right) \sin\left(\frac{2\pi H_o y}{\lambda}\right) \tag{104}$$

The kernel of convolutions (101, 103 and 104) with R(y) given according to

$$R(y) = \frac{dy}{(y^2+1)^{3/2}} \exp\left(-t \frac{\sqrt{y^2+1}}{y}\right) \tag{105}$$

is plotted in Fig. 132 with $0<y_{max}<1$, and $R(y)\big|_{y\to\infty} \sim \frac{1}{y^3}$.

It is evident that for $H_o/\lambda \leq 1$ the integrals A and B are positive and $A \approx \frac{H_o}{\lambda} B$.

$$\dot{H} = \frac{\pi I_{\omega P}}{H_{vap}\rho}\left(1 - 2E_3(\kappa H_o) + 2E'(\kappa H_o)\kappa h\right) \tag{106}$$

substituting eqs. (87), (102) and (103) into eq. (106) and neglecting A in comparison with B at $H_o/\lambda \ll 1$ the following equation is obtained

$$\dot{h} = \frac{2\pi I_{\omega P}}{H_{vap}\rho} B\kappa t \tag{107}$$

This equation has the exponentially growing solution

$$h = h_o \exp\left(\frac{2\pi I_{\omega P}}{H_{vap}\rho} B\kappa t\right) \tag{108}$$

Taking into account the small coefficient A eq. (86) will lead to a time dependent shift of the modulation

$$H(x,t) = H_o(t) + h(t)\sin\left(\frac{2\pi(x - \delta(t))}{\lambda}\right), \tag{109}$$

but its amplitude h in this case will grow with the same rate as in eq. (87).

The analytical consideration thus confirms that modulation of the shielding layer exists at both stages direct heating and heating by radiation at least in the linear approximation. The calculated modulation of erosion shows time dependent modulation wavelengths, because these modulations take place at different shielding layer thicknesses H_o. At early times with small H_o and consequently also small λ there are about 20 periods of modulation with λ = 5 cm. At later times the modulation wavelength has increased two times to $\lambda \approx 10$ cm and the radiation has even a larger wavelength ($\lambda \approx 20$ cm). From this it is concluded that after 100 μs the most unstable mode should have $\lambda \approx 20$ cm.

14.2 Experimental results on modulated erosion and comparison with numerical results

At the plasma gun facility MK-200 UG hot plasma target experiments were performed at tilted targets to verify the theoretically predicted modulation of erosion [48]. The MK-200 UG was operated under standard conditions [44]. The hot plasma consists of Maxwellian electrons of temperature of 200 eV and of monoenergetic hydrogen ions of ions of impact energy of 1.5 keV. As target material quartz was used. Because of the rather low heat conductivity of quartz erosion in one single shot is sufficiently large to be detected. The target inclination angle against the guiding magnetic field lines and thus against the impacting hot plasma was 20°.

A typical 3 dim erosion pattern obtained after one single plasma exposure is shown in Fig. 67a. The direction of the impacting hot plasma stream is also indicated. As predicted by theory a modulation is to be seen. The inclination of 20° resulted in an exposure length of about 14 cm. Fig. 67b shows the erosion depth profile along the y direction at the position of the peak power density of the hot plasma. From the experimental results a modulation wavelength of about 7 cm was determined. It has to be stressed that the quartz plate before exposure to the hot plasma was carefully polished. The maximum local deviation from plate flatness was well below 0.1 μm. Thus the experimentally determined modulation of erosion is at least a factor 2 above the maximum deviation from flatness.

The MK-200 UG conditions were modeled with FOREV-2. Numerical results of the calculated erosion profile in y direction are shown in Figs. 67c and 68 for quartz and graphite. Modulation of erosion is obtained. The modulation wavelength is 7 cm and thus is in agreement with the experimental value. Thus it is concluded that the numerically and analytically predicted modulation of erosion is a real effect and it is verified by experiment.

14.3 Modulation of erosion in toroidal direction

The consequences of modulation of erosion in toroidal direction were analysed. The hot plasma hits the divertor plates at an inclination angle of about 5°. Therefore

despite the assumed homogeneity of deposited energy in toroidal direction there should occur a modulation of erosion.

In 1dim calculations such effects can't be analysed. There the inclination is taken into account by a 1½D MHD model and by appropriate coordinate transformation with $\hat{x} = x/\sin\alpha$ and $Q_o = Q_{||} \sin\alpha$ with α the angle of inclination in toroidal direction and $Q_{||}$ the power density along the field lines. Thus inclination in 1dim means changes in the energy deposition and in the MHD expansion.

First 2 dim calculations were performed to determine whether modulation of erosion in toroidal direction results in higher peak erosion and if yes in determination of the ratio of peak erosion with modulation to erosion without modulation. Two calculations where performed up to now. The geometry together with the results are shown in Figs. 137a and b at 260 μs. For both cases the target heat load is 1 MW/cm^2. There was used a constant power density along y. For the inclined case the computational area was 450 x 30 cm^2. This region was covered by 270 x 30 meshes. The width of the incoming hot plasma was 20 cm. This means for an inclination angle of 5° a distance of 2 m along the target. The modulation wavelength λ is 10 cm. Thus one modulation length is covered by 8 meshes. For the case of perpendicular target the computational area was 250 x 20 cm^2 covered by 50 x 40 meshes. The calculations were performed with 24 Rosseland group opacities.

Erosion results are compared in Fig 138. At 260 μs, peak erosion for the inclined target is 3 μm average erosion for the perpendicular target (standard 1dim calculations) is 1,5 μm. Thus modulation of erosion if properly taken into account increases the erosion. The time evolution of the ratio peak to average still has to be determined.

15. Enhanced erosion

The contributions of hot plasma electrons to erosion needs to be quantified. Therefore experiments were performed at the GOL-3 facility [16]. Results for graphite and tungsten are shown in Figs. 135a and b. For graphite and for energy densities of the impacting hot electrons above 10 MJ/m^2, there was observed rather large erosion

which at energy densities of 30 MJ/m^2 reached 500 microns. For tungsten and an energy density of the hot electrons of 13 MJ/m^2 erosion reached values around 150 μm.

15.1 Energy deposition of hot electrons

In order to understand the mechanism of large erosion a more detailed analysis of the interaction of hot electrons with graphite was performed. Their energy deposition in graphite was measured with a special multiplate calorimeter consisting of 9 graphite plates. The temperature of each layer was measured during the experiment, thus enabling a determination of the distribution of the energy deposition. Results are shown in Fig. 140 for two different energy densities of the hot electrons. A graphite screen was used in front of the multiplate calorimeter which absorbs electrons of energies below 36 keV.

The energy spectrum dN_e/dE of the hot electrons of GOL-3 was measured by a multifoil analyzer and a magnetic analyser. Results are shown in Fig. 141 for an energy density of the hot electrons of 22 MJ/m^2. The energy density in the energy range 50 - 200 keV amounts up to 1 MJ/m^2, whereas in the energy range 0.5 - 0.7 MeV it amounts up to 7.5 MJ/m^2.

The specific energy deposition of electrons of energy E is calculated according to

$$\frac{1}{\rho A}\frac{\Delta Q(x)}{\Delta x}=\int_{E_0}^{E_{max}}\frac{\Delta\phi(E)}{\Delta E}K(x,E)dE \qquad (110)$$

$$with\ \frac{\Delta\phi(E)}{\Delta E}=\int_0^{t_{irrad.}} v(E)\frac{dN_e}{dE}dt, \qquad (111)$$

the time integrated flux of the incident electrons, dN_e/dE the energy spectrum of the hot electrons, ρ the density of the bulk material, A the impact area and K(x,E) the distribution of the energy deposition into the depth of the target. It is assumed that dN_e/dE does not depend on the energy density of the hot electrons. K(x,E) is the approximation formula for calculatin of energy deposition for perpendicular impact of monoenergetic electrons of energy E. The energy deposition of the hot electrons was

calculated according to eq. (110) with E_0 = 36 keV and E_{max} = 1 MeV. As seen from Fig. 140 there is rather good agreement between the calculated and the measured distribution of the deposited specific energy. Taking into account the plasma electrons and the suprathermal electrons up to energies E_0 = 36 keV increases the energy deposition at shallow depth because of the smaller range of these electrons as indicated in Fig. 140 at curve 2. The energy deposition in this case exceeds the threshold for three atomic vaporization of graphite (20.5 kJ/g). Therefore surface evaporation takes place in all discussed cases, but the evaporation depth remains below 10 μm for graphite.

Calculated specific energy depositions are shown in Fig. 142 for different energy densities of the hot electrons. Again it was assumed that the energy spectrum of the hot electrons is independent from the energy density of the hot electrons. For calculation of the specific energy deposition a measured energy spectrum of the hot electrons is used. However in comparison with Fig. 140 the voltage in the quasiplanar diode was reduced by about 10 % resulting in a lower energy of the hot electrons and thus in a reduction of the energy deposition into the depth of the target. Combining the calculated specific energy deposition with the experimentally determined erosion values (see Fig. 139a) allows to determine the destruction threshold for graphite. According to Fig. 142a threshold value of 9 - 10 kJ/g is obtained. This value is considerably less than the vaporisation enthalpy. For tungsten similar calculations were performed. For fitting the calculated erosion values to the measured ones a destruction threshold value of 0.3 - 0.8 kJ/g was obtained thus demonstrating that the heat for melting is sufficient for initiating enhanced erosion.

15.2 Physical base of enhanced erosion

If bulk material is heated volumetrically the temperature inside the material is determined by the energy deposition, the heat capacity and the heat conductivity of the target and the heat loss from the surface. Due to volumetric heating the inside temperature may reach the critical phase transition temperature which for graphite as seen from Fig. 143 is at about ~ 4100 K [52, 53]. The specific energy (enthalpy)

needed for heating of graphite up to this phase transition is about 10 kJ/g. Upon reaching the phase transition, some bonds inside the lattice or between grains are broken. For destruction then it is sufficient to apply week external forces such as thermal tension, vapor pressure inside the material and forces created under the action of electric currents occurring in the target when the plasma stream reaches the target.

For understanding the character of enhanced target erosion and for quantification of its consequences for ITER disruptions a one-dimensional code was developed. Heating, evaporation and damage (melting) of graphite was calculated taking into account volumetric heating of the substance by the hot electrons. In this case phase transitions inside the solid target may occur at moving boundaries. This problem is known as the Stefan problem [54]. The temperature distribution in each phase is determined by the heat conductivity equation:

$$c_{pi}(T)\,\rho_i(T)\,\frac{\partial T}{\partial t}=\frac{\partial}{\partial x}\left(\kappa_i(T)\frac{\partial T}{\partial x}\right)+S(x) \tag{112}$$

with specific heat $c_{pi}(T)$, density $\rho_i(T)$, and $\kappa_i(T)$ thermal conductivity depending on temperature and state of the substance i = 1 for solid, i = 2 for melted material, S(x) is the external heat source given by the volumetric energy deposition of the hot electrons. S(x) is given as

$$S(x)=\frac{1}{\rho A\Delta t}\frac{\Delta Q(x)}{\Delta x} \tag{113}$$

and thus is calculated according to eqs. (110). The condition at the moving melt-solid phase boundary is given as

$$\kappa_1\frac{\partial T}{\partial x}_{x=\varsigma+0}-\kappa_2\frac{\partial T}{\partial x}_{x=\varsigma-0}=-\rho H_m v_m \tag{114}$$

with H_m the enthalpy for melting (7.9 kJ/g)for graphite and 53 kJ/gmol for tungsten, ζ the melt front position and v_m the velocity of movement of the phase transition boundary. In accordance with [54] the Stefan problem is solved by the following way: eq. (112) with the condition at the phase transition boundary can be rewritten according to

$$(c_p(T)\rho+H_m\delta(T-T_m))\frac{\partial T}{\partial t}=\frac{\partial}{\partial x}(\kappa(T)\frac{\partial T}{\partial x})+S(x) \tag{115}$$

With
$$c_p(T)=\begin{cases}c_{p1}(T) & T<T_m\\ c_{p2}(T) & T\geq T_m\end{cases}$$
$$\kappa(T)=\begin{cases}\kappa_1(T) & T<T_m\\ \kappa_2(T) & T\geq T_m\end{cases} \tag{116}$$

with T_m the temperature of melting, δ $(T-T_m)$ the Dirac function.

For the numerical calculation the δ function is changed to the numerical function δ $(T-T_m,\Delta)$ defined within the intervall $(T_m-\Delta, T_m+\Delta)$ with the normalization condition

$$\int_{T_m-\Delta}^{T_m+\Delta}\delta(T-T_m,\Delta)dT=1 \tag{117}$$

The problem with smoothed coefficients reduces to an initial problem for $\Delta \rightarrow 0$. The numerical δ function can be represented by the following step function

$$\delta(T-T_m,\Delta)=\frac{1}{2\Delta} \tag{118}$$

Numerical calculations have shown that the smoothed region should cover 2 - 3 points and the δ-function can be replaced by a step function. The coefficients of heat conductivity $\kappa(T)$ are also smoothed on the same section coinciding with $\kappa_1(T)$ in the region $T < T_m - \Delta$, and with $\kappa_2(T)$ in the region $T > T_m + \Delta$.

15.3 Boundary conditions and thermophysical data

The heat load to the surface is going into vaporization and via heat conduction is transported into the solid target. This is described by

$$\kappa(T)\frac{\partial T}{\partial x}=-\rho v_s H_{vap}+S_w \tag{119}$$

with S_w surface energy deposition of the disruptive plasma stream, H_{vap} the vaporisation enthalpy and v_s the velocity of the evaporating surface. According to [54, 55] v_s equals 2.6 cm/s at T_s = 4000 K. For solution of eq. (112) under the condition (114) a coordinate system moving with the velocity v_s was used.

The thermophysical properties of graphite were taken from [52,55,56]. For 4000 K c_p = 2.1 J/gK and κ = 0.2 W/cmk. The enthalpy values used in the calculations are shown in Fig. 143.

16. Enhanced erosion for runaway electrons

Analysis of occurrence of enhanced erosion under ITER disruption conditions was done for runaway electrons. Runaway electrons heat the target volumetrically. Because of the rather low threshold for target damage in case of volumetric heating it has to be checked whether hot electrons can cause explosive like erosion under ITER disruption conditions. The energy density of the hot electrons at GOL-3 with 30 MJ/m^2 is close to the value expected for runaway electrons. However the maximum electron energy at GOL-3 is only 1 MeV. Therefore extrapolation of the GOL-3 conditions to the conditions for runaway electrons has to be done.

The energy deposition of runaway electrons in graphite was calculated with the Monte Carlo code EMSH [39] for an inclination angle of 5°. The energy density of the impacting beam was assumed to be 30 MJ/m^2. Results for graphite are presented in Fig. 144. For electron energies in the range 20 - 100 MeV they are in agreement with those from reference [57]. The destruction threshold of 10 kJ/g for explosive erosion is not reached in this case. If the energy of the electrons decreases the specific energy deposition increases in the near surface region. For energies below 20 MeV the damage threshold of 10 kJ/g can be reached and enhanced erosion could occur.

For a realistic estimation of enhanced erosion heat conduction into the bulk target has to be taken into account during the runaway impact time. Calculated temperature profiles are shown in Fig. 145. From these profiles it is seen that enhanced erosion occurs. The erosion depth as function of impact time is shown in Fig. 146 for 2 MeV and 10 MeV runaway electrons. After 1 ms erosion for graphite can reach up to 650 μm.

17. First analysis of erosion experiments at metallic targets

17.1 Electron beam facilities

Additionally to the results of erosion experiments at the GOL-3 facility there are available experimental results on erosion of metallic targets from the facility JUDITH [17, 18]. In GOL-3 due to the high power density, the short time duration of the pulse and the rather deep penetration of the incoming hot electrons phase transitions inside the material occur. The damage depth is the distance between the moving boundary of vaporization and the coordinate where the phase transition ends. All material above the position of the phase transition is removed instantaneously as a mixture of droplets, fragments and vapor. From the experiments performed at GOL-3 a threshold energy for damage of 53 kJ/gmol was obtained for tungsten. This value indicates that a phase transition from solid to liquid is sufficient for initiating enhanced erosion.

In the facility JUDITH a 120 keV monoenergetic electron beam of time duration up to 5 ms and energy density up to 7 MJ/cm^2 impacting perpendicularly onto the target is used. Despite completely different time scales and power densities of the heat loads of GOL-3 and JUDITH it was assumed that the damage mechanism is enhanced erosion and is the same in both facilities. The time for subsequent removal of the different damaged layers (instantaneous splashing or delayed splashing) in case of JUDITH conditions is rather unimportant because this time in any case remains considerably below the overall duration of the heat load. Therefore instantaneous splashing is assumed as soon as melt temperature is achieved and as soon as a certain damage energy threshold is overcome.

Erosion results for Be as obtained at the JUDITH facility are shown in Fig. 147. The experimental values were obtained by profilometry and thus are describing the maximum erosion per pulse. Results of calculation of melt layer erosion are shown in Fig. 147 for comparison. The calculated thickness of the melt layer is shown together with the calculated results for enhanced erosion for different values of the damage threshold. The curves 1 to 3 are valid for a solid-melt phase transition. For a solid vapor phase transition with zero enthalpy for boiling, the damage threshold is 50 kJ/gmol (melt enthalpy and heat capacity from melting up to boiling). For this condition the calculated erosion is identical to curve 3. Assuming a solid melt phase

transition with a damage threshold of 55 kJ/gmol the agreement between measurement and calculation is quite satisfactory. This indicates that enhanced erosion is the dominating mechanism for erosion of Be in case of volumetric energy deposition. At energy densities of the e^--beam above 8 MJ/m^2 erosion becomes larger than the melt layer thickness.

In Fig. 148 are shown calculated results for aluminum and copper for JUDITH conditions with duration of the e^--beam of 5 ms. For both materials is shown the enhanced erosion with different damage threshold energies of the phase transition solid $\rightarrow$ melt. Interesting is that for aluminum up to energy density values of the impacting hot electrons of 6 MJ/m^2 and for copper up to 7 MJ/m^2 there is only a weak dependence of erosion on the damage threshold. The thickness of the melt layer is also given in Fig. 148. Performance of further experiments at JUDITH with aluminum and copper targets would allow to decide definitely whether enhanced erosion is the dominating damage mechanism in case of volumetric energy deposition or whether other damage mechanisms contribute to the erosion process.

17.2 Plasma gun facilities

The plasma gun facilities VIKA [18], QSPA [19] and PLADIS [58] use a hydrogen plasma stream of rather low impact energy and high density for performance of experiments on melt layer erosion. The target always has been perpendicular to the impacting plasma. The energy deposition in such facilities is onto the surface. Therefore in this case the maximum temperature always will be achieved at the target surface. If the incident energy flux is not compensated by the sum of the heat conductivity flux into the target and the heat flux for surface evaporation then the surface temperature can exceed boiling temperature. In this case overheating of the near surface material can occur. If the energy absorbed in the overheated region is sufficient for converting the material into vapor ($E_{abs} > m(cT + H_B)$ with H_B the specific heat for boiling, volumetric boiling with bubble formation, bubble collapse and splashing of melted material occurs. Because of surface energy deposition, the phase transition first is occurring at the surface. Therefore enhanced erosion is not occurring.

VIKA and QSPA results on melt layer erosion of aluminum are shown in Fig. 149 for a pulse duration of 200 μs. Additionally shown are results of calculations of melt layer erosion by volumetric boiling for aluminum and beryllium. For energy densities of the incoming plasma up to 20 MJ/m^2 calculated and measured results for aluminum are in satisfactory agreement. At higher energy densities the calculation yields smaller erosion values. Fig. 149 shows also a comparison of calculated and measured erosion values for beryllium. The experimental results were obtained at the PLADIS facility. Pulse duration in this case was 100 μs. The agreement again is quite good demonstrating that in the heat load range above 5 MW/cm^2 volumetric boiling is indeed the dominating mechanism for melt layer erosion. Fig. 150 shows a comparison of calculated and measured results for aluminum for a pulse duration of 360 μs. Measurement and calculation show opposite trends. The measured erosion depth for the 360 μs case is considerably larger than for the 200 μs case whereas the calculation yields only slightly increased erosion values for the 360 μs case consistent with the fact that the reduced power density of the incoming plasma means a lower beam pressure thus lower overheating and thus a reduced splashing velocity. The considerably higher experimental values for the 360 μs indicate that there could be active another effect for melt layer erosion.

Recently fluiddynamic instabilities were discussed as a possible mechanism for melt layer erosion [59]. An experimental proof of these models is still lacking. The only presented comparison of experimental results with calculations for aluminum and pulse duration of 200 μs shown in Fig. 151 [59] repeat what is shown in Fig. 149 and for energy densities only up to 20 MJ/m^2. The results fully are explained by volumetric boiling, bubble collapse and subsequent splashing. Therefore existence of fluiddynamic instabilities and adequacy of theoretical modelling up to now are not demonstrated. A more detailed numerical analysis has to be performed and more systematic experiments are needed and especially inclined targets have to be investigated [60]. For these experiments a magnetized hot plasma stream is mandatory.

18. Conclusions

In this report development, validation and application of the two-dimensional R-MHD code FOREV-2 to the analysis of erosion and two-dimensional MHD motion in a simplified ITER slot divertor model are described. For the first time consistent two-dimensional results based on a 2½ dim MHD model combined with two-dimensional radiation transport are presented. Several quite interesting features have been detected. First the importance of the MHD movement of the target plasma on erosion was clearly demonstrated and the nature of the MHD flow across the vacuum magnetic field lines was clarified. Second modulation of erosion theoretically predicted firstly in 1996 meanwhile was confirmed experimentally and thus supports the quality of the two-dimensional modelling results. Third the magnitude of the radiation fluxes to side walls first predicted in 1995 was further specified and it was shown that side wall erosion is of concern for metallic targets. Use of Beryllium at the slot divertor side walls must be excluded because of rather large damages if melt layer splashing can't be excluded.

The 2 dim code FOREV-2 was applied for power densities of the hot plasma above 1 MW/cm^2. Application for lower heat loads has still to be done. This application because of the rather important question of existence and efficiency of a plasma shield for those long lasting not normal events needs to be addressed as next.

In concluding, 2 dim modelling of hot plasma target interaction with consistent angular dependent, multigroup 2 dim radiation transport and 2½ dim MHD is quite well advanced. The code FOREV-2 due to the introduction of an artificial background mass and the consequently achieved 10 fold increase of the time step size allows to handle quite large numbers of spatial meshes with at least 24 frequency groups. Calculations routinely were performed for deposition times up to 1 ms, in a few cases up to 10 ms.

The hydrodynamics part of FOREV-2 was tested against results from the 1 dim Lagrangian code FOREV-1. The MHD part of FOREV-2 was and still is to be tested against experimental results obtained and to be performed at the plasma gun disruption simulation facilities MK-200 CUSP, MK-200 UG and QSPA-Kh50. Flow of target plasma along the inclined target surface was observed in interferometry measurements in agreement with the prediction from the 2 dim numerical modelling.

Agreement also exists between measured and calculated dependence of erosion from the inclination angle.

Interferometry measurements at the MK-200 CUSP facility performed with perpendicular graphite targets at peak power densities of 42 MW/cm^2 showed the existence of plasma jets displaced laterally to a position outside of the impact point of the peak heat load. At power densities of around 20 MW/cm^2 these plasma jets disappeared. Results of FOREV-2 calculations confirmed these findings.

The simulation experiments are of big importance for code validation and for confirmation of unexpected but theoretically predicted results. The relevance of disruption simulation experiments for code validation and quantification of damage of the ITER divertor was clarified. A summary of these points is given in Table 4. From there it is seen that the simulation experiments can't cover all aspects important for the damage evaluation. Especially for the rather important question of plasma shield stability and long term MHD behaviour of the plasma shield no experimental answers can be obtained from the simulation experiments. However the detailed validation of FOREV-2 against results from 3 different simulation facilities demonstrates that FOREV-2 correctly describes the initial phase of the hot plasma target interaction, the early MHD behaviour of the plasma shield and the radiative energy transport.

Besides modulation of erosion and influence of 2 dim MHD motion on erosion, impurity transport in the slot divertor was studied. According to the 2 dim results obtained a giant ELM ultimately will trigger a current quench disruption because the target material evaporated during such an event about 1.5 ms later will appear at the x point. The mainly singly ionized impurities will have densities of several 10^{15} cm^{-3}. During a time period of 0.5 ms the impurity flux at this position remains at a level of 2 $\cdot$ 10^{21} ions/cm^{2}s, being much too high to be handled in a normal discharge.

The 2 dim results obtained demonstrate that a realistic analysis of disruptive erosion of the divertor target and the ITER slot divertor has to be performed with a 2 dim code. Vertical targets in comparison with horizontal ones favourably reduce the upward directed movement of the plasma shield in the slot and the target erosion for downstream separatrix, but result in comparable erosion in case of upstream separatrix and penalize with drastically increased radiation fluxes to the side walls

resulting in larger damage by melt layer erosion. The reduced upward directed movement means improved retention of impurities in the divertor slot. Now for the first time the tools for a consistent damage analysis of the rather complicated ITER slot divertor are available.

Concerning melt splashing the analysis performed has demonstrated that up to now no adequate validation of models is available. The experiments performed up to now at the plasma gun facilities VIKA, PLADIS and QSPA are not at all tokamak typical and because of power densities above 2 MW/cm^2 mainly result in volumetric boiling but not in triggering of fluiddynamic instabilities. Therefore models claimed to exist for describing those instabilities can't be verified and conclusions for the tokamak situation can't be drawn up to now.

Enhanced erosion as observed in e-beam experiments with several 10 keV electron energies at the facilities GOL-3 and JUDITH is quite well understood. The numerical results based on volumetric heating and phase transition inside the material are in remarkably good agreement with the experimental results.

19. Acknowledgement

The authors thank Valeri Safronov and his team at TRINITI Troitsk for the results from simulation experiments performed in the frame of the russian german WTZ cooperation agreement under RUS 524-96. The authors also thank Vladimir Tereshin and his team at IPP Kharkov for the experimental results at the QSPA facility performed in the frame of the WTZ agreement under UKR 276.1. Thanks are also due to Vasili Koidan and his team at INP Novosibirsk for the experimental results obtained at the GOL-3 facility on enhanced erosion. This work was supported by the WTZ cooperation agreement under RUS-525-96. Thanks are due to Boris Bazylev and Vladimir Tolkach from Lykov Institute of Heat and Mass Transfer, Minsk, for providing the 2 dim S_N code for calculation of radiation transport and for support in calculation of optical properties for carbon, quartz and tungsten. This work was performed in the frame of the WTZ project WEI 022.2. The authors also thank Jörg Vetter, FZK-PKF, for his continuous support during all stages of this work. The

authors would also like to thank Jörn Sonnenburg and Tilo Gutewort from IB-DLR for their continuous support in handling visits of Russian scientists to FZK in the frame of the different WTZ projects. Finally we thank Heide Hofmann from FZK-INR for typewriting this report as usual skillfully and with great patience.

20. References

[1] Parker, R.R., et al., J. Nucl. Mater, 241 - 243 (1997) 1.

[2] Sestero, A., Nucl. Fusion 35 (1995).

[3] Sestero, A., Nucl. Fusion 17 (1997) 115.

[4] Hassanein, A., Konkashbaev, I., J. Nucl. Mater. 220 - 222, 244 (1995)

[5] Lalousis, P., et al., Proc. 22nd European Conf. Controlled Fusion and Plasma Physics, Bournemouth, England, 3. - 7. July, 1997, Vol. 19C, Part II, p. 285.

[6] Würz, H., et al., J. Nucl. Mater. 212 - 215, 1349, (1994).

[7] Würz, H., et al., J. Nucl. Mater. 220 - 222 (1995) 1065.

[8] Würz, H., et al., Fusion Technology 32 (1997) 45.

[9] Piazza, G., et al., FZKA 5983, April 1998

[10] Bazylev, B., et al., Proc. 22nd European Conf. Controlled Fusion and Plasma Physics, Bournemouth England July 3 - 7 (1995), Vol. 19C, Part II, 277.

[11] Würz, H., et al., J. Nucl. Mater. 233 - 237 (1996) 798.

[12] Piazza, G., et al., in Fusion Technology (Proc. 19th Symp. , Karlsruhe, 1994), Vol. 1, Elsevier Amsterdam and New York (1995), 319.

[13] Landman, I., Würz, H., Report FZKA 6192, 1998, Electric fields and ExB drifts in hot plasma cold plasma interactions.

[14] Würz, H., et al., in Fusion Technology (Proc. 19th Symp., Lisboa, 1996), Vol. 1, Elsevier, Amsterdam and New York (1997) 191.

[15] Würz, H., et al., Fusion Technology 30 (1996), 739.

[16] Astrelin, V.T., et al., Nucl. Fusion, Vol. 37, No. 11, 1997.

[17] Linke, J., et al., Fusion Technology 1996, Vol. 1, p. 271, 1997.

[18] Linke, J., et al., J. Nucl. Mater. 212 - 215, 1994, p. 1195.

[19] Belan, V.G., et al., J. Nucl. Mater. 233 - 237, 1996, p. 763.

[20] Lingertat, J., et al., J. Nucl. Mater. 241 - 243, 1997, 402.

[21] Belozerkovsky, O.M., Davidov. Yu.M., The method of large particles in gas dynamics, M. Nauka (1982) (in Russian).

[22] S.I. Braginskij, Transport phenomena in plasmas. In: "The problems of plasma theory" edited by M.A. Leontovitch, 'Atomizdat', Vol. 1 (1963), p. 183. (in Russian).

[23] Nemchinov, I.V., Appl. Math. And Mech 34, 4, p. 706, 1970.

[24] Bazylev B., The 2 dim S_N radiation transport code TWORAD, to be published as FZKA report.

[25] V.I. Derziev, A.G. Zidkov, S.I. Jakovlenko, Radiation in nonequilibrium dense plasma. Moscow Energoizdat 1986 (in russian).

[26] L.A. Vainstein, I.I. Sobelman, E.A. Jukov, The excitation of atoms and the spectral line broadening. M. Nauka 1979 (in russian).

[27] L.D. Landau, E.M. Lifshitz, Statische Physik, Akademie Verlag, Berlin, 1966.

[28] H.R. Griem, Astrophys. Journal Vol. 132, p. 883, 1960.

[29] Bazylev, B., et al., Phys. Eng. J. 58, 6, 1012 (1990) (in russian).

[30] I.I. Sobelman, Introduction to the Theory of Atomic Spectra, Moscow Nauka 1963, p. 640 (in russian).

[31] V. Tolkach, G. Miloshevky, H. Würz, FZKA-report , Optical properties of plasmas of high Z elements, to be published.

[32] B.A. Kamenshikov, Yu. A. Plastinin et al., Radiation properties of high temperature gases, Moscow Mashinostoenie 1979 (in russian).

[33] K.P. Huber, L. Herzberg, Molecular spectra and molecular structure, Vol. 4 Constants of diatomic molecules, New York 1979.

[34] J.F. Ziegler, Handbook of Stopping Cross-Sections for Energetic Ions in Elements, Vol. 5 Pergamon Press New York 1980.

[35] Th.A. Mehlhorn, J. Appl Phys. 52 (12) 1981, p. 6522.

[36] A.G. El Cushian et al. Charge state equilibrium and nonequilibrium modelling of the carbon pellet plasma interaction, Phys. Fluids B Vol. 4 No. 12, 1992, p. 4166.

[37] J. Linhard, M. Schroff, B. Schiott, Königl. Danske Videnskab. Selkab. Mat. Phys. Medd. 33 (1963).

[38] A.V. Arzhannikov, Report BINP 91-115 (in russian).

[39] V.A. Tayursky, The Monte-Carlo Programm EMSH, Rep. INP 89-16, Budker Inst. of Nucl. Phys. Novosibirsk (1989).

[40] B. Bazylev et al., Energy losses by energetic electrons in magnetized plasma, Internal report of the Academy of Science of Belarus, Minsk 1994.

[41] Sedov, L.I., Similarity and Dimensional Methods in Mechanics (Ed. M. Holt) Academic Press NY 1959.

[42] Landau, L.D., Lifshitz, E.M., Electrodynamics of continuous media, Pergamon Press Oxford, London, NY, 1996.

[43] Arkhipov, N.I., et al., Fusion Technology 1994, Vol. 1, p. 423, 1995.

[44] Arkhipov, N.I., et al., J. Nucl. Mater. 233 - 237, 1996, p. 767.

[45] Arkhipov, N.I., et al., Fusion Technology, 1996, Vol. 1, 507, 1997.

[46] Chebotarev, V.V., et al., Fusion Technology 1996, Vol. 1, p. 351, 1997.

[47] Spitzer, L. Jr., Physics of fully ionized gases, J. Wiley NY, 1996.

[48] Safronov, V., private communication.

[49] Tereshin V.I., et al., ITER workshop on Material Effects of Disruptions, St. Petersburg, Russia, November 24 - 26, 1997.

[50] Pestchanyi, S., et al., 24th EPS Conf. Controlled Fusion and Plasma Physics, Vol. 21A, Part III, p. 981, 1997.

[51] Würz, H., et al., Fusion Technology 1998, Proc. 20th SOFT Marseile, France, 7 - 11. September 1998, Vol. 1, p. 271.

[52] Gmelin Handbuch der Anorganischen Chemie, Kohlenstoff Teil B, Verlag Chemie, Weinsheim (1967).

[53] H.R. Leidner et al., Carbon Vol. 11, Pergamon Press Oxford (1973) 555.

[54] A.A. Samarsky, Theorie der Differenzverfahren, Akad. Verlagsgesellschaft Geestland Porter Leipzig (1984).

[55] Thermodynamic Properties of Individual Substances, Vol. 2, Nauka, Moscow 1978.

[56] C.A. Klein et al., J. Appl. Physl 65 (1989) 3425.

[57] H.W. Barthels in Fusion Technology (Proc. 17th Symp. Rome, 1992), Vol. 1, Elsevier Amsterdam and New York (1993) 181.

[58] J.M. Gahl et al., J. Nucl. Mater. 196 – 198, 1992, p. 692.

[59] A. Hassanein et al., J. Nucl. Mater. 241 – 243, 1997, p. 288.

[60] H. Würz et al., Status and relevance of model validation, Workshop on Disruption Erosion, Nov. 24 – 26, 1997, St. Petersburg.

Table 1 Typical values of erosion and melt layer thickness for horizontal targets with and without plasma shield

hot plasma		carbon erosion (μm)		beryllium erosion (μm)		beryllium melt layer (μm)	
power density (MW/cm^2) along magnetic field lines	Time duration (ms)	with plasma	without shield	with plasma	without shield	with plasma	without shield
100	0.1	1.5	60	2	100	27	9
10	1	1.0	50	1.5	85	75	50
10	10	5	400	3.5	800	180	200
1	10	0.2	20	1	50	180	200
1	100	1	600	3.5	10000	300	350
0.1	100	-	-	0.1	25	80	450
	1000	0.1	250	2.5	1000	600	1400

still to be investigated:
existence and efficiency of plasma shield at power densities below 1 MW/cm^2

Table 2 Features of the 2D radiation magnetohydrodynamic code FOREV-2

- two separate spatial grids for solid and vapor
- stopping power models for ions and Maxwellian distributed electrons with inclined impact
- heat conduction into the bulk target
- erosion and melt front propagation into the bulk target
- 2½ dim MHD model
- use of nonuniform mesh with $\Delta x_n = \Delta x_1 g^q$ ($q = 1.03 \div 1.07$)
- solid target heating

ion beam with surface energy deposition electrons: Maxwellian distributed with 32 beamlets with volume energy deposition

- momentum transfer to target plasma by external ion beam
- energy exchange between plasma electrons and ions
- 2 dim radiation transport by improved forward-reverse method (IFRM) with multigroup opacities
- radiative heat conduction option
- frequency group optimization: possibility to describe line shapes by several frequency groups
- use and handling of different kinds of opacity tables
- calculation of effective charge and internal energy from optical data
- non-LTE multigroup opacities and optical data for C, Be, W
- special feature for ten fold increase of time step (TS) size

Table 3

- separating into E, L substeps according to Belocerkovsky
- Belocerkovsky formalism for not rectangular meshes (inclined target)
- heat conduction equation solved according to LOD (locally 1D) method
- linearity of time dependence of parameters in each time step
- quadratic terms for evolution of magnetic field (magnetic energy in rarefied region » than plasma energy)
- atomic density of background bg plasma $n_a = 10^{12}$ cm^{-3}
- TS size in MHD systems related with Alfven velocity

mass of bg plasma increased artificially TS size typically 10^{-9} s

- typical 2D example with 2½D MHD:

Δt up to 1 ms

size of computational region 300 x 30 cm^2

number of meshes 60 - 100 in x direction

20 - 60 in y direction ($\alpha = 5°$)

routinely 24/69 frequency groups

CPU time on WS 25 hours

Table 4 Comparison of erosion and dominating target heat load source

facility	target material	target arrangement	erosion (μm) measured	erosion (μm) calculated	dominating target heat load
2 MK-200 CUSP	graphite	perp.	0.2	0.25	electron heat conduction
	quartz	perp.	0.8	0.75	$q_{el}^{quartz} > q_{el}^{carbon}$
MK-200 UG	graphite	perp.	0.4	0.45	$q_{el} \approx q_{rad} \approx 0.25$ MW/cm^2
		tilted (20°)	0.22	0.25	"
	quartz	perp.	--	2.5	
		tilted (20°)	0.45	1.2	$q_{rad} \approx 0.1$ MW/cm^2 and dominating
				0.7	q_{rad} reduced by factor 2.5
QSPA[1]	graphite	perp.	2	1.4	electron heat conduction $q_{el} = 0.2$ MW/cm^2
	quartz	perp.	7.0	6.5	$q_{el} = 0.15$MW/cm^2
		tilted (20°)	7.0	0.7	dominated by radiation $q_{rad} = 0.03$MW/cm^2

[1] Valid assuming a rather pure hot plasma stream. In this case rather high plasma temperatures are obtained in the plasma shield.

Table 5 Relevance of disruption simulation experiments for ITER tokamak divertor damage

	simulation experiments	ITER
energy transfer from hot plasma to target	electron heat conduction and radiation direct energy deposition negligible	Impact energy of hot plasma 10 keV a) $q_{\parallel} \geq 50$ MW/cm^2 direct energy deposition and radiation b) $q_{\parallel} < 50$ MW/cm^2 only direct energy deposition Impact energy 1 keV electron heat conduction and radiation, direct energy deposition negligible
MHD of plasma shield (PS), 2 dim problem	Flow pattern in plasma shield may change (CUSP facility) with time because of short pulse duration	Flow pattern depends on power density profile (Gaußian, realistic) and tilting of target
long term stability of PS	No experimental answer	Important for erosion
shielding efficiency against radiation (side wall damage), 2 dim problem	Tokamak typical results available	Important for erosion

Simulation experiments are important for code validation but are of limited value for direct conclusions on ITER erosion

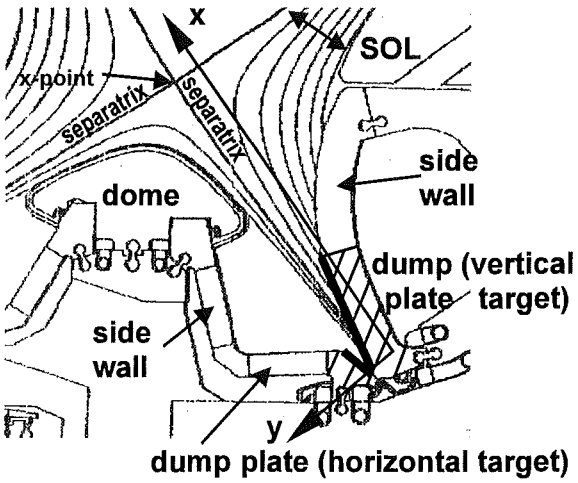

Fig.1a. Poloidal cross section of the outboard wing of the ITER slot divertor and coordinate system for the 2dim calculation.

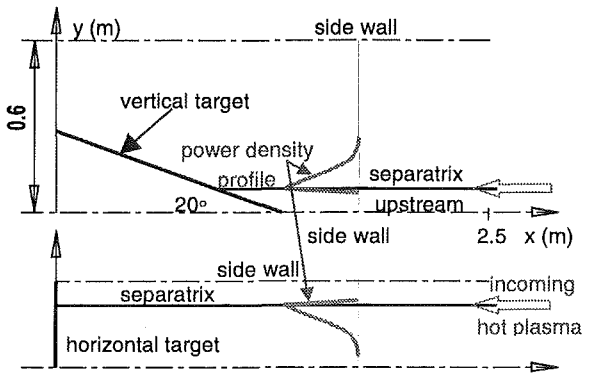

Fig.1b. Simplified geometry for 2dim calculation for the slot divertor with vertical and horizontal target (dump plate) in poloidal plane. Incoming hot plasma along magnetic field lines $\vec{B}_0 = (B_x, B_y, B_z) = (0.5T, 0,5T)$.

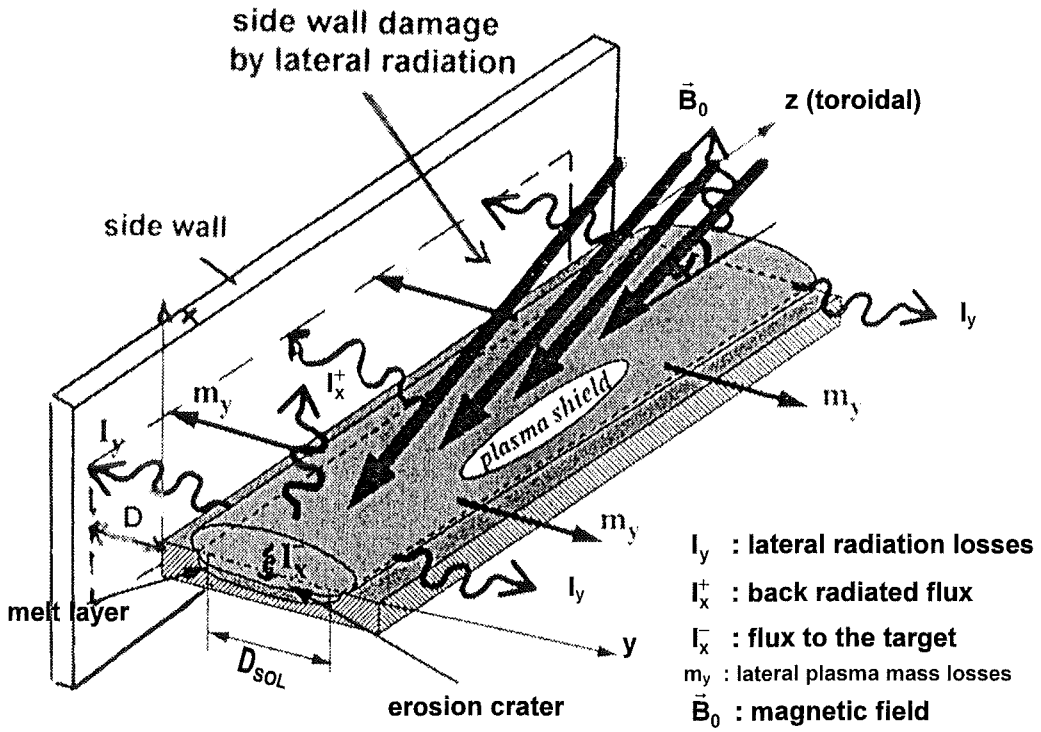

Fig.1c. Horizontal divertor target with side wall and plasma shield schematically

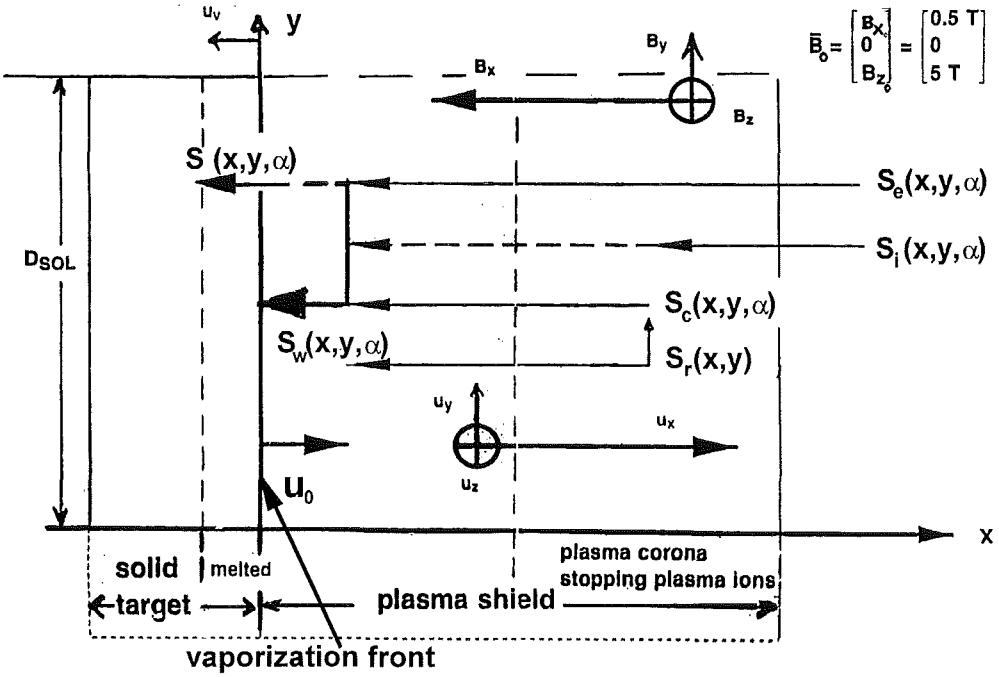

Fig.1d. Schematical description of 2 dim problem with 21/2 dim MHD model.

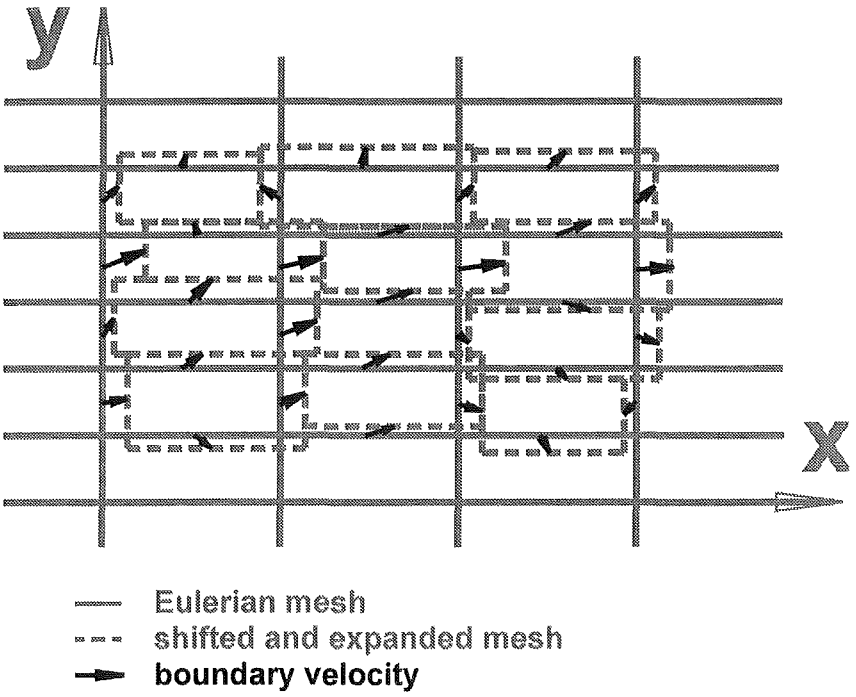

Fig.2. Mesh transformation in each time step according to the mesh boundary velocities schematically.

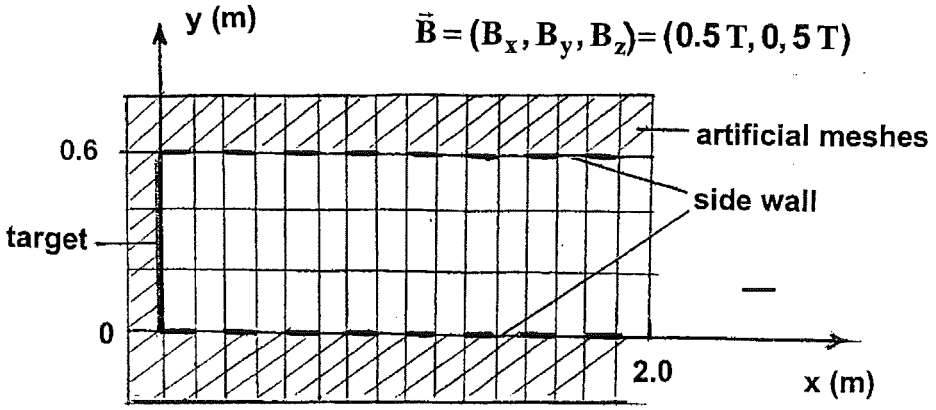

Fig.3a. Horizontal target (inclination angle toroidally is 5°). Typical size of computational area 2.0×0.6 m. Number of meshes typically 100×30.

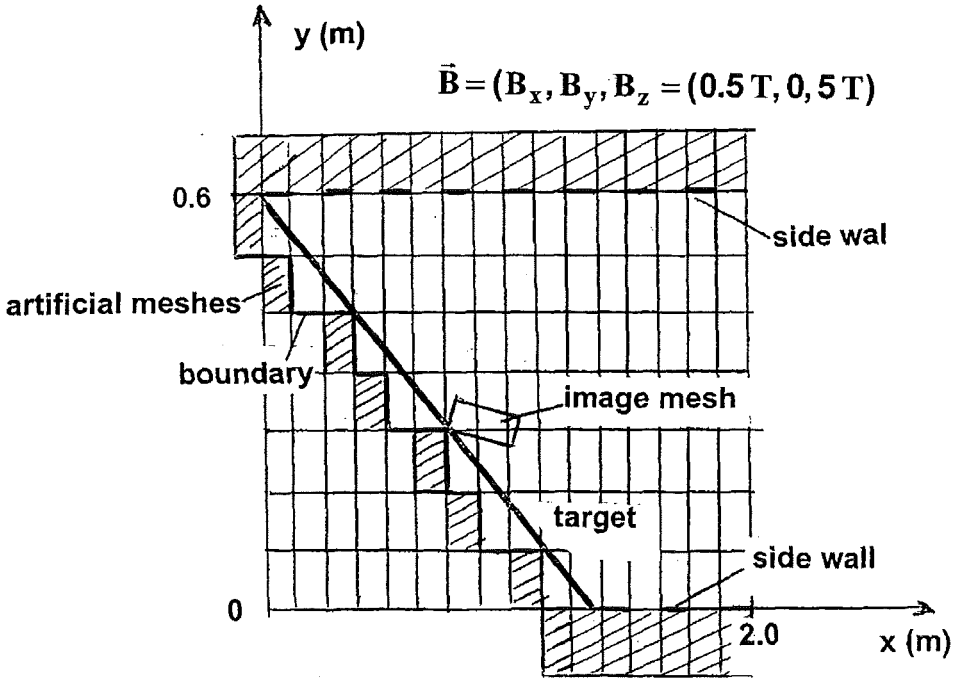

Fig.3b. Vertical target (target tilted in poloidal plane). Typical size of computational area and number of meshes see Fig.3a. Tilting angle used in the 2 dim calculations is 20°.

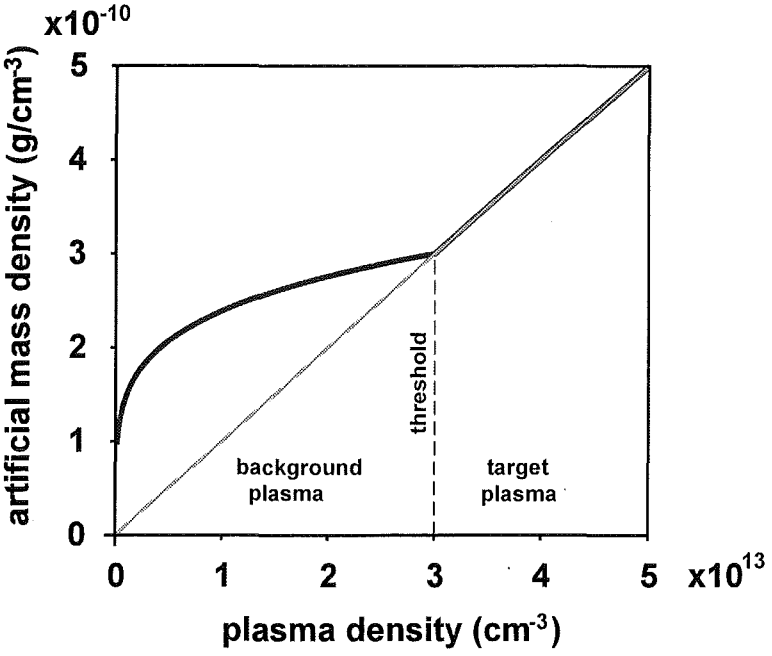

Fig.4. Density of artificial background plasma.

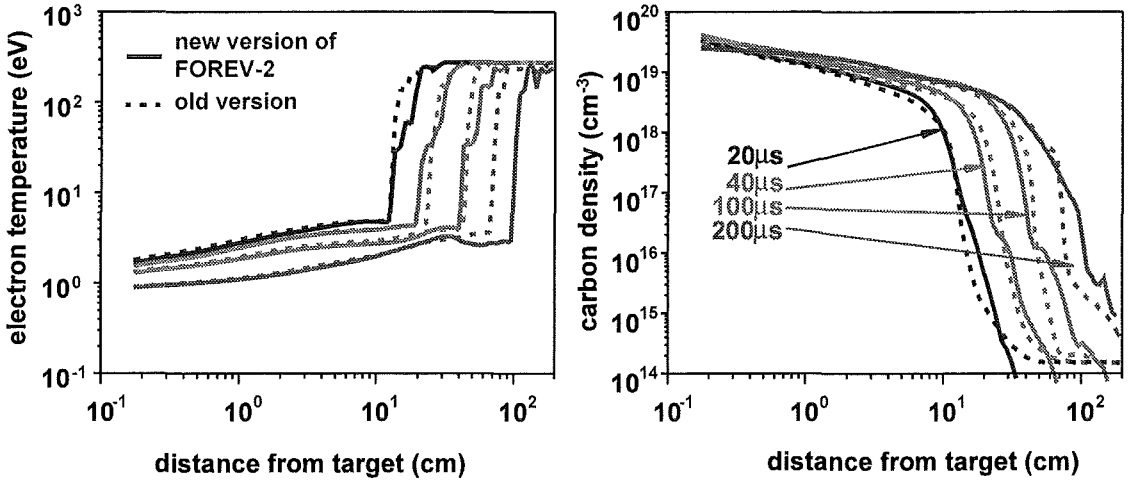

Fig.5. Comparison of calculated values of carbon density and plasma temperature for the old and new versions of FOREV2.

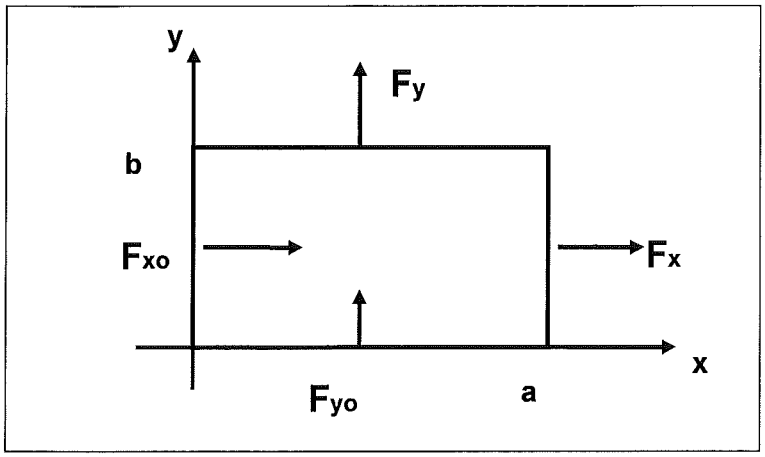

$$F_x^{out} = A_{xx}F_{xo} + A_{xy}F_{yo}$$

$$F_y^{out} = A_{yx}F_{xo} + A_{yy}F_{yo}$$

Fig.6. Incoming and outgoing radiation fluxes schematically for empty mesh.

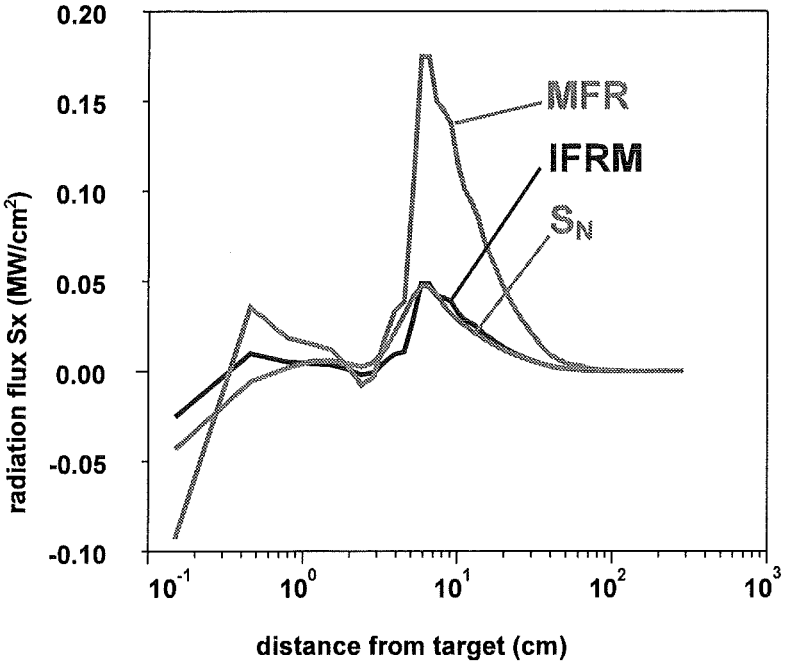

Fig.7a. x-component of radiation fluxes at the middle section of the calculation region calculated by S_n method, IFRM and 2D forward-reverse method.

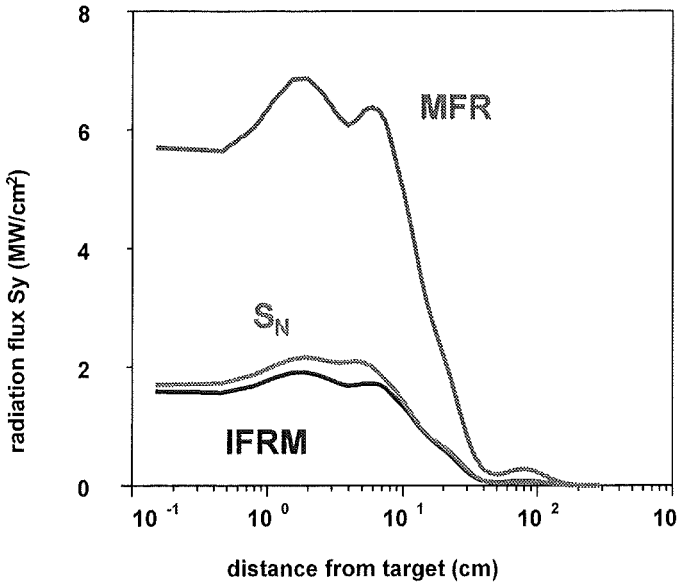

Fig.7b. Lateral radiation fluxes calculated by S_n method, IFRM and 2 dim forward-reverse method.

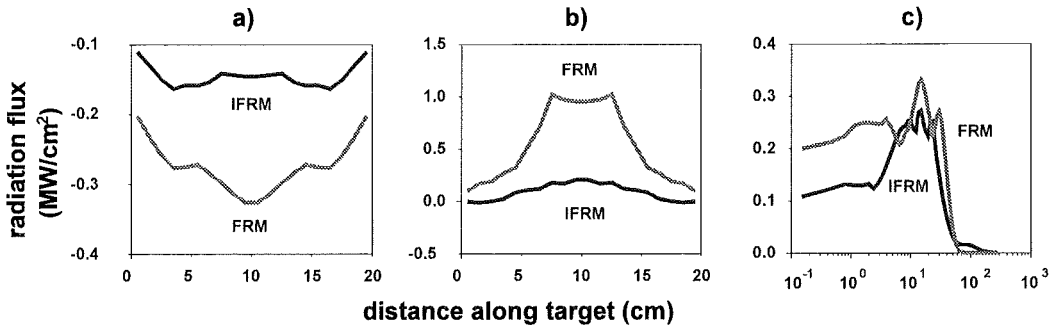

Fig.8a. x- and y-component of radiation flux

a) to the wall, b) x-component of radiation fluxes at 20cm from target, c) lateral radiation fluxes

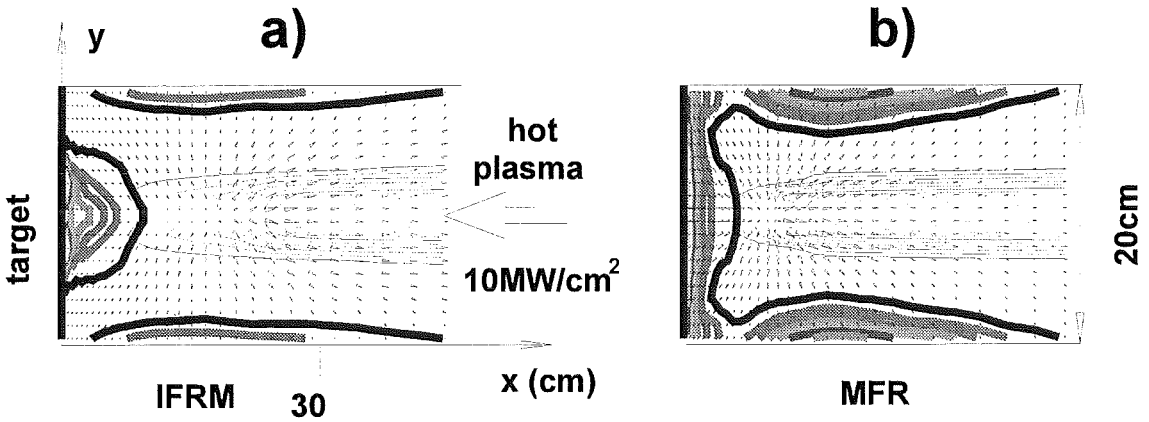

Fig.8b. Comparison of plasma density and radiation field for IFRM and MFR method at 100 μs.

Fig.8. Comparison of 2 dim radiation fluxes calculated with MFR and IFRM and comparison of 2 dim contours of plasma density for a horizontal target. Gaussian power density profile with peak power density of 100 MW/cm².

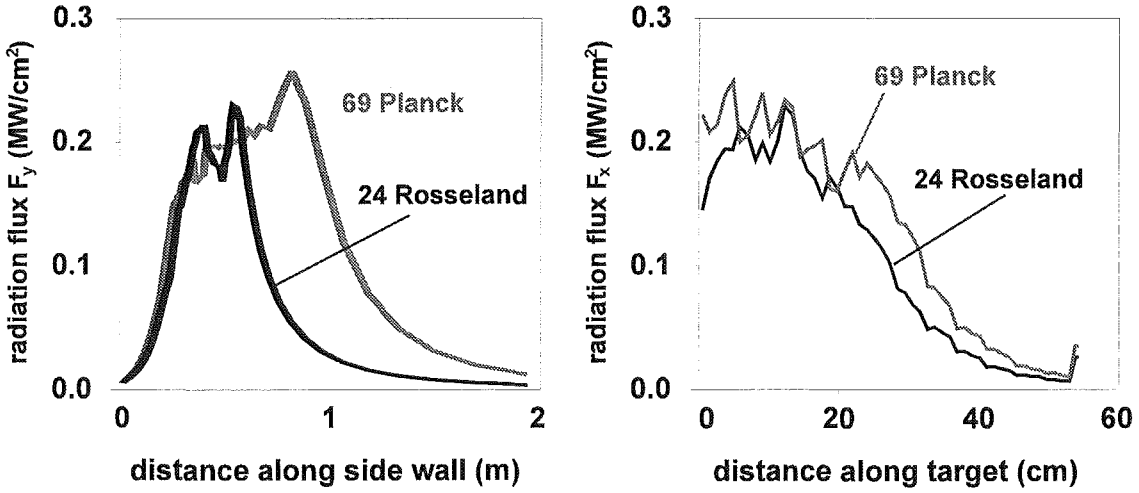

Fig.9. Comparison of radiation fluxes to the target (x-component) and to the side walls (lateral radiation y-component) using Plank and Rosseland opacities. Vertical graphite target, realistic power density profile in the hot plasma, peak power density along the separatrix 100 MW/cm^2.

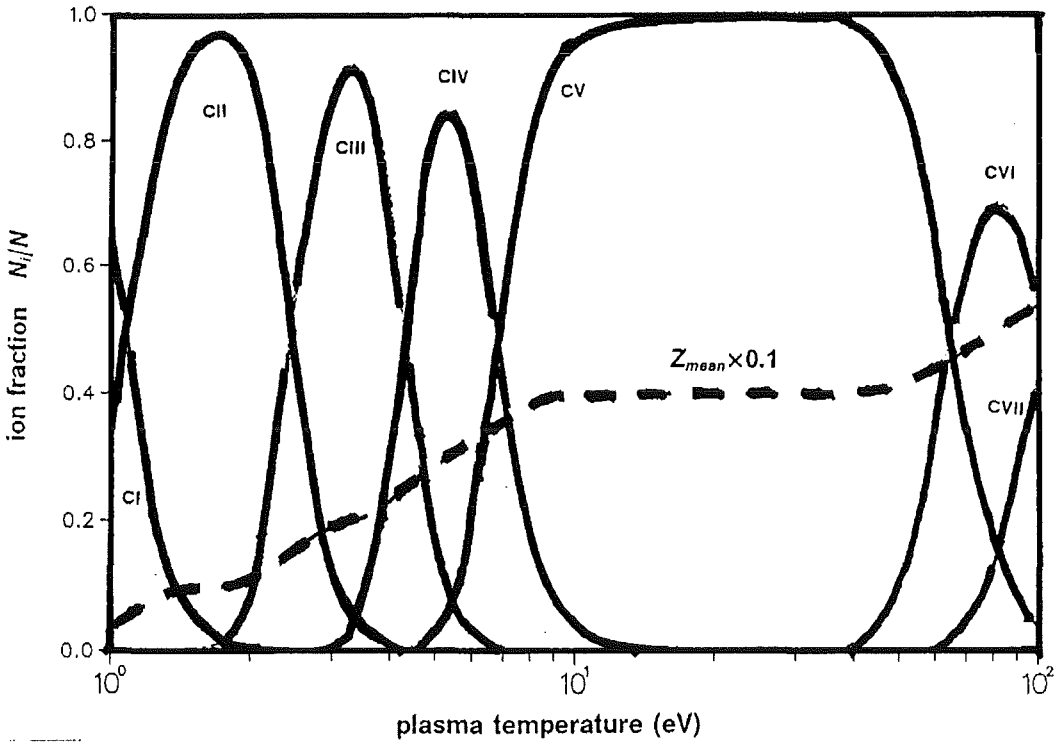

Fig. 10 Ion concentrations and mean charge for carbon plasma. Plasma density 10^{17} cm^{-3}.

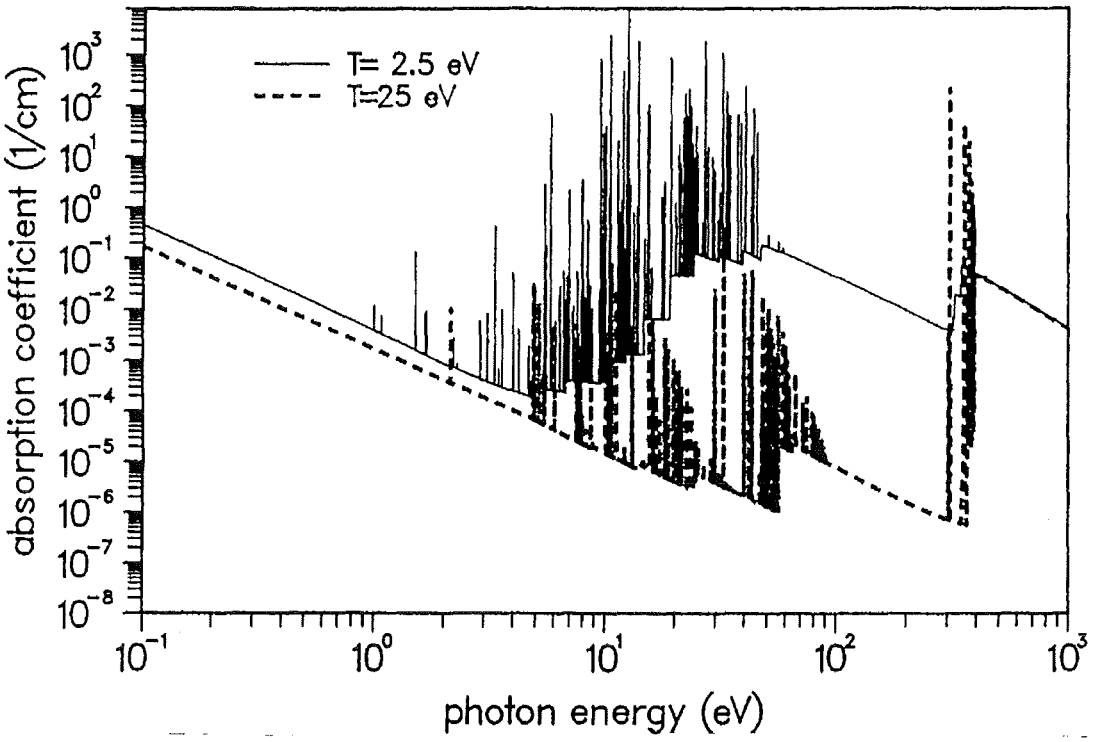

Fig. 11. Absorption coefficient for carbon plasma for two plasma temperatures. Plasma density 10^{17} cm^{-3}.

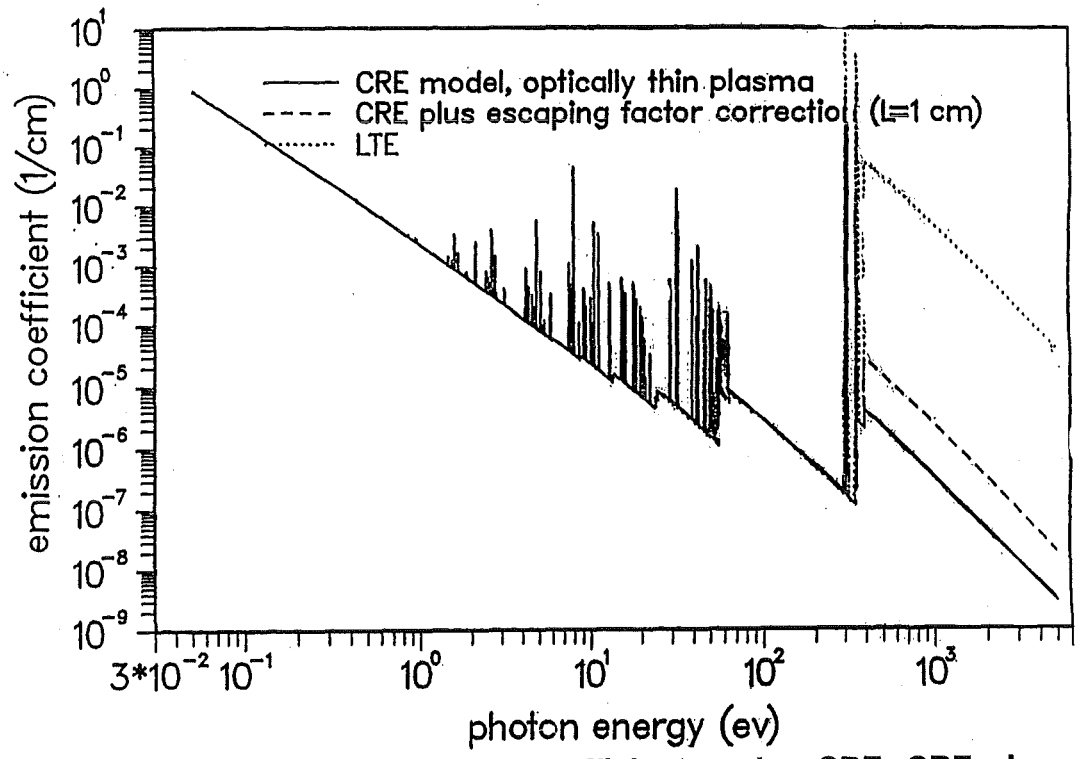

Fig. 12. Comparison of emission coefficients using CRE, CRE plus escaping factor correction and LTE conditions. Carbon plasma, density 10^{17} cm^{-3} temperature 20 eV.

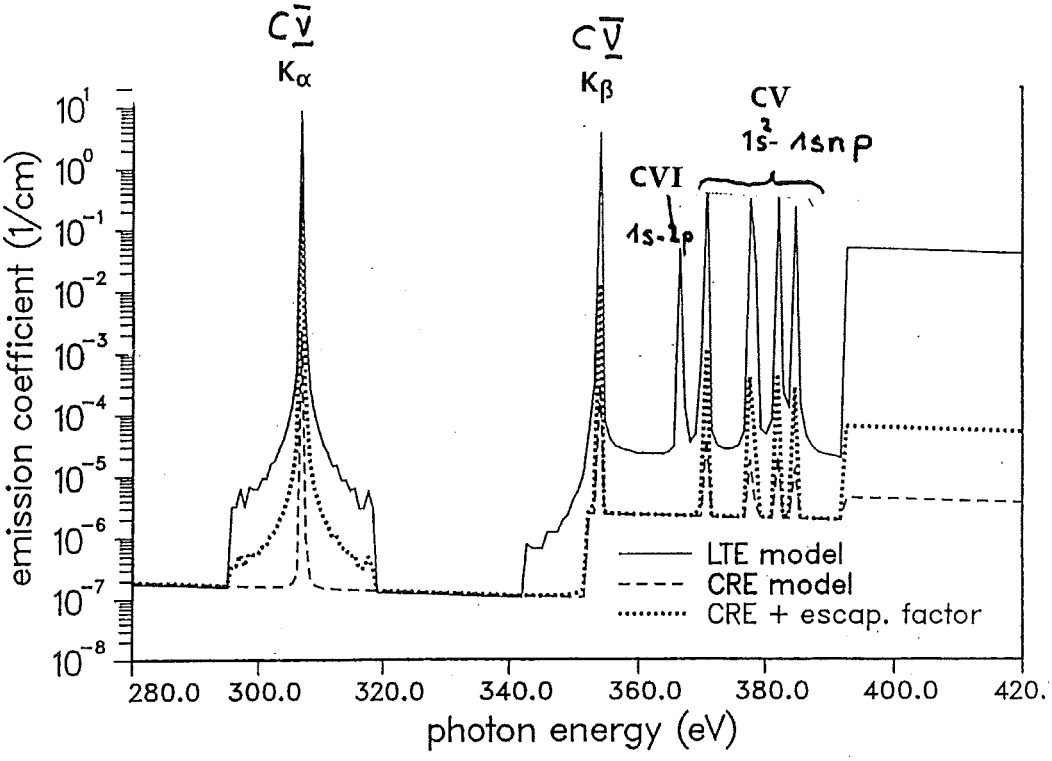

Fig. 13. Comparison of emission coefficients for lines from K shell for carbon plasma, density 10^{17} cm^{-3} temperature 20 eV.

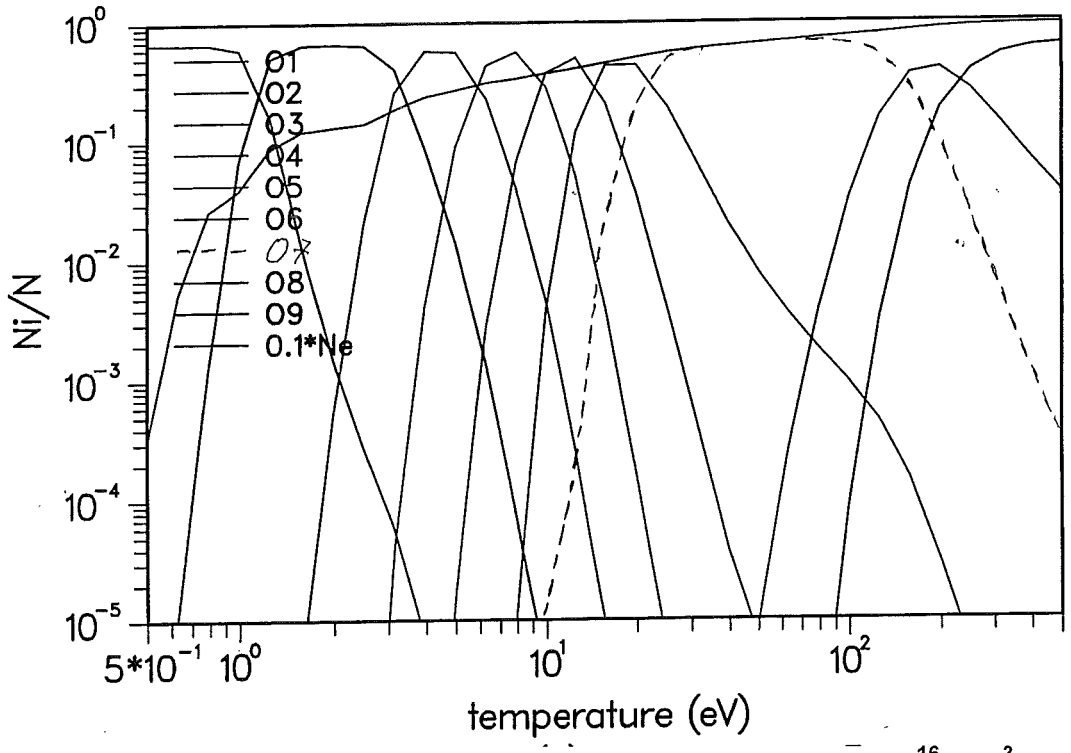

Fig. 14a. Ion concentrations for oxygen plasma at density of 10^{16} cm^{-3}.

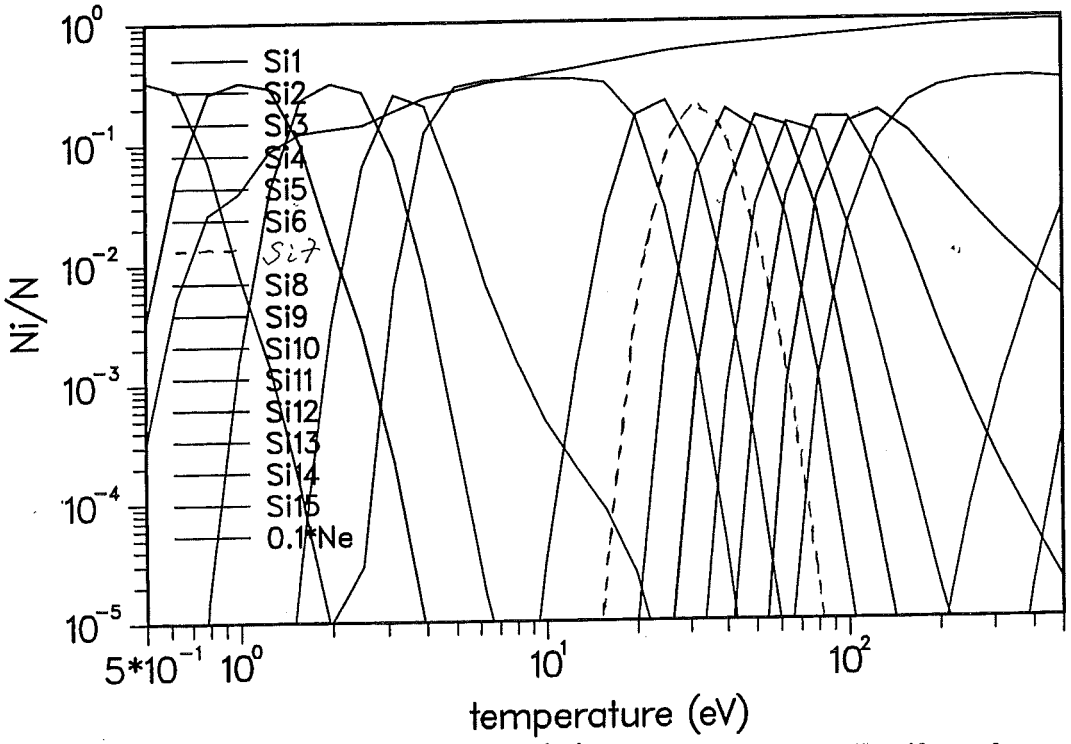

Fig. 14b. Ion concentrations for silicon plasma at density of 10^{16} cm^{-3}.

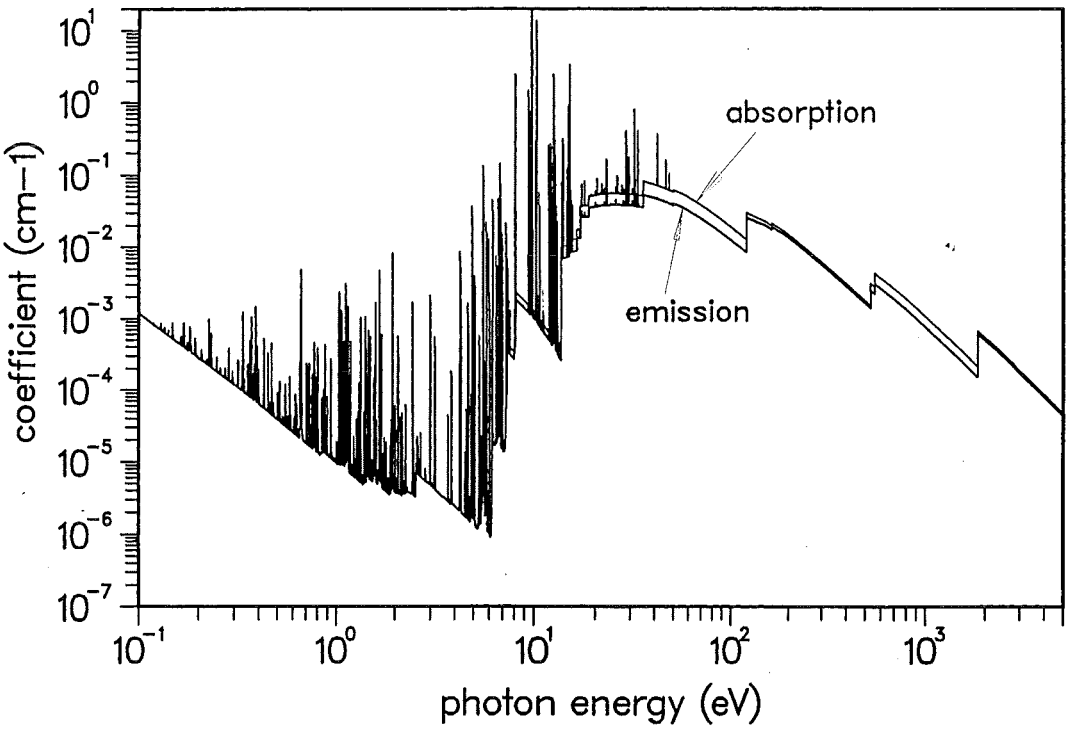

Fig. 15a. CRE optical coefficients for quartz plasma. Plasma temperature 1 eV, density 10^{16} cm^{-3}.

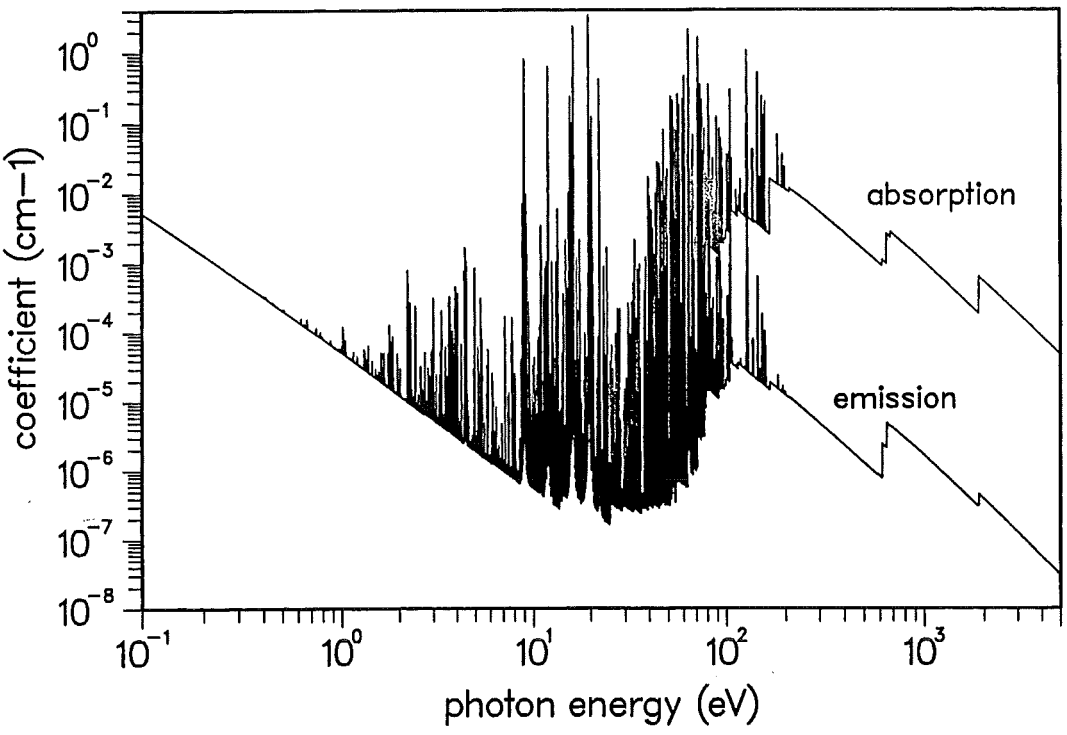

Fig. 15b. CRE optical coefficient for quartz plasma. Plasma temperature 10 eV, density of 10^{16} cm^{-3}.

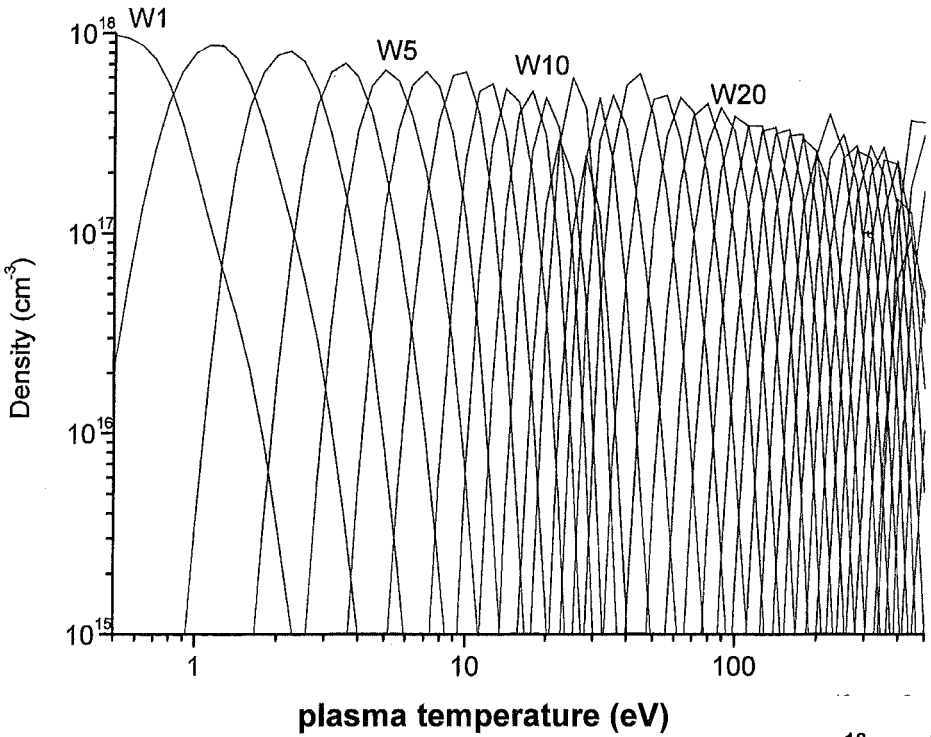

Fig. 16. Ion concentrations for tungsten plasma at density of 10^{18} cm^{-3}.

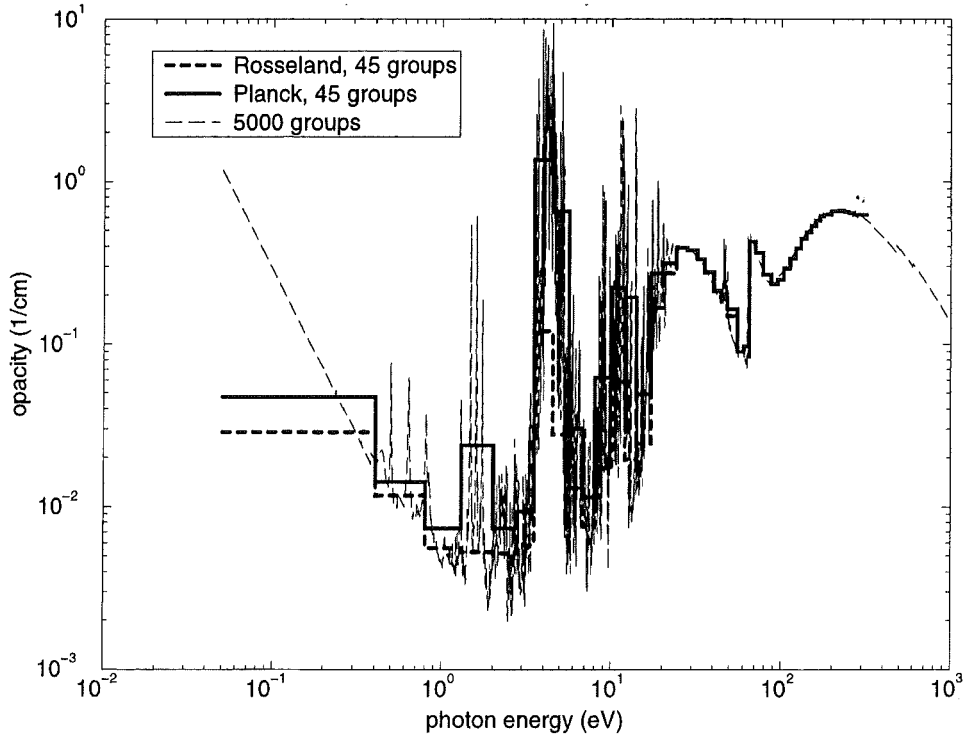

Fig. 17a. Absorption coefficient for tungsten. Plasma temperature 1 eV, density 10^{17} cm^{-3} and comparison with 45 group Planck and Rosseland opacities.

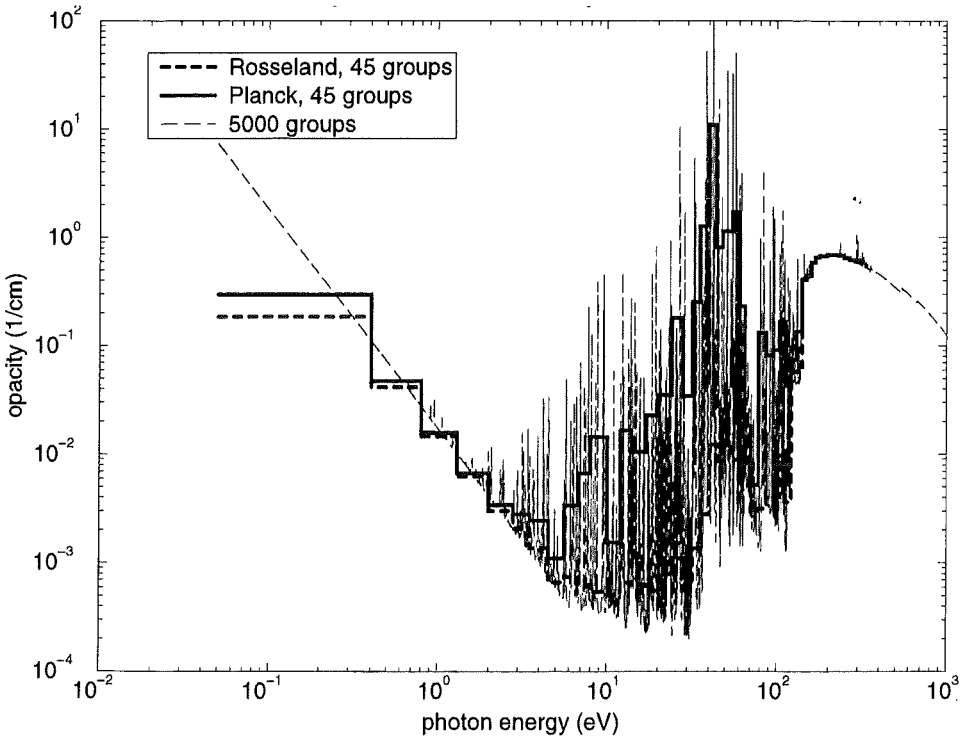

Fig. 17b. Absorption coefficient for tungsten. Plasma temperature 10 eV, density 10^{17} cm^{-3} and comparison with 45 group Planck and Rosseland opacities.

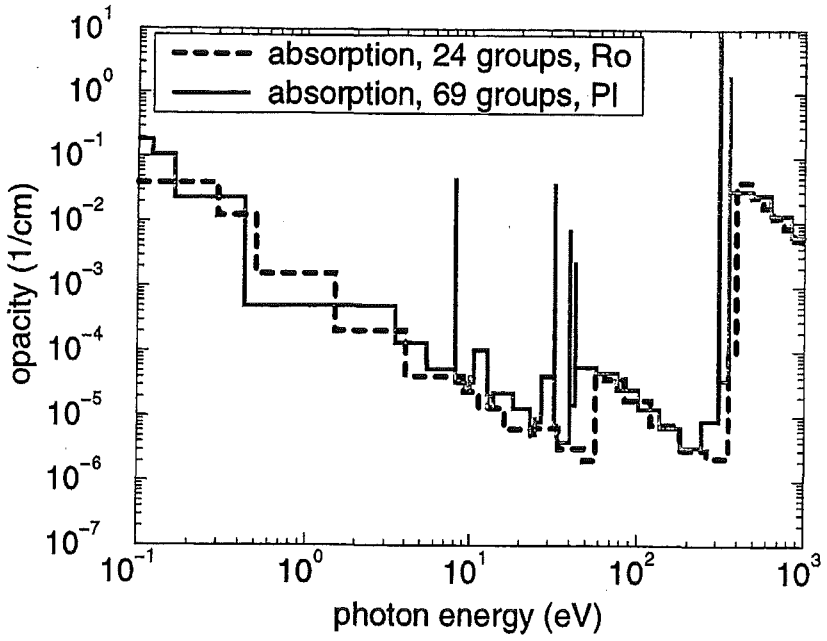

Fig. 18a. Comparison of 24 group Rosseland and 69 group Planck non-LTE opacities for absorption for a carbon plasma of temperature 20 eV, and density 10^{17} cm^{-3}.

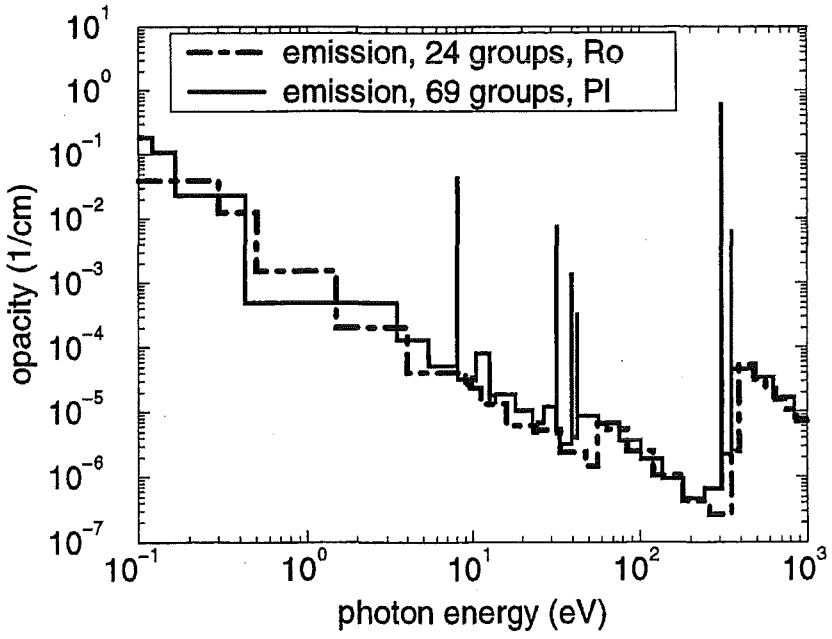

Fig. 18b. Comparison of 24 group Rosseland and 69 group Planck non-LTE opacities for emission for a carbon plasma of temperature 20 eV, and density 10^{17} cm^{-3}.

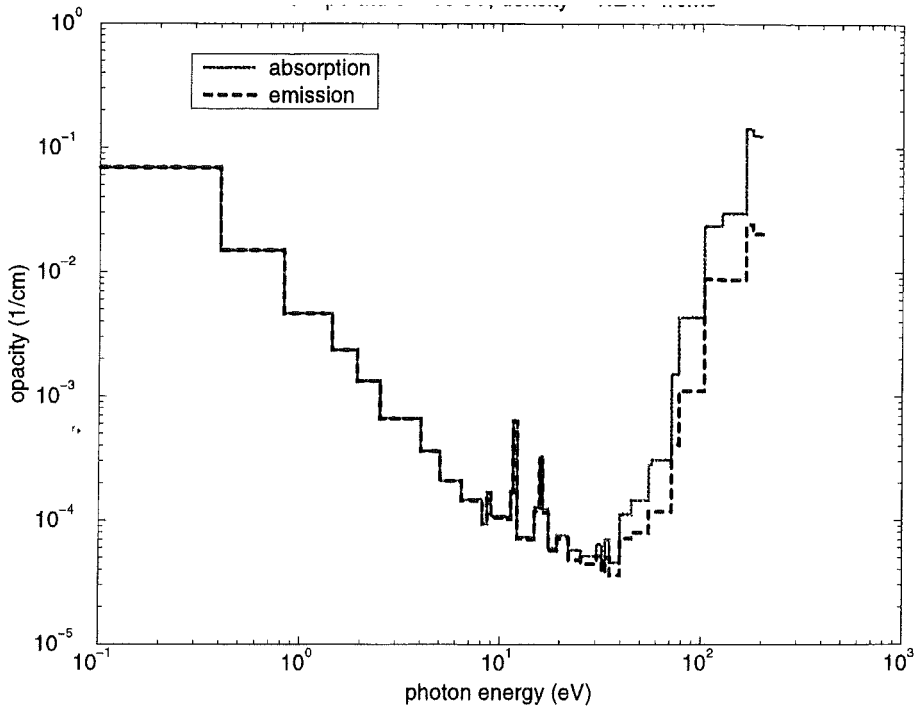

Fig. 19a. 40 group Rosseland non-LTE opacities for absorption and emission for quartz plasma. Plasma temperature 10 eV, density 10^{17} cm^{-3}.

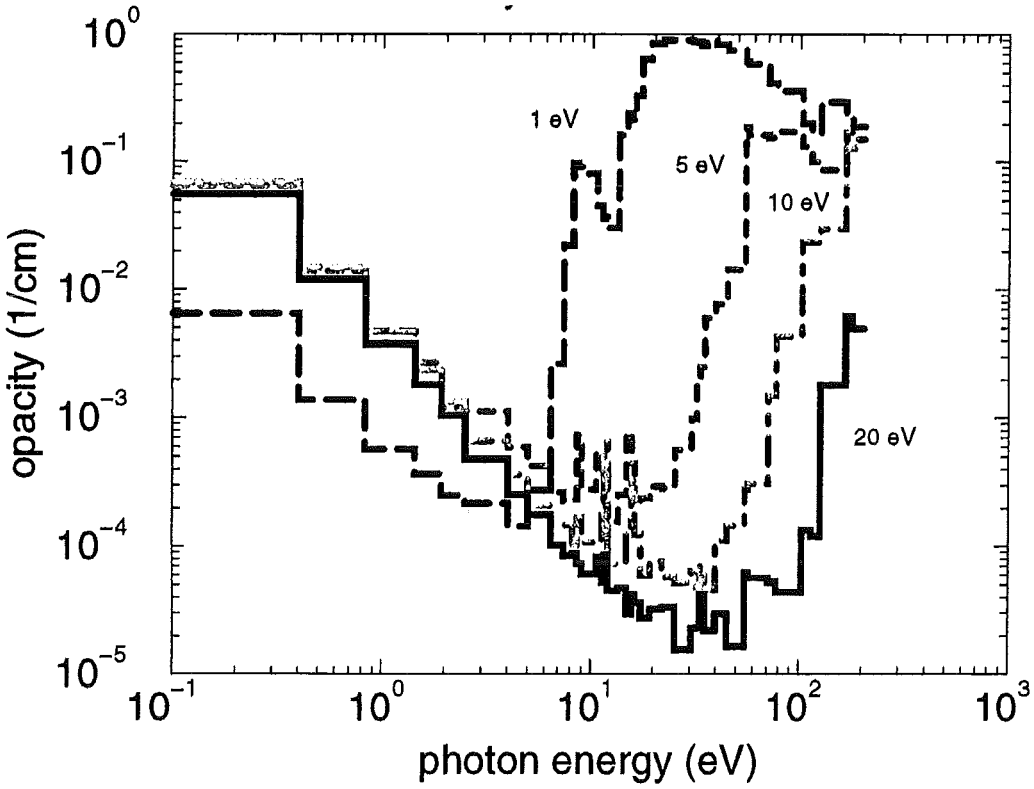

Fig. 19b. 40 group non-LTE Rosseland opacities for absorption for a quartz plasma for different plasma temperatures. Plasma density is 10^{17} cm^{-3}.

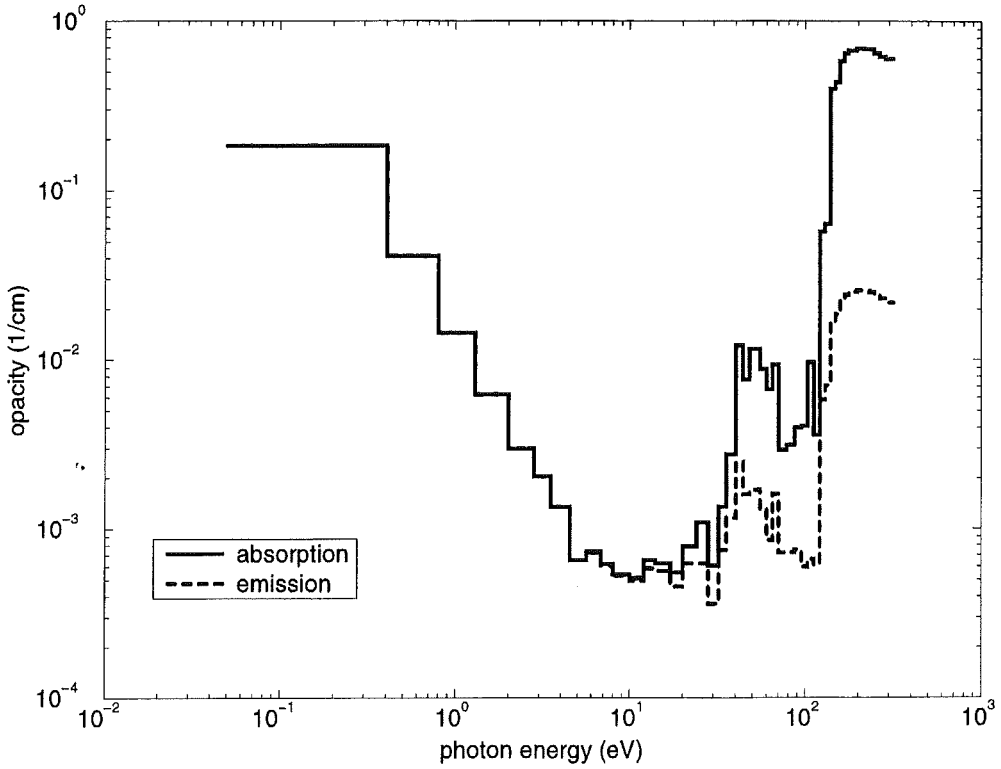

Fig. 20. 45 group non-LTE Rosseland opacities for absorption and emission for tungsten. Plasma temperature is 10 eV, density is 10^{17} cm^{-3}.

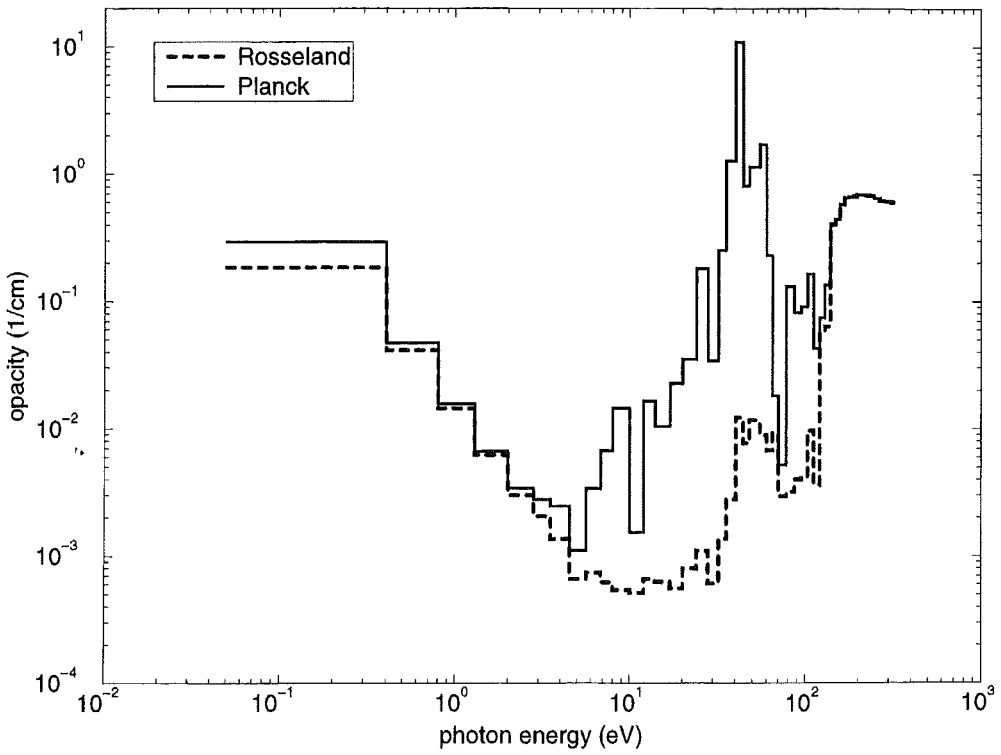

Fig. 21. Comparison of 45 group Rosseland and Planck non-LTE opacities. Plasma temperature is 10 eV, density is 10^{17} cm^{-3}.

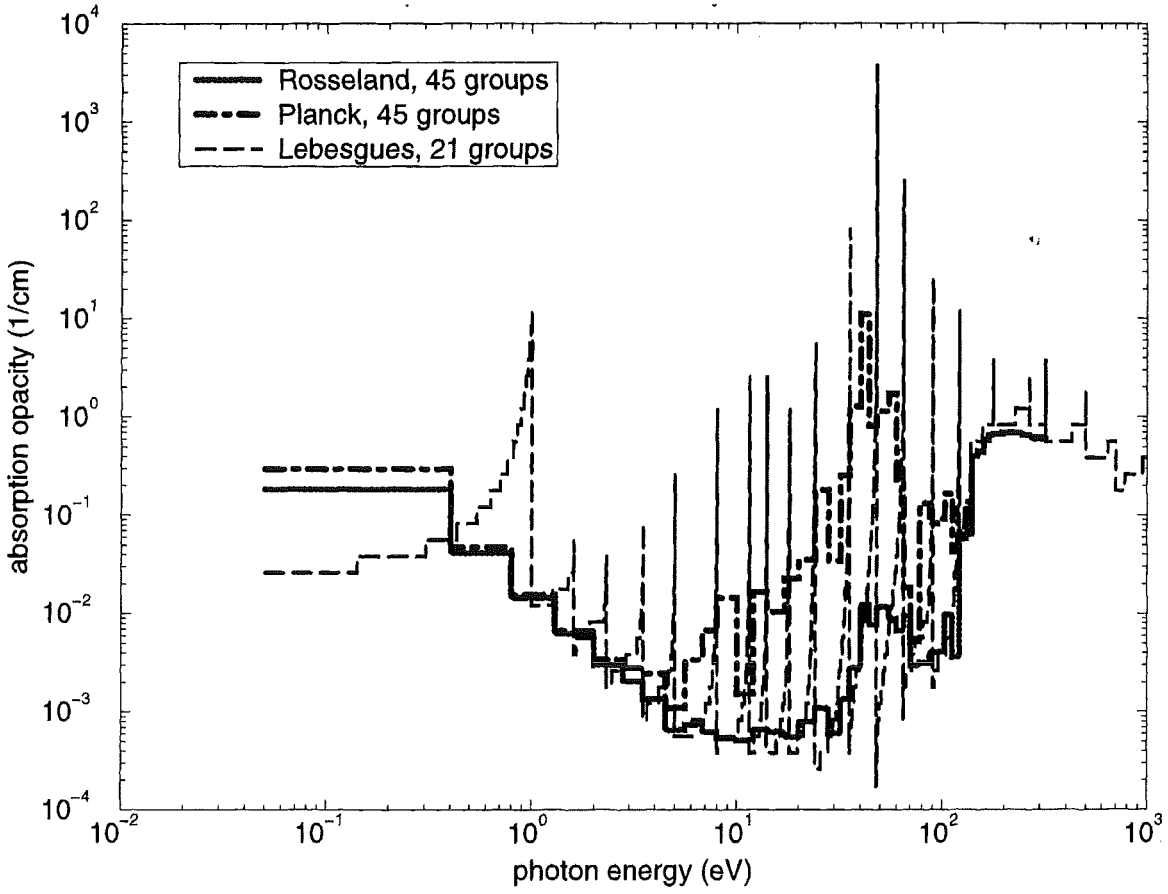

Fig.22. Comparison of 45 group Rosseland and Planck opacities and 21 group Lebesques opacities for tungsten plasma.

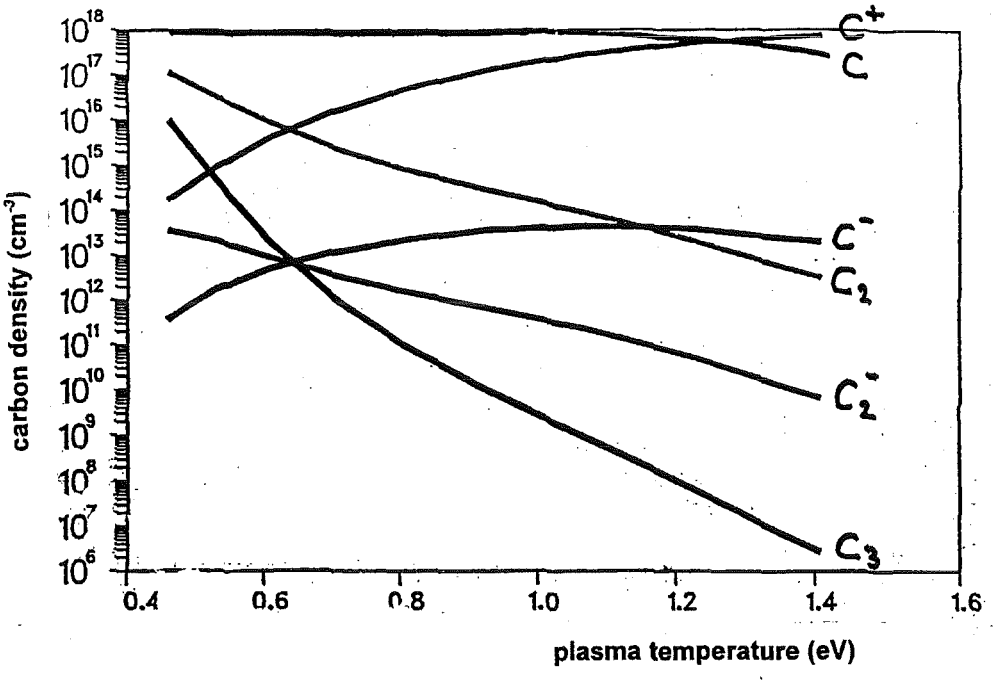

Fig. 23a Temperature dependent concentrations of molecules and atoms in carbon plasma of density of 10^{18} cm^{-3}.

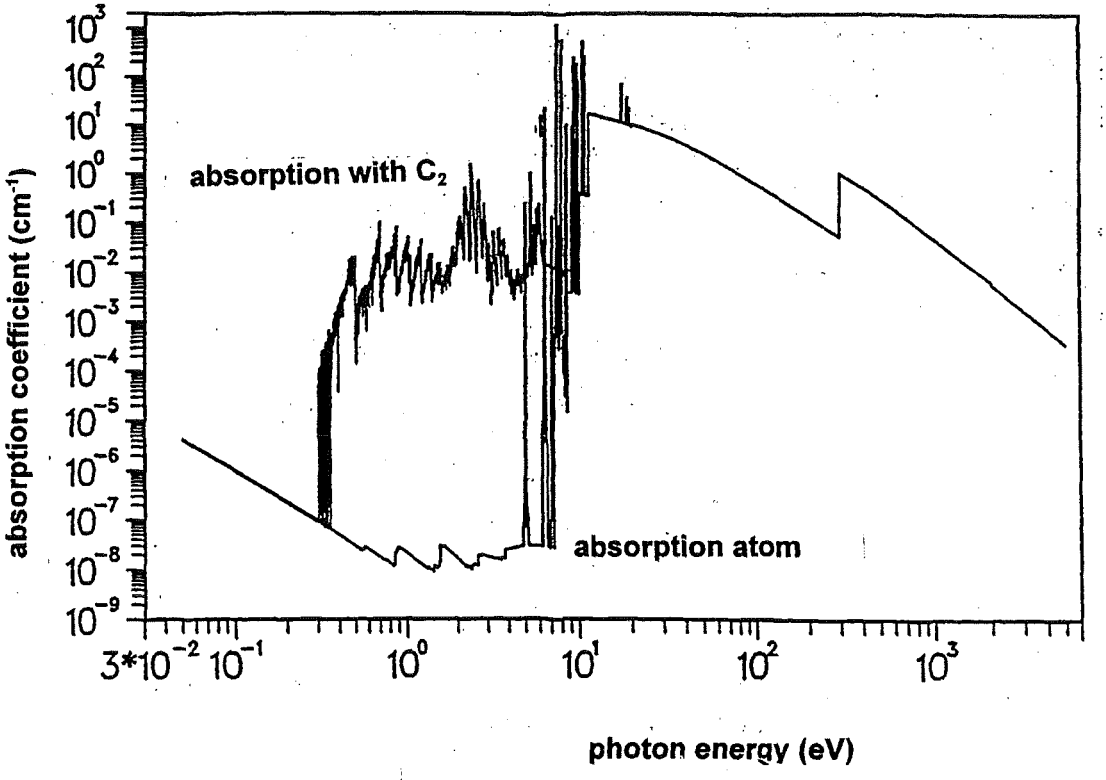

Fig. 23b Comparison of absorption coefficients for carbon plasma with and without carbon molecules. Plasma temperature 0.5 eV, plasma density 10^{18} cm^{-3}.

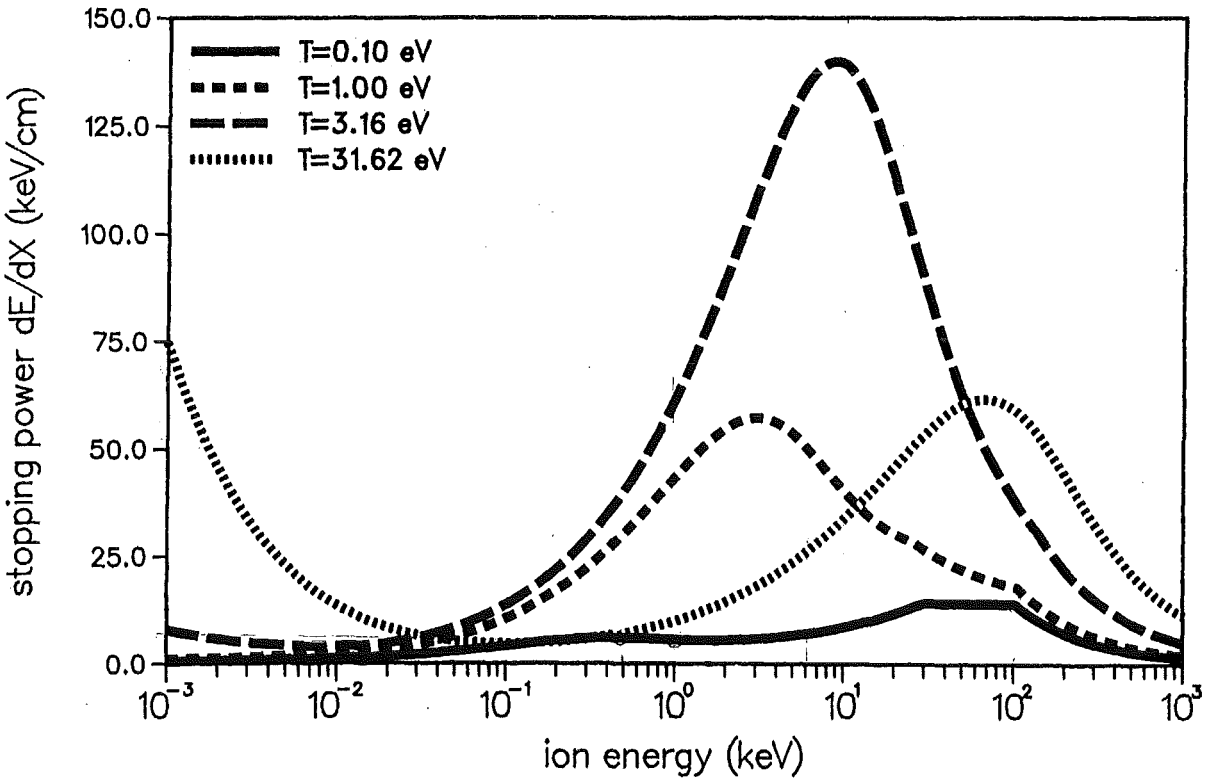

Fig. 24a. Stopping power of protons in carbon plasmas of different temperature as function of proton energy. Plasma density 10^{18} cm^{-3}.

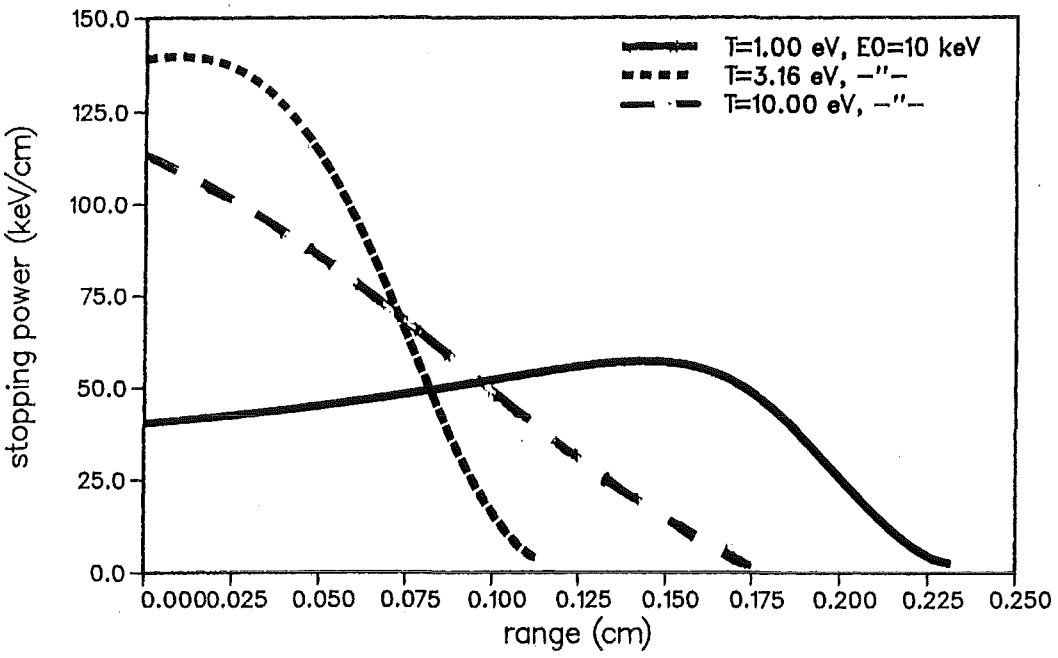

Fig. 24b. Stopping power for 10 keV protons in carbon plasmas of different temperature. Plasma density 10^{18} cm^{-3}.

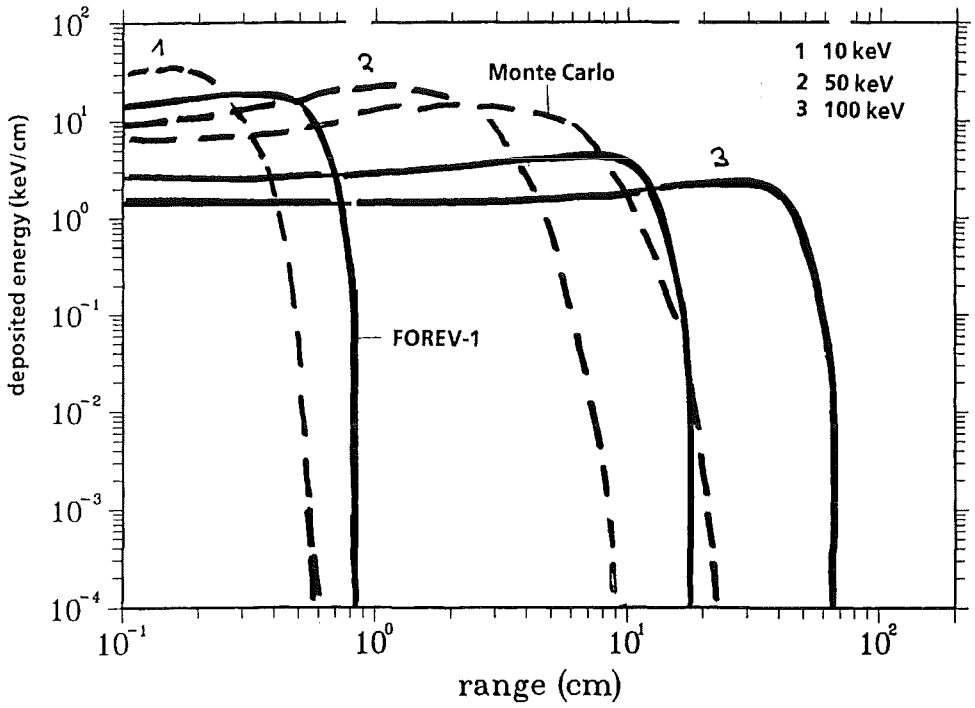

Fig. 25. Comparison of deposited energy for monoenergetic electrons in a carbon plasma of density of 10^{18} cm^{-3} and temperature 5 eV. Beam impact angle 5°.

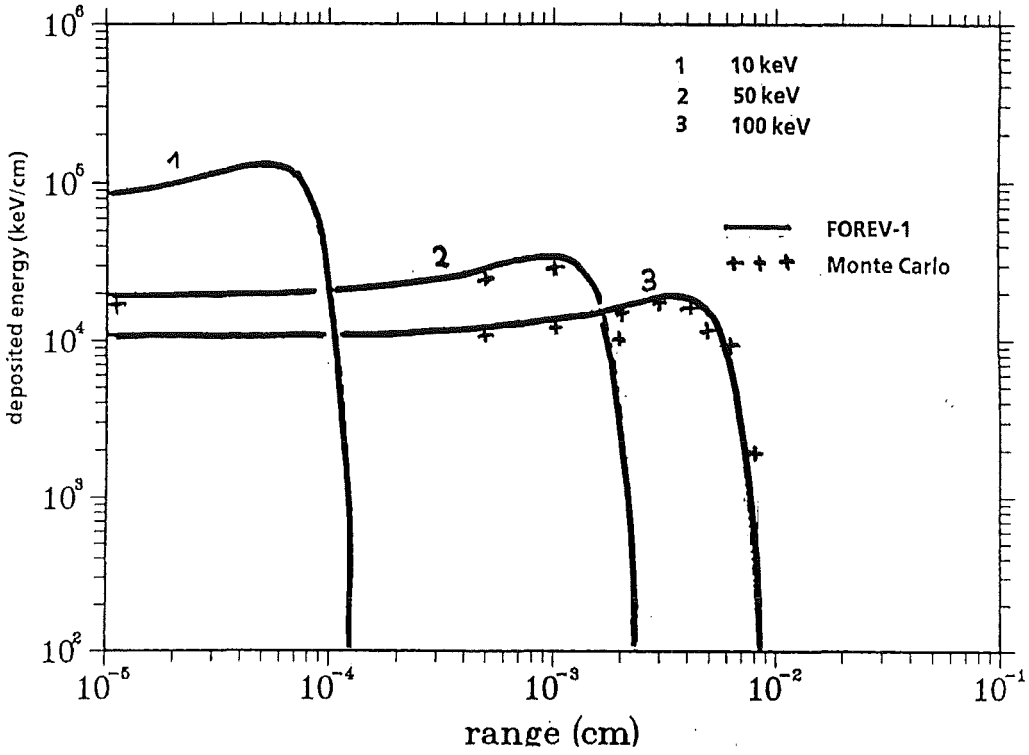

Fig. 26. Comparison of deposited energy for monoenergetic electrons with perpendicular impact in solid carbon.

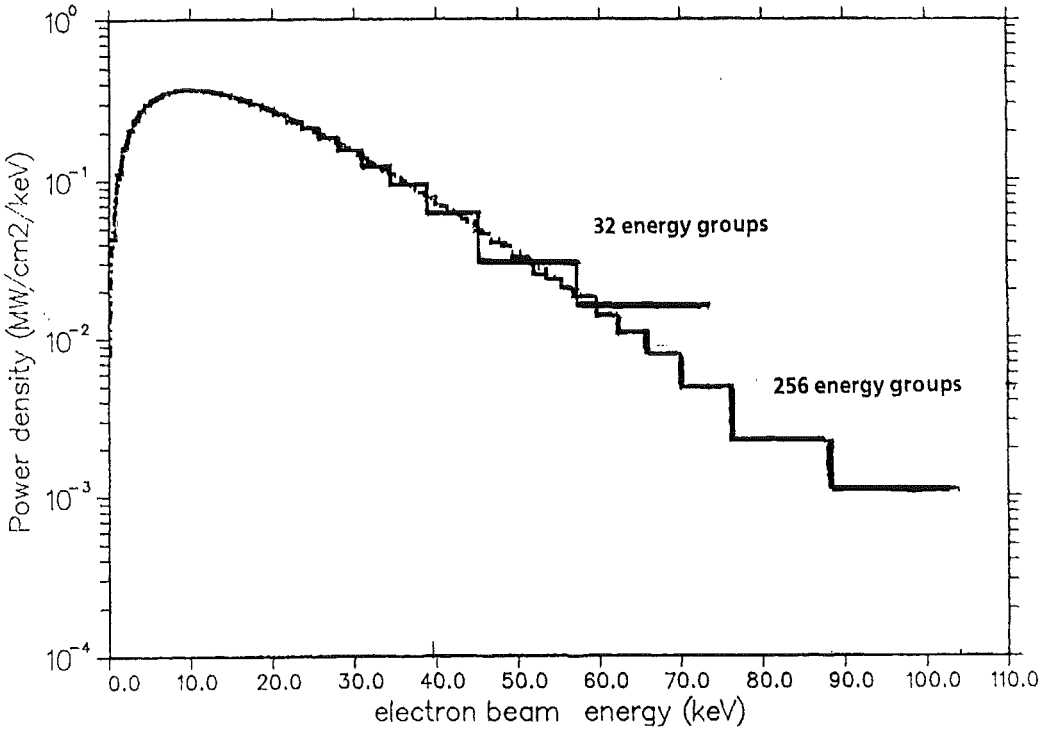

Fig. 27. Power density distribution of Maxwellian electrons of temperature 10 keV and approximation by 32 and 256 energy groups. Total power density 10 MW/cm^2.

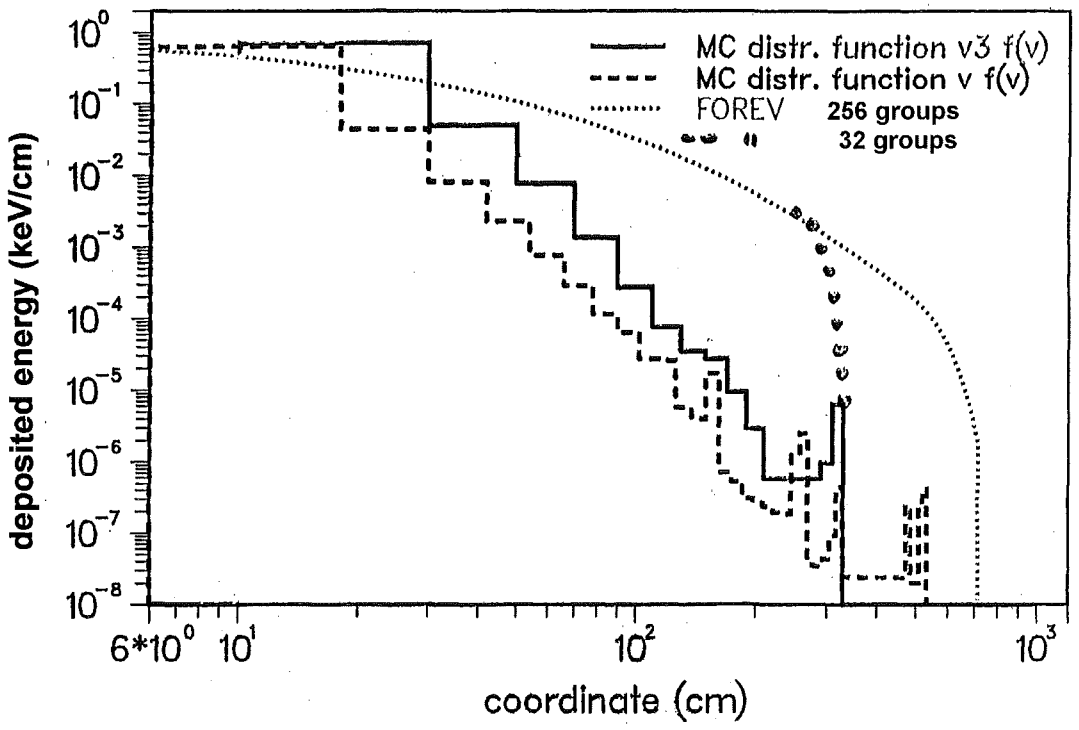

Fig. 28. Comparison of distribution of deposited energy for Maxwellian electrons of temperature 10 keV in a carbon plasma of density of 10^{18} cm^{-3} and temperature 10 eV for perpendicular impact of the hot electrons

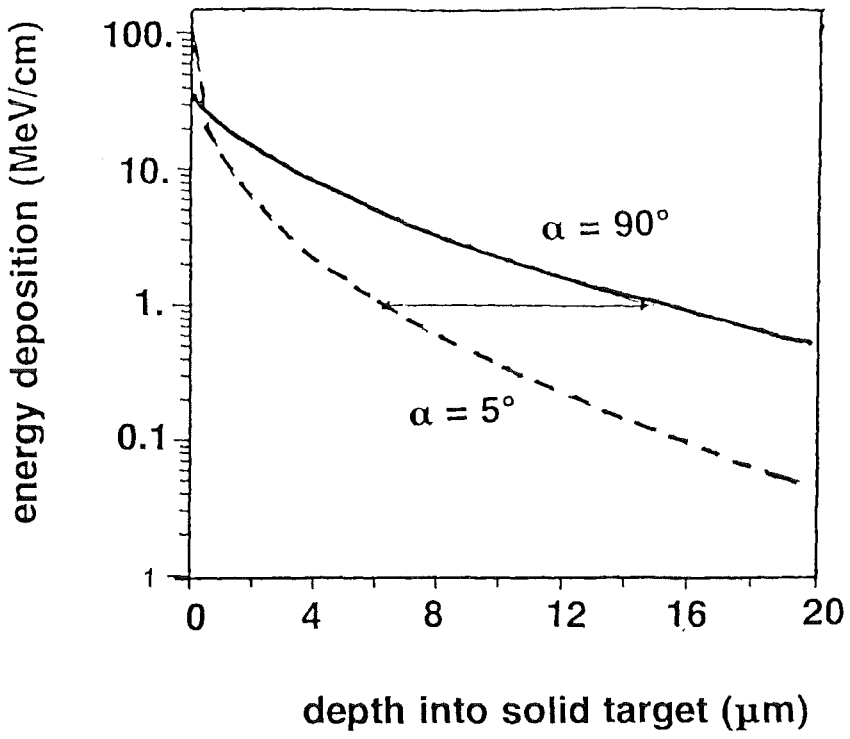

Fig. 29. Energy deposition into a solid graphite target for 10 keV Maxwellian electrons of power density of 10 MW/cm^2 and impact angle 5° at different times.

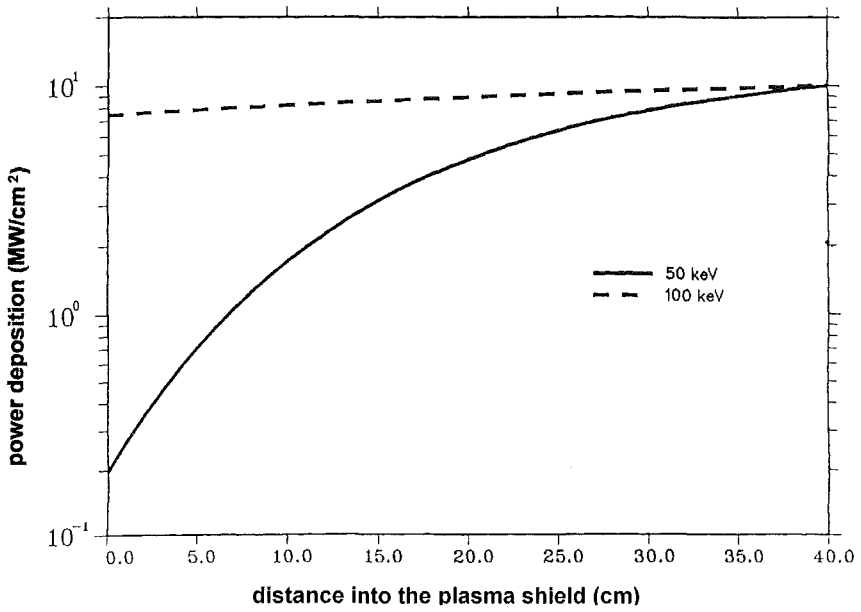

Fig. 30. Distribution of power deposition of monoenergetic electrons with perpendicular impact in a carbon plasma of density $5 \cdot 10^{18} cm^{-3}$ and temperature 3 eV. Initial power density is 10 MW/cm^2. Thickness of the plasma layer is 40 cm.

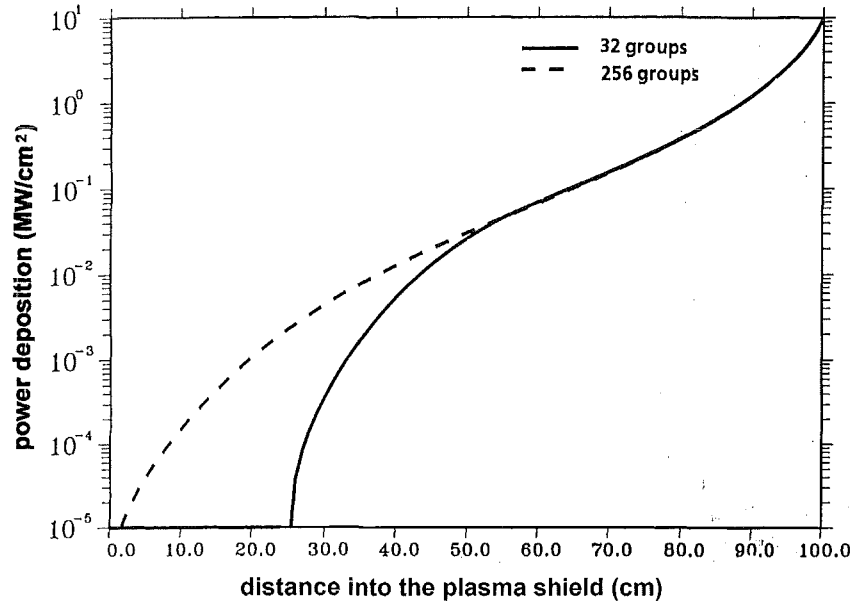

Fig. 31. Comparison of distribution of power density of Maxwellian electrons of temperature 10 keV in a carbon plasma of density of $5 \cdot 10^{18}$ cm^{-3} and temperature 3 eV calculated with FOREV-1. Initial power density is 10 MW/cm^2, the beam impact angle is 90°.

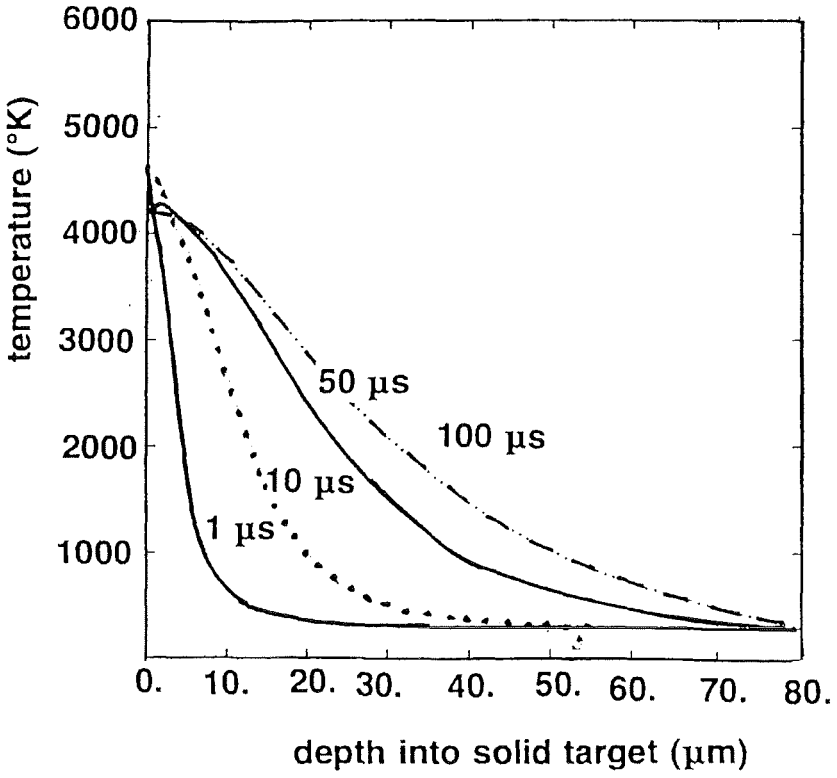

Fig. 32. Temperature distribution inside the bulk graphite target for 10 keV Maxwellian electrons of power density of 10 MW/cm^2 and impact angle 5° at different times.

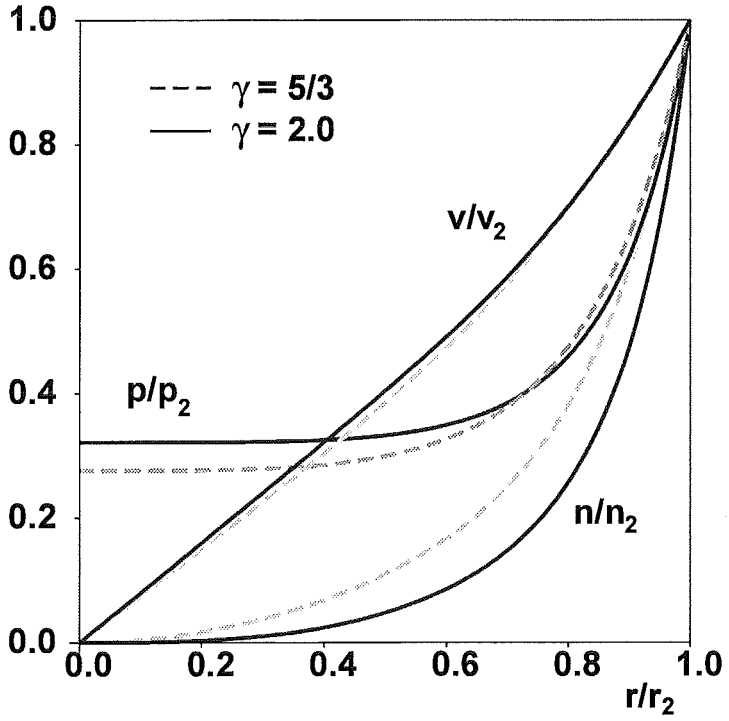

Fig.33. Analytical solution for the 2 dim hydrodynamic problem of large explosion for the quantities pressure P, density N and velocity v behind the shock wave front.

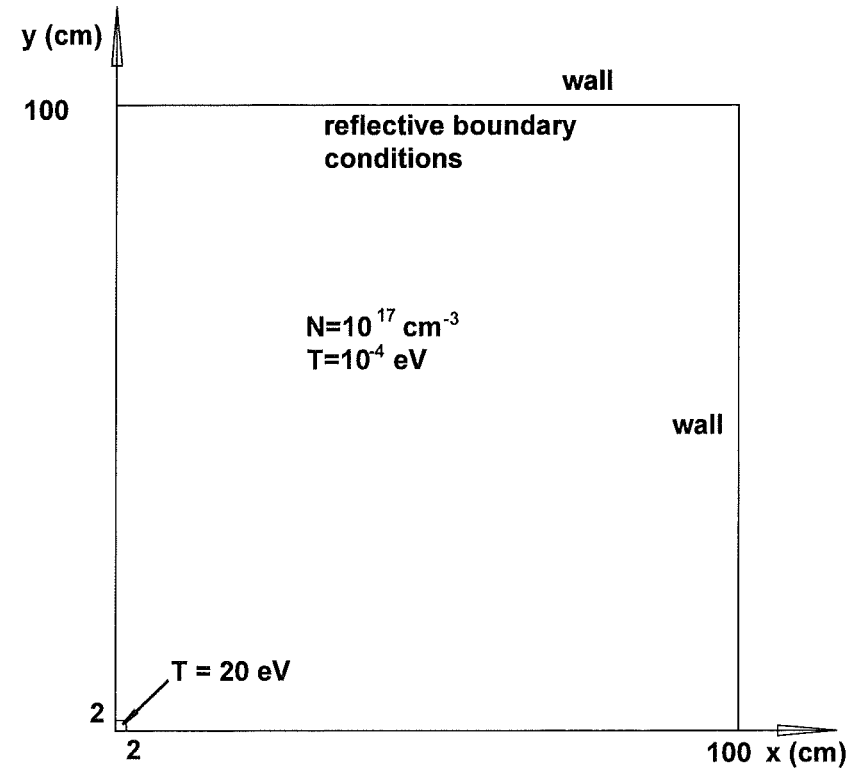

Fig. 34. Geometry used for the comparison of an analytical and a numerical solution for a shock wave problem.

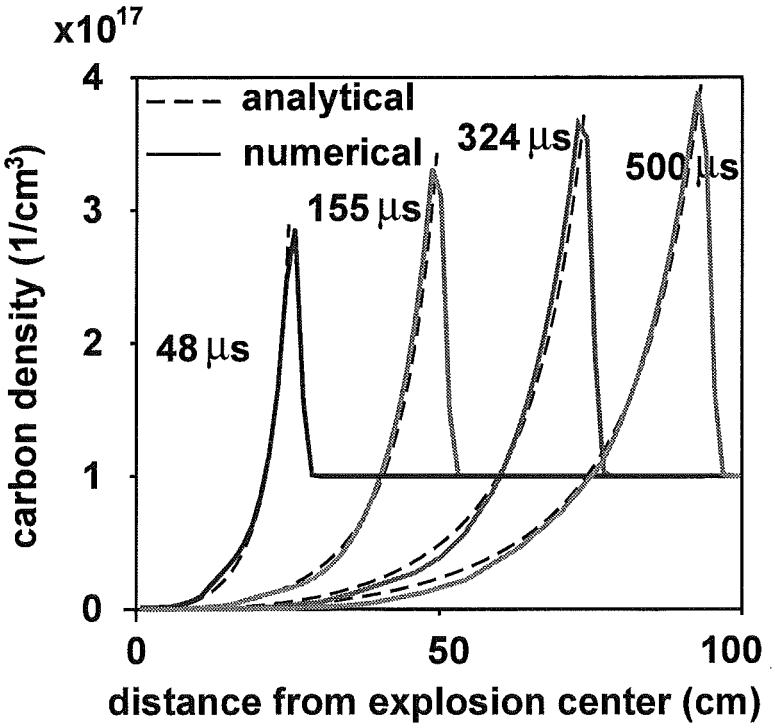

Fig. 35. Comparison of numerical and analytical results of evolution of plasma density for the 2 dim hydrodynamic problem of large explosion.

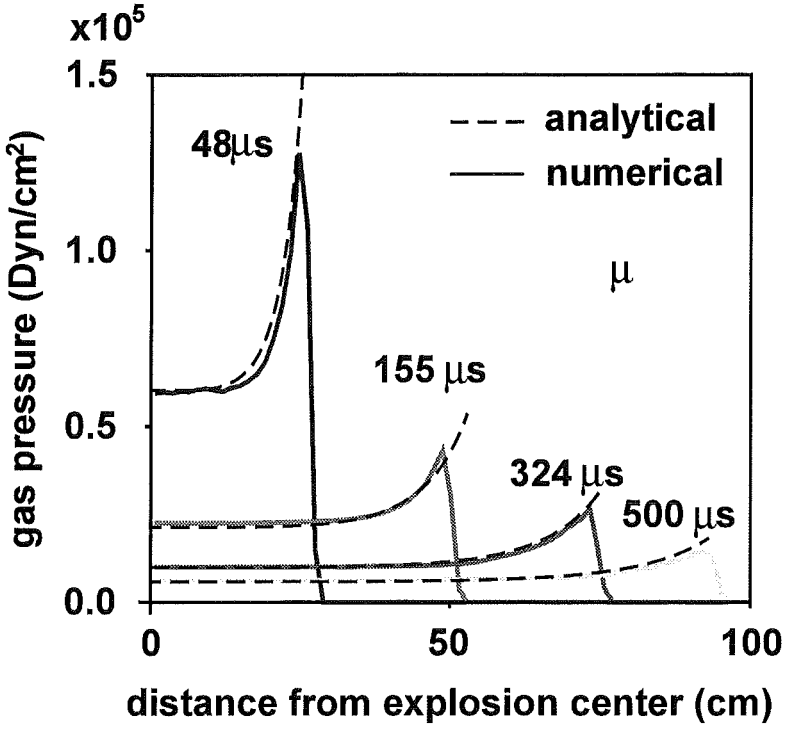

Fig.36. Comparison of numerical and analytical results of evolution of plasma velocity for the 2 dim hydrodynamic problem of large explosion.

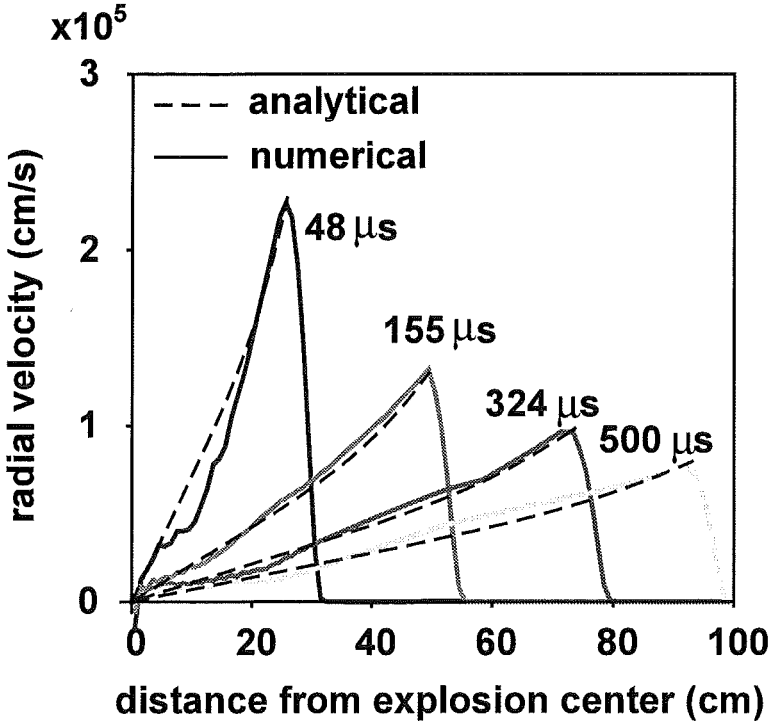

Fig.37. Comparison of numerical and analytical results of evolution of plasma velocity for the 2 dim hydrodynamic problem of large explosion.

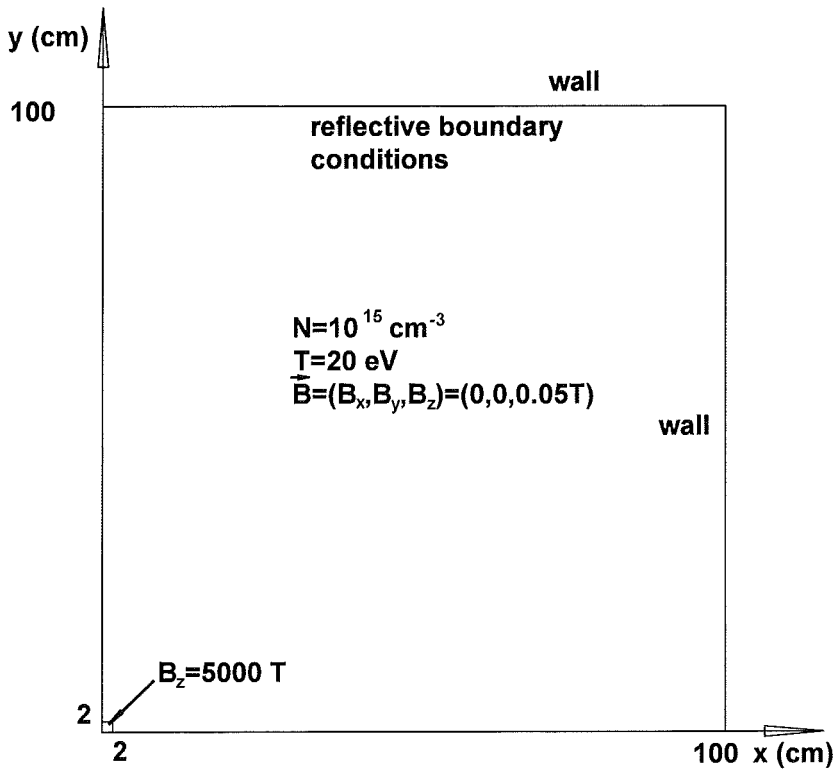

Fig. 38. Geometry used for comparison of analytical and numerical results for a MHD problem.

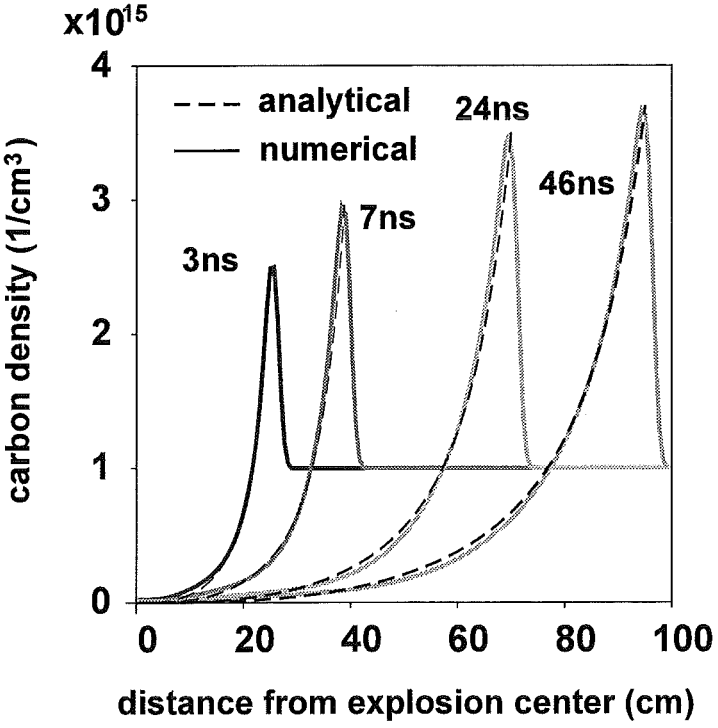

Fig.39. Comparison of numerical and analytical results for the 2 dim MHD problem of large explosion with frozen in magnetic field.

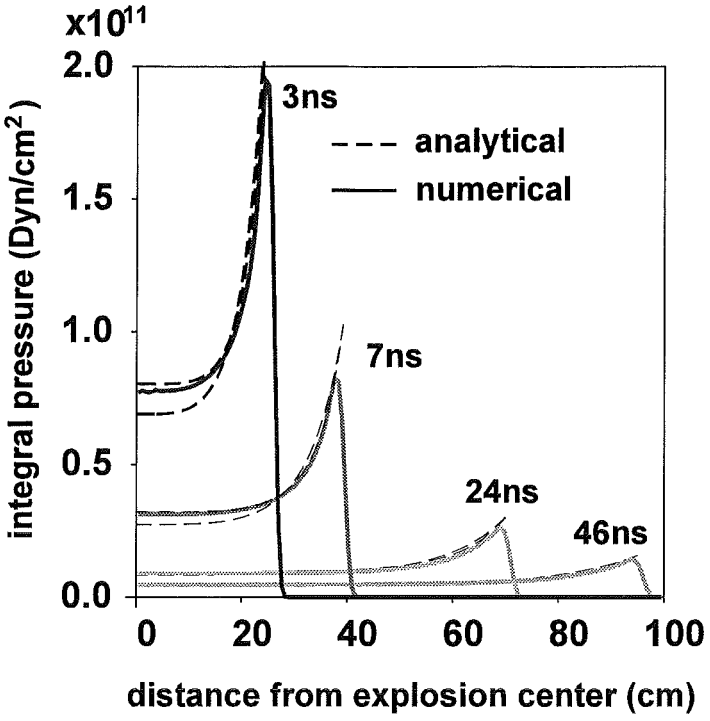

Fig.40. Comparison of numerical and analytical results for the 2 dim MHD problem of large explosion with frozen in magnetic field.

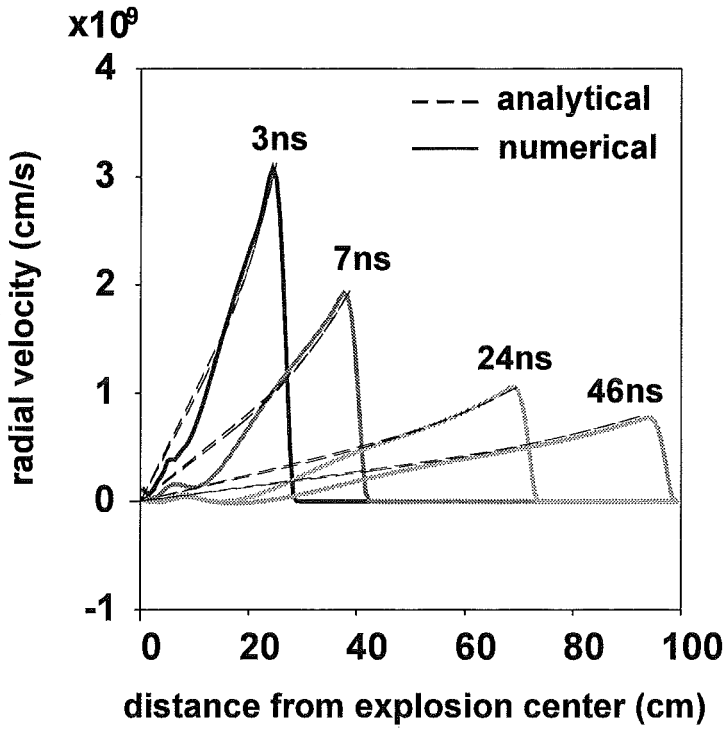

Fig.41. Comparison of numerical and analytical results for the 2 dim MHD problem of large explosion with frozen in magnetic field.

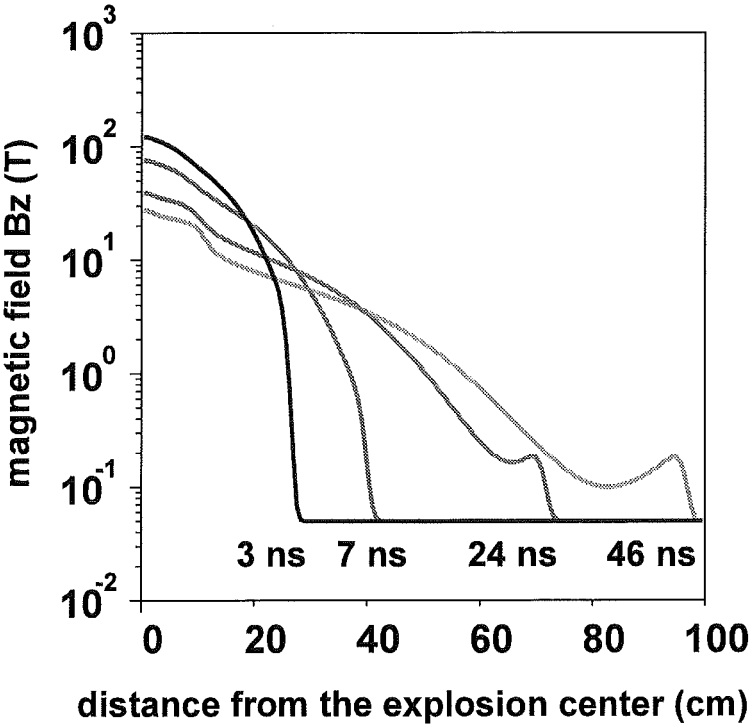

Fig.42a. Calculated time evolution of the magnetic field in the 2 dim MHD problem

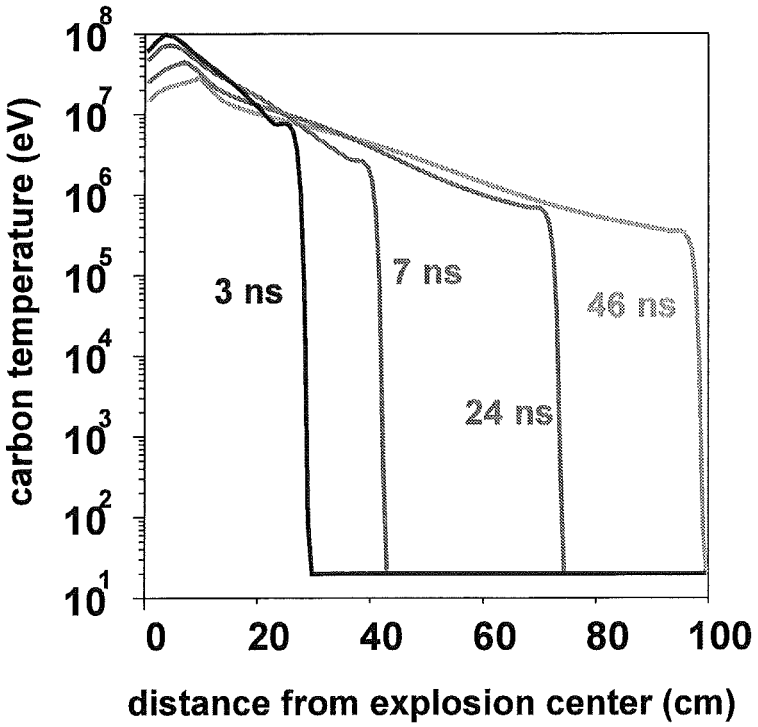

Fig.42b. Temperature evolution for the 2 dim MHD problem with frozen in magnetic field.

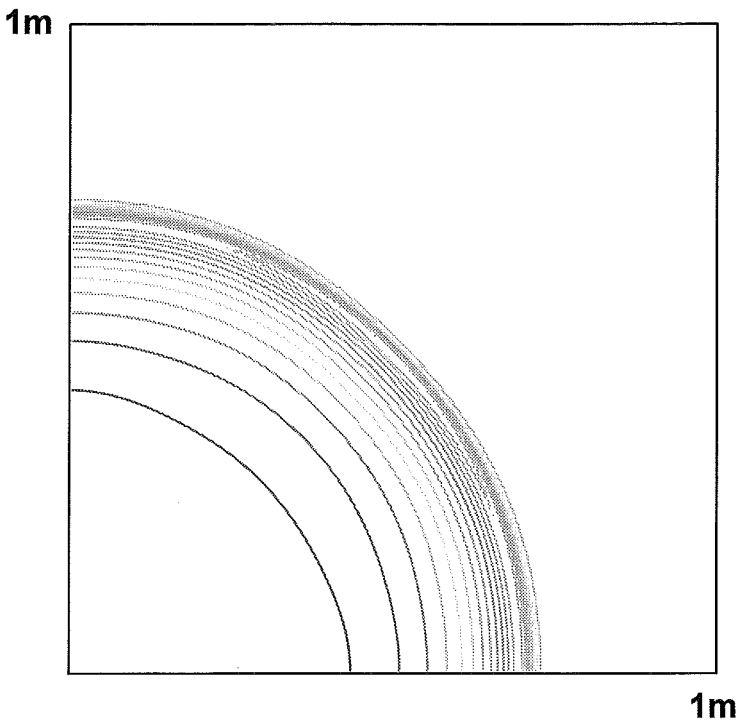

Fig.43. 2 dim contour plot of carbon density at 24 ns demonstrating the quality of the circular shock wave simulation on rectangular mesh.

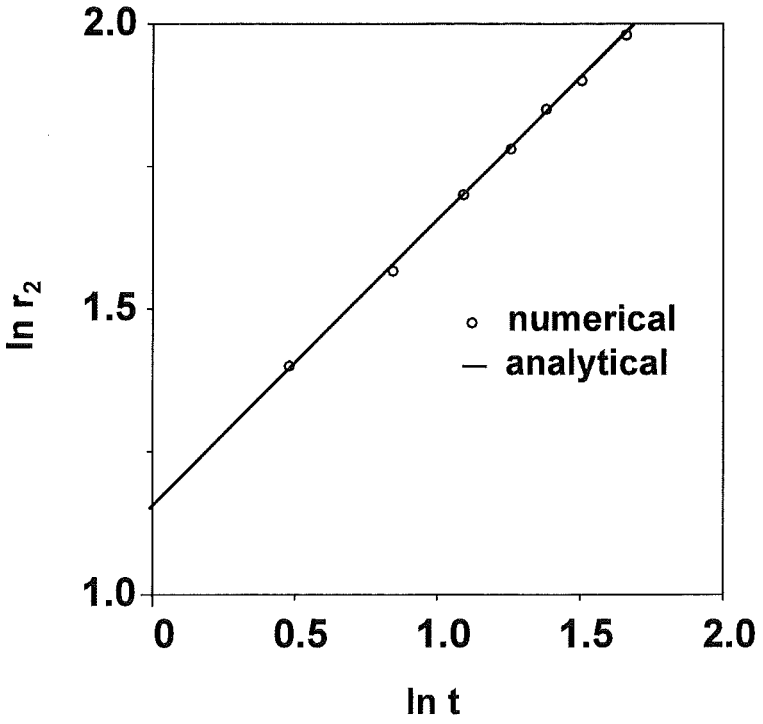

Fig.44. Comparison of time dependent front position of the shock wave for the 2 dim MHD problem with frozen in magnetic field.

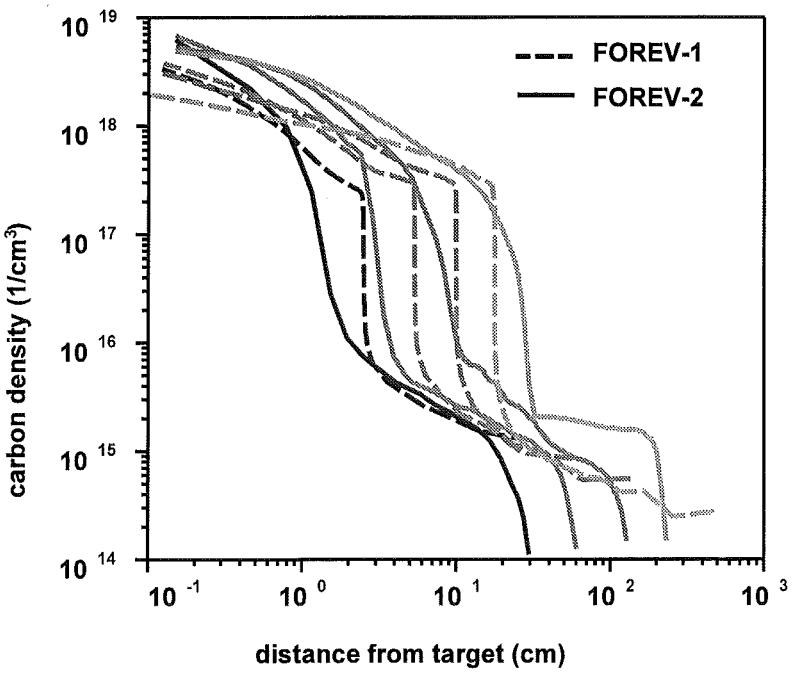

Fig.45. Comparison of carbon plasma density profiles from FOREV-1 and FOREV-2 at 50, 100, 200 and 500 μs for a horizontal target. Power density along the inclined magnetic field lines is 10 MW/cm^2. Impact energy of the hot plasma is 10 kev.

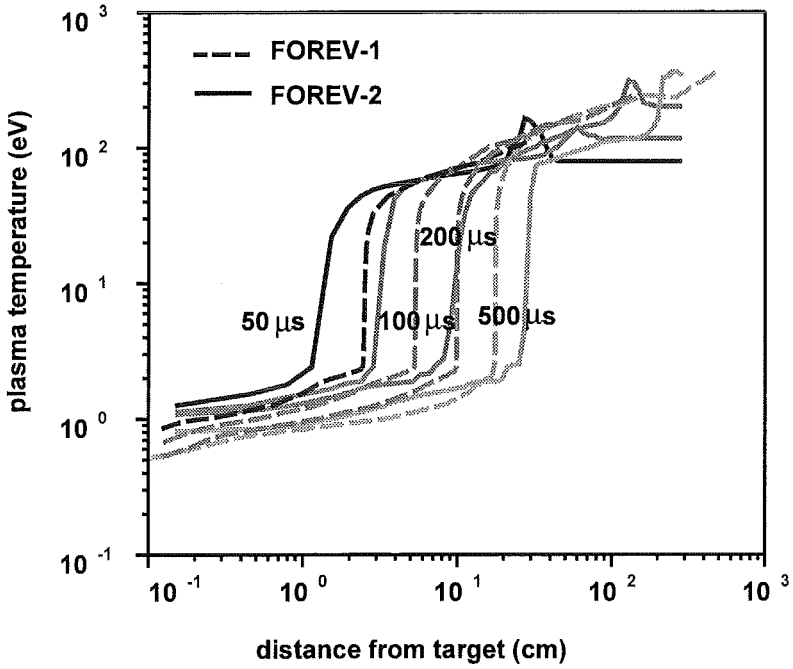

Fig.46. Comparison of carbon plasma temperature profiles from FOREV-1 and FOREV-2 at 50, 100, 200 and 500 μs for a horizontal target. Power density along the inclined magnetic field lines is 10 MW/cm^2. Impact energy of the hot plasma is 10 kev.

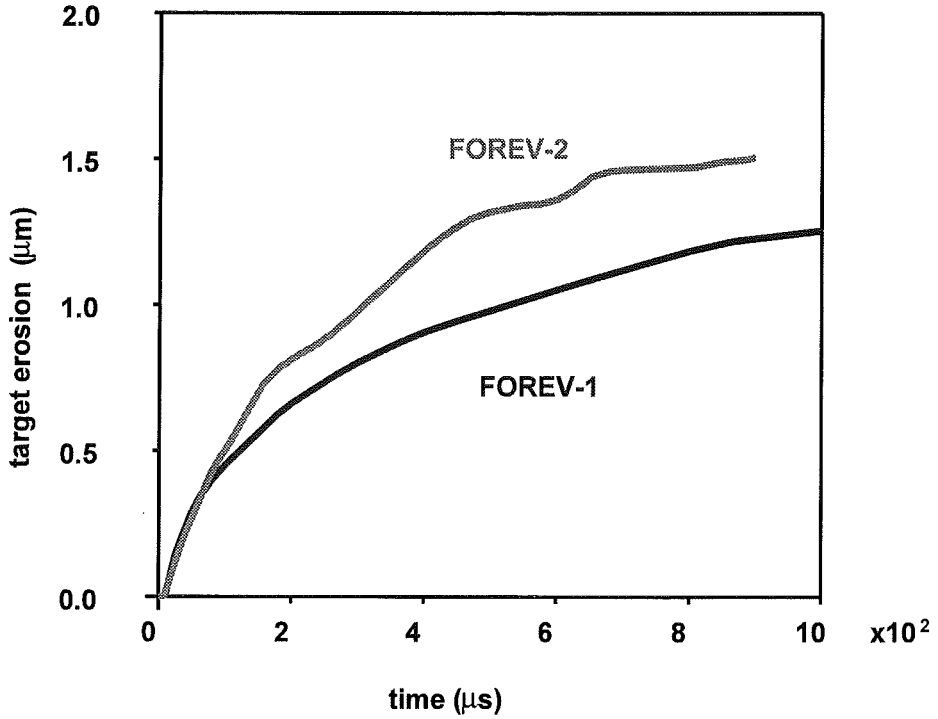

Fig.47. Comparison of time dependence of erosion from FOREV-1 and FOREV-2. Power density is 10 MW/cm^2. Impact energy of the hot plasma is 10 kev.

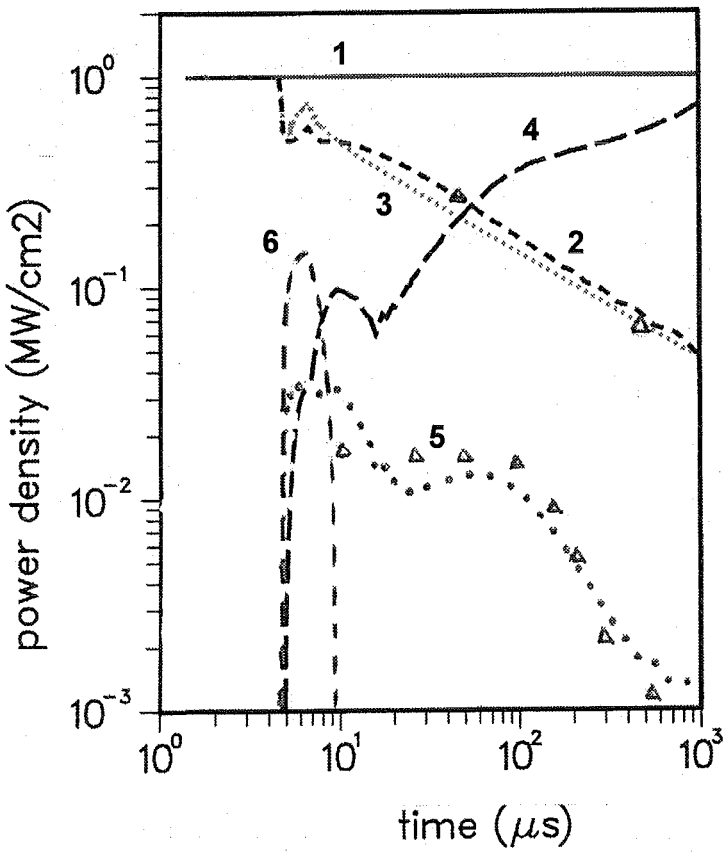

1 – power density of the hot plasma
2 – target heating by hot plasma
3 – heat flux into the target
4 – total lateral radiation
5 – radiation flux onto target
6 – electron heat conduction flux
Δ – results from FOREV-2

Fig.48. Time evolution of target heat fluxes for a horizontal graphite target. Constant power density profile in y direction, power density along the inclined magnetic field lines is 10 MW/cm^2. Impact energy of the hot plasma is 10 kev

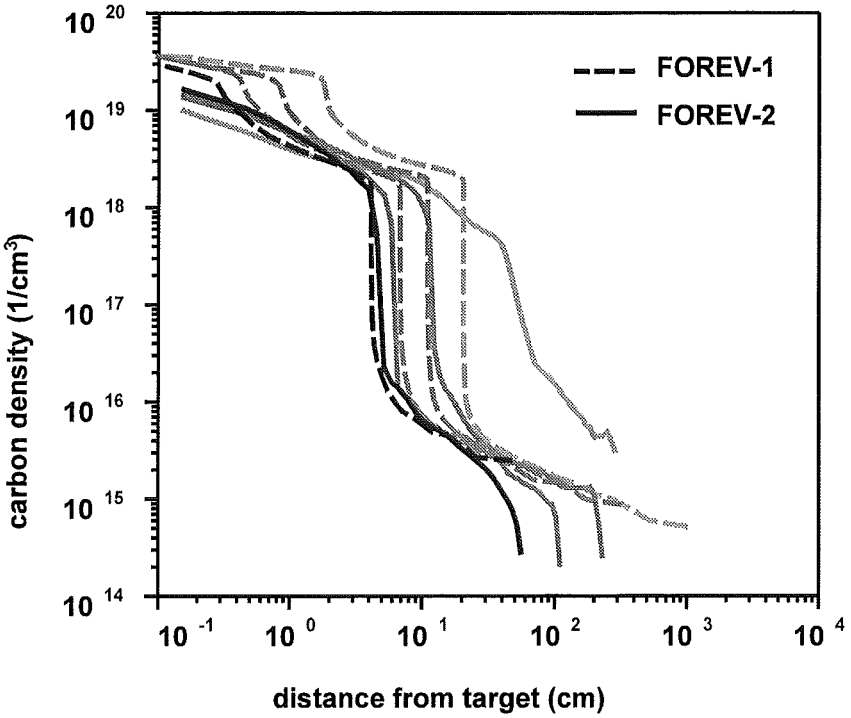

Fig.49. Comparison of plasma density profiles from FOREV-1 and FOREV-2 At 50, 100, 200 and 500 μs for a horizontal target. The power density along the inclined magnetic field lines is 100 MW/cm^2. Impact energy of the hot plasma is 10 kev.

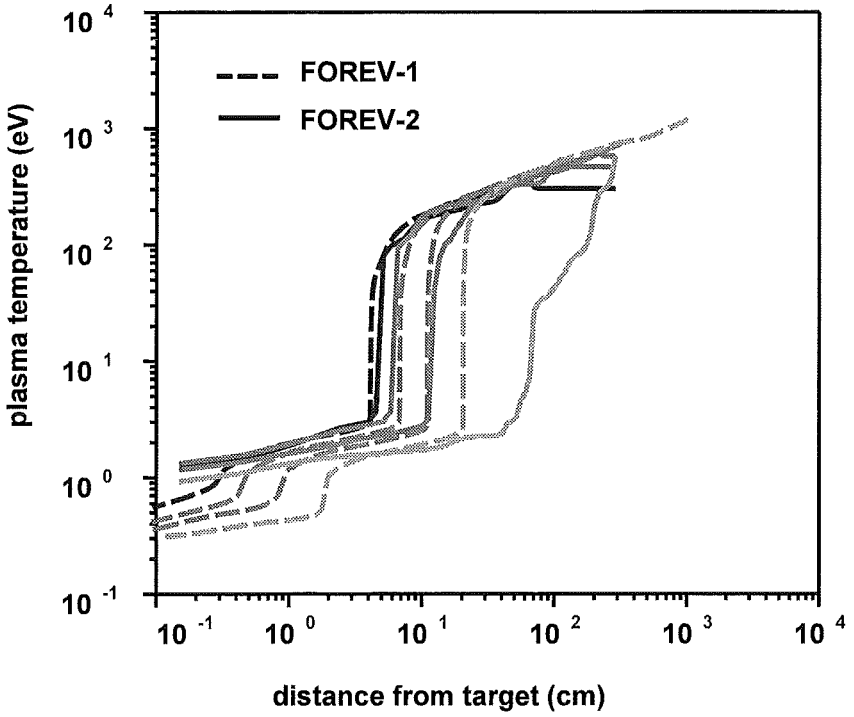

Fig.50. Comparison of carbon plasma temperature profiles from FOREV-1 and FOREV-2 at 50, 100, 200 and 500 μs for a horizontal target. Power density along the inclined magnetic field lines is 100 MW/cm^2. Impact energy of the hot plasma is 10 kev.

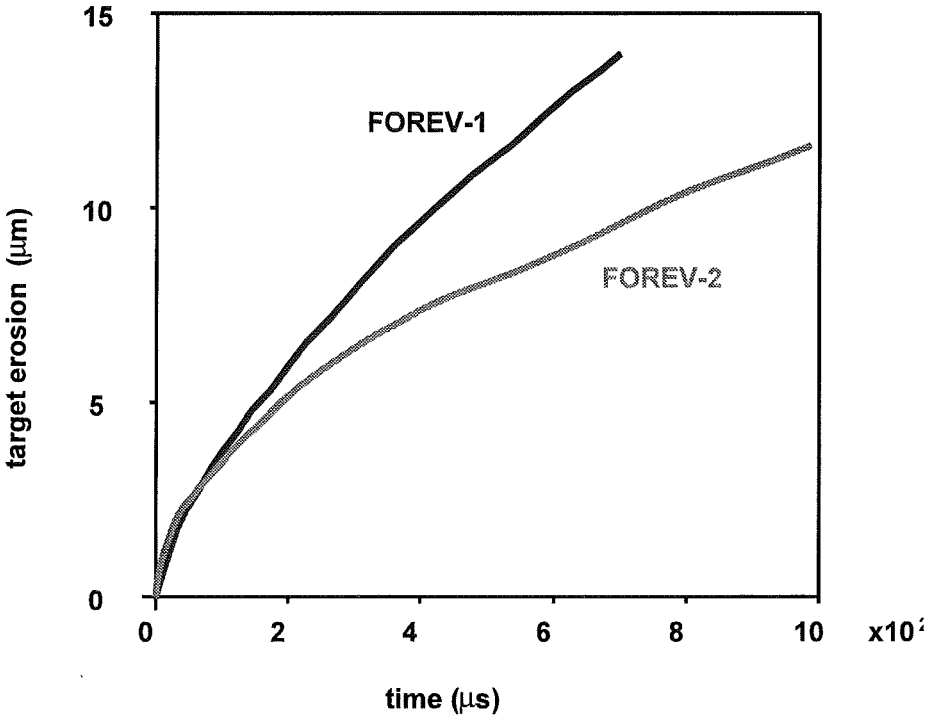

Fig.51. Comparison of time dependence of erosion from FOREV-1 and FOREV-2. Power density is 100 MW/cm^2.

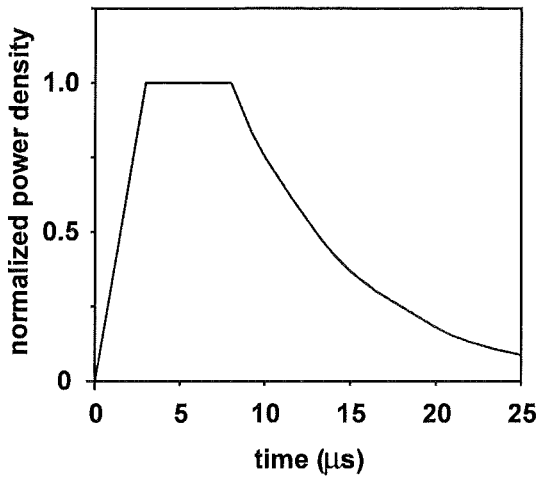

Fig.52a. Time dependent peak power density as used in the simulation calculations for the MK-200 CUSP facility. Peak power densities up to 42 MW/cm^2 are achieved. Guiding magnetic field is 3.3 T.

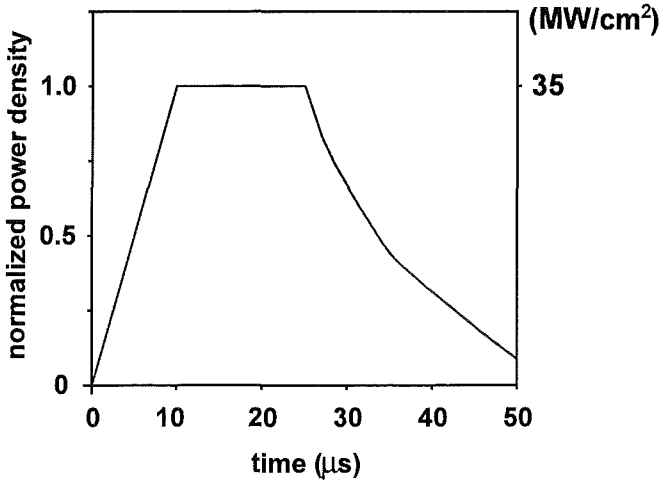

Fig.52b. Time dependent peak power density as used in the simulation calculations for the MK-200 UG facility. Peak power densities up to 35 MW/cm^2. Guiding magnetic field is 2 T.

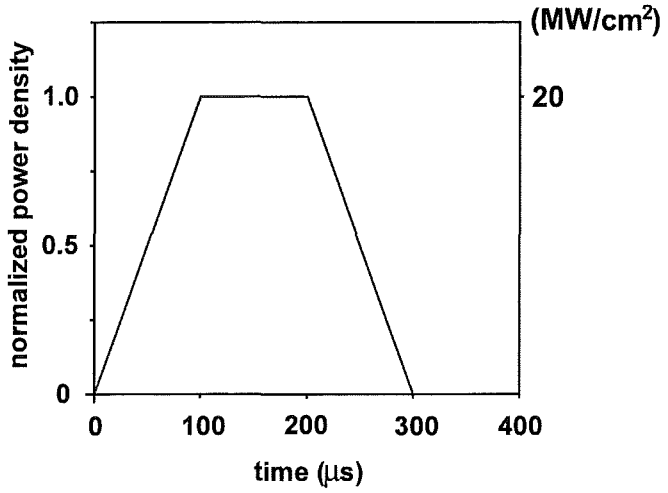

Fig.52c. Time dependent peak power density as used in the simulation calculations for the QSPA facility. Peak power density is 20 MW/cm^2. Guiding magnetic field is 0.55 T.

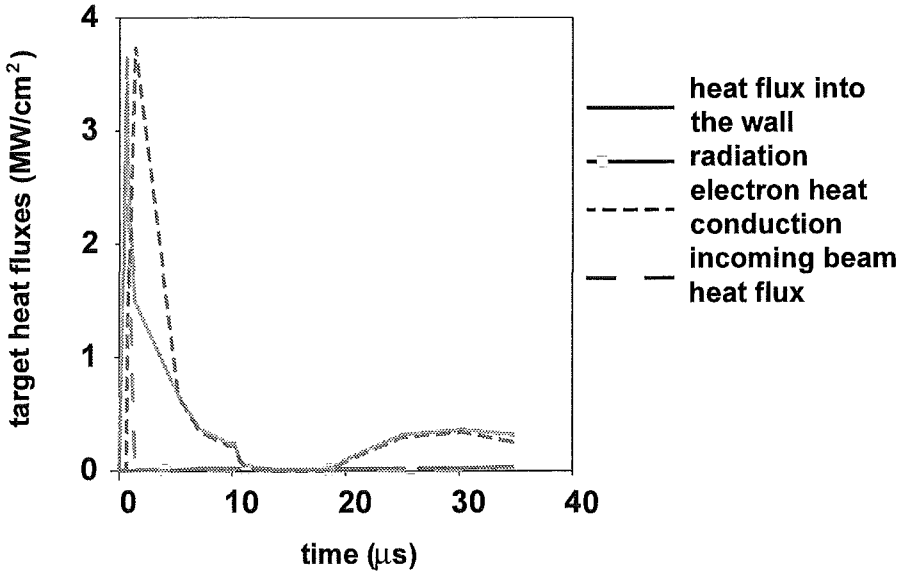

Fig. 53. Calculated target heat fluxes for a perpendicular graphite target at the 2MK-200 CUSP facility.

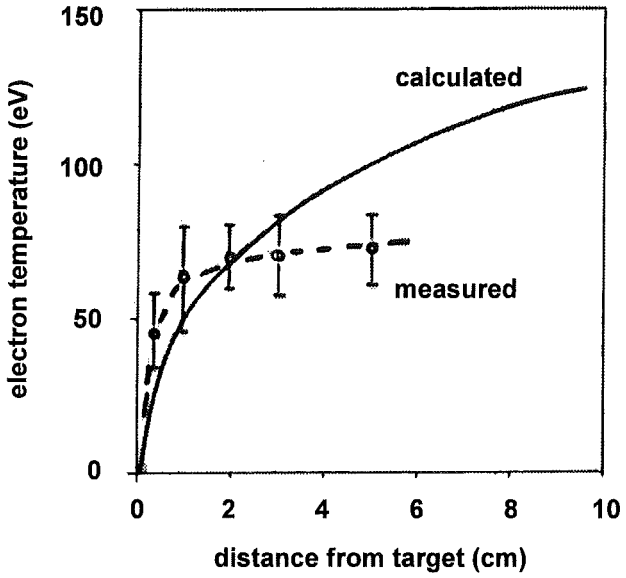

Fig.54. Comparison of measured and calculated electron temperature profiles in a carbon plasma shield at 10 μs at the 2MK-200 CUSP facility. Peak power density is 18 MW/cm^2.

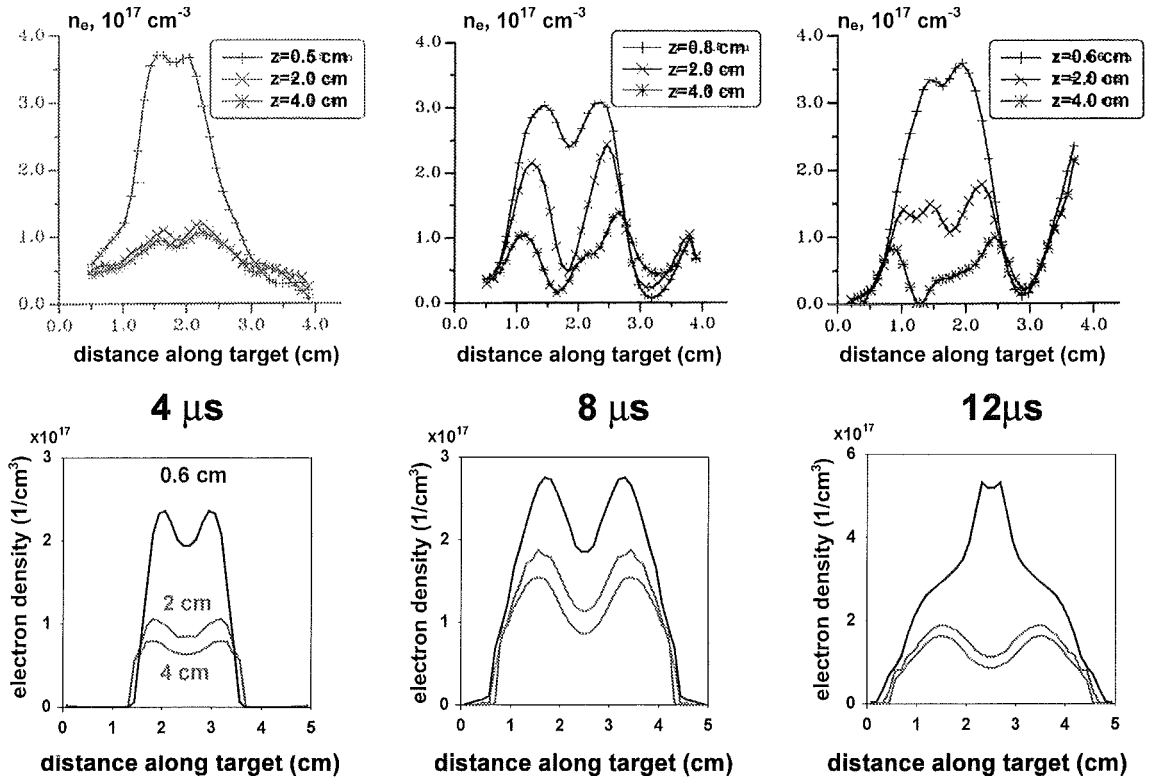

Fig.55. Comparison of measured (above) and calculated (below) electron density profiles in a carbon plasma shield at different times and distances from the perpendicular target at the MK-200 CUSP facility. For the calculation a Gaussian power density profile with peak power density of 42 MW/cm^2 was used for the hot plasma. The guiding magnetic field perpendicular to the target surface is 3.3T. the magnetic field at the target was assumed to be frozen in.

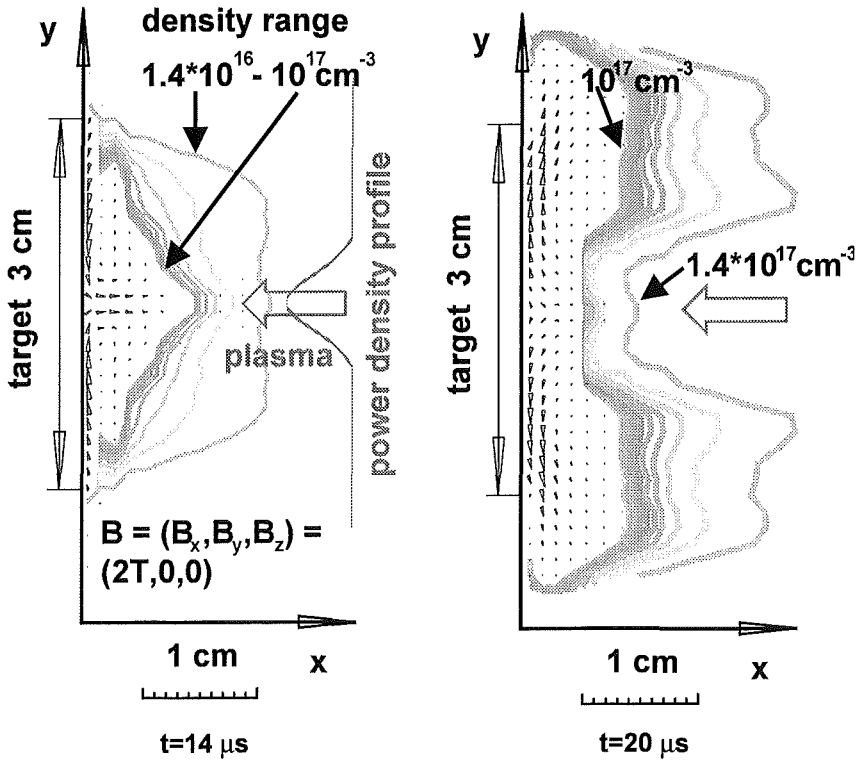

Fig.56. Contour plot of plasma density and plasma flow (Γ=nv, arrows) in a carbon plasma shield. Perpendicular graphite target, Gaussian power density profile with peak value of 20 MW/cm^2. The guiding magnetic field perpendicular to the target surface is 2T

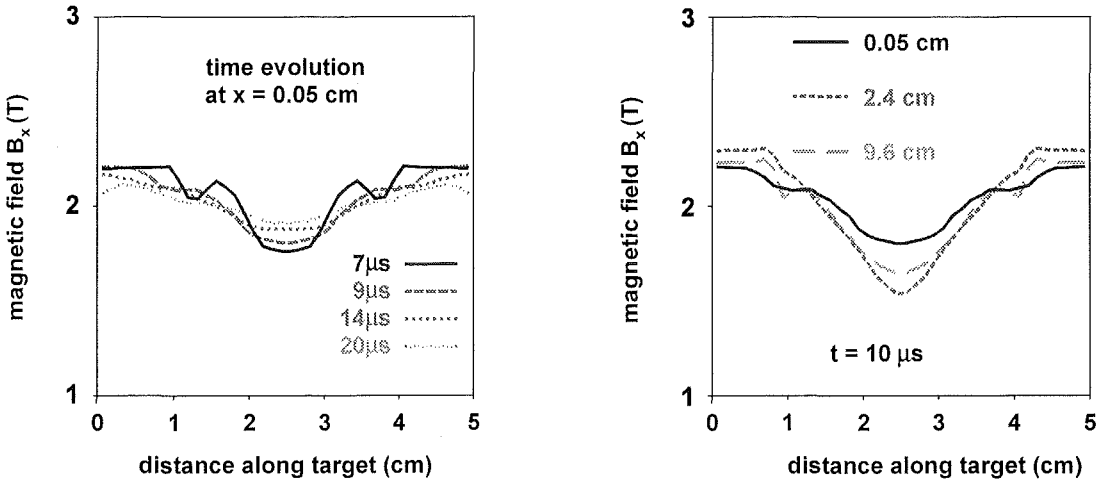

Fig.57a. Time and space dependent change of B_x by the evolving carbon plasma shield for different distances from a perpendicular graphite target.

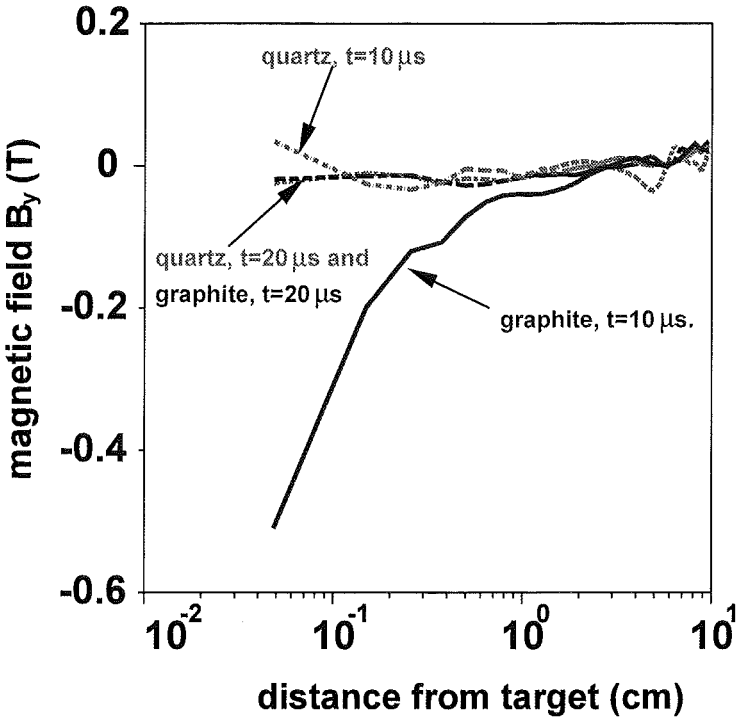

Fig.57b. B_y component of magnetic field below the separatrix in carbon and quartz plasma shield at two different times.

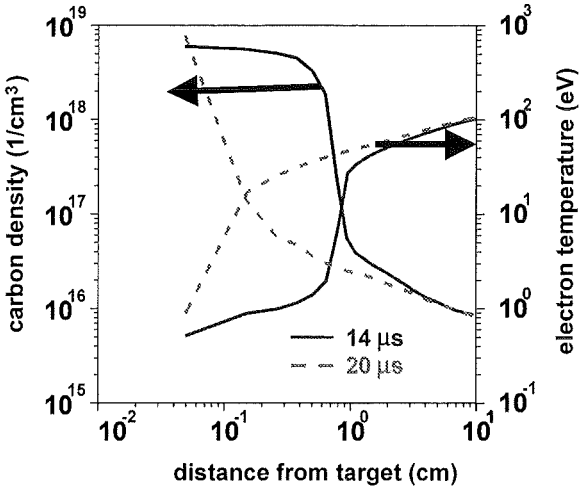

Fig.58. Plasma density and electron temperature profile at two different times in a carbon plasma shield along the separatrix for a perpendicular target. Gaussian power density profile with peak value 20 MW/cm^2..

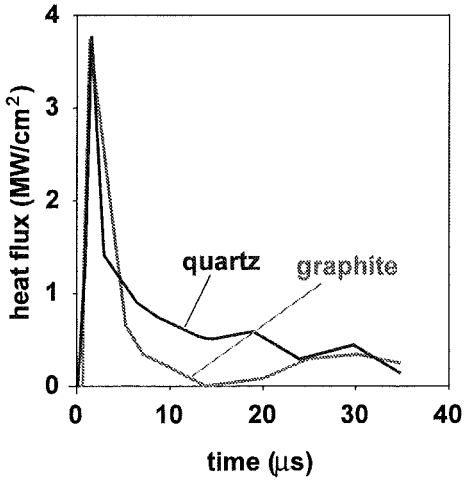

Fig.59. Comparison of electron heat conduction fluxes at position of separatrix strike point for perpendicular graphite and quartz target. Gaussian power density profile with peak value 20 MW/cm^2. FWHM=0.8cm.

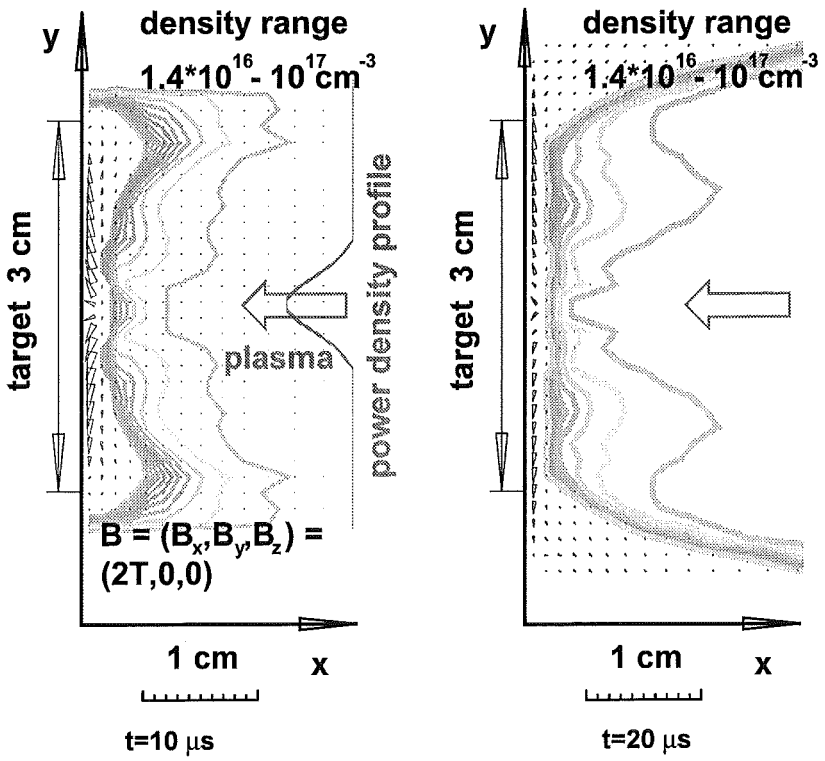

Fig.60. Contour plot of plasma density and plasma flow (Γ=nv, arrows) in an quartz plasma shield for perpendicular quartz target. Gaussian power density profile with peak value of 20 MW/cm^2. Guiding magnetic field is 2T.

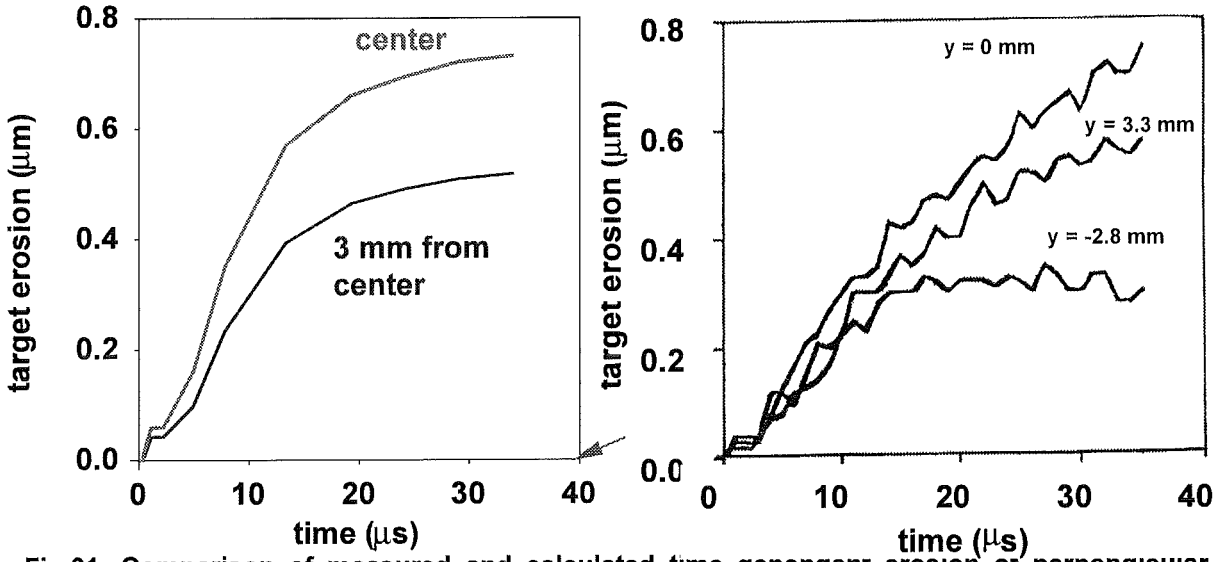

Fig.61. Comparison of measured and calculated time dependent erosion of perpendicular quartz at different target positions. Peak power density is 20 MW/cm^2.

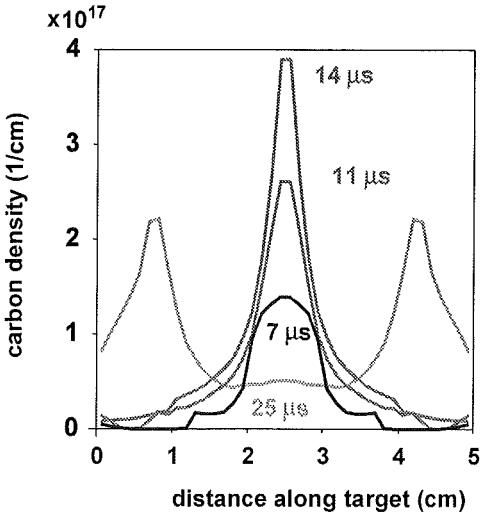

Fig.62. Distribution of carbon mass density in the plasma shield for perpendicular graphite target. Transparent boundary conditions at the side walls. Peak power density is 20 MW/cm^2.

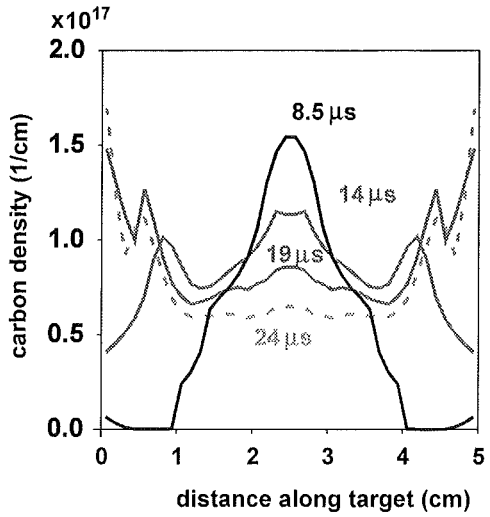

Fig.63. Distribution of quartz mass density in the plasma shield. for perpendicular quartz target. Transparent boundary conditions at the side walls. Transparent boundary conditions at the side walls. Peak power density is 20 MW/cm^2.

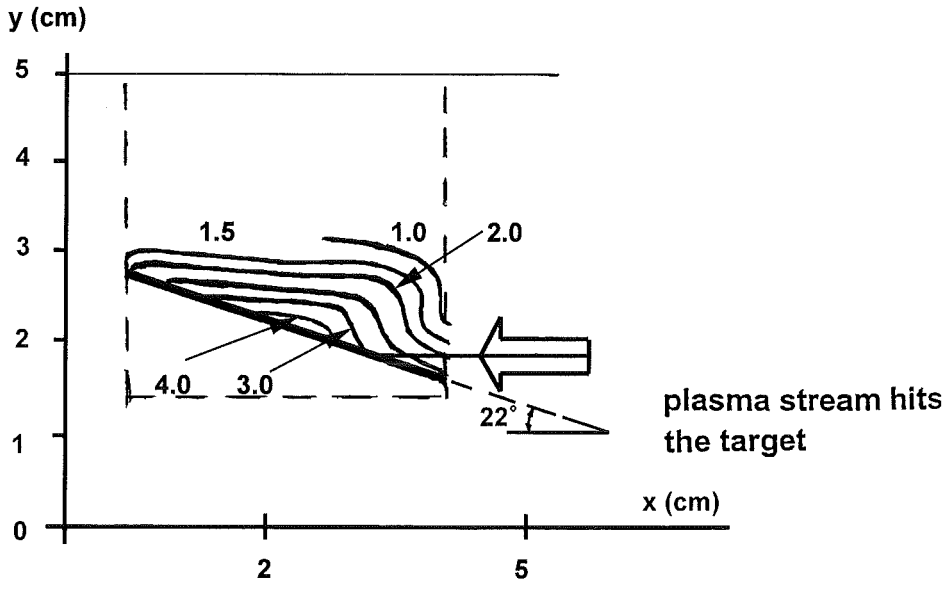

Fig.64a. Electron density distribution ($\times 10^{17}$ cm^{-3}) in a carbon plasma shield at 10 μs for a vertical graphite target. Experimental results from the MK-200 CUSP facility. Peak power density along the separatrix is 42 MW/cm^2.

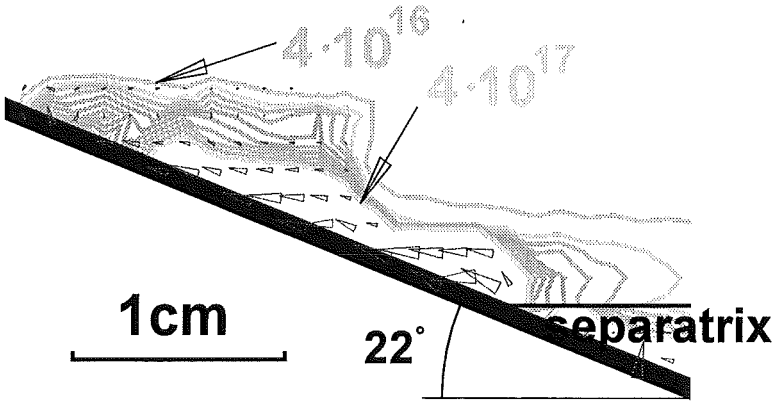

Fig.64b. Calculated 2 dim contour plot of electron density and plasma flow in a carbon plasma shield for vertical graphite target. Electron density range $4 \cdot 10^{16} \div 4 \cdot 10^{17}$. Gaussian power density profile with peak power density of 42 MW/cm^2 at the separatrix.

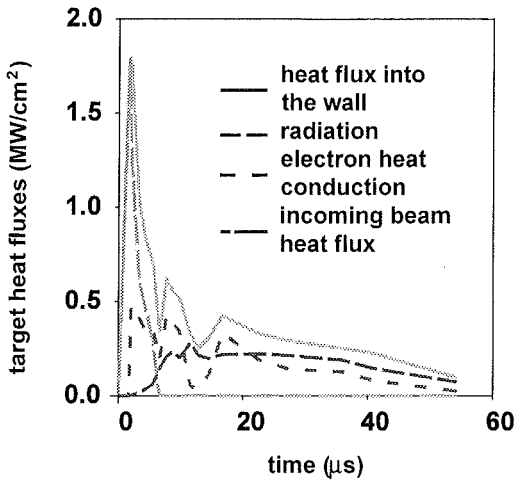

Fig. 65. Calculated target heat fluxes for a tilted graphite target at the MK-200 UG facility. Tilting angle 20°, Gaussian power density profile with peak power density of 35 MW/cm^2 at the separatrix.

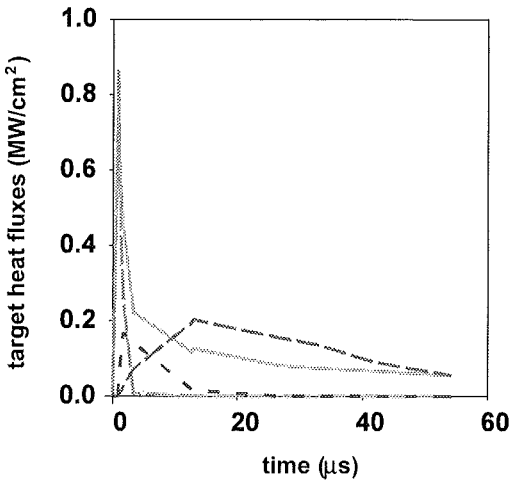

Fig. 66. Calculated target heat fluxes for a tilted quartz target at the MK-200 UG facility. Tilting angle 20°, Gaussian power density profile with peak power density of 35 MW/cm^2 along the separatrix.

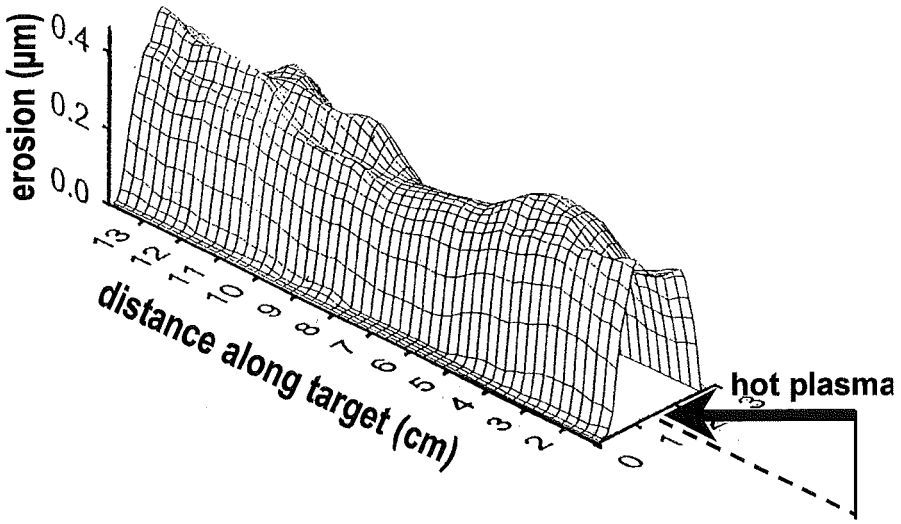

Fig. 67a. Erosion pattern for a tilted quartz target measured at the MK-200 UG facility.

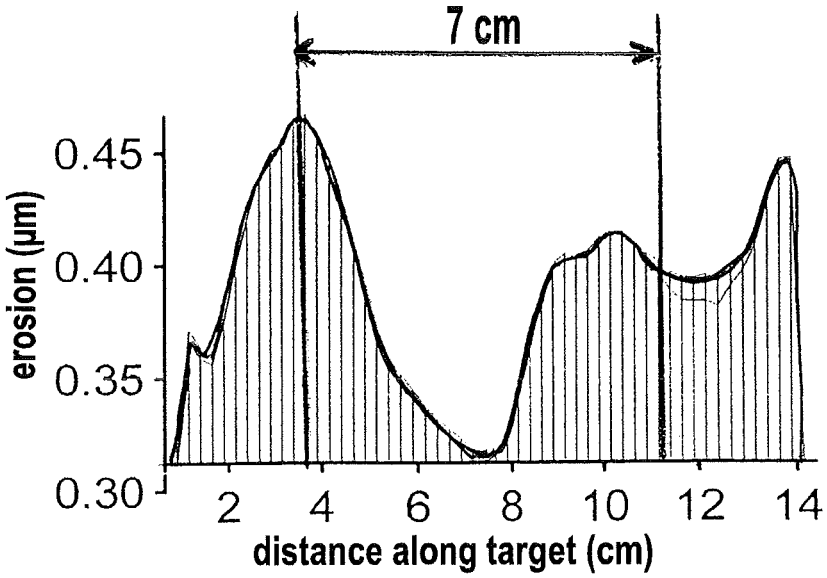

Fig. 67b. Measured erosion profile along the flow direction of the hot plasma. Modulation wavelength is about 7 cm.

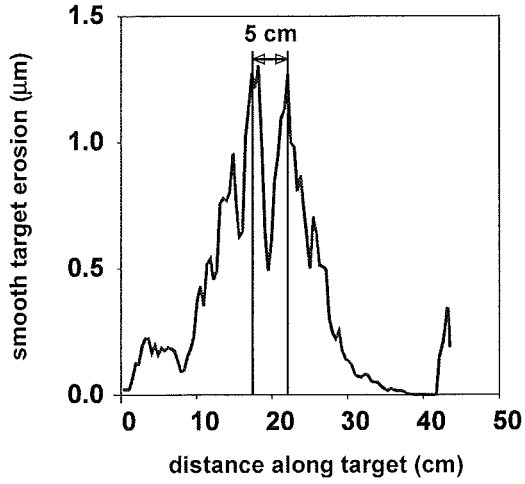

Fig. 67c. Calculated erosion pattern for a tilted quartz target. Modulation length is about 5 cm.

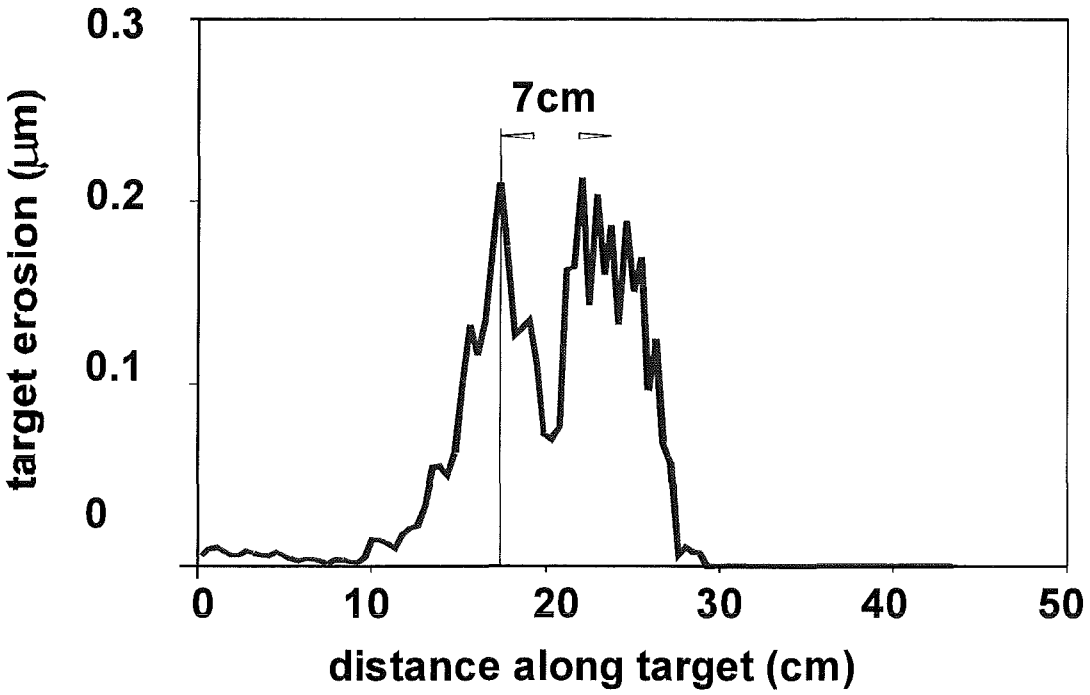

Fig. 68. Calculated erosion profile for a tilted graphite target for the MK-200 UG conditions.. Modulation wavelength is about 7 cm.

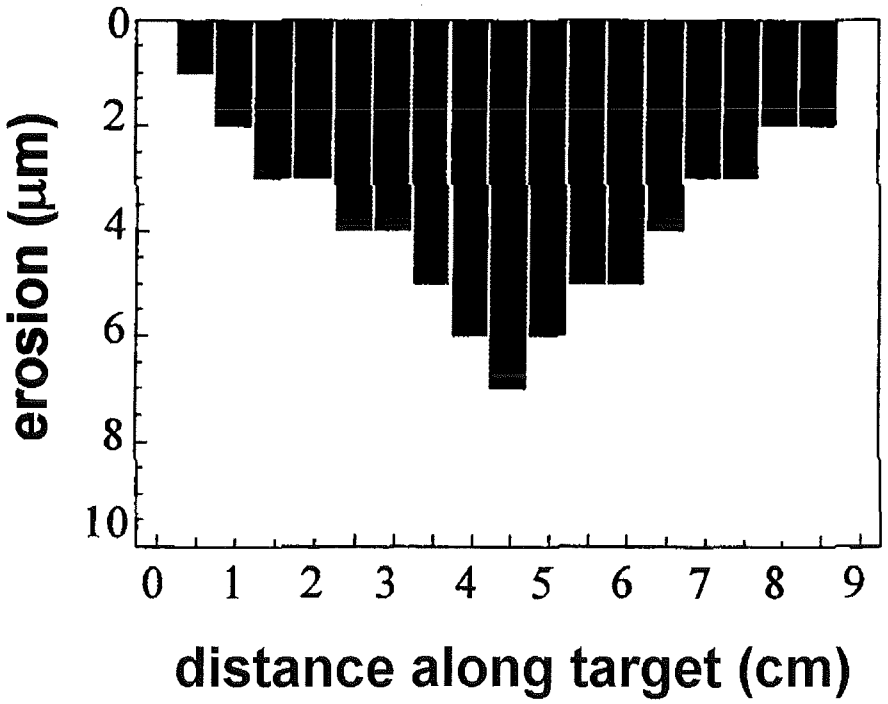

Fig. 69a. Erosion profile for a perpendicular polished quartz target measured at QSPA facility. Gaussian power density profile with peak power density 20 MW/cm^2. The guiding magnetic field is 0.55T

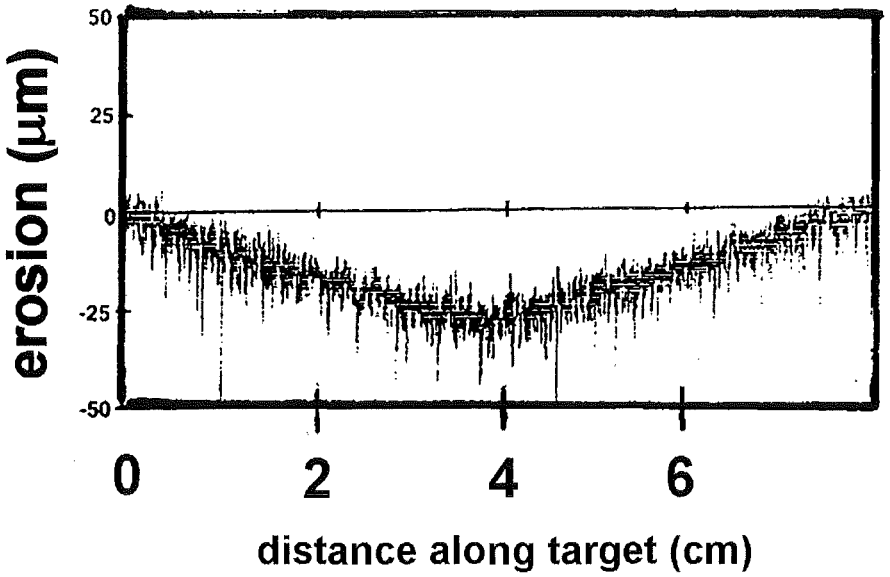

Fig. 69b. Erosion profile for a perpendicular MPG graphite target after 15 irradiations measured at QSPA facility. Gaussian power density profile with peak power density of 20 MW/cm^2. The guiding magnetic field is 0.55T

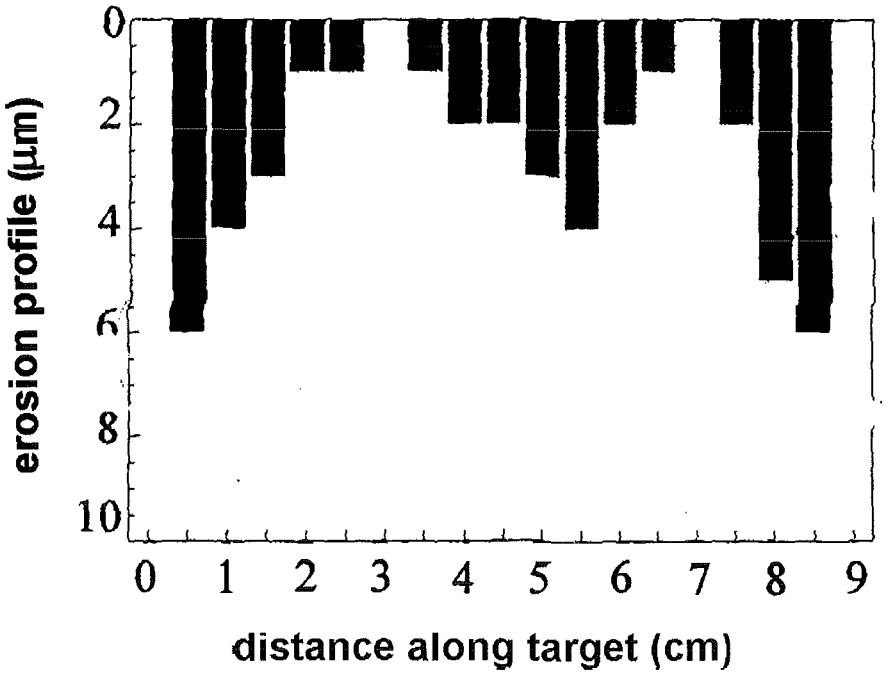

Fig. 69c. Erosion profile for a tilted quartz target, tilting angle is 20° measured at QSPA facility. Gaussian power density profile with peak power density 20 MW/cm^2 along the guiding magnetic field lines.

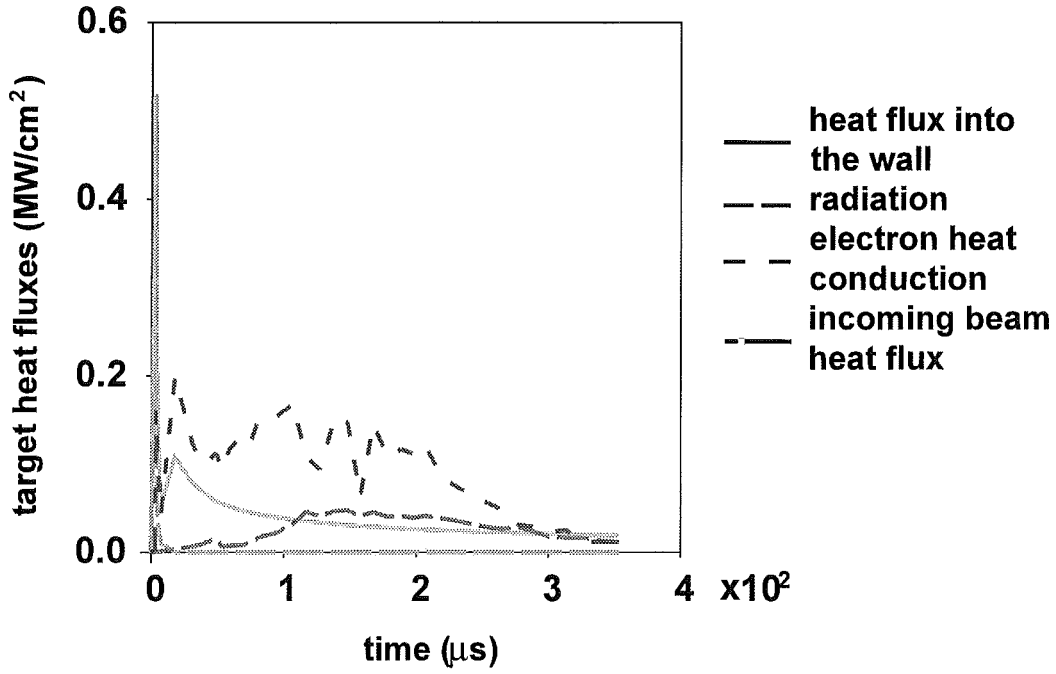

Fig. 70a. Calculated time evolution of target heat fluxes at the separatrix position for a perpendicular quartz target measured at QSPA facility. Gaussian power density profile with peak power density of the impacting hot plasma was 20 MW/cm^2.

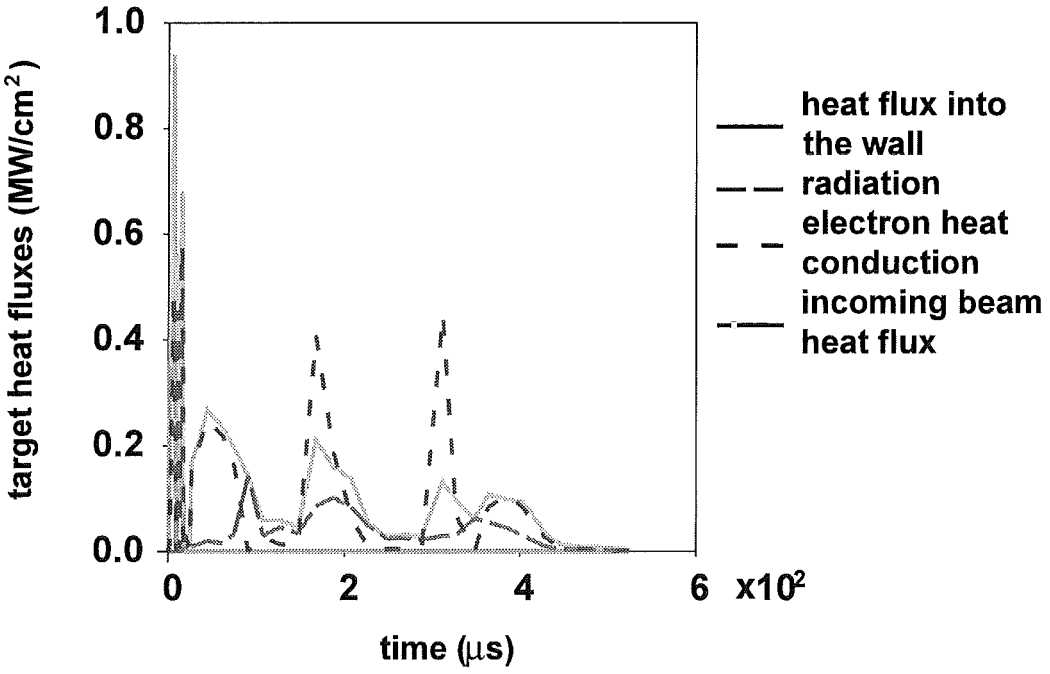

Fig. 70b. Calculated time evolution of target heat fluxes at the separatrix position for a perpendicular graphite target measured at QSPA facility. Gaussian power density profile with peak power density of the impacting hot plasma was 20 MW/cm^2.

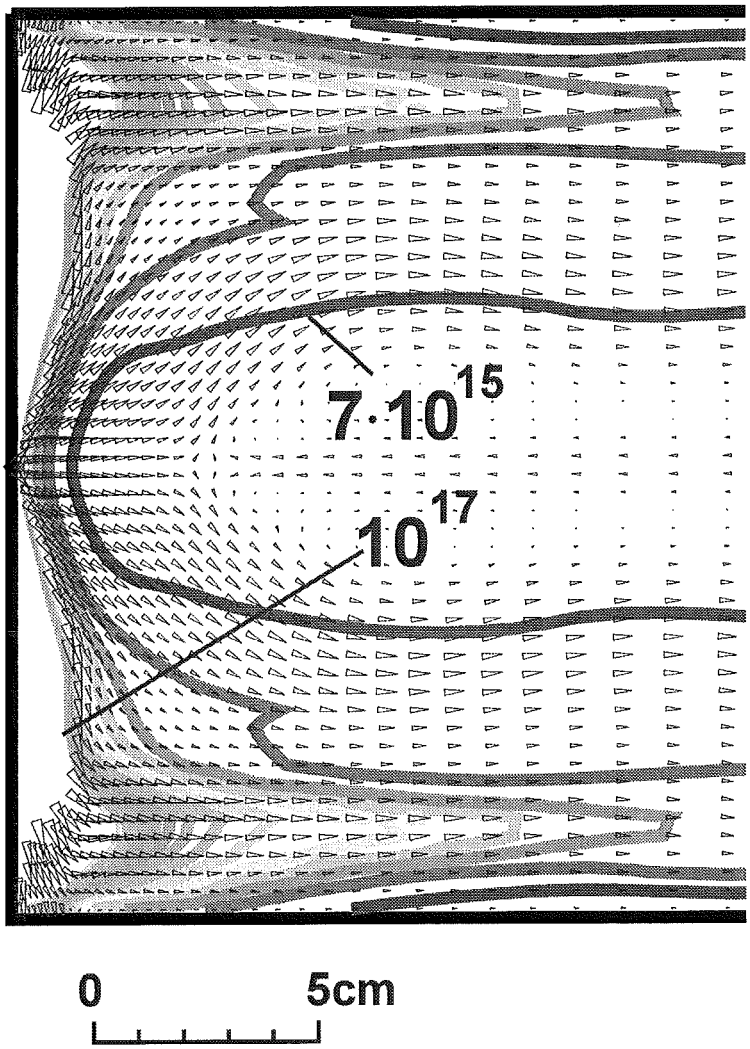

Fig. 71. Calculated 2 dim plasma density contour lines and plasma flow pattern (Γ=nv, arrows) in a quartz plasma shield for a perpendicular quartz target at 103 μs at the QSPA facility.

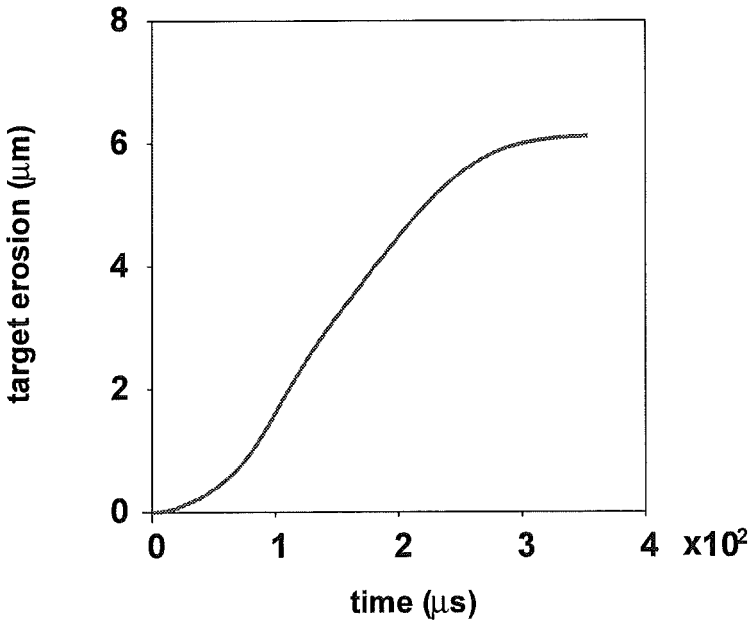

Fig. 72. Calculated time dependent peak erosion for a perpendicular quartz target at the position of the separatrix strike point for the QSPA facility.

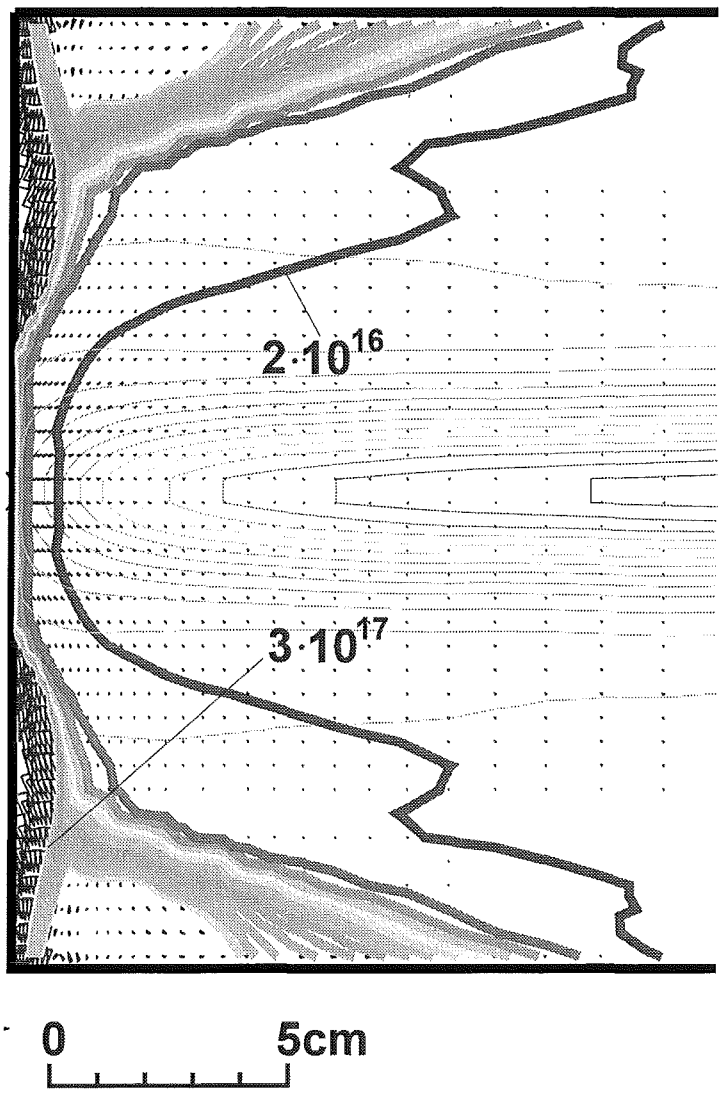

Fig. 73. Calculated 2 dim plasma density contour lines and plasma flow pattern (Γ=nv, arrows) in a carbon plasma shield for a perpendicular graphite target at 167 μs at the QSPA facility.

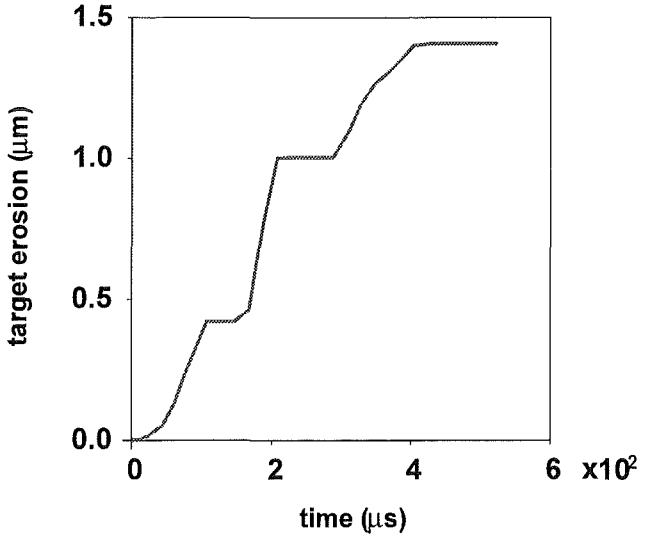

Fig. 74. Calculated time dependent peak erosion for a perpendicular graphite target for the QSPA facility.

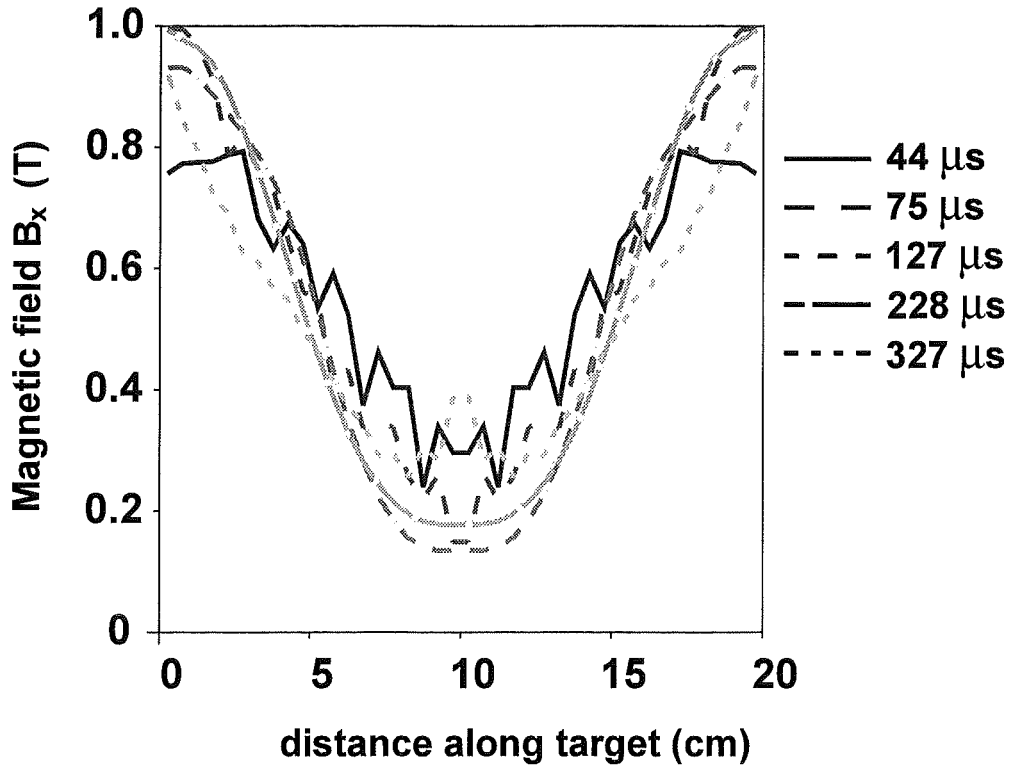

Fig. 75. Time dependent behavior of the guiding magnetic field B_x with B_{x0}=0.55 T close to the target for a carbon plasma shield with perpendicular graphite target.

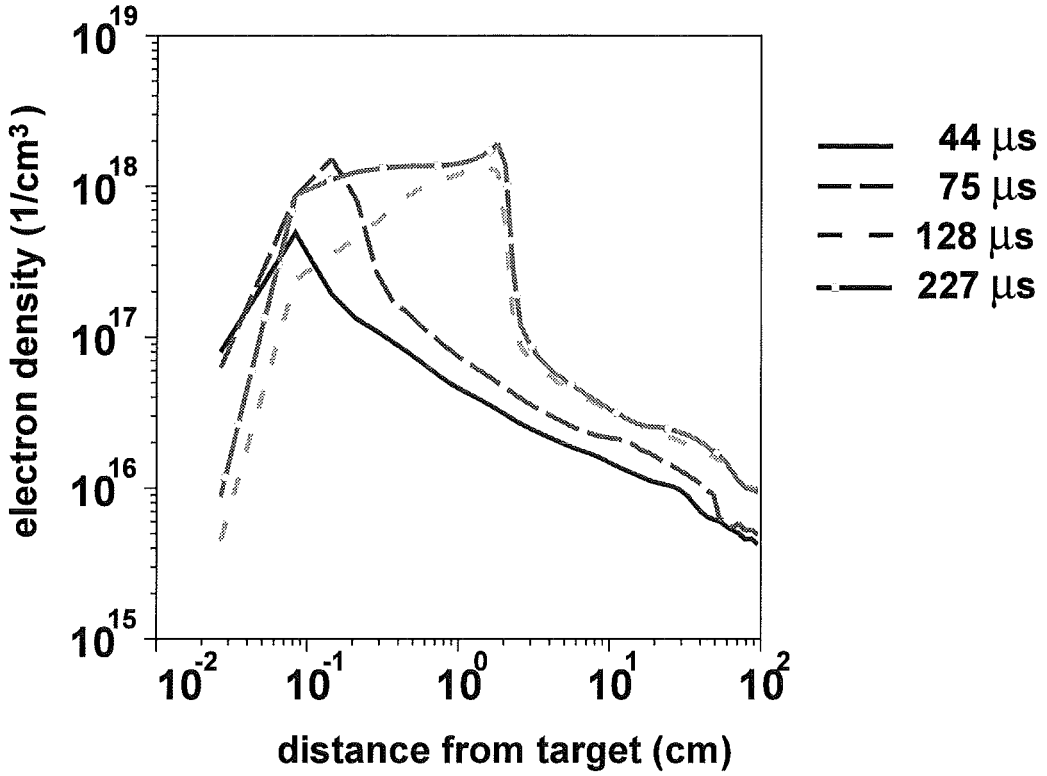

Fig. 76a. Calculated time dependent electron density profiles along the separatrix in a carbon plasma shield for a perpendicular graphite target for the QSPA facility.

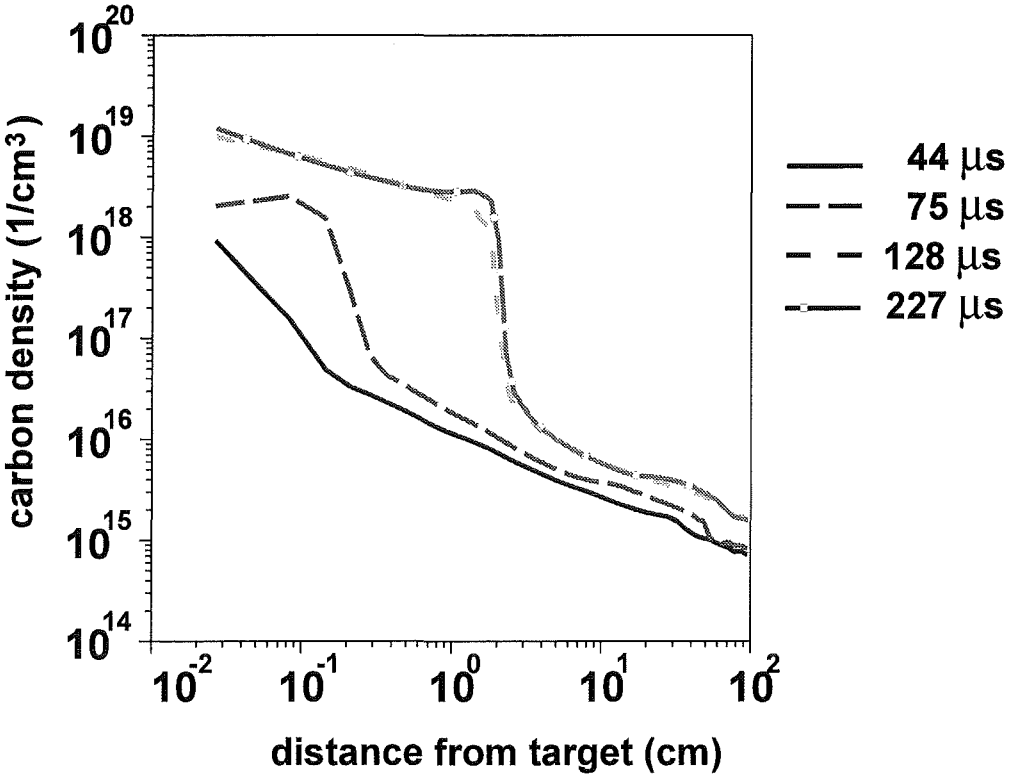

Fig. 76b. Calculated time dependent carbon density profiles along the separatrix in a carbon plasma shield for a perpendicular graphite target for the QSPA facility.

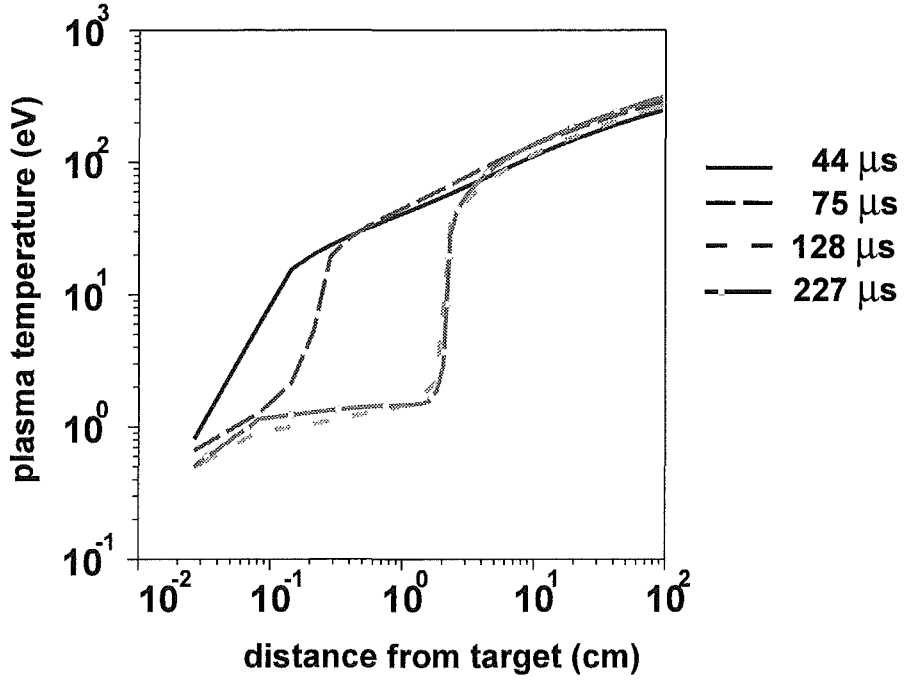

Fig. 77. Calculated time dependent plasma temperature profiles along the separatrix in a carbon plasma shield for a perpendicular graphite target for the QSPA facility.

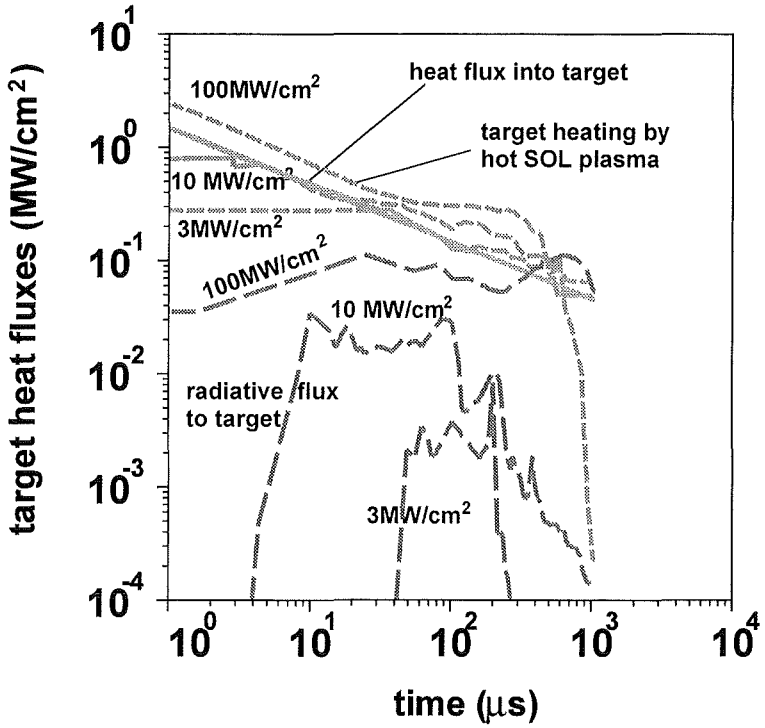

Fig.78. Time evolution of target heat fluxes at the position of maximum erosion for different peak power densities. Horizontal graphite target. Gaussian power density profile with peak power densities of 3, 10 and 100 MW/cm^2.

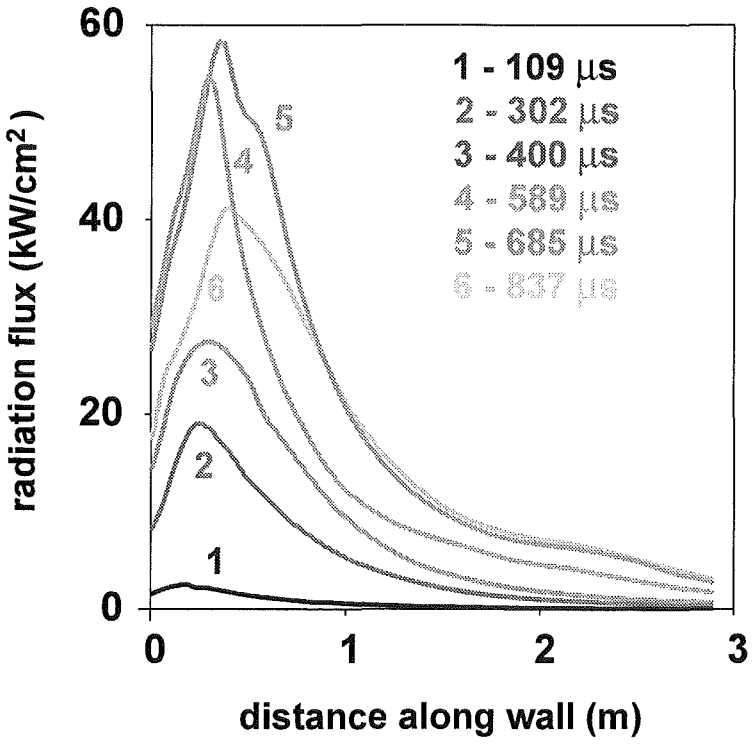

Fig.79. Radiative fluxes to the side wall. Horizontal graphite target, side wall distance 60 cm, Gaussian power density profile, peak power density 10 MW/cm^2.

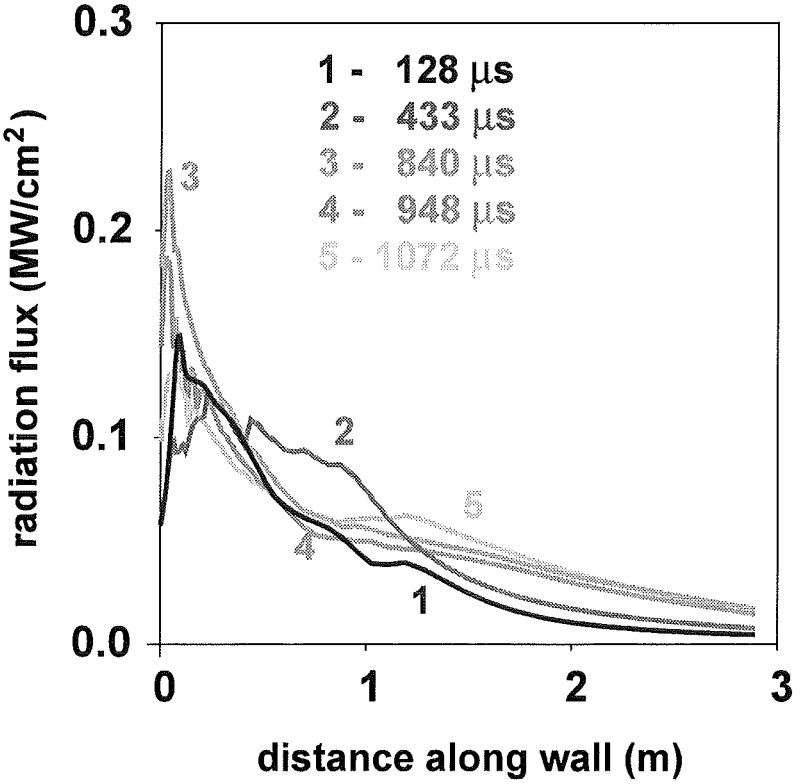

Fig.80. Radiative fluxes to the side wall. Horizontal graphite target, side wall distance 60 cm, Gaussian power density profile, peak power density 100 MW/cm^2.

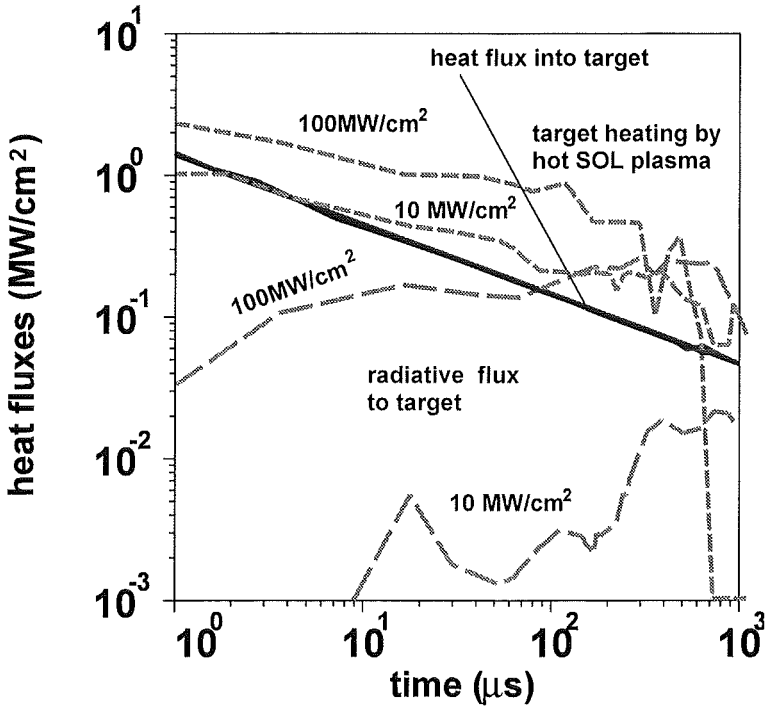

Fig.81. Time evolution of target heat fluxes at the position of the separatrix strike point for different peak power densities for a horizontal graphite target. Realistic power density profiles with peak power densities of 10 and 100 MW/cm^2 were used.

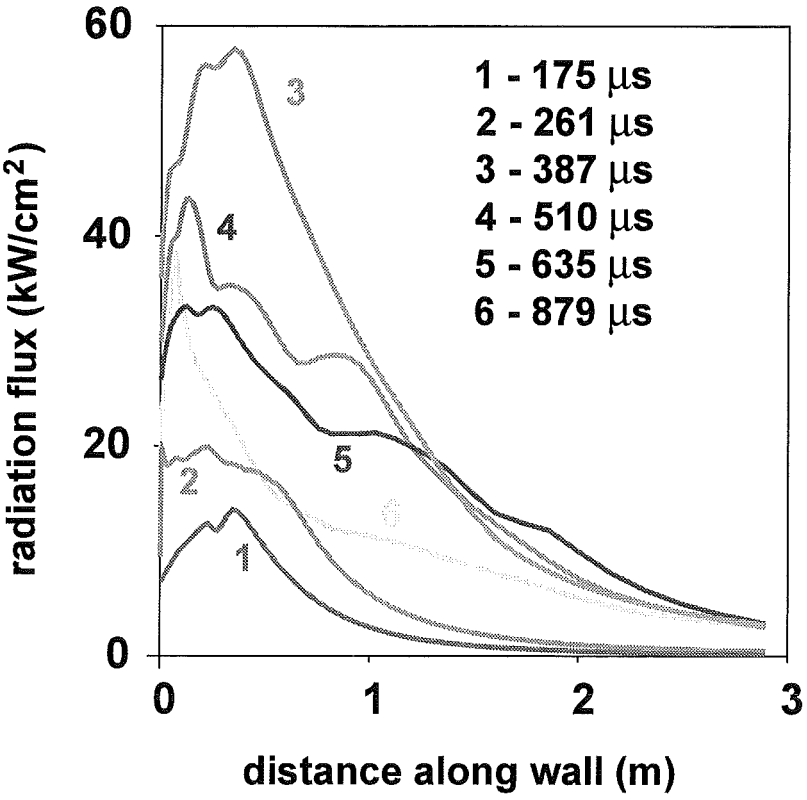

Fig. 82. Radiative fluxes from a carbon plasma to the side wall. Horizontal graphite target, side wall distance 60 cm, realistic power density profile, peak power density 10 MW/cm^2.

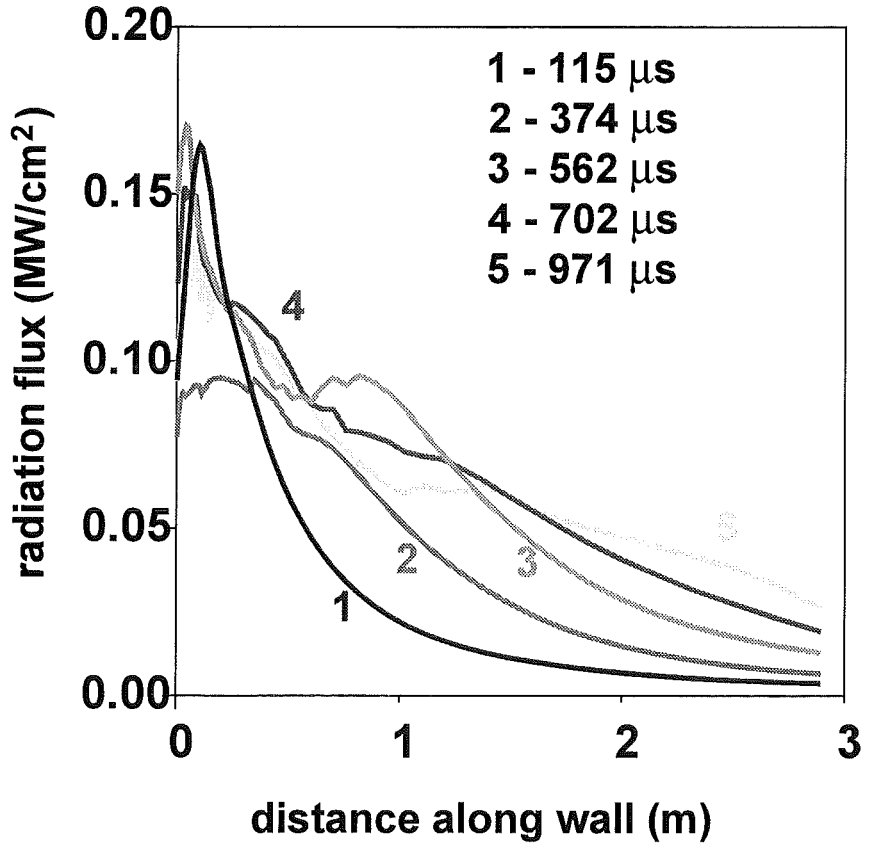

Fig.83. Radiative fluxes to the side wall. Side wall distance 60 cm, horizontal graphite target, realistic power density profile, peak power density 100 MW/cm^2. Evaporation of the side wall starts after 60 μs

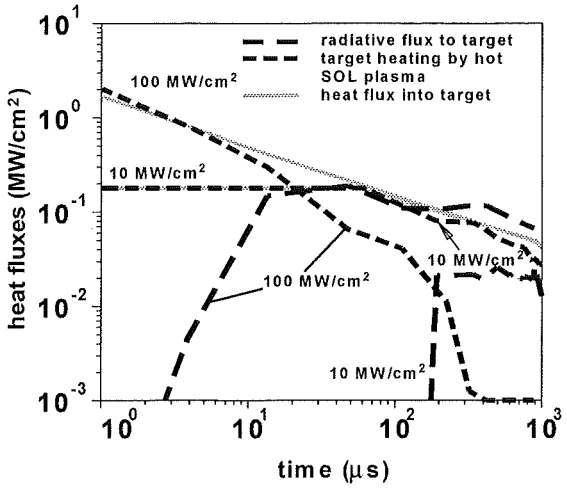

Fig.84a. Comparison of the time evolution of target heat fluxes for vertical graphite target and downstream separatrix for two peak power densities along magnetic field lines. The heat fluxes belong to the point of maximum erosion.

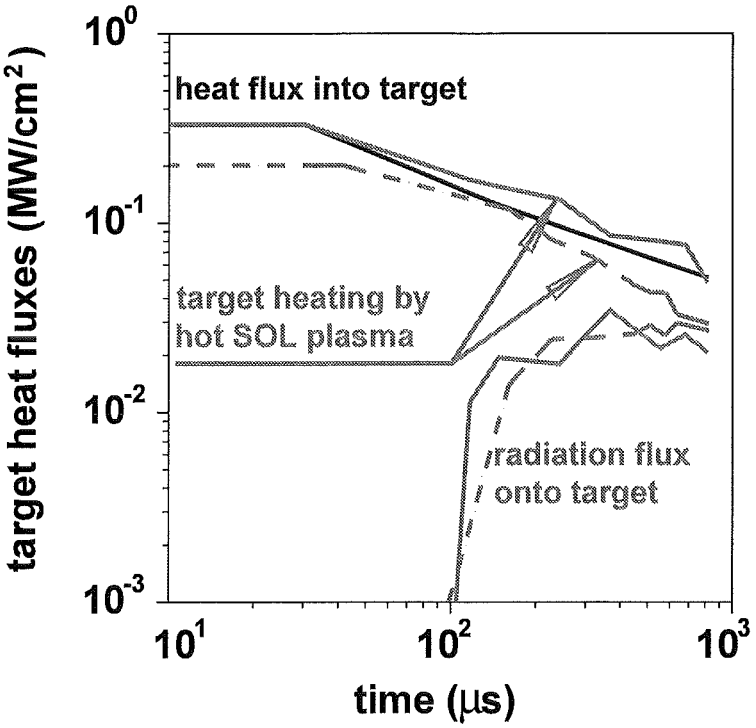

Fig.84b. Comparison of the time evolution of target heat fluxes for a vertical graphite target and upstream (solid line) and downstream (dashed line) separatrix. Peak power density is 10 MW/cm^2 along the separatrix.

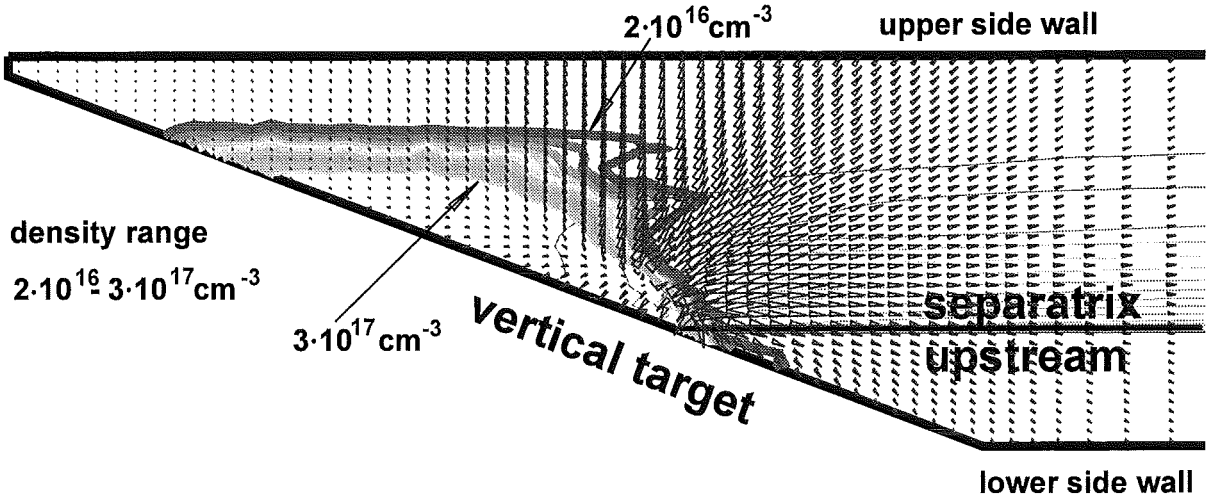

Fig.85. 2 dim radiation field (arrows) and plasma density for vertical target at 367 μs. Peak power density is 10 MW/cm^2 along the separatrix.

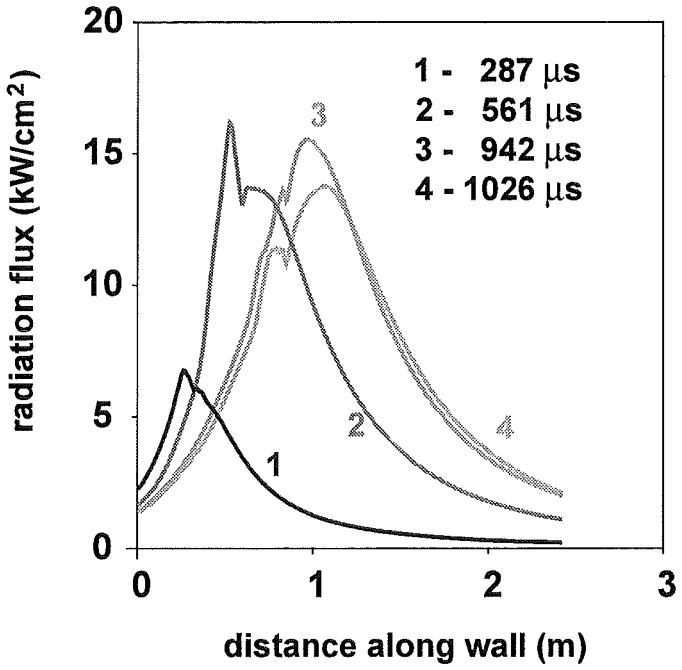

Fig.86. Radiative fluxes from carbon plasma shield to upper side wall of the ITER slot divertor. Vertical graphite target, realistic power density profile, separatrix downstream side wall distance 60cm. Peak power density is 10 MW/cm^2 along magnetic field lines.

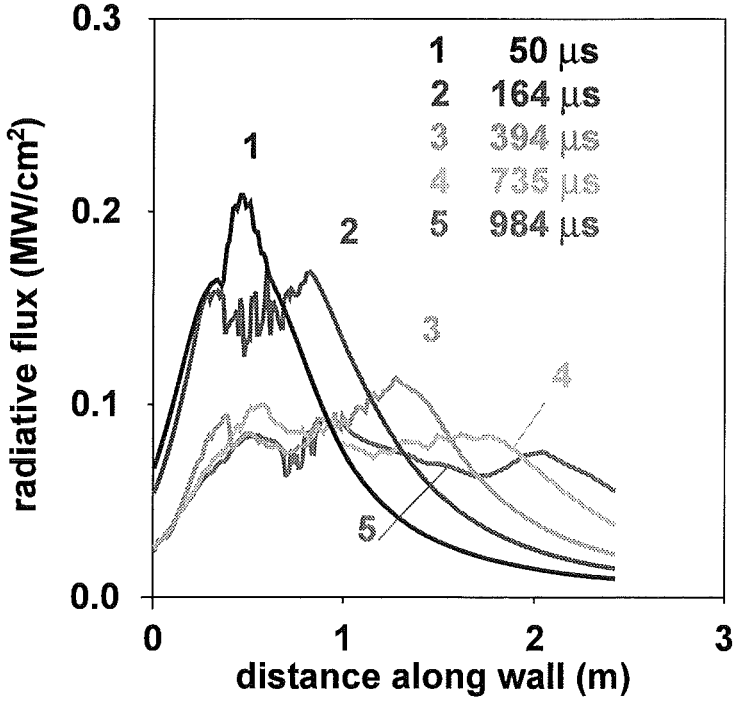

Fig.87. Radiative fluxes from carbon plasma shield to upper side wall of the ITER slot divertor. Vertical graphite target, realistic power density profile, separatrix downstream side wall distance 60cm. Peak power density is 100 MW/cm^2 along magnetic field lines. Evaporation of upper side wall starts after 100 μs, lower side wall starts to evaporate after 300 μs.

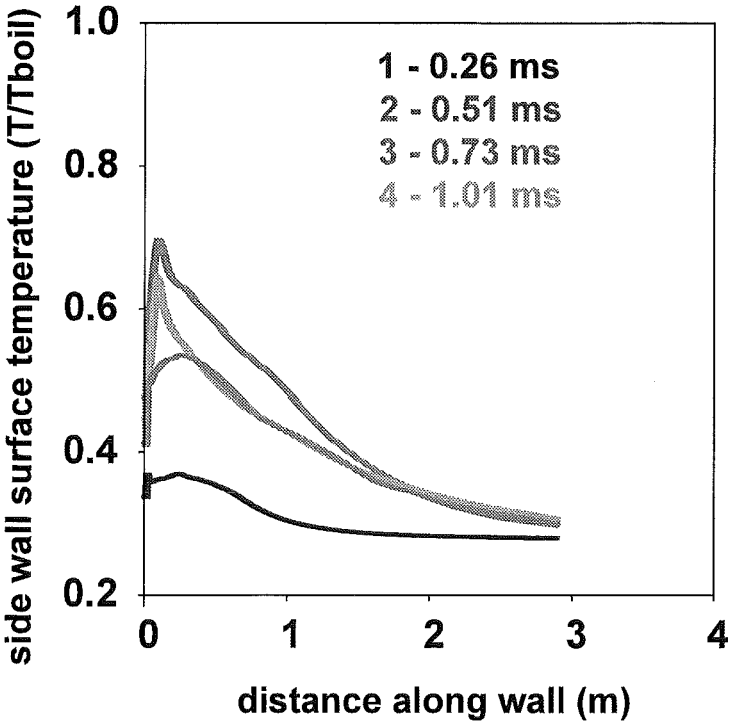

Fig.88. Time dependent surface temperature profiles at graphite side walls. Horizontal target, realistic power density profile of the impacting hot SOL plasma with peak power density of 10 MW/cm^2 along magnetic field lines.

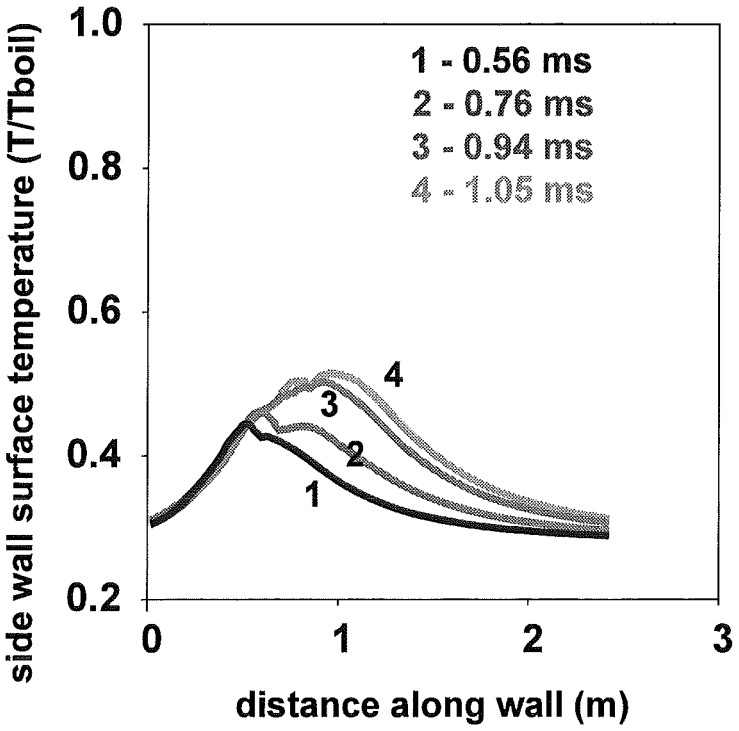

Fig.89. Time dependent surface temperature profiles at graphite side walls. Vertical target, realistic power density profile of the impacting hot SOL plasma with peak power density of 10 MW/cm^2 along magnetic field lines.

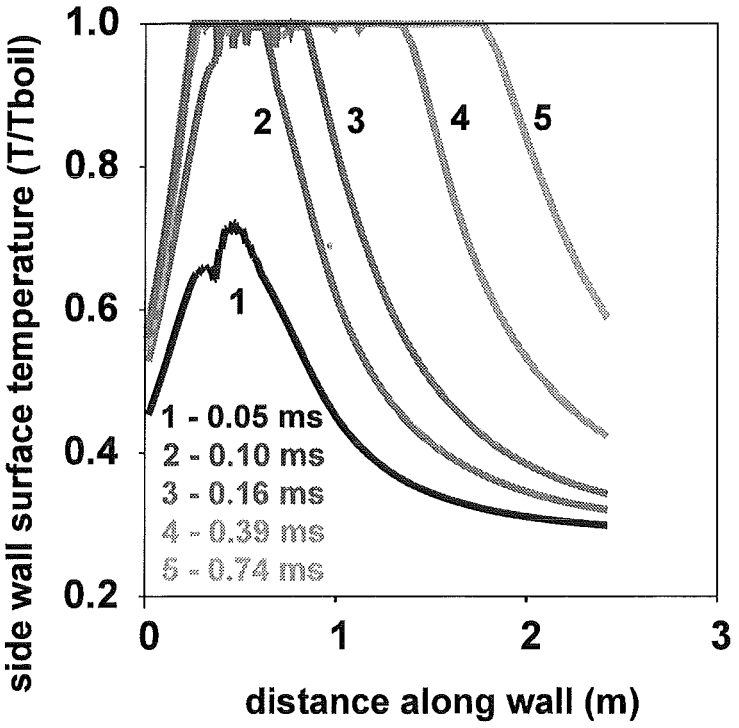

Fig.90. Surface temperature evolution at upper graphite side wall. Vertical target, realistic power density profile of the impacting hot SOL plasma with peak power density of 100 MW/cm^2 along magnetic field lines.

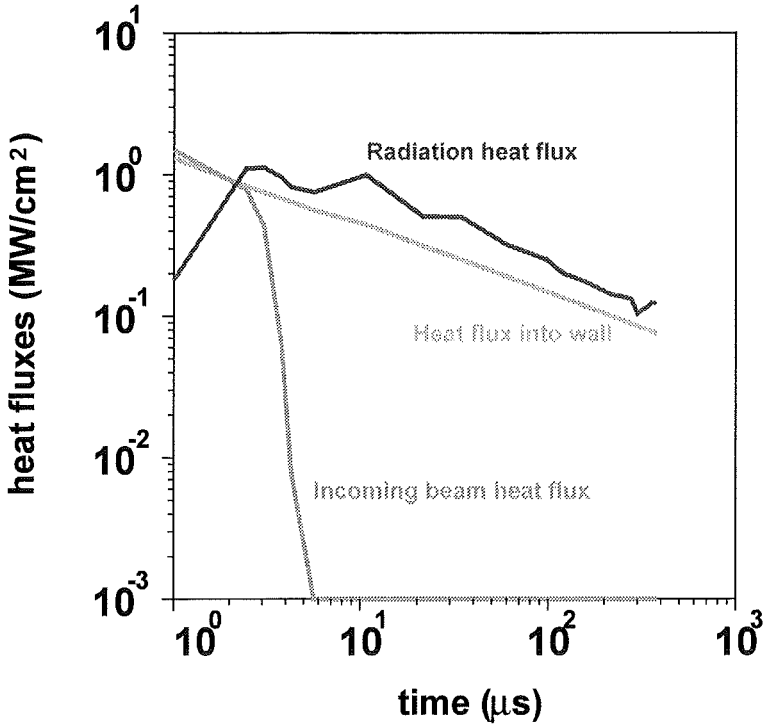

Fig.91. Time evolution of target heat fluxes for a vertical graphite target and upstream separatrix. Peak power density along magnetic field lines is 1000 MW/cm^2.

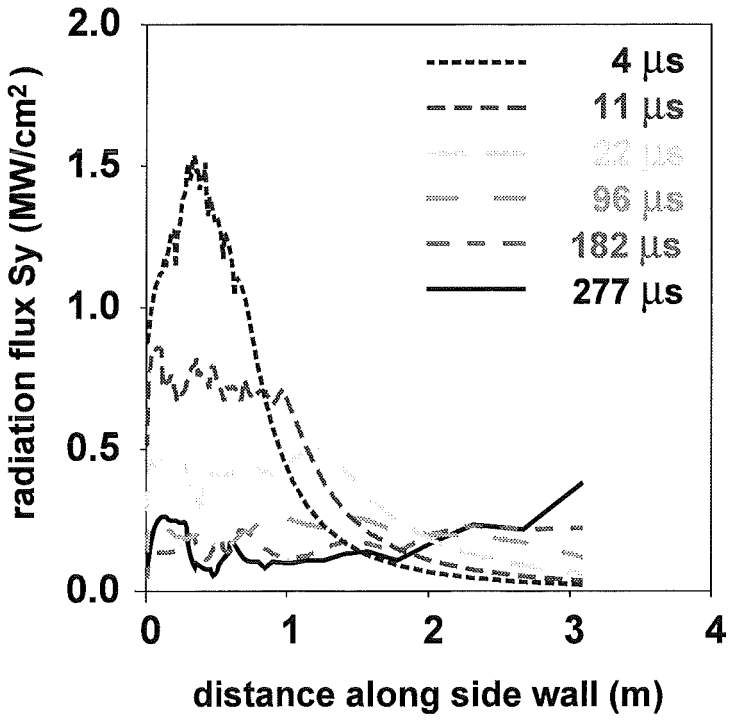

Fig.92. Radiative fluxes from carbon plasma shield to upper side wall of the ITER slot divertor. Vertical graphite target, realistic power density profile, separatrix upstream side wall distance 60cm. Peak power density is 1000 MW/cm^2 along magnetic field lines.

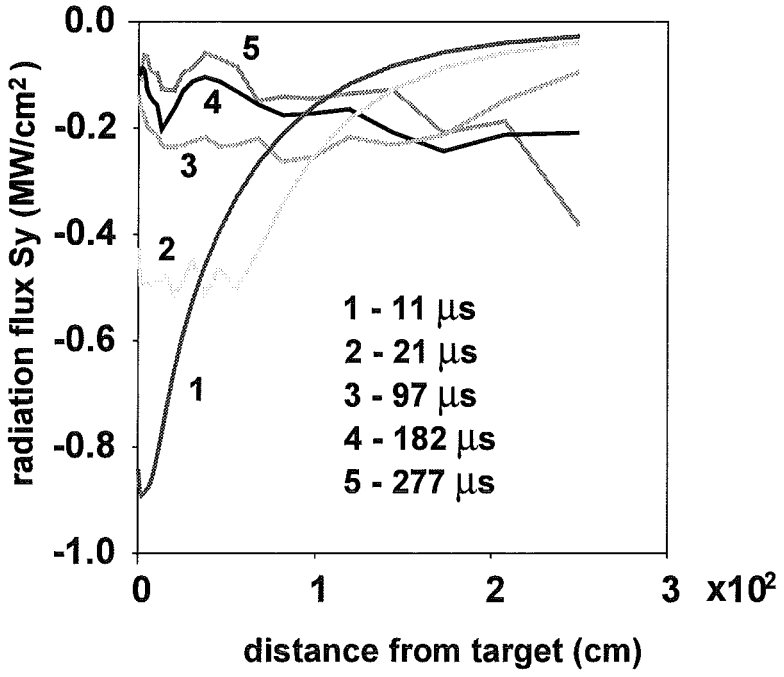

Fig.93. Radiative fluxes from a carbon plasma shield to the lower side wall of the ITER slot divertor. Vertical graphite target, realistic power density profile, separatrix upstream, side wall distance 60cm. Peak power density is 1000 MW/cm^2 along magnetic field lines.

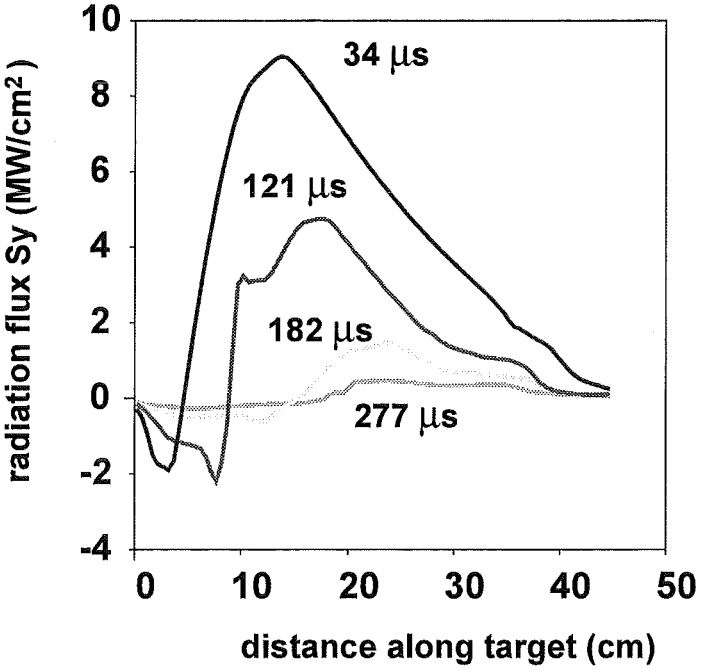

Fig.94. Profiles of the y component of the radiation flux in a carbon plasma shield at different times.

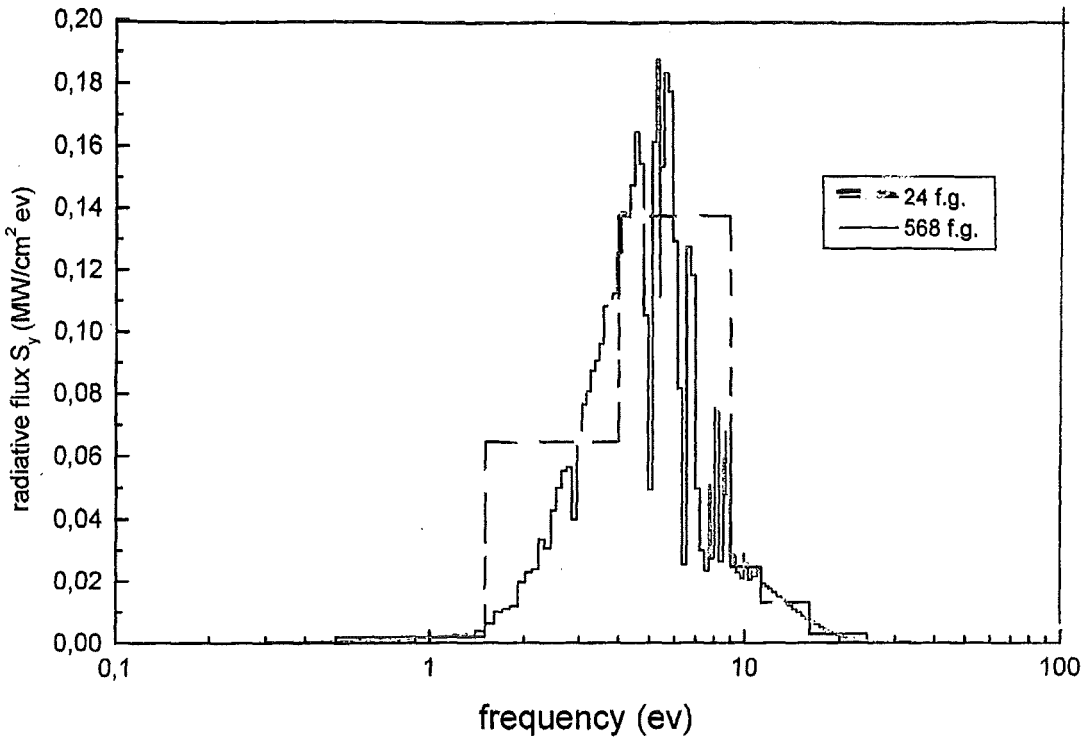

Fig. 95a. Comparison of spectral radiation fluxes at 182 μs calculated with 24 and 568 frequency groups. Plasma temperature 1 eV.

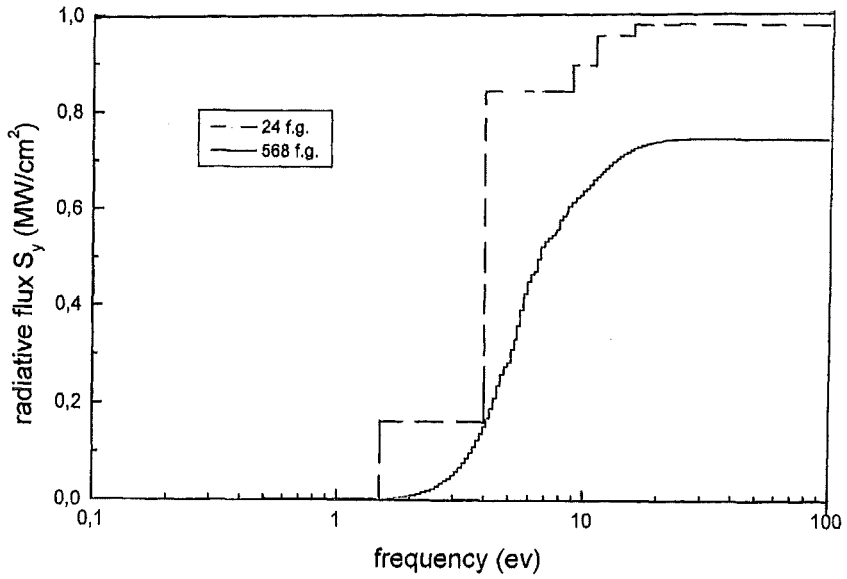

Fig. 95b. Frequency integrated radiation flux for 24 Rosseland and 568 Planck frequency groups. Plasma temperature 1 eV.

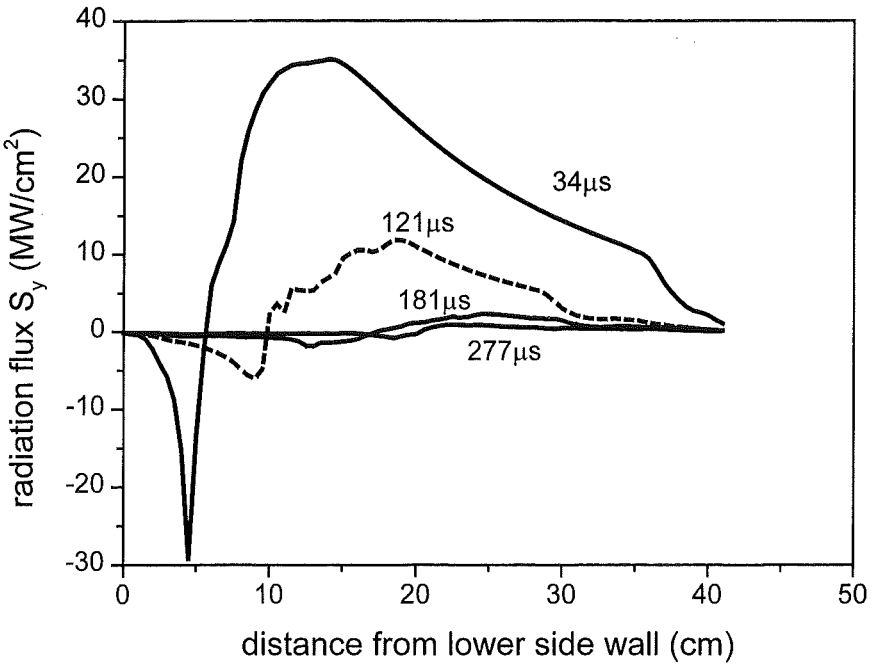

Fig. 96. Profiles of the radiative flux Sy in a carbon plasma shield calculated with 69 frequency group Planck opacities.

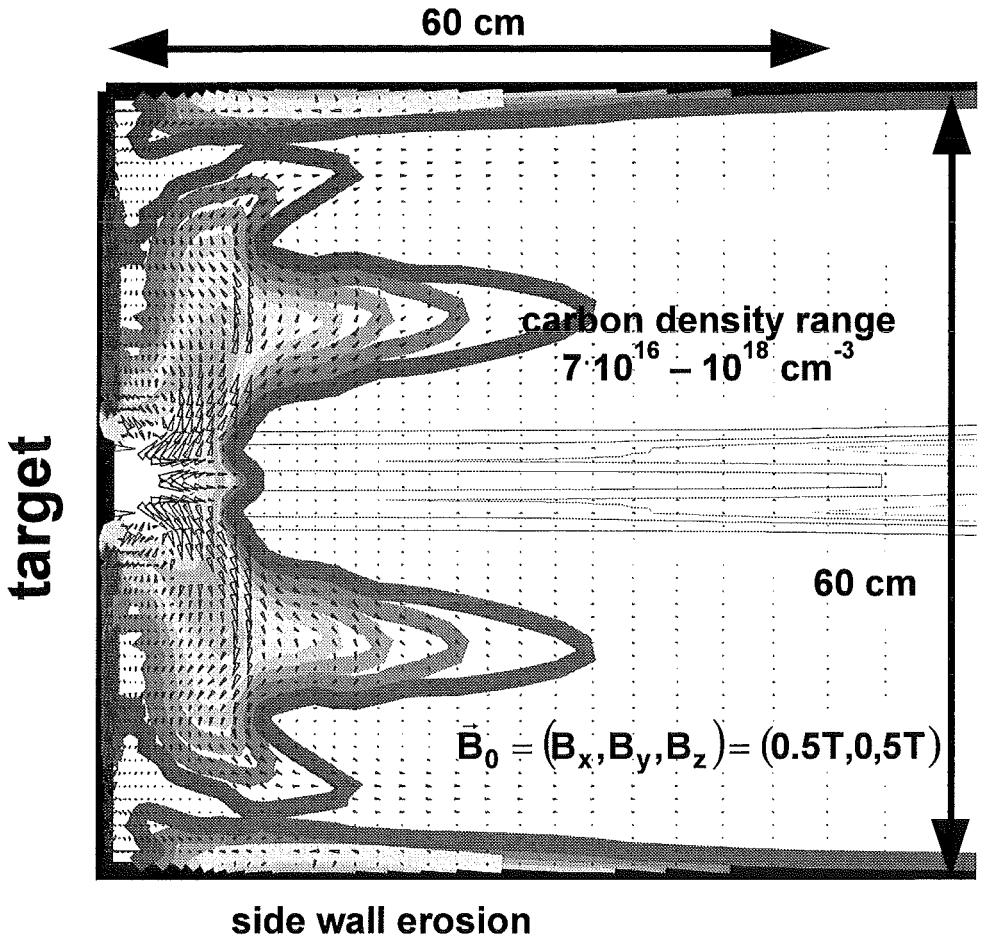

Fig.97. Contour plot of plasma density and plasma flow (Γ=nv, arrows) at 400 μs for horizontal target. Incoming hot plasma 10keV. Gaussian power density profile with halfwidth of 5 cm, peak power density is 100 MW/cm^2.

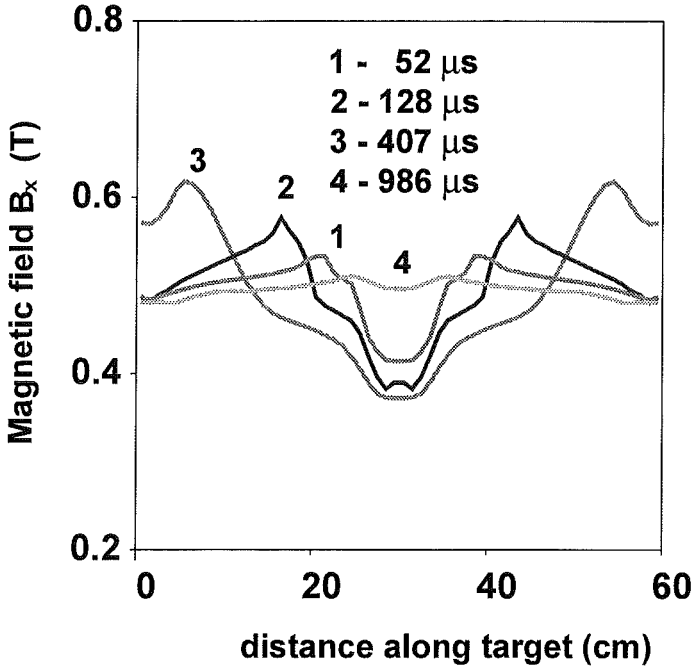

Fig.98. Evolution of Bx (poloidal magnetic field) at x=1.5cm. Horizontal target, Gaussian power density profile, peak power density along the separatrix is 100 MW/cm^2.

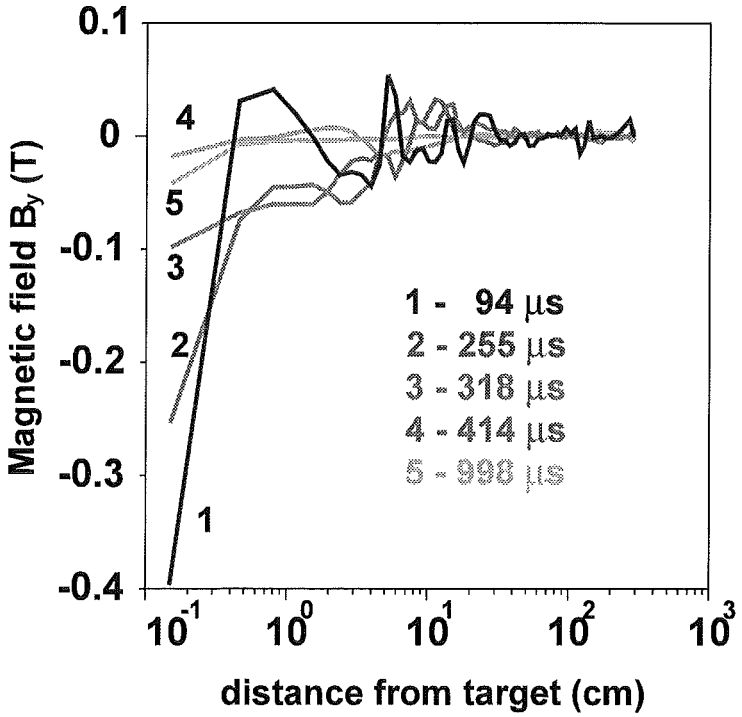

Fig.99. Time evolution of B_y. Horizontal target, Gaussian power density profile, peak power density along separatrix is 100 MW/cm^2.

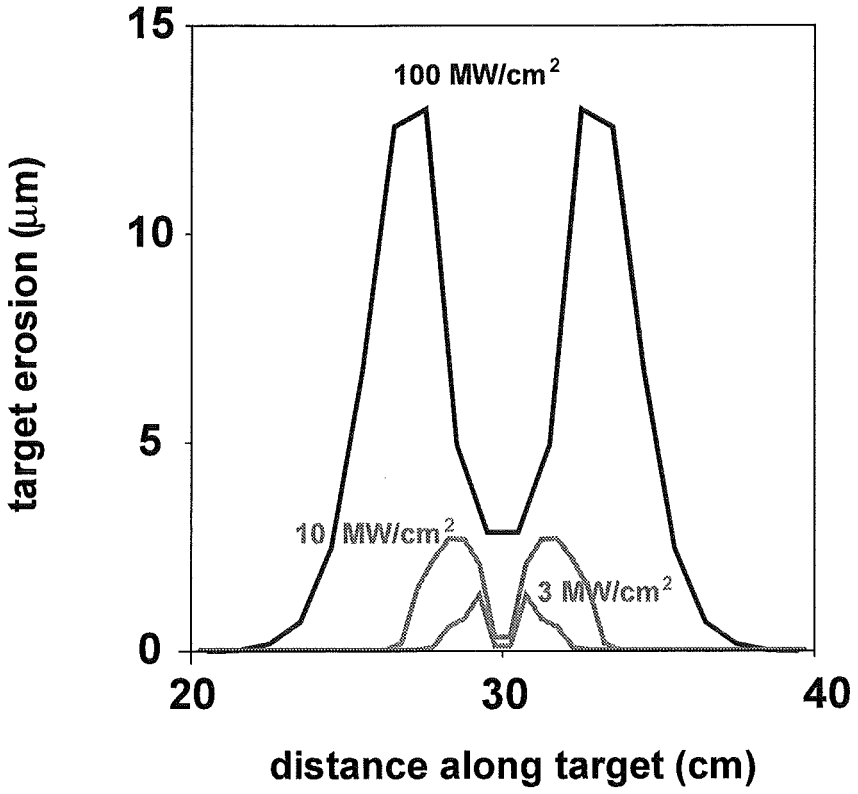

Fig.100. Comparison of erosion profiles at 1 ms for different peak power densities for a horizontal target and Gaussian power density profile of the impacting hot plasma.

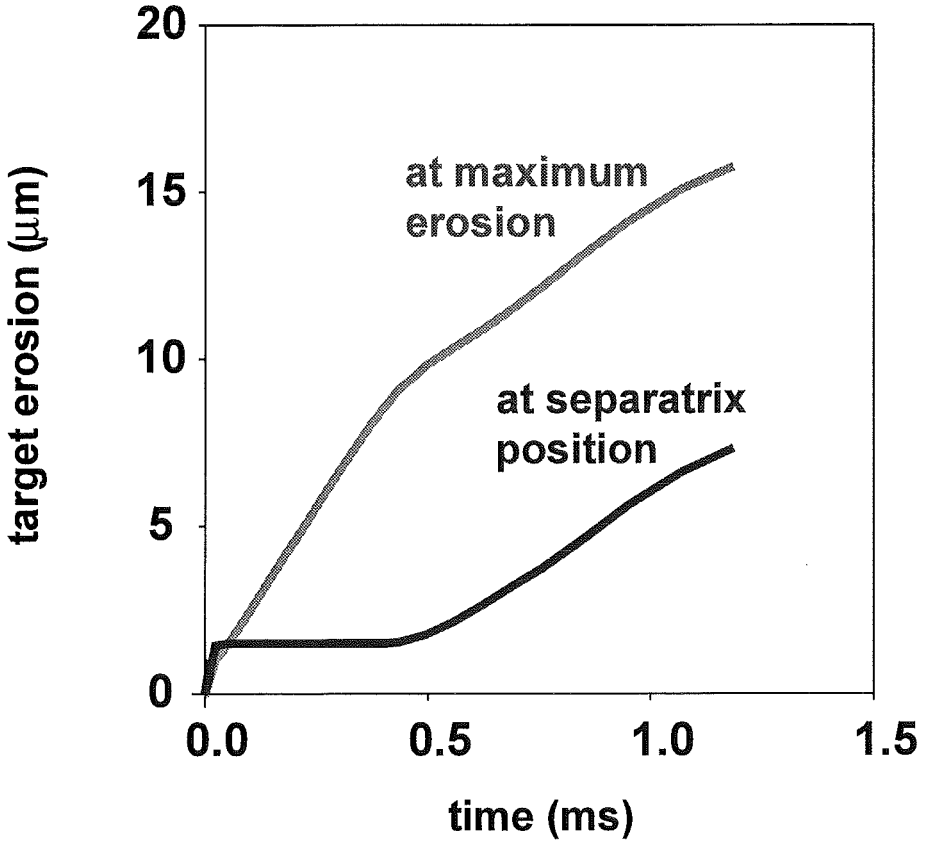

Fig.101. Calculated time dependence of erosion. Horizontal target, Gaussian power density profile, peak power density is 100 MW/cm^2.

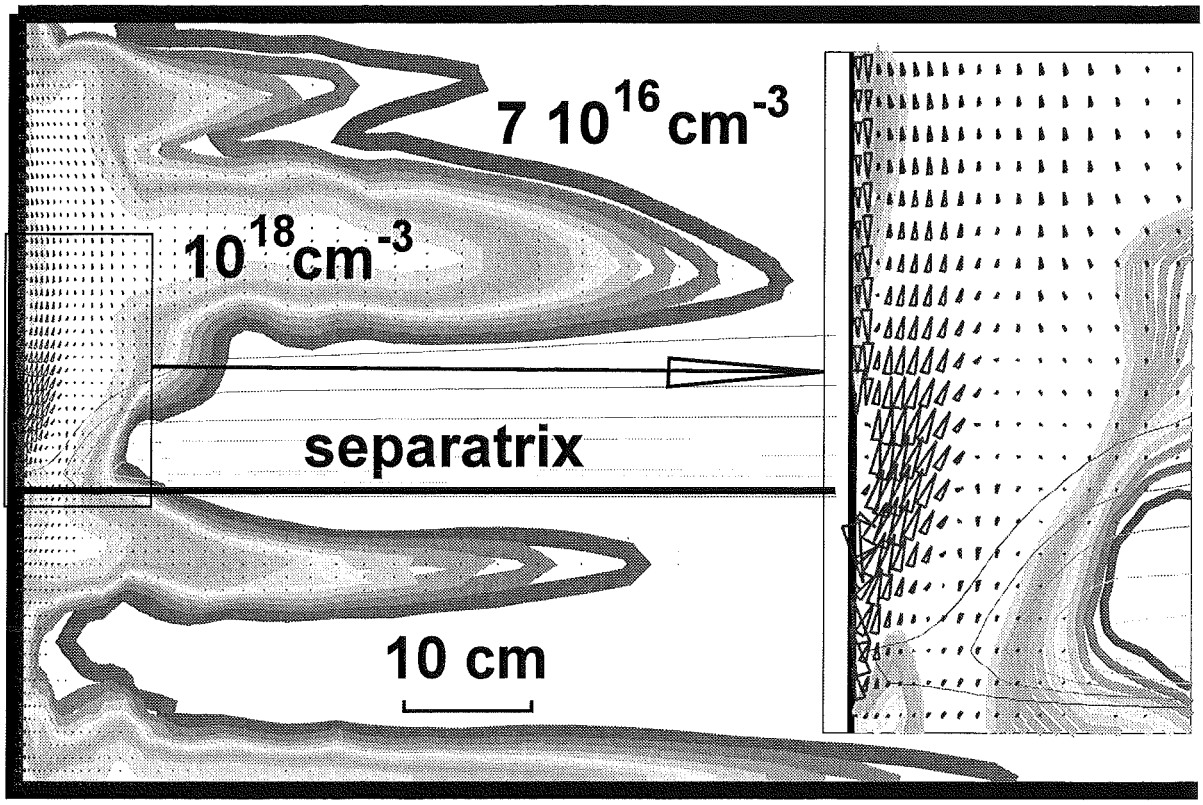

Fig.102. Calculated 2 dim plasma density and plasma flow (arrows) at 500 μs. Incoming hot plasma 10 keV, realistic power density profile, halfwidth 5 cm, peak power density is 100 MW/cm^2.

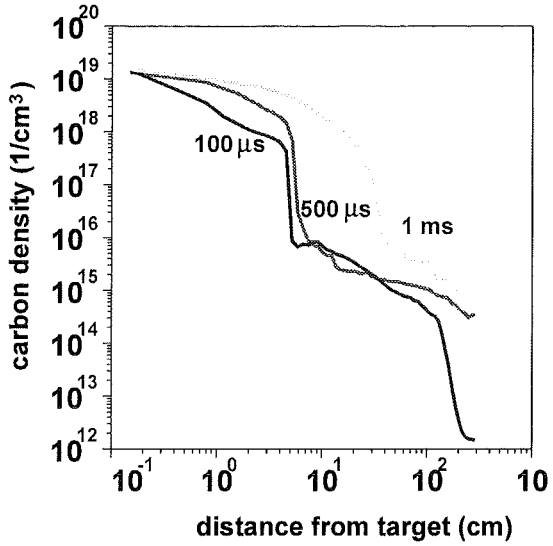

Fig. 103a. Carbon plasma density profiles along the separatrix at different times. Horizontal target realistic power density profile, peak power density 100 MW/cm^2.

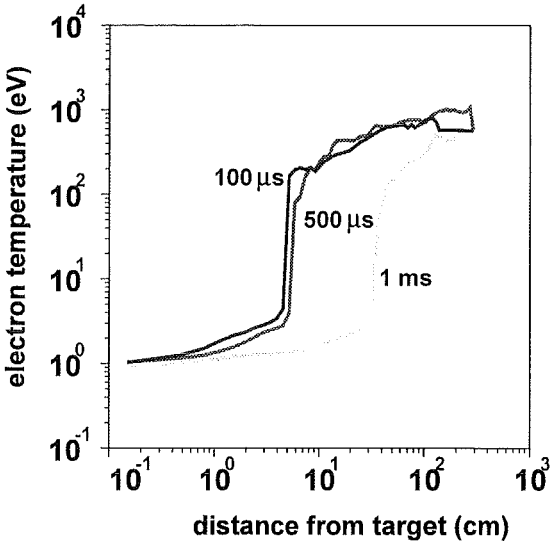

Fig. 103b. Plasma temperature profiles along the separatrix. Same conditions as in Fig. 103a.

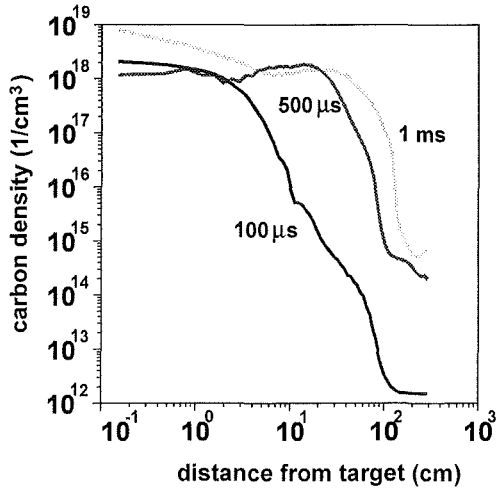

Fig. 104a. Carbon plasma density profiles at distance 20 cm from the separatrix. Same conditions as in Fig. 103a.

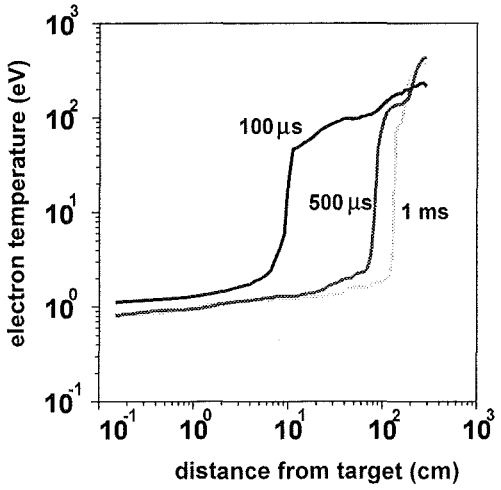

Fig. 104b. Plasma temperature profiles at distance 20 cm from the separatrix. Same conditions as in Fig. 103a.

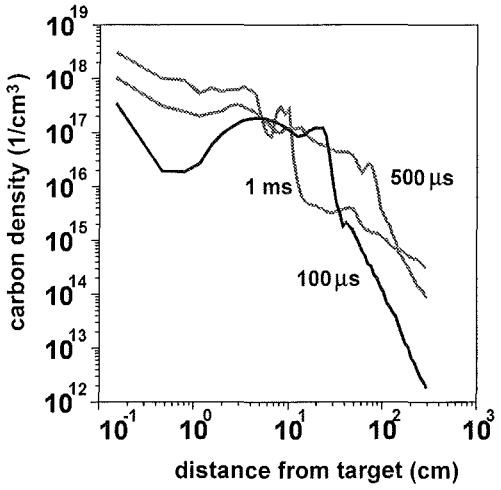

Fig. 105a. Carbon plasma density profiles along the separatrix at different times. Horizontal target, peak power density 10 MW/cm^2.

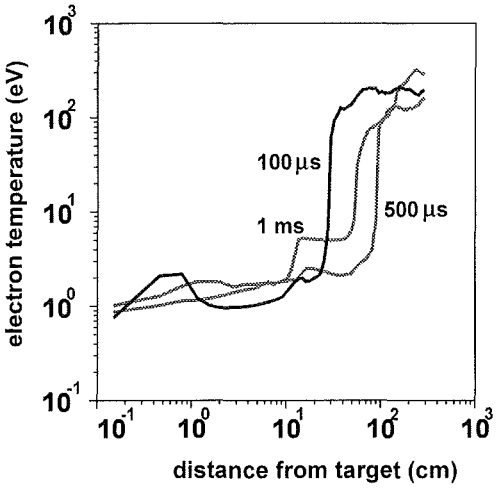

Fig. 105b. Plasma temperature profiles along the separatrix. Same conditions as in Fig. 105a.

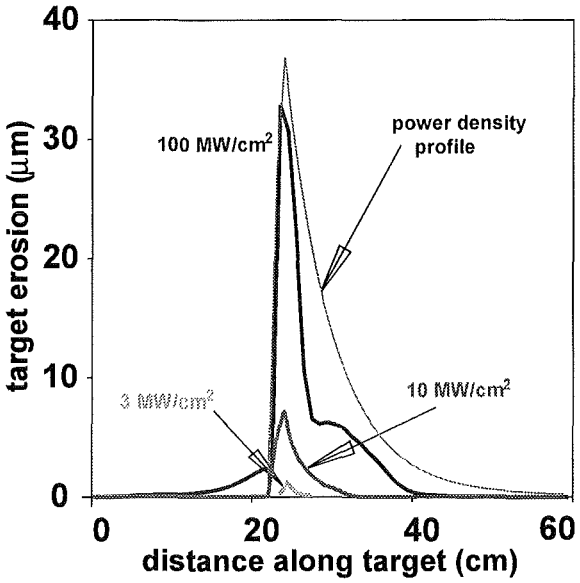

Fig.106. Calculated target erosion for horizontal graphite target at 1 ms. Realistic power density profile with different peak power densities.

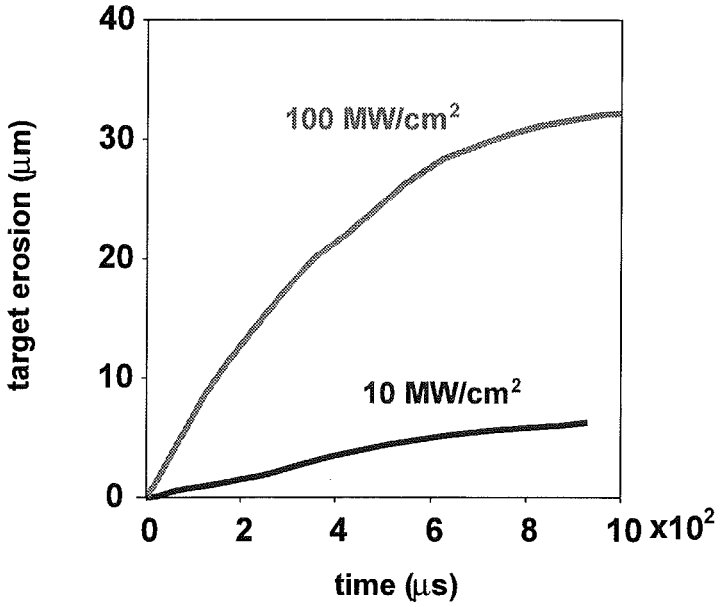

Fig. 107. Time dependent target erosion at SSP for a horizontal target and realistic power density profile for two different peak power densities of the impacting hot plasma.

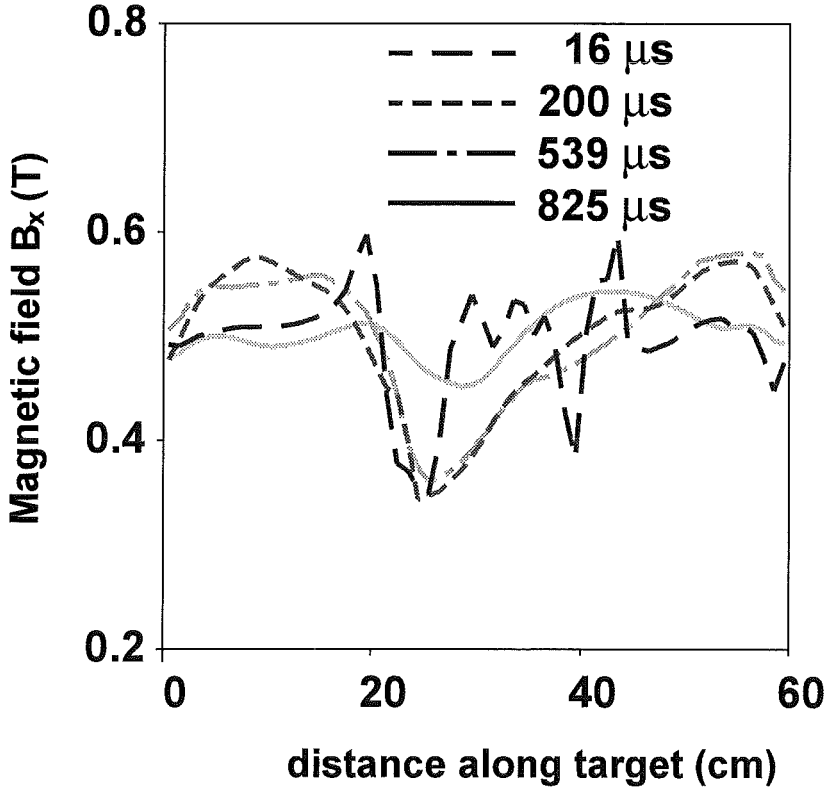

Fig. 108a. Time evolution of B_x in a carbon plasma shield. Horizontal target realistic power density profile, peak power density along the separatrix is 100 MW/cm^2.

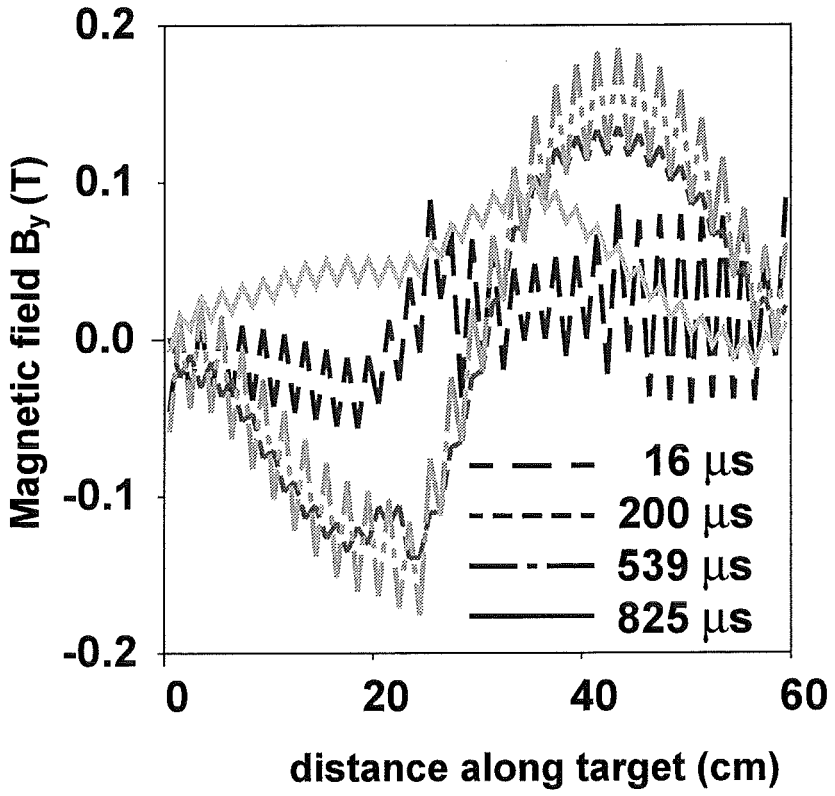

Fig. 108b. Time evolution of B_y in a carbon plasma shield. The same conditions as in Fig. 108a.

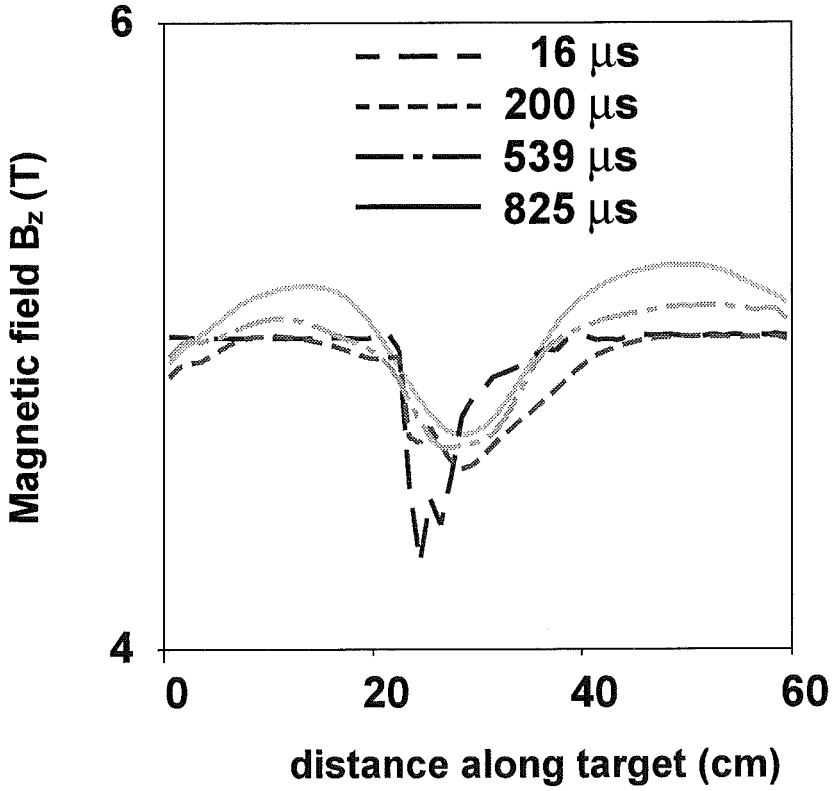

Fig. 108c. Time evolution of B_z in a carbon plasma shield. The same conditions as in Fig. 108a.

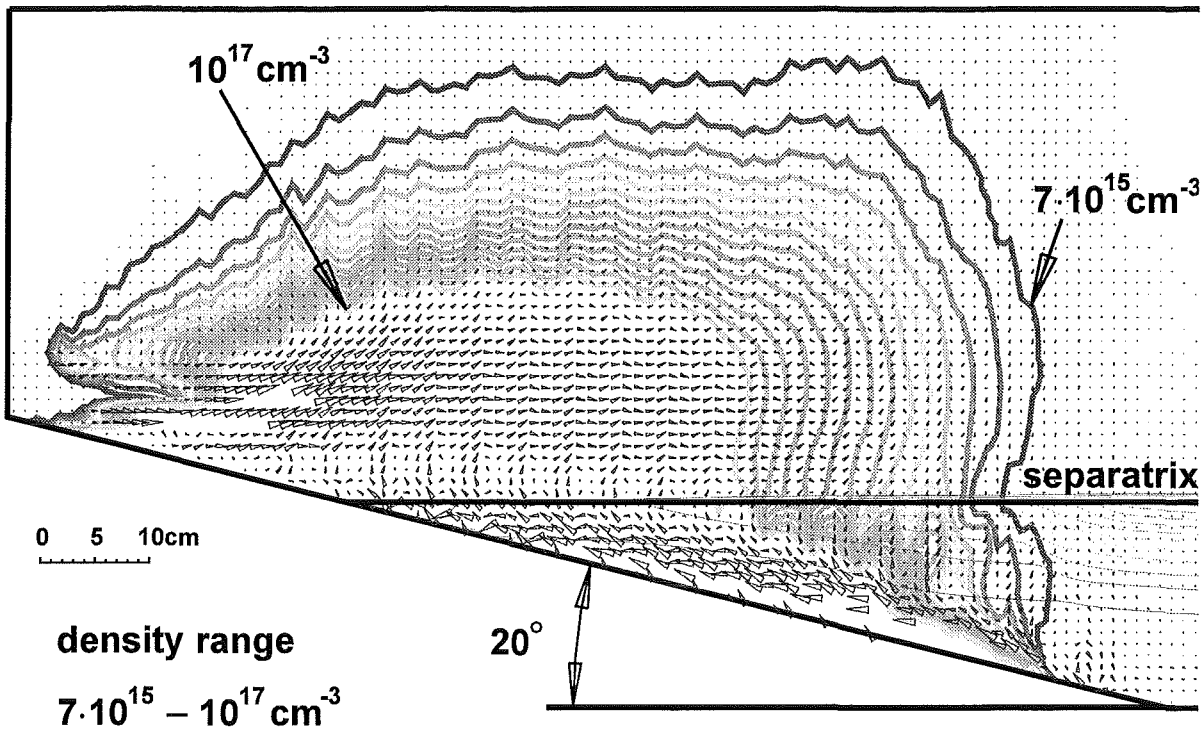

Fig.109. 2 dim plasma density contours and plasma flow pattern (arrows) in the plasma shield at 740 μs for vertical target with downstream separatrix. Slot width 60 cm, peak power density along magnetic field lines 10 MW/cm^2.

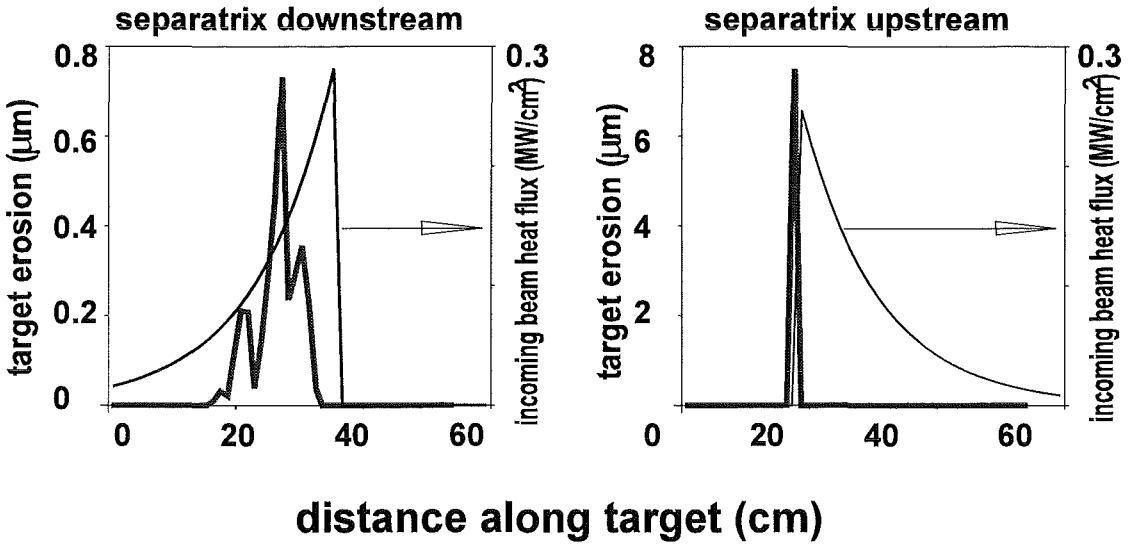

Fig.110. Erosion at 1 ms and hot plasma power density profiles for a vertical graphite target. Peak power density along the separatrix is 10 MW/cm^2.

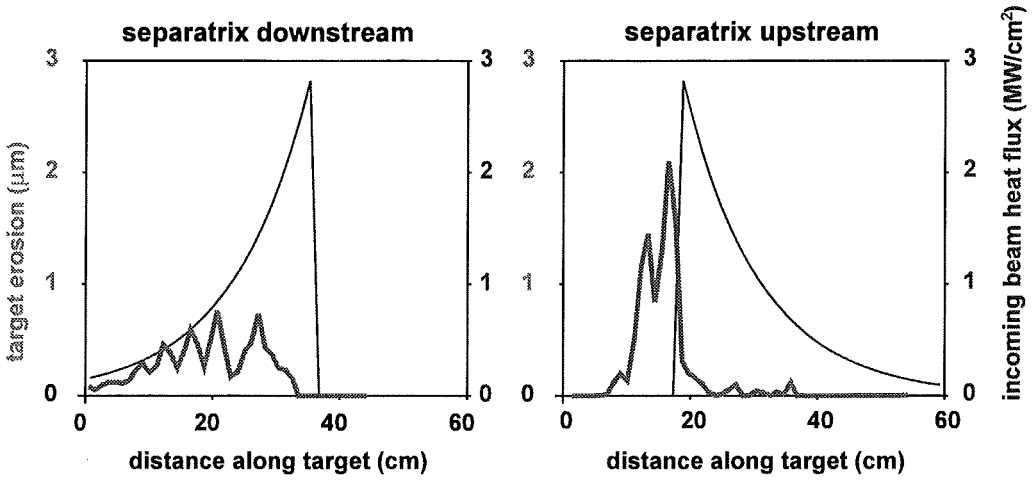

Fig.111. Erosion at 1 ms and hot plasma power density profiles for a vertical graphite target. Peak power density along the separatrix is 100 MW/cm^2.

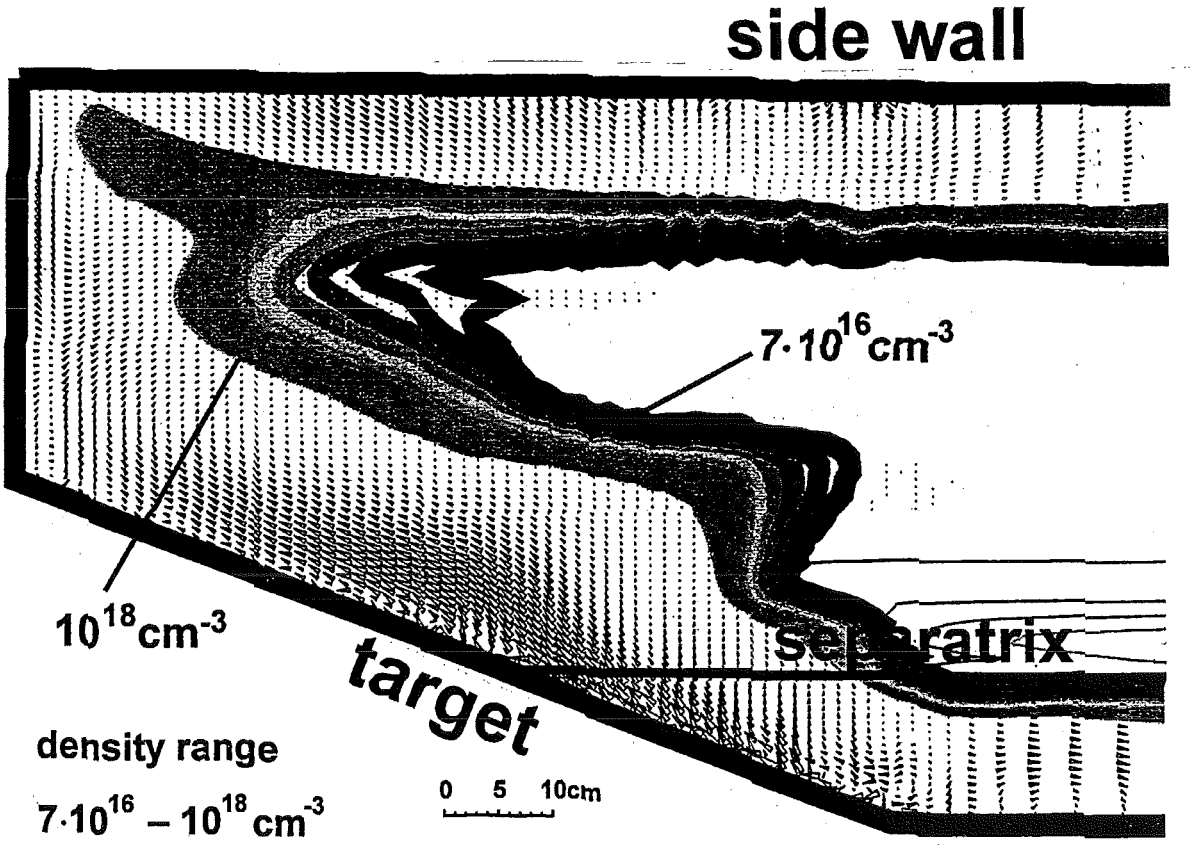

Fig.112 Plasma density and plasma flow (arrows) at 800 μs for vertical target with separatrix upstream. Realistic power density profile, peak power density along the separatrix 100 MW/cm^2.

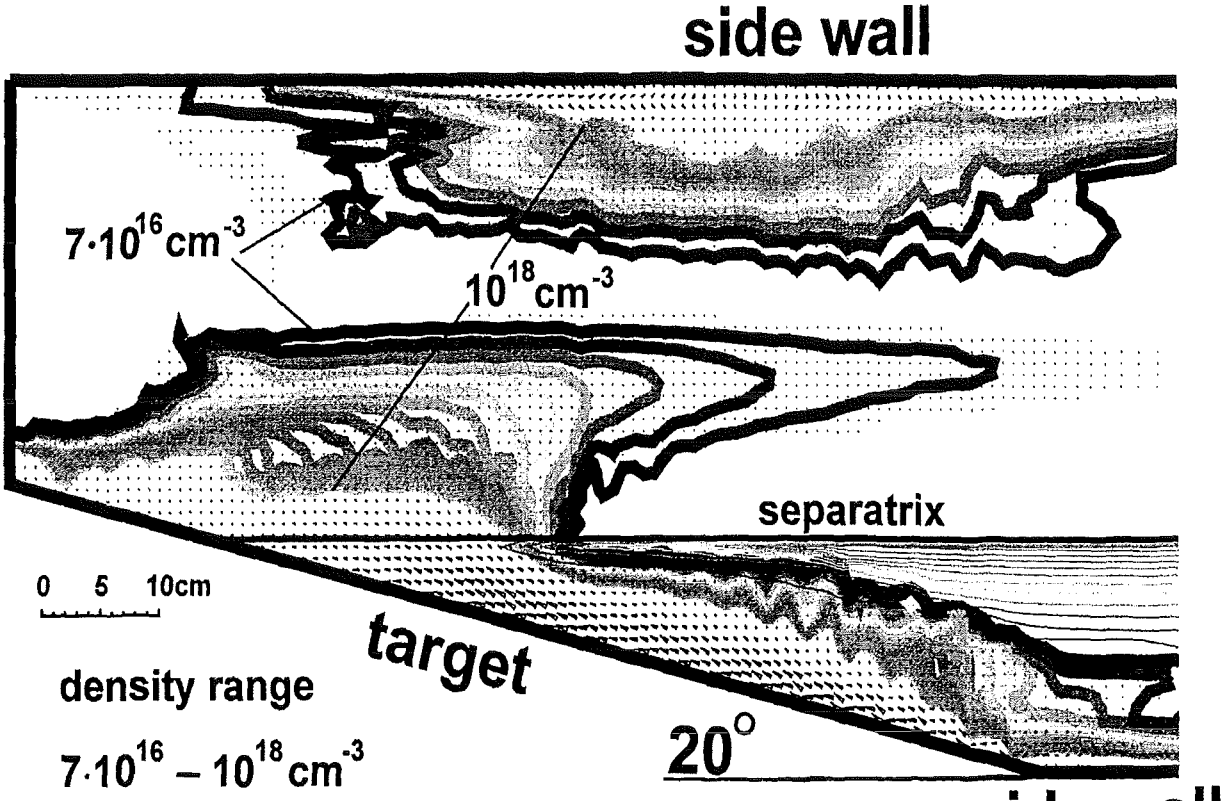

Fig. 113 Plasma density and plasma flow (arrows) at 800 μs for vertical target with separatrix downstream. Realistic power density profile, peak power density along the separatrix 100 MW/cm^2.

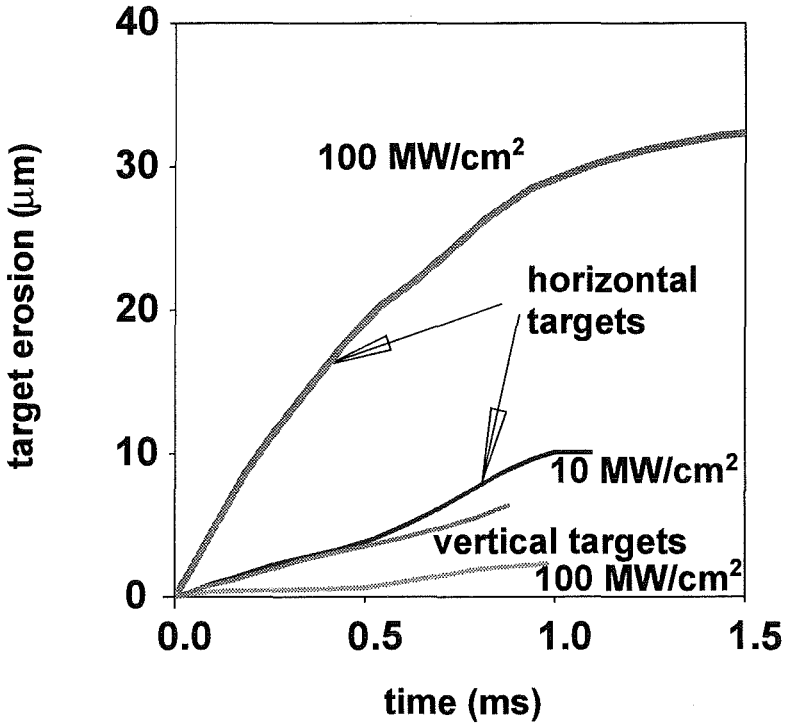

Fig.114. Comparison of target erosion for horizontal and vertical graphite target with upstream separatrix. Realistic power density profiles with peak power densities of 10 MW/cm^2 and 100 MW/cm^2 along the separatrix.

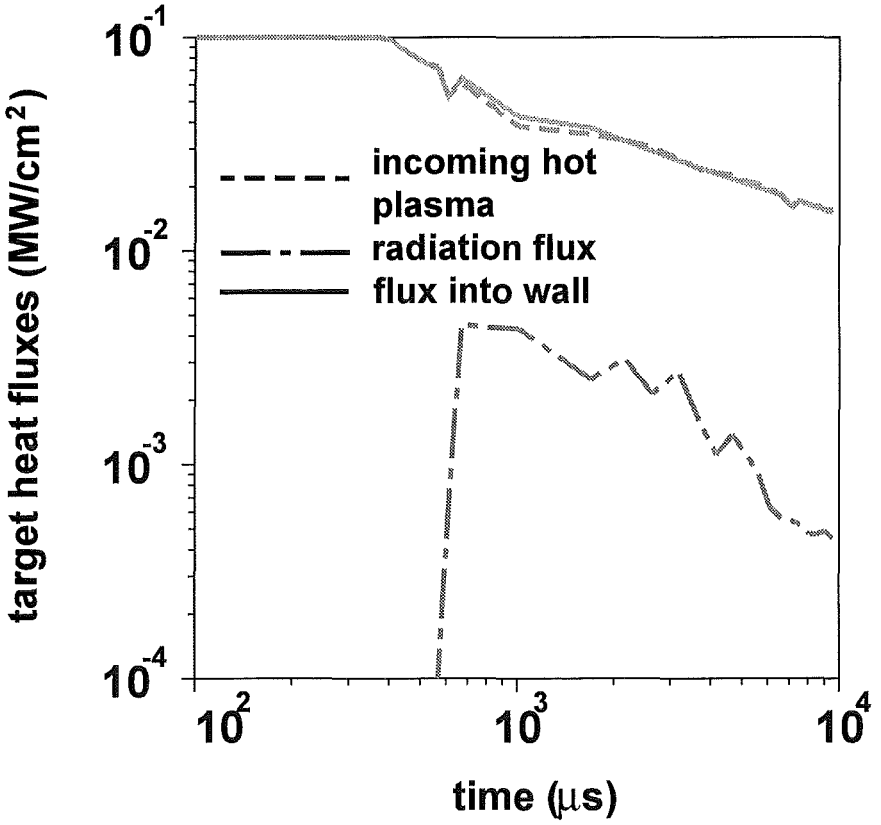

Fig. 115. Target heat fluxes at SSP. Vertical target, realistic power density profile, upstream separatrix, peak power density 3 MW/cm^2 along separatrix.

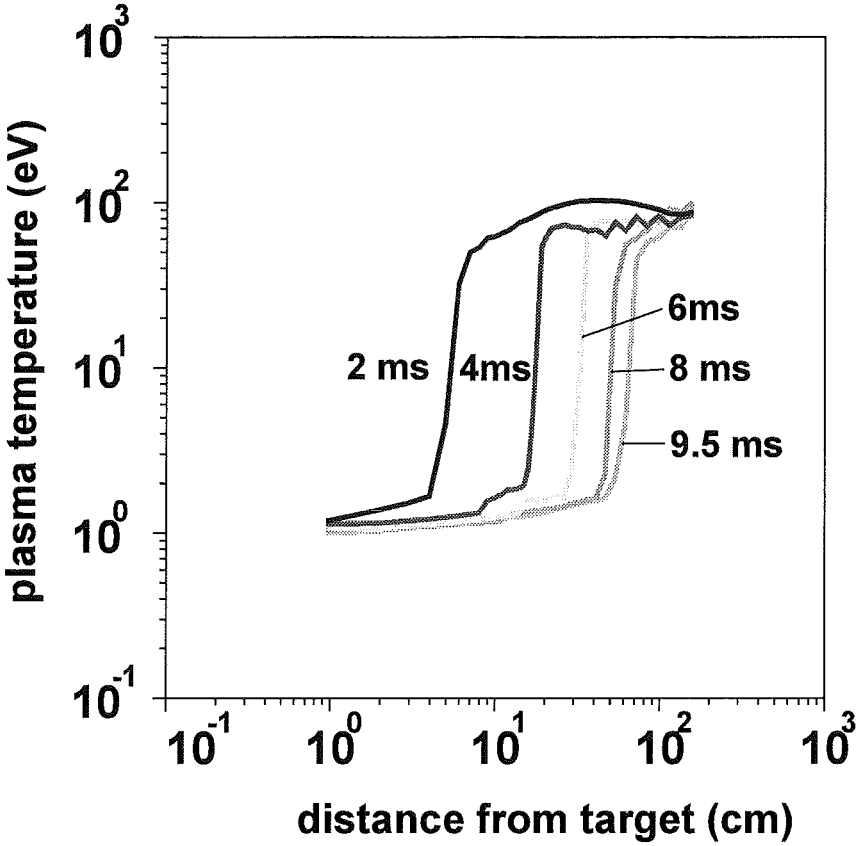

Fig. 116a. Plasma temperature profiles along the separatrix. Vertical target, realistic power density profile, upstream separatrix, peak power density 3 MW/cm^2 along the separatrix.

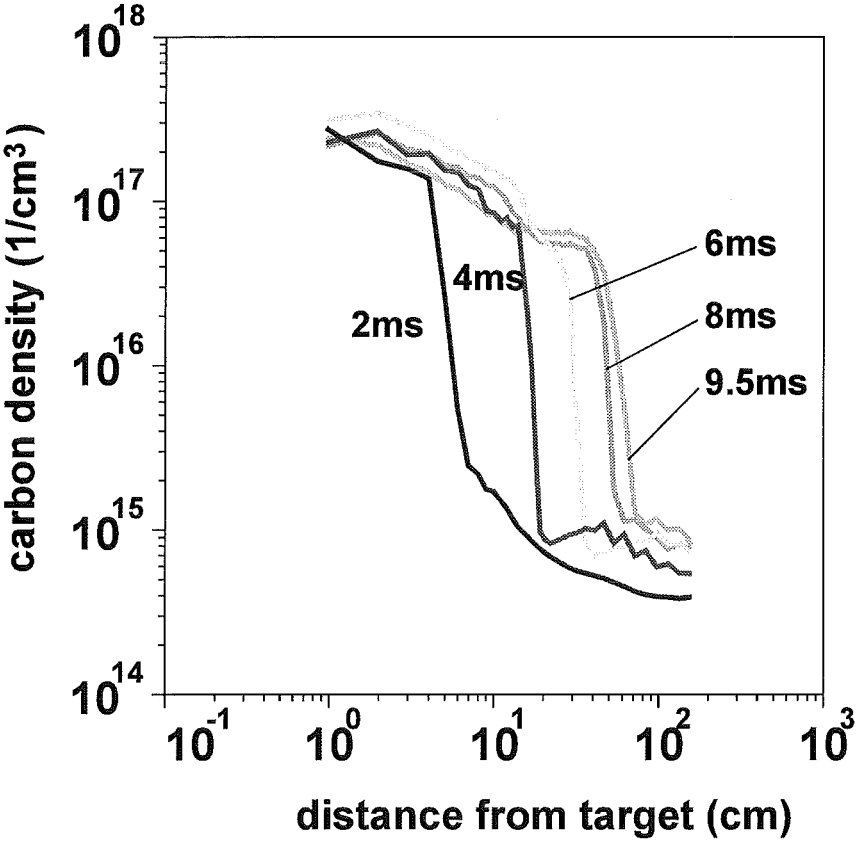

Fig. 116b. Carbon density profiles along the separatrix. Same conditions as in Fig. 116a.

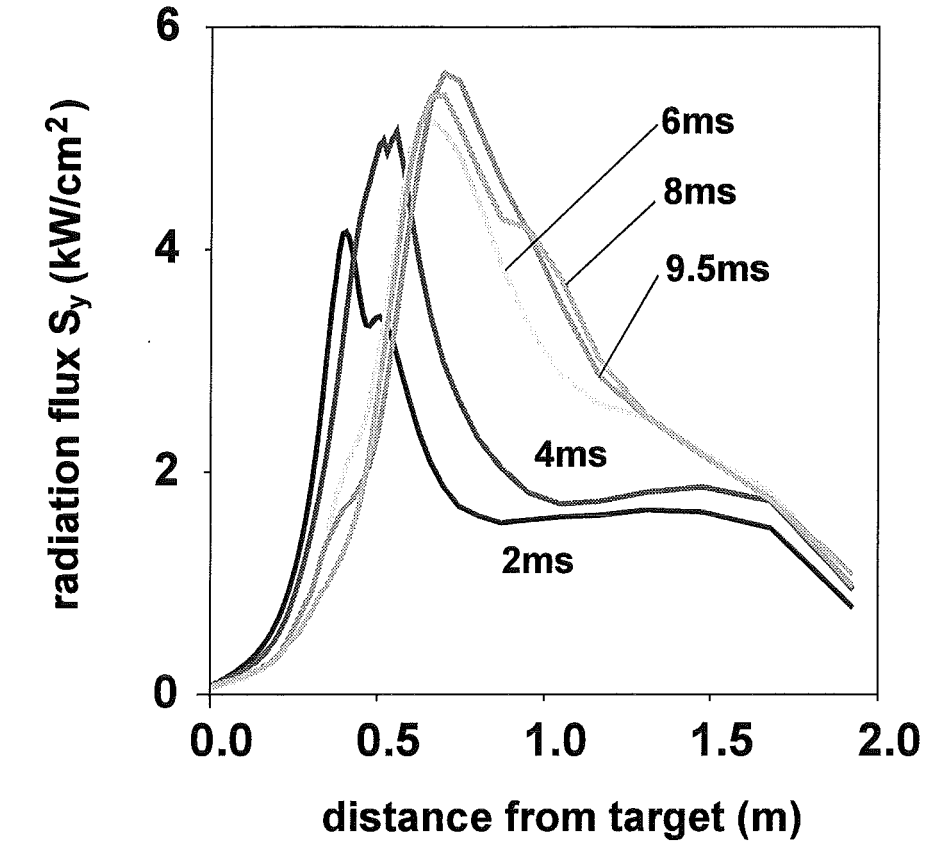

Fig. 116c. Lateral radiation fluxes to the upper side wall. Same conditions as in Fig. 116a.

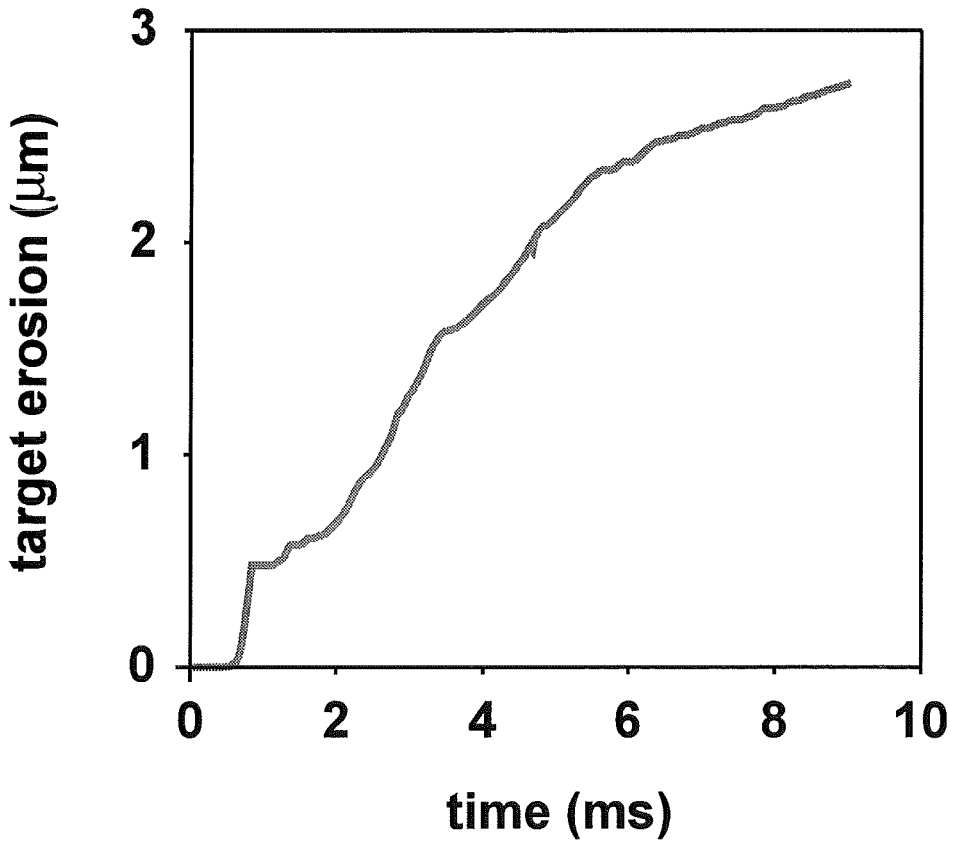

Fig. 117. Time dependence of target erosion at the SSP. Same conditions as in Fig. 116a.

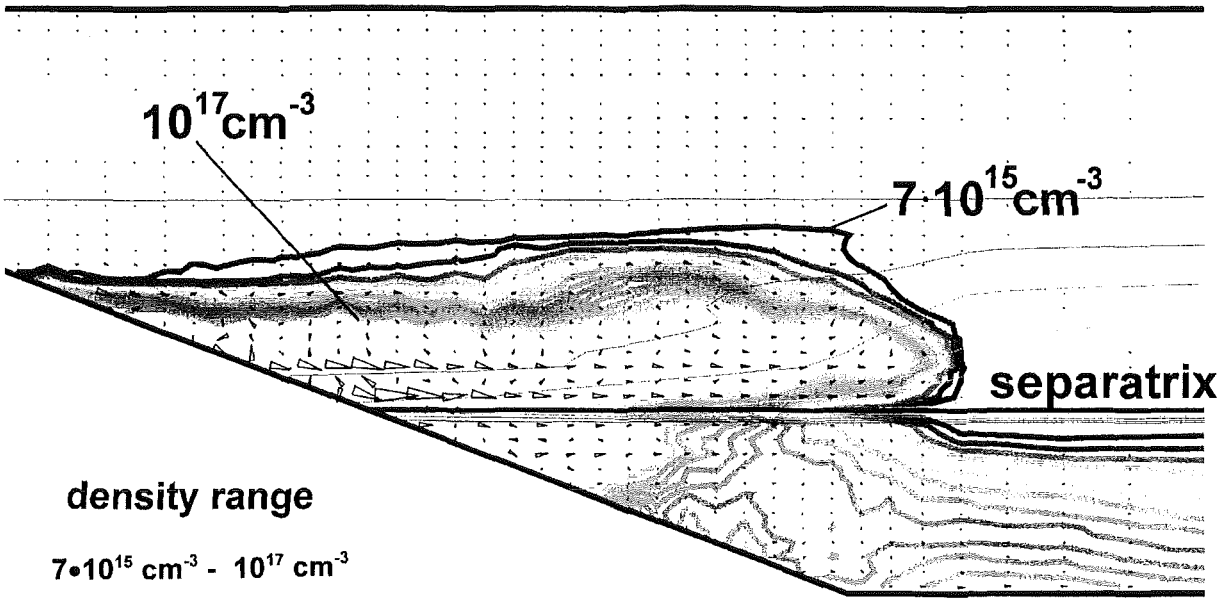

Fig. 118. Density contour plot plus flow pattern at 4 ms. Separatrix upstream.

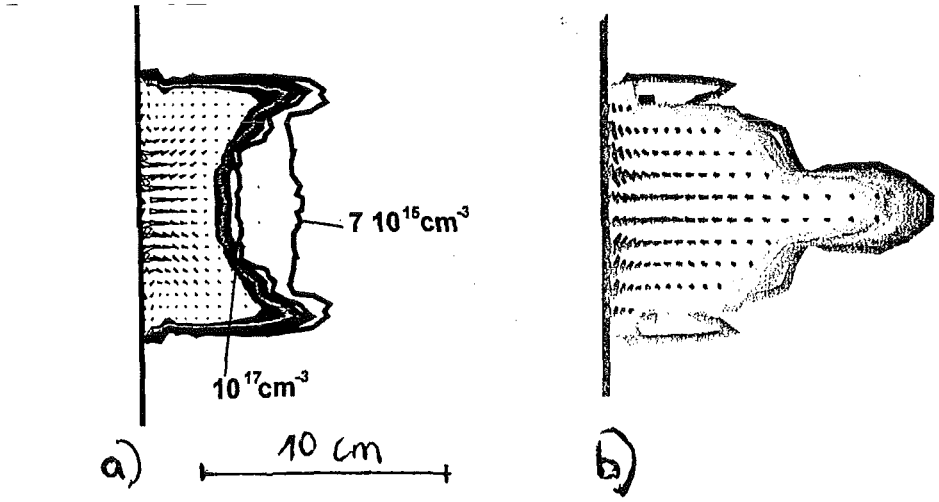

Fig. 119. Comparison of 2 dim contour plots of plasma density and plasma flow in a carbon plasma shield at 40 μs with a) Bohm diffusion coefficient and b) classical diffusion. Horizontal target, Gaussian power density profile, peak power density 100 MW/cm^2. The density range is the same for both plots.

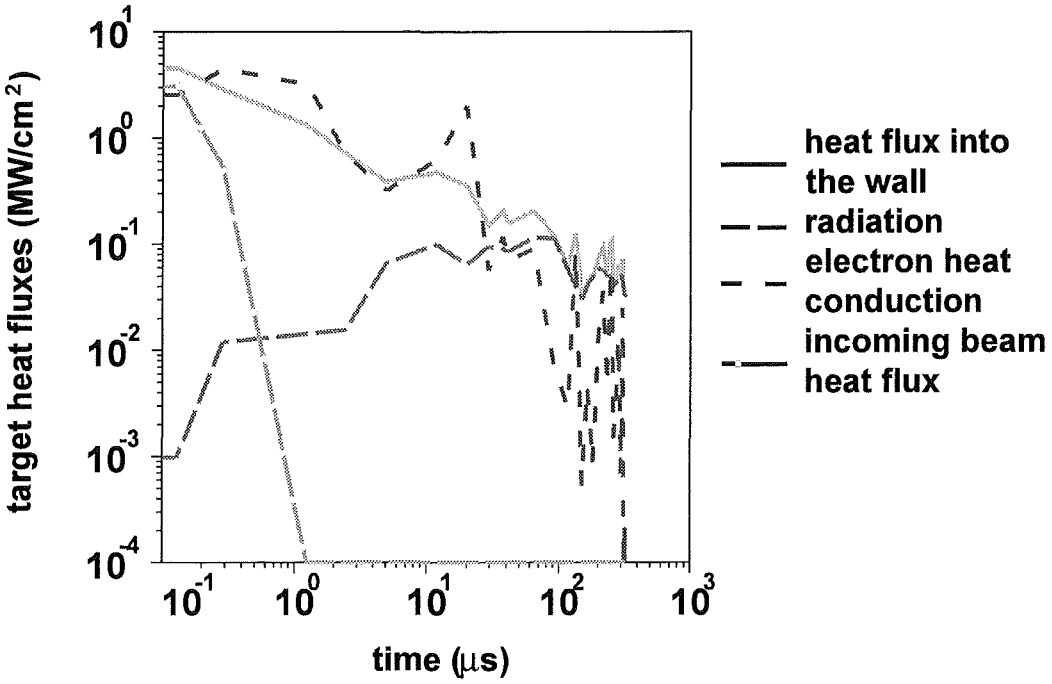

Fig. 120. Time evolution of target heat fluxes for a horizontal graphite target. Impact energy of the hot plasma is 1 keV. Realistic power density profile, peak power density is 100 MW/cm^2 along the separatrix

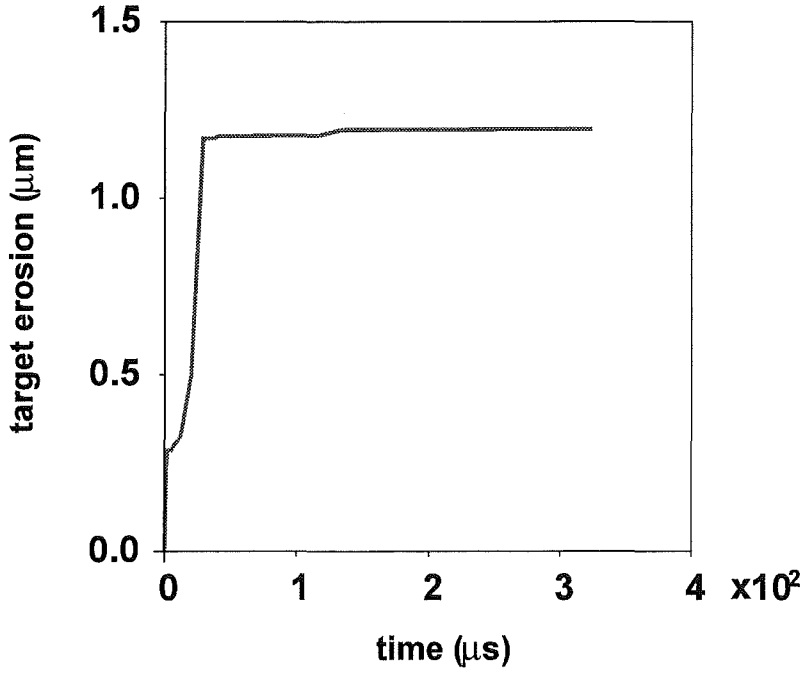

Fig. 121. Time dependent erosion for a horizontal graphite target. Realistic power density profile, peak power density is 100 MW/cm^2 along the separatrix. Impact energy of the hot plasma is 1 keV.

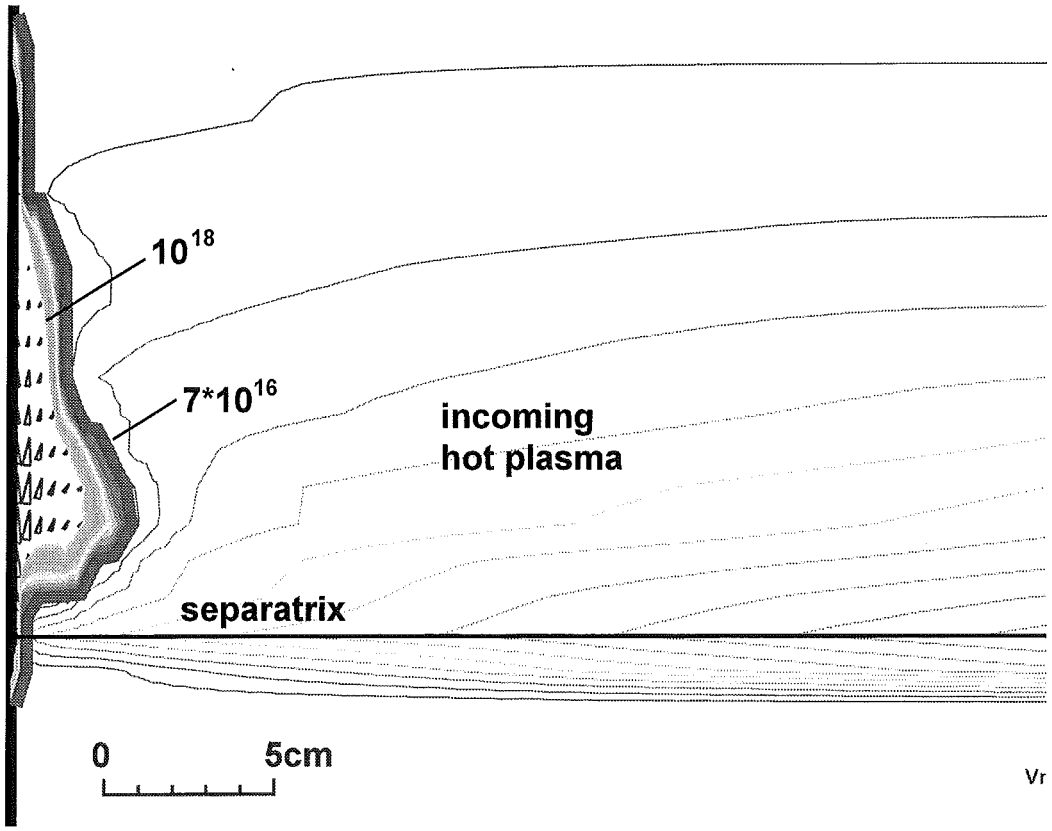

Fig. 122. Contour plot of plasma density and plasma flow (Γ=nv, arrows) at 20 μs for a horizontal graphite target. Impact energy of the hot plasma is 1 keV. Peak power density is 100 MW/cm^2.

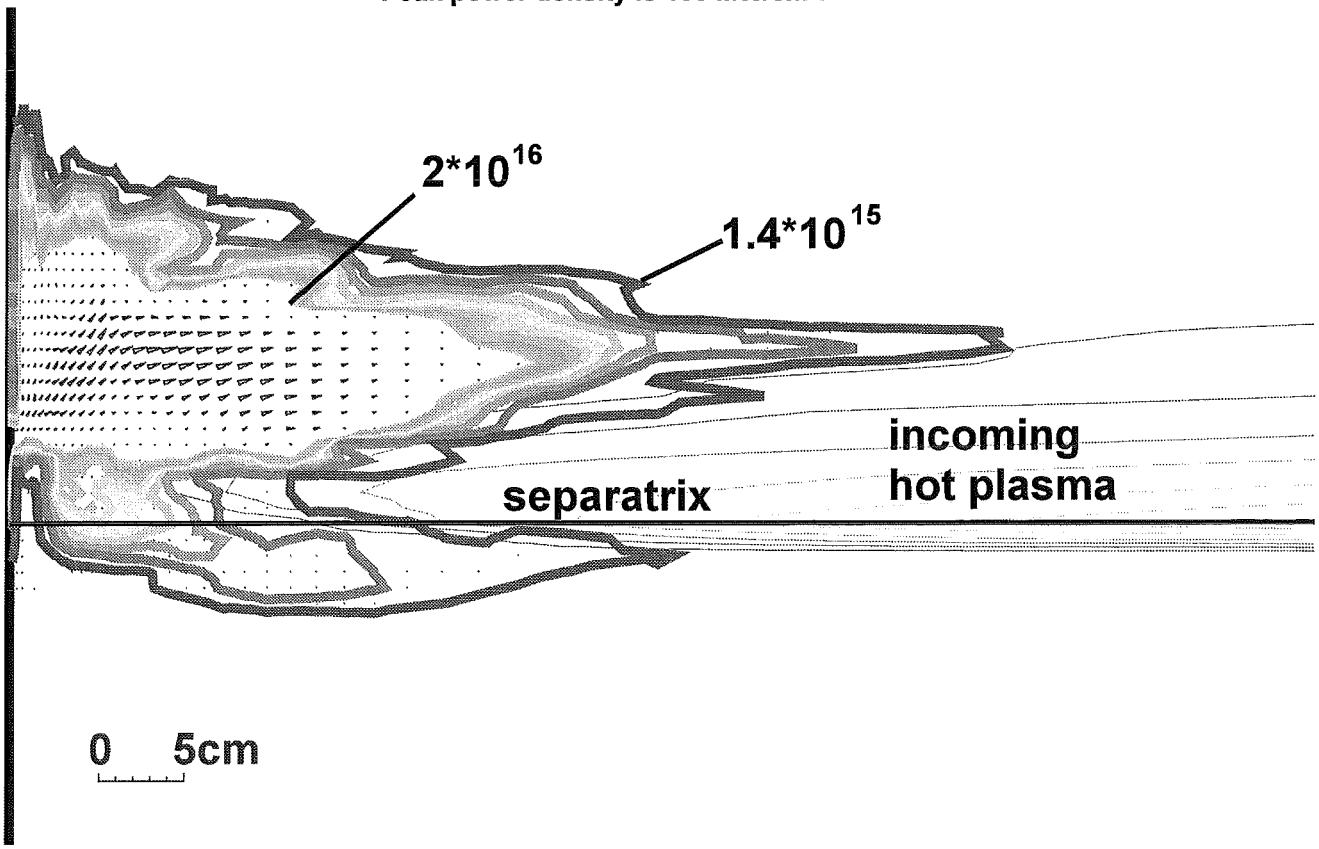

Fig. 123. Plasma density and plasma flow at 92 μs for a horizontal graphite target. Max. density inside the plasma bubble is 10^{18} cm^{-3}. Impact energy of the hot plasma is 1 keV. Peak power density is 100 MW/cm^2.

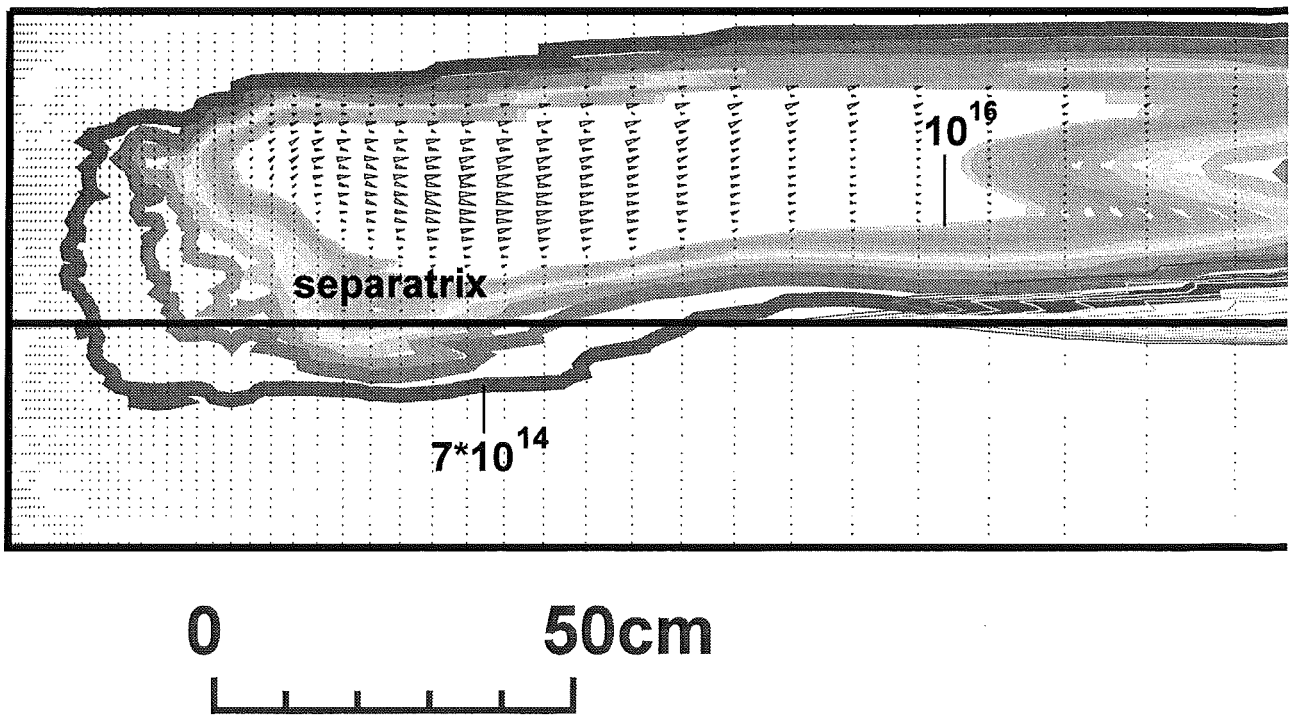

Fig. 124. Plasma density and plasma flow in a carbon plasma shield at 353 μs for a horizontal graphite target. Max. density inside the plasma bubble is 10^{17} cm^{-3}. Impact energy of the hot plasma is 1 keV. Peak power density is 100 MW/cm^2.

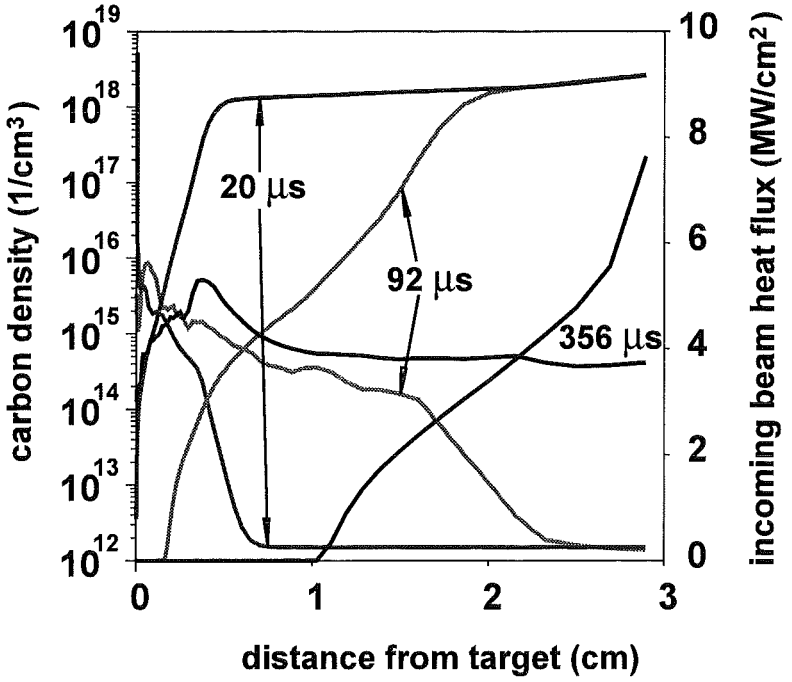

Fig. 125. Carbon density profiles and energy deposition of the impacting hot plasma along the separatrix for 3 different times. Impact energy of the hot plasma is 1 keV. Peak power density is 100 MW/cm^2.

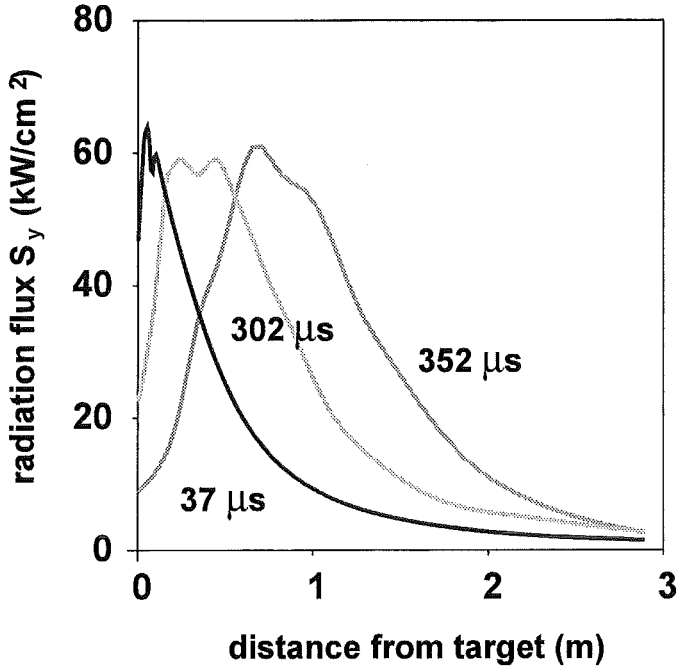

Fig. 126. Radiative fluxes from a carbon plasma shield to the side wall. Horizontal graphite target, side wall distance 60 cm, impact energy of the hot plasma is 1 keV. Peak power density is 100 MW/cm^2.

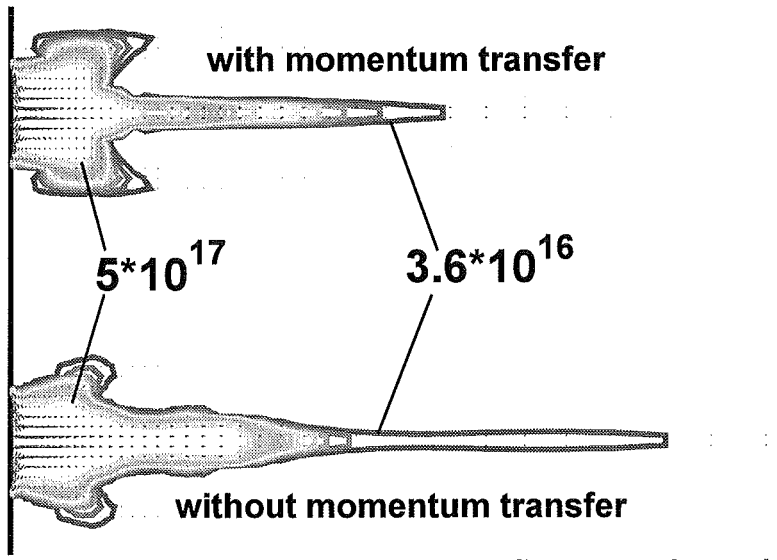

Fig. 127. Comparison of density distribution and plasma flow pattern in a carbon plasma shield at 100 μs with and without momentum transfer from the hot plasma ions for a horizontal graphite target. Gaussian power density profile with peak power density of 100 MW/cm^2.

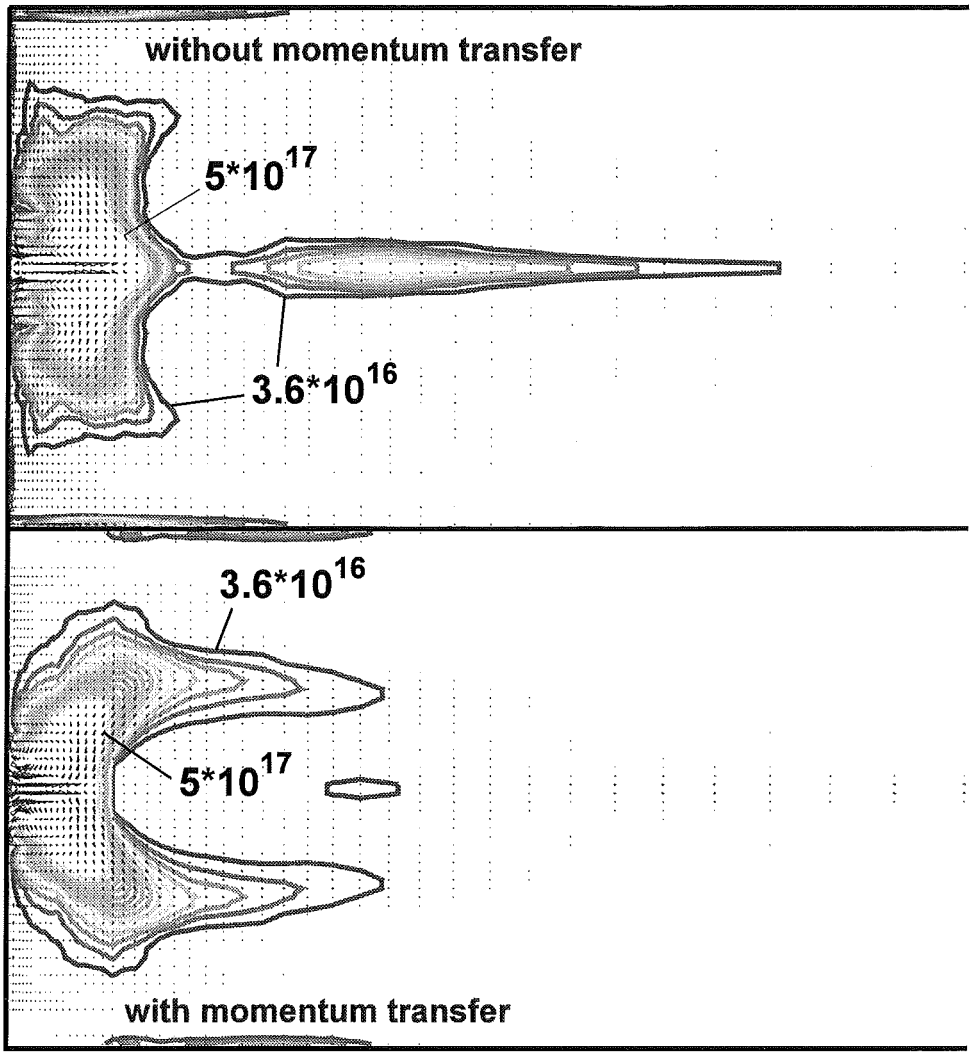

Fig. 128. Comparison of density distribution and plasma flow pattern in a carbon plasma shield at 300 μs with and without momentum transfer from the hot plasma ions. Same conditions as Fig. 127.

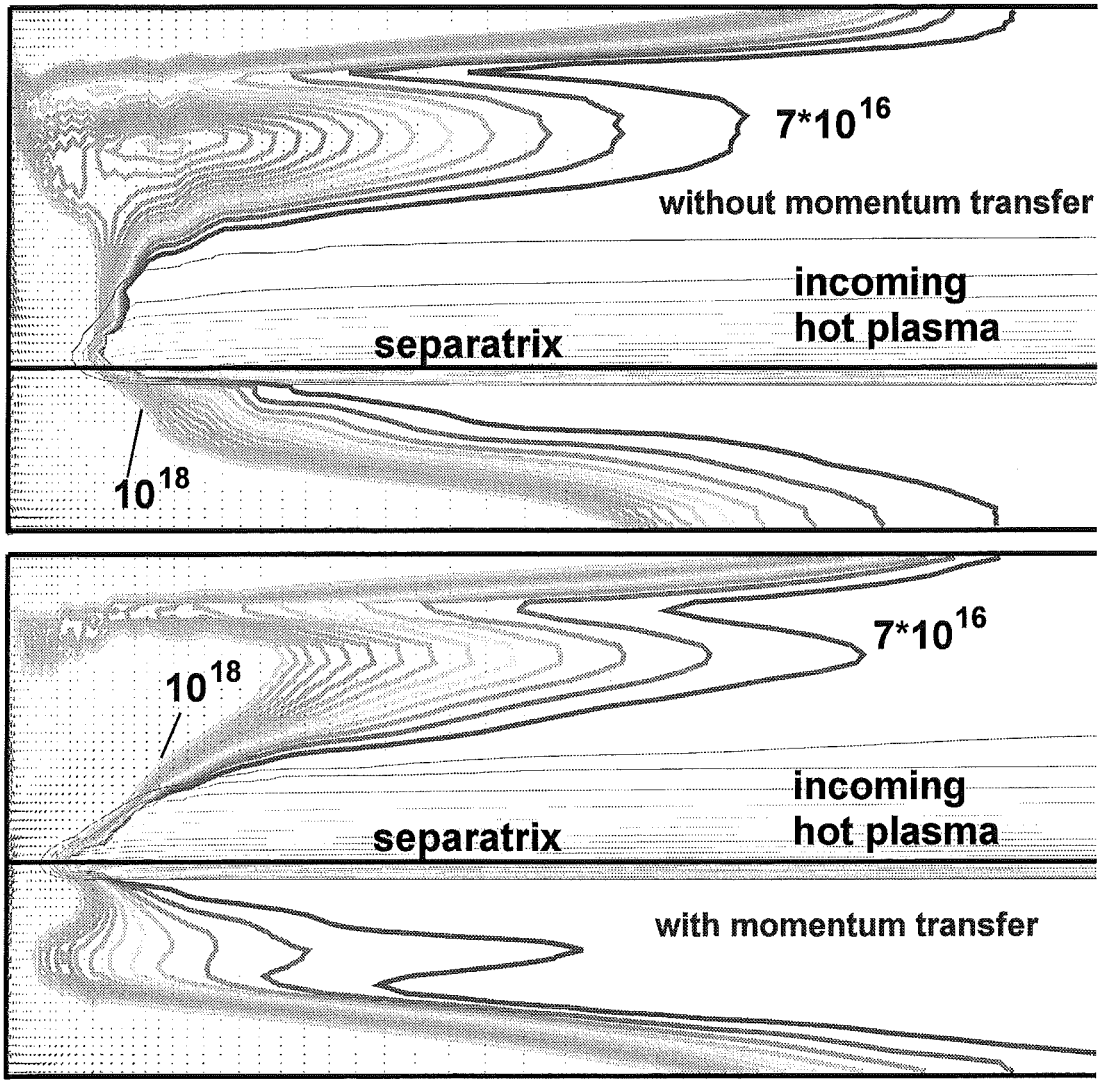

Fig. 129. Comparison of density distribution and plasma flow pattern in a carbon plasma shield at 715 μs with and without momentum transfer from the hot plasma ions for a horizontal graphite target realistic power density profile with peak power density of 100 MW/cm^2. Thick lines – contour plot of plasma density, thin lines – contour plot of incoming hot plasma power density.

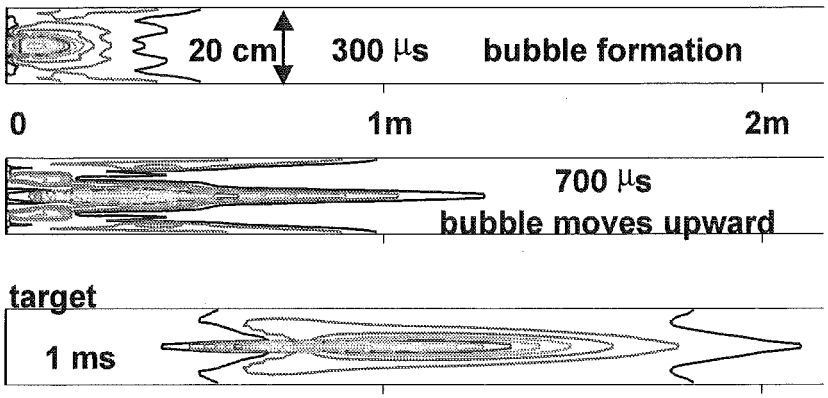

Fig.130. Impurity transport in the slot divertor. Gaussian power density profile with FWHM = 5cm and peak power density of 10 MW/cm^2. Time duration of the heat load is 40μs. Plasma density ranges are are $6\cdot10^{15}$-$7.2\cdot10^{16}$ cm^{-3}, $3.2\cdot10^{15}$-$3.9\cdot10^{16}$ cm^{-3} and $2.0\cdot10^{15}$-$2.3\cdot10^{16}$ cm^{-3} for upper, middle and lower plot correspondingly.

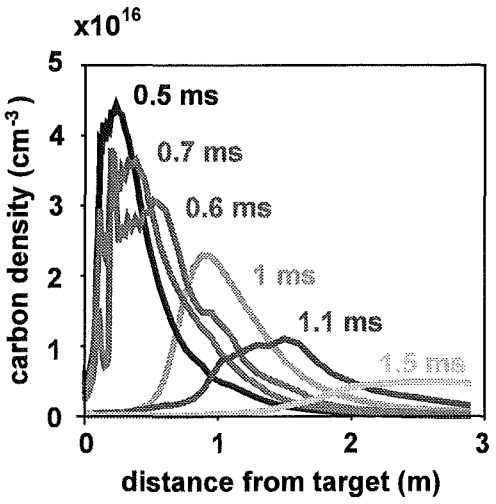

Fig.131. Time evolution of carbon density profiles in the slot center

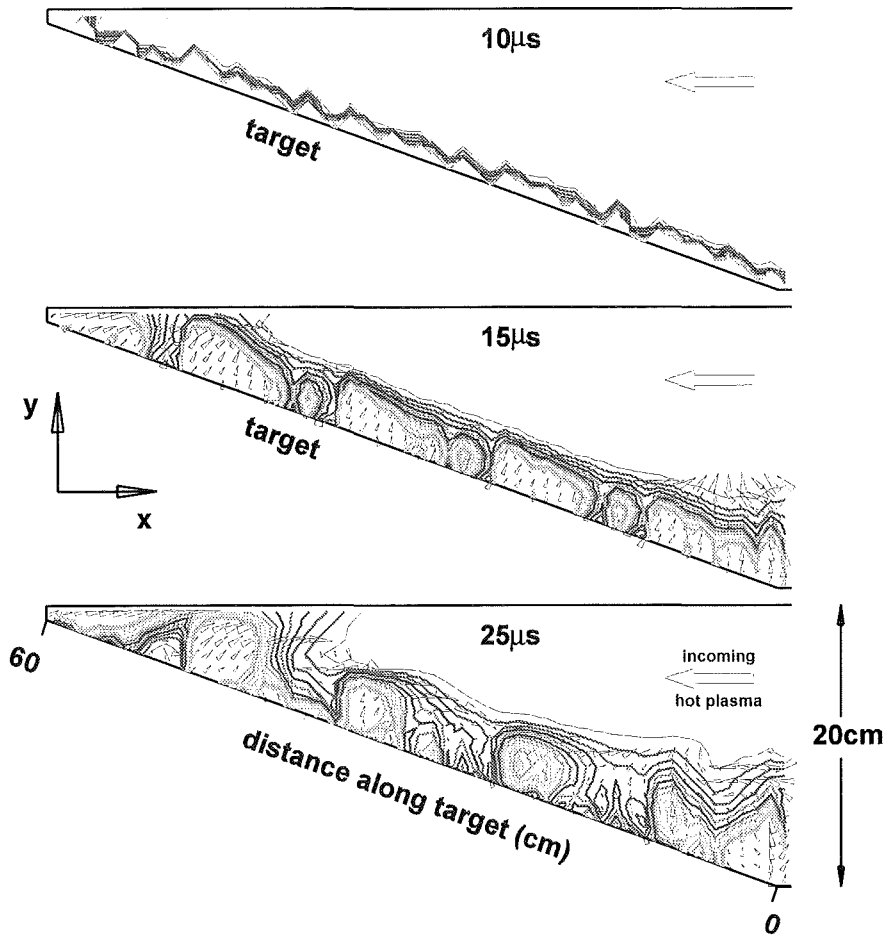

Fig. 132. Plasma density and velocity in a carbon plasma shield for a vertical target. Constant power density in y direction, power density is 5 MW/cm^2.

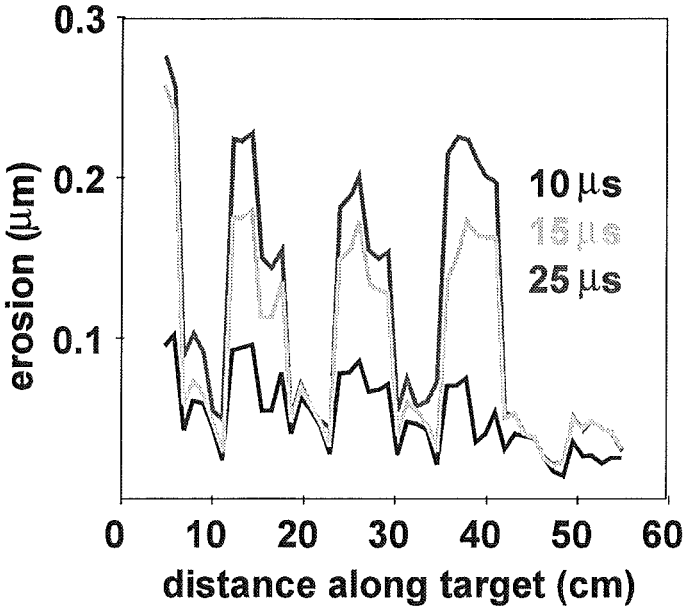

Fig. 133 Erosion profiles along the target for 3 different times.

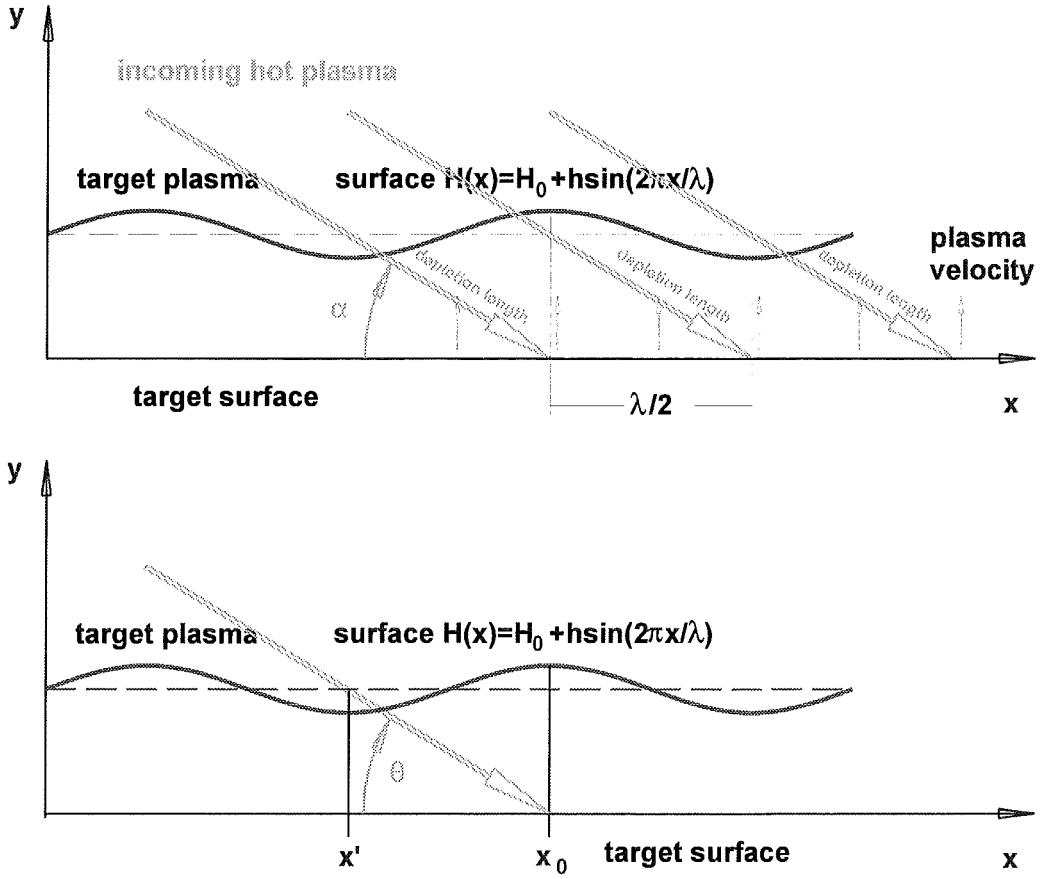

Fig. 134. Scheme for analytical modeling of plasma shield modulation

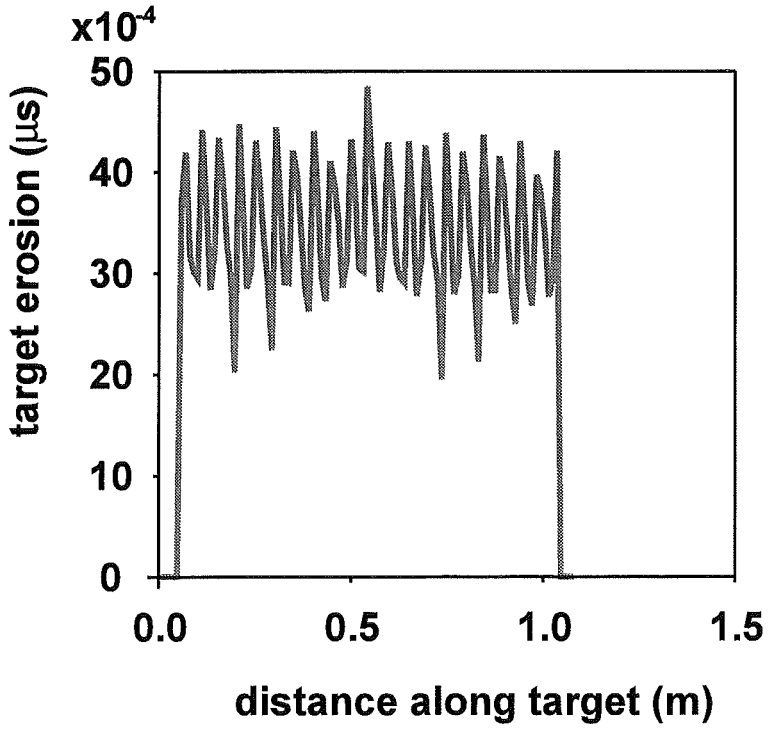

Fig.135a. Modulation of target erosion at early time of instability development (1 μm) with short wavelength.

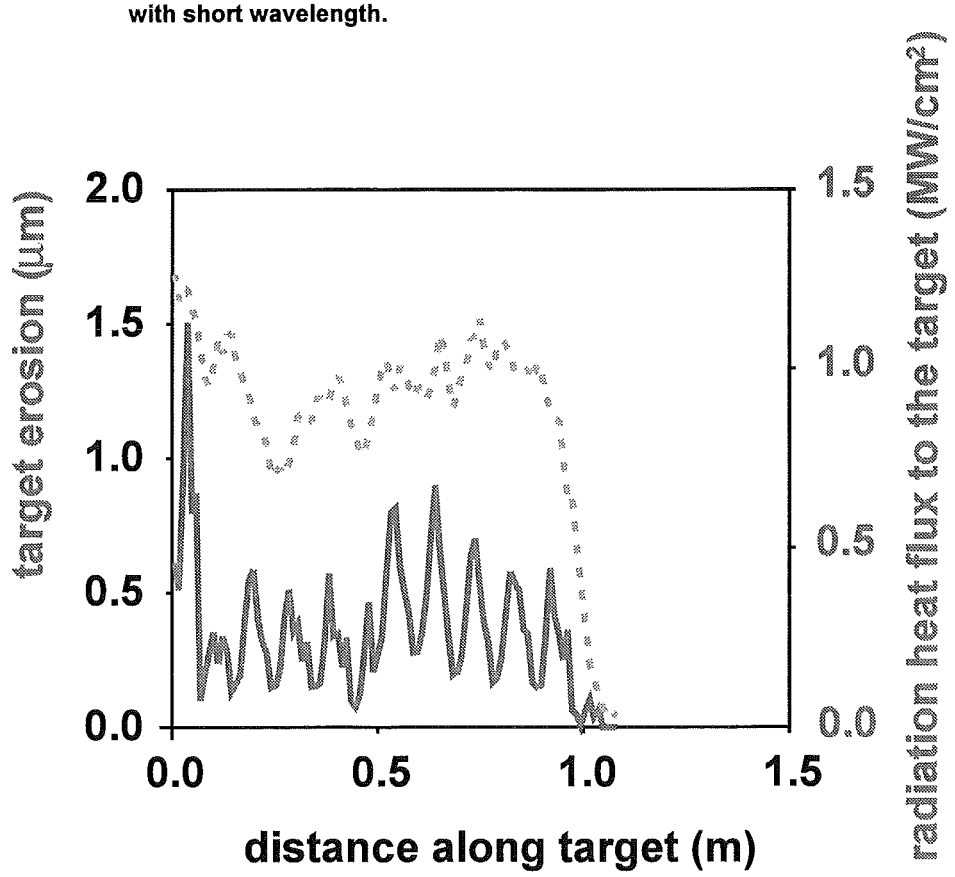

Fig.135b. Modulation of erosion at 100 μs showing twice longer wavelength in comparison with Fig.135a. The dotted line shows the radiation flux at the same time.

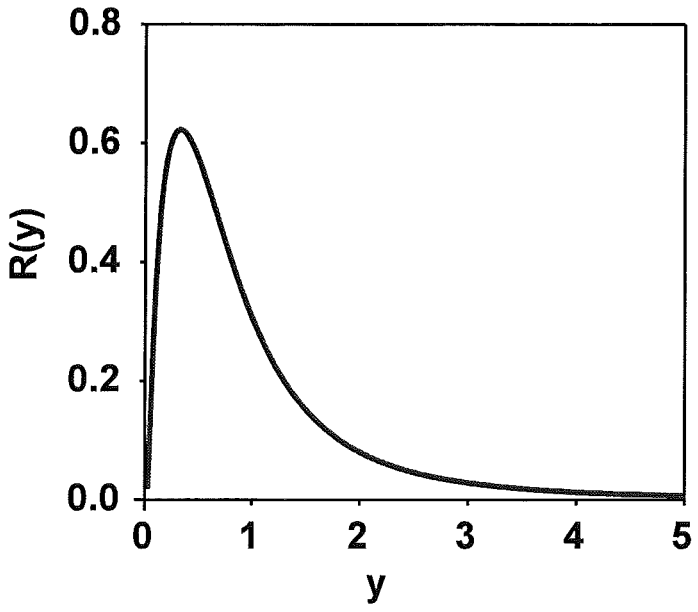

Fig. 136. The kernel R(y) (eq.44) used in the eqs. 40, 42 and 43 for t-0.1.

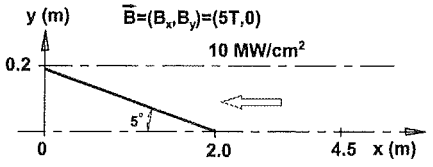

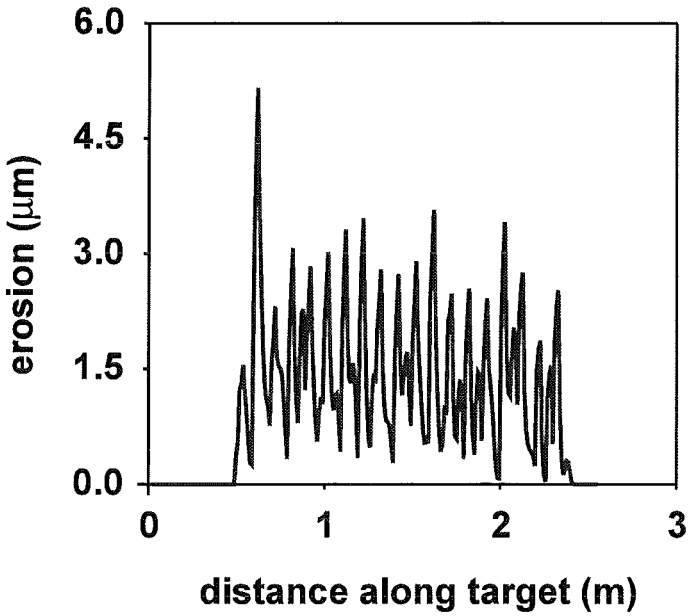

Fig. 137a. Erosion profile at 260 μs and geometry for inclined impact of hot plasma on a horizontal graphite target. Power density is 10 MW/cm^2 and constant along y direction.

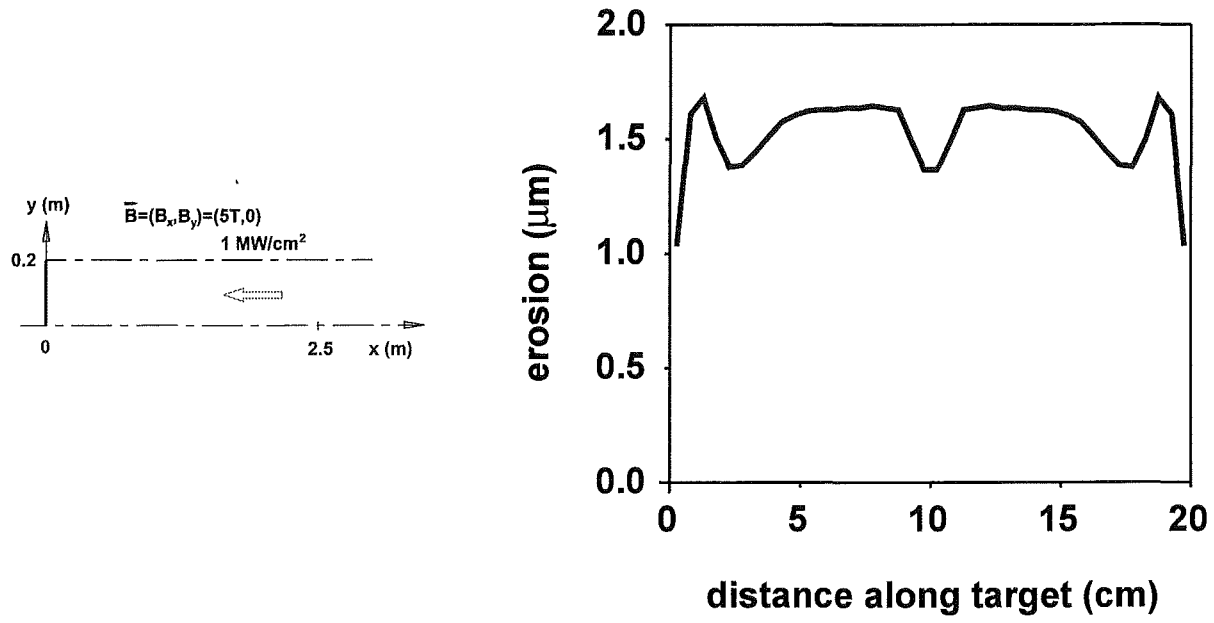

Fig. 137b. Erosion profile at 260 μs and geometry for perpendicular impact of hot plasma. Power density is 1 MW/cm^2. It is constant along the y direction.

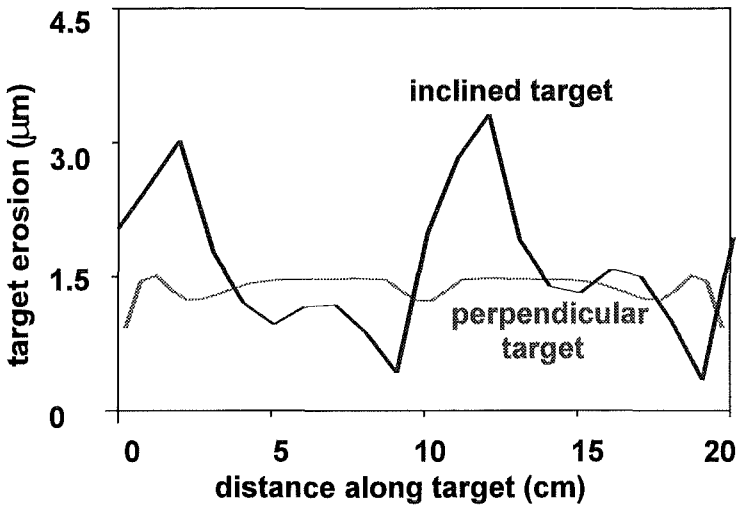

Fig. 138. Comparison of erosion for perpendicular and inclined impact of hot plasma at 260 μs. Target heat load is 1 MW/cm^2.

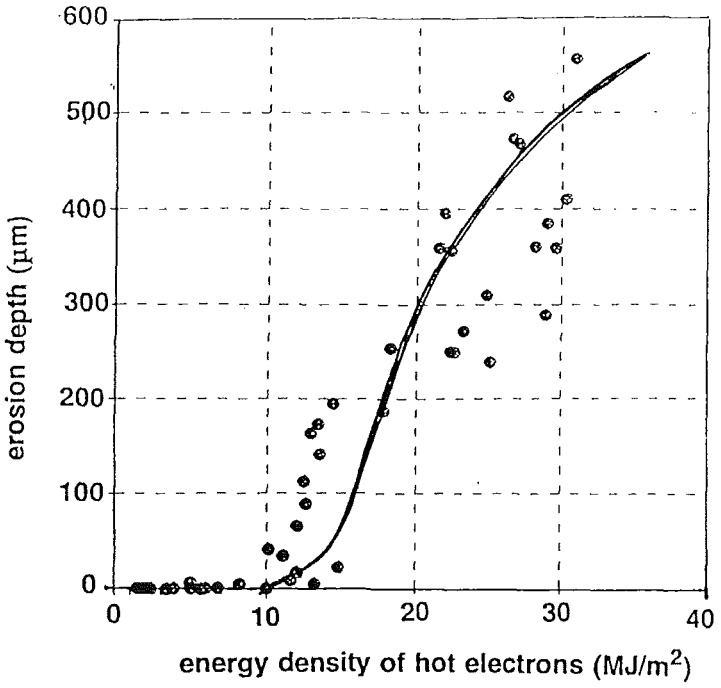

••• experimental results,
— calculated using a threshold value for destruction of 10 kJ/g and using calculated energy deposition profiles

Fig. 139a. Graphite target erosion as function of energy density of the impinging hot electrons. Impact angle 90°.

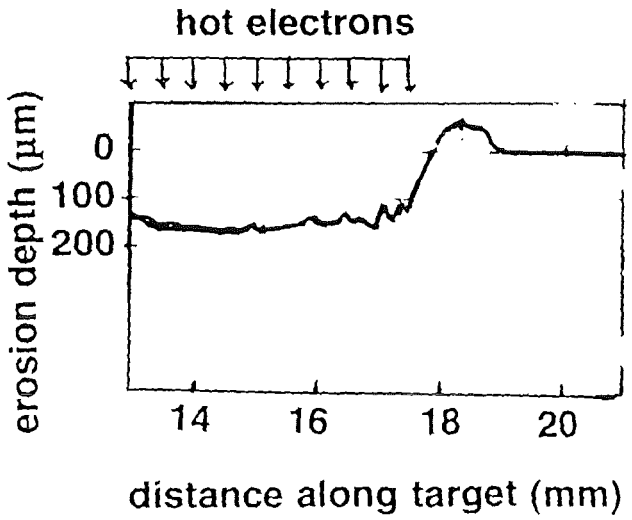

Fig. 139b. Erosion profile for a perpendicular tungsten target. Energy of the hot electrons 12 MJ/m².

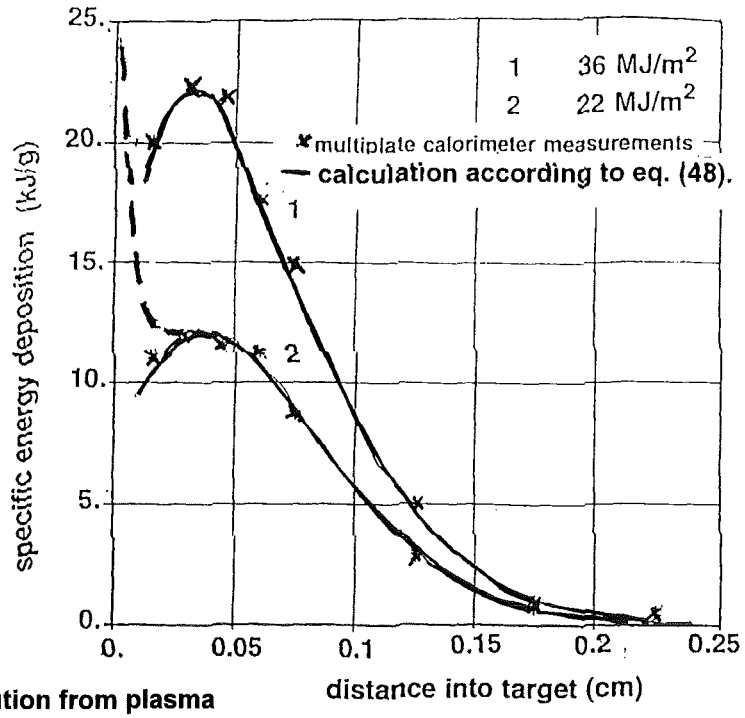

Fig. 140. Comparison of measured and calculated specific energy deposition of hot electrons of energy above 36 keV into graphite for two different energy densities of the incoming hot electrons.

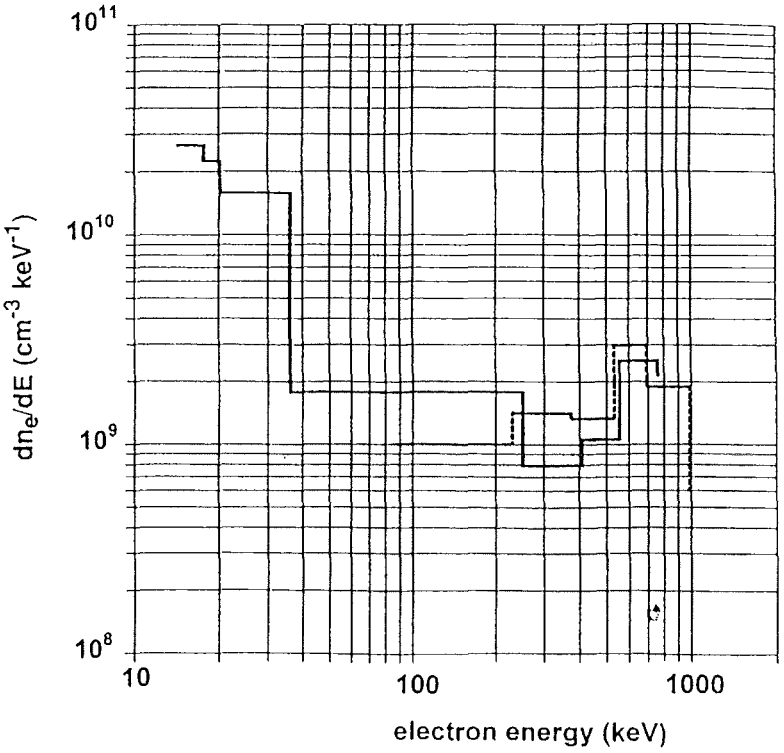

Fig. 141. Energy spectrum of the hot electrons. Solid line results from multifoil analyzer, dashed line from magnetic analyzer.

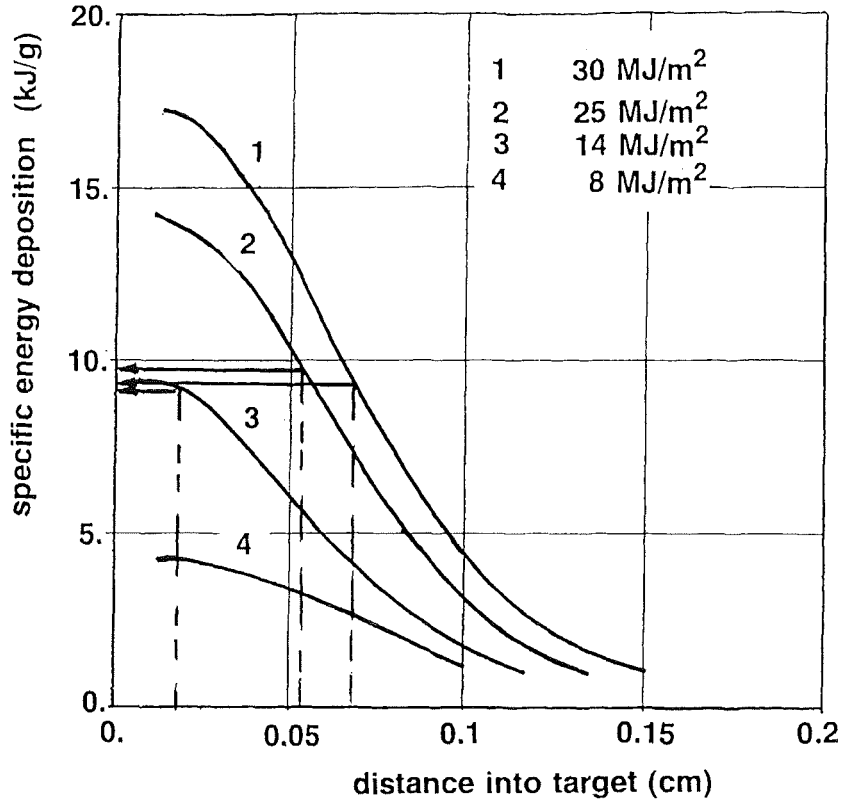

Fig. 142. Calculated specific energy deposition of the hot electrons in graphite and determination of the threshold for graphite enhanced erosion.

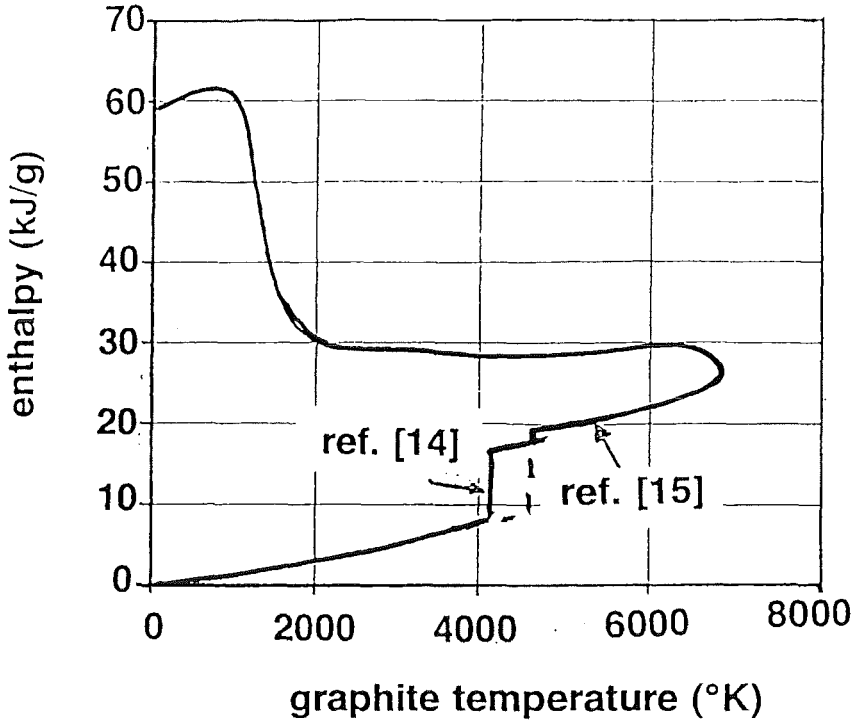

Fig. 143. Enthalpy diagram for carbon.

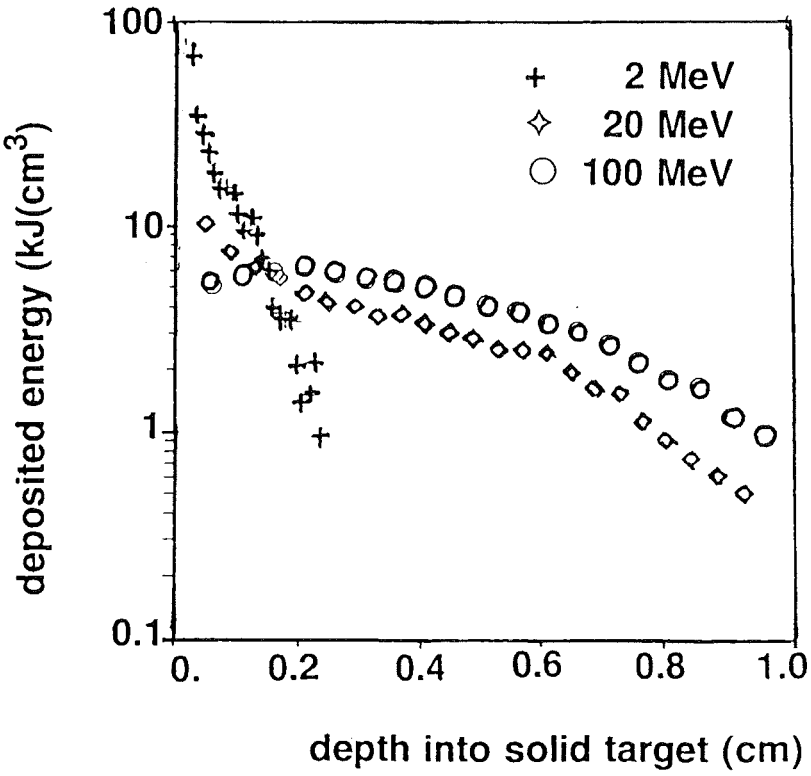

Fig. 144. Energy deposition of runaway electrons of different energies in graphite. Energy density of the runaways 30 MJ/m^2, inclination angle 5°,

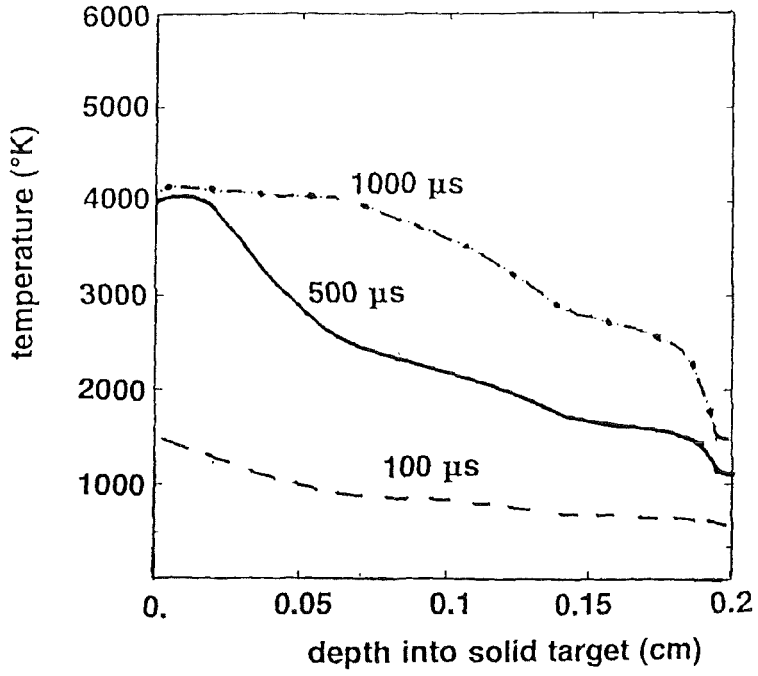

Fig. 145. Temperature profiles inside graphite for runaway electrons of energies 10 MeV and power density of 3 MJ/cm^2 at different times. Inclination angle is 5°.

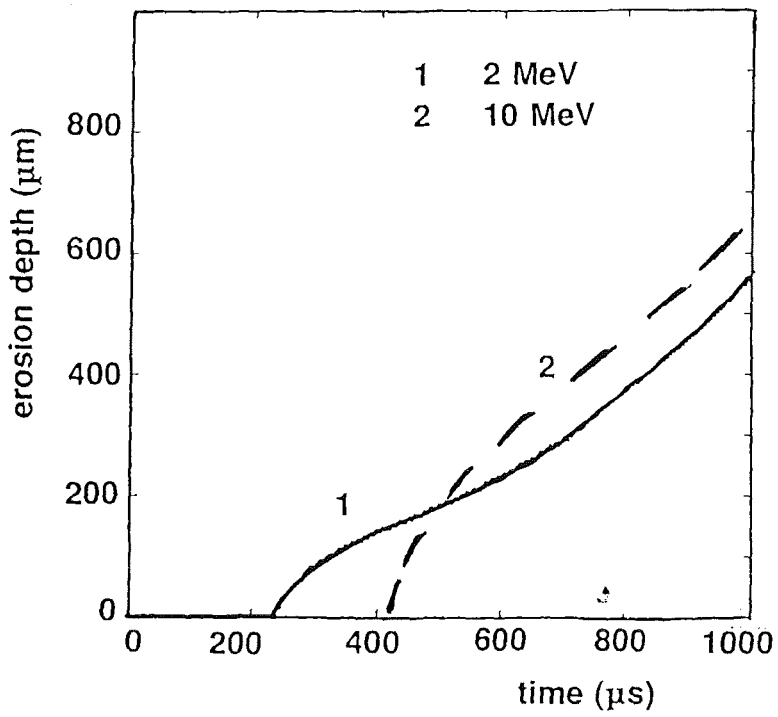

Fig. 146. Damage erosion for runaway electrons of beam power density of 3 MJ/cm^2 for two different electron energies. The inclination angle of the hot electrons is 5°.

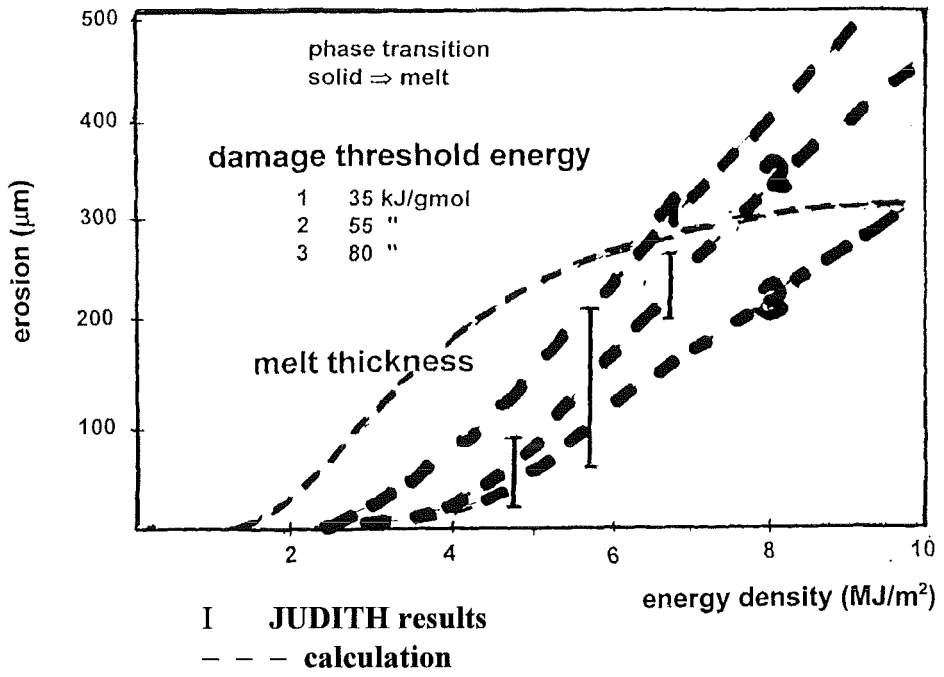

Fig. 147. Comparison of the calculated and measured erosion for Be using an e-beam of 120 keV and duration 5 ms.

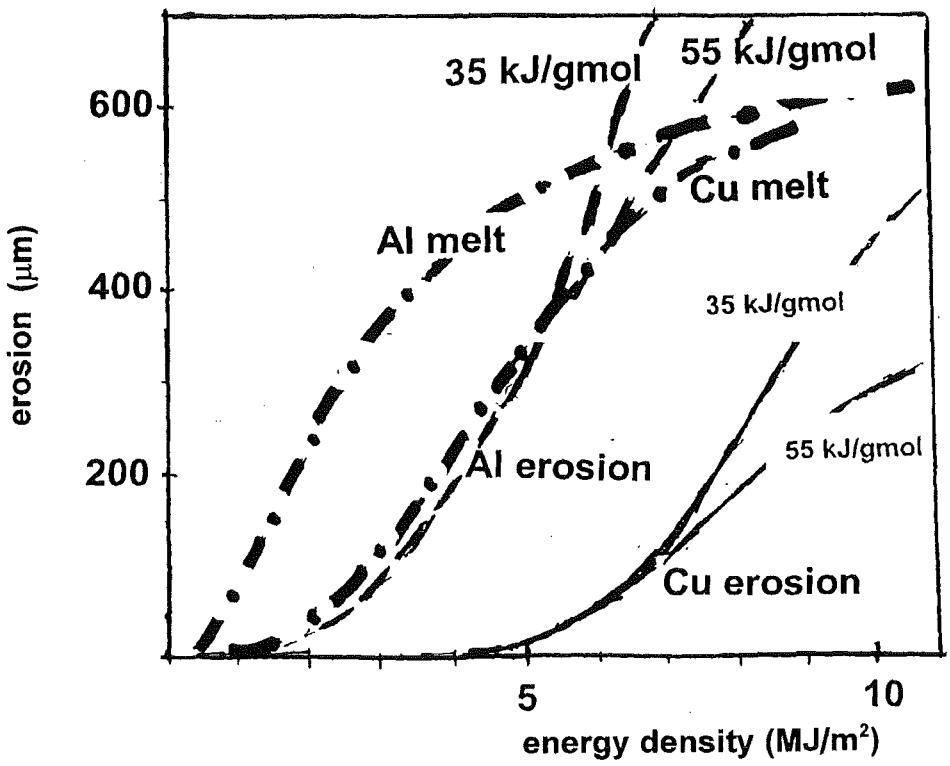

Fig. 148. Calculated results for melt layer thickness and enhanced erosion for aluminum and copper for the two damage threshold values 35 and 55 kJ/gmol for the conditions of the JUDITH facility with electrons of energy of 120 keV and pulse duration of 5 ms.

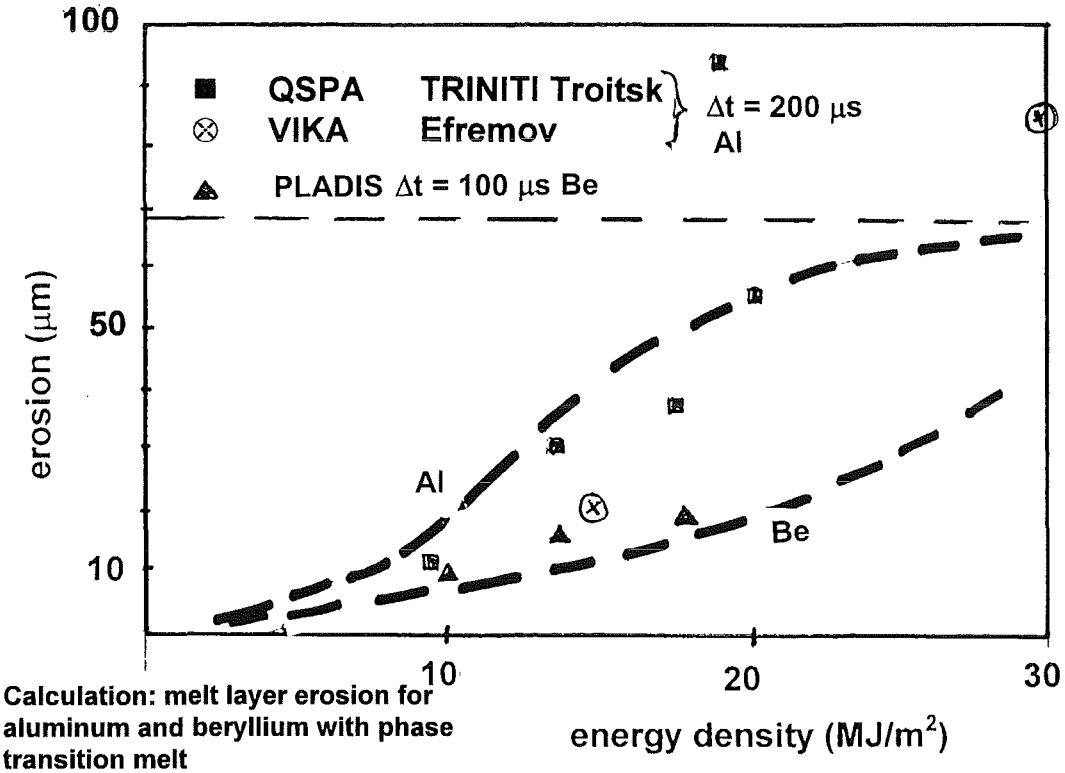

Calculation: melt layer erosion for aluminum and beryllium with phase transition melt
→ boiling close to the surface.
Experimental results: no errors are given

Fig. 149. Erosion of aluminum and beryllium under intense heat loads from plasma streams

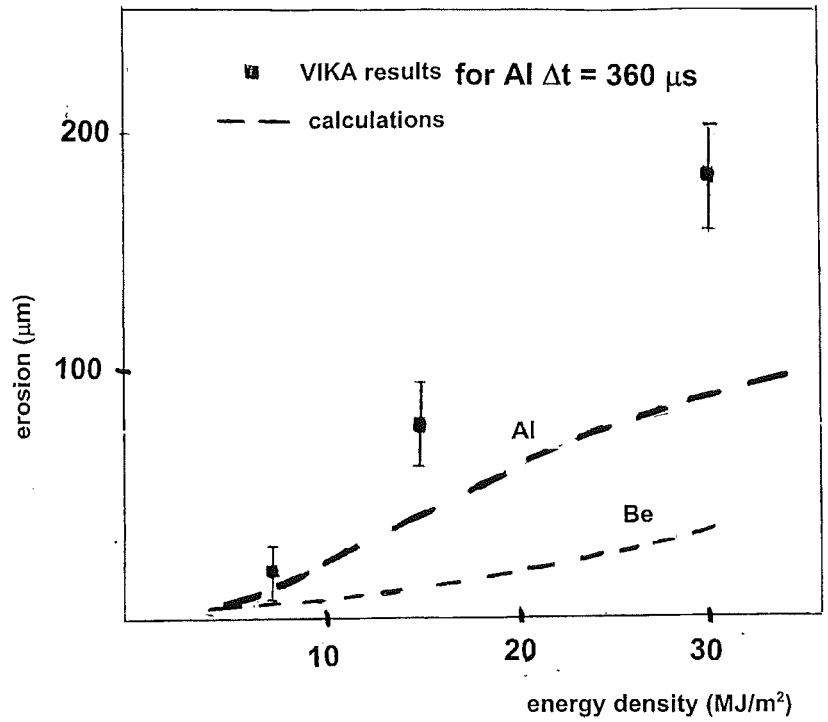

Fig. 150. Comparison of experimental data and calculations for erosion of aluminum. Duration of plasma stream is 360 μs. perpendicular impact of unmagnetized plasma.
The error bars indicate the difference of erosion values as obtained from profilometry and mass measurements.

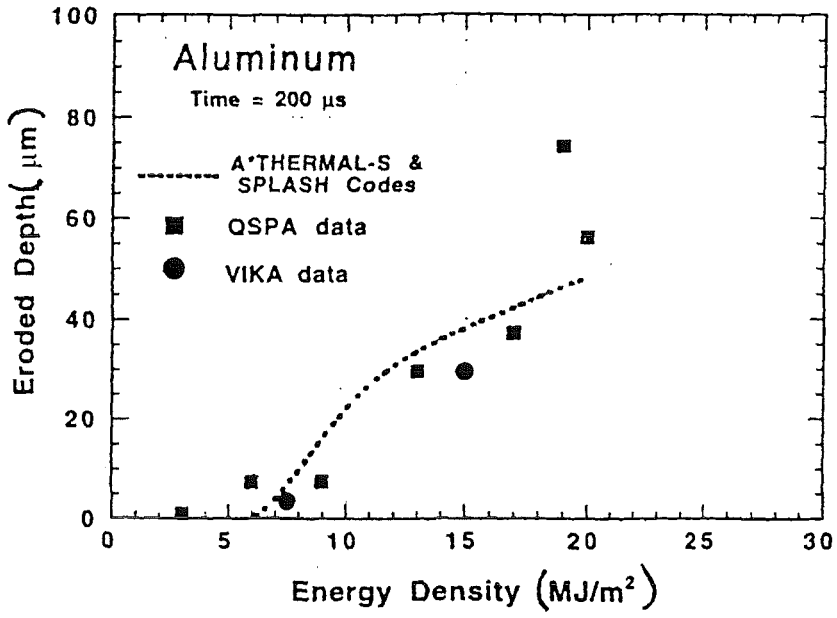

Fig. 151. Comparison of experimental data and calculation from [27].